Investigating the Photophysics of New and Stable Singlet Fission Materials

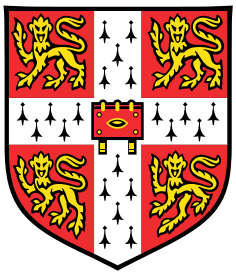

Peter Budden

Supervisor: Prof. Sir R. H. Friend

Department of Physics
University of Cambridge

This dissertation is submitted for the degree of
Doctor of Philosophy

Gonville and Caius College January 2021

I would like to dedicate this thesis to my parents.

Declaration

I hereby declare that except where specific reference is made to the work of others, the contents of this dissertation are original and have not been submitted in whole or in part for consideration for any other degree or qualification in this, or any other University. This dissertation is the result of my own work and includes nothing which is the outcome of work done in collaboration, except where specifically indicated in the text. This dissertation is less than 60,000 words including the abstract, tables, footnotes and appendices. The use of the first person plural is strictly a matter of style in keeping with standard scientific convention.

Peter Budden
January 2021

Acknowledgements

I have many people to thank for their help and support over the past four years, without whom this thesis could never have been written. First and foremost, I am grateful to my supervisor Prof. Sir Richard Friend for all of his guidance, enthusiasm and encouragement. It has been a pleasure to learn from such an excellent scientist and mentor. Thank you also to Dr Andrew Musser, Dr Akshay Rao, and Dr Hugo Bronstein, all of whom have generously advised me in various capacities along the way. Thanks goes to Dr Hannah Stern for getting me started on singlet fission and inspiring my early interest in the subject. Dr Leah Weiss has been a wonderful mentor and collaborator, who it has been a pleasure to work with.

All of the work presented here is the result of various collaborations with talented and creative synthetic chemists who provided me with more interesting materials than I possibly had time to investigate. My thanks go to Dr Kealan Fallon for the cibalackrots, Prof. Uwe Bunz and Dr Matthias Müller for the "butterfly-winged" acenes, and the group of Prof. John Anthony for the tetracene derivatives. I was also incredibly fortunate to have the opportunity to collaborate with the group of Prof. Jan Behrends at the Freie Universität, Berlin for ESR and ODMR measurements, which have greatly enriched my understand of singlet fission and the materials I have studied. Thanks go to Dr Naitik Panjwani for his patience and dedication, to Prof Robert Bittl for spirited discussions of my experimental results, and the rest of the group in Berlin for being so welcoming. In my third year I was extremely fortunate to be able to take a three-month internship at the Committee on Climate Change. I thank all of the talented and devoted team there for keeping the true motivation for this work at the forefront of my mind.

In Cambridge I have had the privilege of being a member of OE, a research group so large it could be its own department. Thank you to Ned Booker, Patrick Conaghan, Mike Price, Nate Davis, Murad Tayebjee and Matt Menke for helping me find my feet at the beginning (especially the Fitness Fridays), to Vincent Kim and Alex Gillett for teaching me how to use the fast lab, and to Simon Dowland for his PLQE wisdom. Thanks to Jeff Gorman, Ture Hinrichsen, Jesse Allardice, Hope Bretscher, Raj Pandya,

Emrys Evans, Sarah Orsborne, Heather Goodwin, David Palecek, Lissa Eyre, Alan Bowman, Stuart MacPherson, Kyle Frohna, and all the other friendly faces around the group who have been alongside me throughout this process. Bluebell Drummond deserves special thanks for her friendship, solidarity, and dedication to beautiful figures, and I thank her, Hope, Jeff, Leah and Alex for their careful reading of this thesis. Thank you to Jennie Nelson, Richard Gymer, and all the other friendly and dedicated administrators and support staff that the group are lucky to rely on. I apologise to all those I have missed, and thank them too.

Outside of the lab I have been blessed to have the friendship and support of Courtney Froehlig, Cameron Smith, Gabby Fiore, Ruby Guyatt, Lucia Corsini, and Debbie Luxon in Cambridge. I am so thankful to Courtney for living together with me throughout almost three years of the shared highs and lows of PhD life, and especially for when she and Chris took me in and gave me a happy and safe place to ride out the anxiety and uncertainty of the first few months of the pandemic.

Supporting me from further afield and always ready to welcome me whenever I needed a break from the lab were Caitlin Turner, Nick de Mulder, Ffion Bevan, Jess Bone, Helen Potts, Tom Bailey, Iisha Williams, Rhys Cumming, Ed Siddons and many others. I am lucky to have you. Thank you to Mum and Dad who have always cheered me on, even when I couldn't satisfactorily explain to them what it actually was I was working on, and to my wonderful siblings, Lucy, Jenny, and George.

Finally, thank you to Horatio for always believing in me. Thank you for showing me that finishing a PhD thesis was even possible, for your unwavering love and support throughout every stage of this journey, and in particular for your companionship whilst writing this thesis through a global pandemic; it made all the difference.

Abstract

In this thesis, we describe our investigations into the mechanism of singlet exciton fission, examining the effects of morphology, aromaticity, and photoluminescence yield on the fission process, and developing generalised principles to aid the design of new materials. Singlet fission is the process of forming two triplet excitations from one photon and is apparent in only a handful of organic molecules due to the requirement for the lowest excited triplet state to have approximately half the energy of the lowest excited singlet state. Through this process, there is potential to improve the efficiency of solar cells by reducing losses to thermalisation. Consequently, new singlet fission materials, particularly those with better photostability, are of great interest.

We have drawn our conclusions by studying three novel singlet fission systems: TIPS-tetrabenzo[a,c,l,n]pentacene (TTBP), a family of indolonaphthyridine derivatives (INDTs), and a series of tetracene derivatives with different solubilising groups. In each system, we apply ultrafast optical techniques in combination with optically pumped magnetic resonance experiments to characterise the physics of photoexcited states in our materials. These characterisations then allows us to deduce structure-function relationships and further our mechanistic understanding of the fission process.

The first two systems expand the narrow library of known singlet fission materials and introduce two new pathways to more photostable fission materials: via benzannulation of acenes in TTBP or via excited state aromaticity in INDTs. Our characterisation of TTBP leads to a new design principle for reducing non-radiative voltage losses by maximising photoluminescence yield. The final study on tetracene derivatives demonstrates that differences in intermolecular packing induced by small changes to molecular structure have a drastic effect on singlet fission. Our findings indicates that a delicate balance must be struck whereby orbital overlap and inter-triplet coupling are neither too weak nor too strong.

Table of contents

List of figures

List of tables

Nomenclature

Acronyms / Abbreviations

2DES 2-dimensional electronic spectroscopy

BPEA 9,10-Bis(phenylethynyl)anthracene

CCD Charge-coupled device

CT Charge transfer

CW Continuous wave

DBTP 6,13-di-benzothiophene-pentacene

DCB Dichlorobenzene

DFG Difference frequency generation

DPA diphenyl-anthracene

DPBF 1,3-diphenyl-isobenzofuran

DPH Diphenyl-hexatriene

DPND dipyrrolonaphthyridinedione

DPP Diketo-pyrrolopyrrole

DTP 6,13-di(2'-thienyl)pentacene

EQE External Quantum Efficiency

ESR Electron spin resonance

GA Genetic algorithm

GHGs Greenhouse gases

GIWAXS Grazing incidence wide angle x-ray scattering

GSB Ground state bleach

HOMO Highest occupied molecular orbital

ICCD Intensified charge-coupled device

IIDDT-Me Isoindigo-di(methylthiophene) copolymer

IND Indolonaphthyridine

INDT Indolonaphthyridine thiophene

IPCC Intergovernmental Panel on Climate Change

IR Infra red

ISC Intersystem crossing

LUMO Lowest unoccupied molecular orbital

MCP Microchannel plate

MEG Multiple exciton generation

MFE Magnetic field effect (on photoluminescence)

NFA Non-fullerene acceptor

NICS Nucleus-independent chemical shift

NIR Near infra-red

NOPA Non-collinear optical parametric amplifier

o-DCB ortho-dichlorobenzene

ODMR Optically detected magnetic resonance

OLED Organic light emitting diode

OPA Optical parametric amplifier

OPV Organic photovoltaic

PBTDOn poly(benzodithiophene-n-thiophene-1,1-dioxide) copolymer

PCE Power conversion efficiency

PDA Polydiacetylene

PDI Perylene diimide

PES Potential energy surface

PIA Photoinduced absorption

PL Photoluminescence

PLQE Photoluminescence Quantum Efficiency

PS Polystyrene

PtOEP Platinum octaethylporphyrin

QDI Quaterrylene diimide

SE Stimulated emission

TA Transient absorption

TCSPC Time-correlated single photon counting

TD-DFT Time-dependant density functional theory

TDI Terrylene diimide

TES Triethylsilylethynyl

TGPL Transient grating photoluminescence

THF Tetrahydrofuran

TIPS Triisopropylsilylethynyl

TMS Trimethylsilylethynyl

TR-2PPE Time-resolved 2 photon photoemission spectroscopy

TRA Triplet-radical annihilation

trESR Transient electron spin resonance

TTA-UC Triplet-triplet annihilation up-conversion

TTBP 10,21-bis(triisopropylsilylethynyl)tetrabenzo[a,c,l,n]pentacene

WLG White light generation

XRD X-ray diffraction

YAG Yttrium aluminium garnet

ZFS Zero-field splitting

Chapter 1

Introduction

Climate change is the defining crisis of our time. An effective response requires the rapid adoption of low-carbon alternatives to fossil fuels in order to meet the world's growing energy demands. Keeping to our international agreements and preventing catastrophic heating of more than 2 °C relative to pre-industrial levels will mean an unprecedented global deployment of renewable energy infrastructure in order to phase out fossil fuels by mid century, alongside improvements in energy efficiency to reduce demand wherever possible. As evidenced by the Intergovernmental Panel on Climate Change (IPCC) Special Report on 1.5 °C[1], every fraction of a degree of warming that can be prevented will make a meaningful difference, from habitat and biodiversity losses, to the frequency and severity of droughts, hurricanes, and other extreme weather events. We must act as fast as we can to bring our emissions of greenhouse gases (GHGs) to zero or make them net negative.

One way to accelerate this transition is through lowering the cost of renewables such as solar energy. Costs per kWh of solar-generated electricity can be reduced by improving the power conversion efficiency (PCE) of solar cells, which is the driving motivation behind the work in this thesis. The dominant solar cell technology today is single-junction cells made from silicon, with record PCE in the lab of 26.7%[2] and commercial cells typically around 20%. The thermodynamic limit for single-junction cells, 33.8%[3], has almost been reached and only very incremental improvements have been made over the past 25 years[4].

Much of the wasted energy in a single-junction solar cell, even at the thermodynamic limit, is due to the fact that only certain wavelengths of the solar spectrum can be utilised - only photons with energy higher than the band gap (for silicon, 1.1 eV), can be absorbed. Additionally, when photons are absorbed in the blue and UV parts of the spectrum, each of which has energy multiple times that of the band gap, the excess

above the band gap is wasted as heat. Now that single-junction silicon is pushing up close to its thermodynamic limit, the route to the next generation of more efficient solar cells involves utilising these different wavelengths more effectively.

Several different wavelength management techniques have been proposed to better take advantage of the full solar spectrum and push solar cell efficiencies beyond the single-junction limit. Tandems and multi-junction solar cells have already exceeded the record single-junction efficiency, by layering multiple sub-cells with different band gaps to each absorb a different part of the spectrum. However, this can be expensive to implement, as it involves complex voltage or current matching, and multi-junction cells perform poorly under spectral variation. There has also been interest in up-conversion and down-conversion strategies. Up-conversion seeks to combine the energy from a pair of sub-band gap photons, which otherwise would not be absorbed in a single-junction cell, and create a photon above the band gap from their combined energy. Down-conversion seeks to reduce losses to heat from photons with energy greater than twice the band gap, by splitting them into multiple excitations, each of which is capable of producing an electron-hole pair.

One down-conversion strategy is to use multiple exciton generation (MEG) in inorganic semiconductor nanostructures[5,6], where multiple excitons can be generated on a single nanostructure from the absorption of one photon. However, the focus of this thesis is on the equivalent process in organic semiconductors, which is known as singlet exciton fission. Under specific conditions, a photoexcited singlet exciton can convert to a pair of triplet excitons, each with approximately half of the energy of the singlet exciton. If these triplet excitons can be separated, and then transferred to a lower band gap material such as silicon, it is possible to generate two electron-hole pairs from one incident photon. This offers a promising route to enhancing the PCE of solar cells, using abundant organic materials that are relatively simple to process. The pay-off in terms of efficiency could be significant, with the thermodynamic limit of a singlet fission enhanced solar cell estimated to be 45.9%[7], a large increase from 33.8% for a single-junction cell[3].

This thesis is concerned with the photophysical characteristics of organic semiconductors, in particular those that are capable of singlet fission. Through case studies of specific molecular systems, we seek to shed light on how chemical structure and intermolecular geometry affect how molecular materials behave after photoexcitation and how that knowledge might be useful for designing materials for devices such as solar cells. Chapter 2 contains a review of the relevant background and theory to

the concepts used in this work. Chapter 3 follows with experimental details for the techniques used.

Chapter 4 describes the photophysics of a modified acene, TTBP, with enhanced stability and high photoluminescence yield. We use this material to highlight the idea of evaluating the photoluminescence yield of a singlet fission candidate to give an indication of the non-radiative losses that would be present if it were used in a fission-sensitized solar cell. Also of importance in Chapter 4 is the discovery of a new method to improve the photostability of acenes (benzannulation to make triphenylene "wings") without compromising their ability to undergo quantitative fission.

In Chapter 5, we extend the library of proven singlet fission systems by characterising the photophysics of a family of indolonaphthyridine derivatives, and in the process put forward a different design strategy for more stable fission materials by exploiting excited-state aromaticity. We also show that fission can only occur at specific fission hot spots in these materials, the density of which can be tuned by changing the material deposition technique or the chemical structure. In addition we show that intramolecular singlet fission can occur in covalent dimers of these molecules, but only under specific solvent conditions and with sufficient conjugation across the covalent bridge.

Chapter 6 looks in detail at the effect of different crystal packings on the fission process in a set of tetracene derivatives, which have identical photophysics in isolation but when in the solid-state exhibit very different behaviour due to their different crystal structures. In particular, we characterise TMS-tetracene, which forms π-stacked dimers that allows endothermic fission to proceed on an unprecedented 50 fs timescale.

Finally, in Chapter 7, we summarise our findings and discuss the outlook for future work building off of these results.

Chapter 2

Background and Theory

Organic semiconductors, made up of conjugated polymers or small molecules, offer the potential to revolutionise many electronic devices. They are produced from generally cheap and abundant raw materials, and their properties, such as solubility, absorption wavelength and mechanical strength, can be tuned by the addition or exchange of functional groups. This flexibility paired with the ability to absorb light, conduct electricity and emit light makes organic semiconductors potentially very useful in a variety of technologies[8]. A great success story for organic electronics has been organic light emitting diodes (OLEDs), which are now common in electronic displays such as smartphones, and offer the possibility of flexible and transparent displays[9]. There has also been significant recent progress in improving the efficiency and durability of organic photovoltaics (OPV), especially with the latest generation of non-fullerene acceptors[10,11].

This thesis will be focused on answering fundamental question about the photophysics of organic semiconductors that are so useful in OLEDs and OPV, and many other exciting possible applications from targeted drug delivery[12] to quantum computing[13]. First, in this chapter we will review the important theoretical concepts that underlie the experimental work undertaken in the rest of this thesis. This will be a brief overview which is heavily informed by more detailed treatments available in textbooks by Pope and Swenberg[14], Köhler and Bässler[8] and Barford[15].

2.1 Electronic Structure in Organic Semiconductors

2.1.1 Atomic and Molecular Orbitals

Organic semiconductors are those made up of small molecules or polymers primarily consisting of carbon and hydrogen, with occasional heteroatoms such as oxygen, nitrogen, or sulphur. Their rich electronic properties originate from conjugation, meaning the delocalisation of electronic wavefunctions across multiple atoms which results from carbon-carbon bonds. To understand how this occurs, we begin with the concept of atomic orbitals.

Hydrogen has one electron in the $1s$ orbital, while the electronic configuration of carbon is $1s^2 2s^2 2p^2$, in $n\alpha^m$ notation where n is the principal quantum number or electronic shell, m is the number of electrons occupying the state, and α is the orbital angular momentum in spectroscopic notation (s, p, d...). This means that each carbon atom has a pair of electrons in each of the $1s$ and $2s$ orbitals and two unpaired electrons in $2p$ orbitals, with the third $2p$ orbital unoccupied. These atomic orbitals are depicted in Figure 2.1. The s orbitals are spherical, in contrast to the $2p$ orbitals, which have lobes in the x, y and z directions and so are known as $2p_x$, $2p_y$, and $2p_z$[8,15].

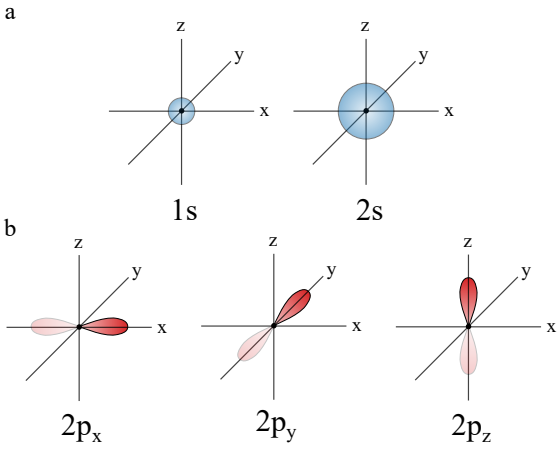

Fig. 2.1 Atomic orbitals. a) depicts schematic diagrams of the atomic 1s and 2s orbitals, and b) depicts the atomic $2p_x$, $2p_y$ and $2p_z$ orbitals.

When a carbon atom bonds with other atoms, the valence orbitals, which in the case of carbon are the $2s$, $2p_x$, $2p_y$, and $2p_z$ orbitals, undergo sp^n hybridisation, as shown in Figure 2.2a. Depending on the number of bonds formed, the $2s$ orbital mixes with 1, 2 or 3 of the $2p$ orbitals, resulting in sp^1, sp^2, and sp^3 hybridisation

respectively. For example, methane (CH_4) consists of one carbon bonded to 4 hydrogen atoms and has sp^3 hybridisation, resulting in 4 equivalent σ-orbitals arranged in a tetrahedral shape, with an angle of 109.5°. Each of these σ-orbitals forms a σ-bond with a hydrogen atom. In ethylene (C_2H_4), depicted in Figure 2.2b, both carbons have sp^2 hybridisation, meaning there are 3 σ-orbitals separated by 120° plus one perpendicular unhybridised $2p_z$ orbital left on each carbon. The two carbons are bonded by a σ-bond, plus a π-bond is formed from the remaining $2p_z$ orbitals, where the electrons are above and below the plane of the σ-bonds. π-bonds are the crucial ingredient for electronic conjugation. Finally, there is sp hybridisation, which occurs when there is a C-C "triple bond", such as in the molecule ethyne (C_2H_2, also known as acetylene). Here, there is 180° between the two σ-orbitals and the $2p_y$ and $2p_z$ orbitals remain. In a C-C triple bond, there is a σ-bond, and π-bonds above and below the σ-bond formed from the $2p_z$ orbitals, as well as in front and behind of the σ-bond formed from the $2p_y$ orbitals[8,15].

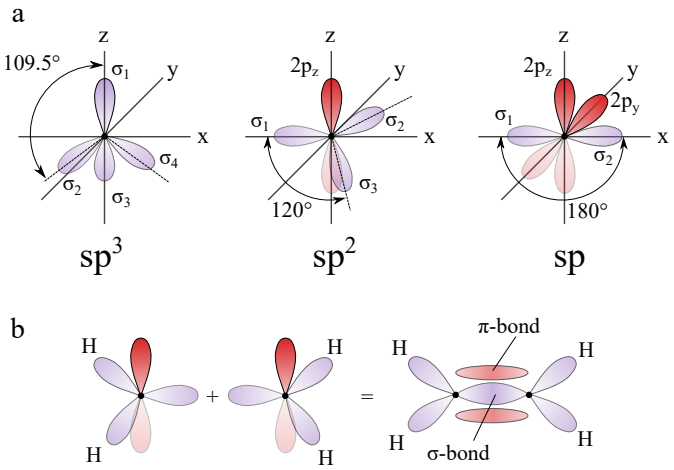

Fig. 2.2 Orbital Hybridisation. a) Schematic diagrams of hybridised sp, sp^2 and sp^3 orbitals in carbon. b) Schematic diagram of molecular bond formation in ethylene (C_2H_4) with sp^2 hybridisation.

Conjugation resulting from π-bonding results in structural rigidity - any rotation around the σ-bond would require breaking the π-bonds and is thus forbidden. When σ- and π-bonds are formed, the pair of electrons involved is now shared between the two atoms, and both electrons are equally likely to be found orbiting either nucleus. When more than one sp^2 carbon is bonded together, the π electrons can delocalise further, with important consequences for the electronic properties of the molecule. As delocalisation increases, π electrons become more weakly associated with individual atoms and are instead better described by molecular orbitals.

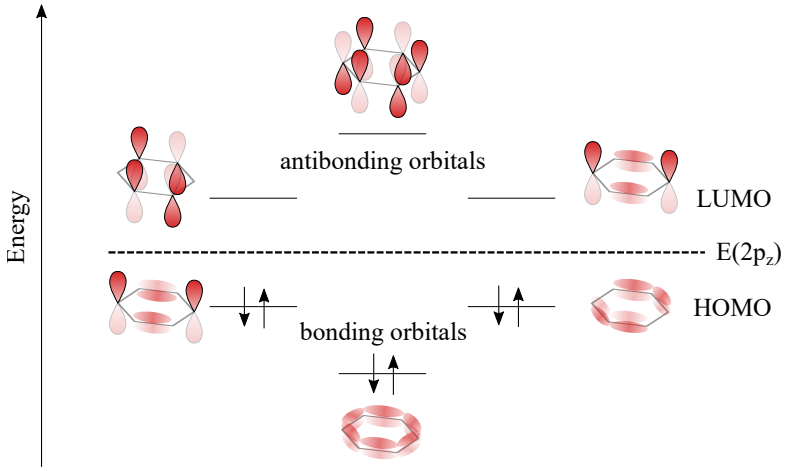

Fig. 2.3 Molecular orbitals of benzene. Schematic showing the wavefunctions of the π-electrons and the relative energies of the six molecular orbitals to the atomic $2p_z$ orbital (dashed line). Occupation of the molecular orbitals in the ground state of benzene is indicated by the arrows representing spin-up or spin-down electrons.

Molecular orbitals and their energies can be calculated by numerous theoretical methods with varying levels of complexity described in detail elsewhere[14–16]. The important concepts can be seen in the schematic description of benzene in Figure 2.3. The molecular orbitals shown, which are combinations of the atomic $2p_z$ orbitals, can be categorised as bonding (π) or anti-bonding ($\pi*$). In bonding orbitals, the atomic wavefunctions interfere constructively, and the increased electron density between the nuclei results in bonding character, lowering the energy of the orbital. Conversely, in anti-bonding orbitals the interference is destructive. The decreased electron density between the nuclei results in anti-bonding character, which can be thought of as the repulsion between the nuclei not being screened by electrons between them, raising the energy of the orbital[8].

In benzene, each of the six carbons contributes one $2p_z$ electron, and they fill the three bonding orbitals in pairs of spin-up and spin-down as these are the lowest energy states, stabilising the molecule. The energy of a stationary state is generally proportional to the second spatial derivative of the wavefunction, which results in higher energies for the molecular orbitals with higher numbers of nodes. This can be seen in Figure 2.3, where the lower energy bonding (π) orbitals have fewer nodes than the higher energy anti-bonding ($\pi*$) orbitals.

Electrons involved in σ bonds remain confined to the atoms in their bond while π electrons are mobile and define the properties of the molecule. Hence, the electronic

wavefunction can be factorised as $\psi = \psi_\sigma \psi_\pi$, and for the transitions within the range of interest, ψ_π can be calculated by treating the nuclei and σ electrons as an effective molecular potential in which π electrons move. This is known as the Hückel approximation[8,17–19].

Delocalised π electrons define a conjugated molecule's optical properties. The gap between the frontier orbitals, the highest occupied molecular orbitals (HOMO) and the lowest unoccupied molecular orbitals (LUMO), is the lowest energy transition of the molecule, known as the optical gap or band gap. This is analogous to the band gap between valence and conduction bands in inorganic semiconductors. The energy of the HOMO is equivalent to the energy required to remove an electron, known as the ionisation potential, while the energy of the LUMO is the energy gained when an electron is added, known as the electron affinity. Promotion of an electron from the HOMO to the LUMO, for example from the absorption of a photon, is a $\pi \rightarrow \pi*$ transition. Despite the occupation of an anti-bonding $\pi*$ orbital, a $\pi \rightarrow \pi*$ transition will not result in the disintegration of the molecule because the bonding characteristics of the remaining σ and π electrons provide adequate bonding energy[14,16].

2.1.2 From Orbitals to States

While molecular orbital theory is a useful tool, each orbital only describes single-electron behaviour, and to address the properties of molecules we need to use the multi-electron states that describe the whole molecule. Molecular orbitals can be written as a sum of atomic orbitals ϕ_i,

$$\psi = \sum_i c_i \phi_i \tag{2.1}$$

The multi-electron wavefunction is approximated as the product of the molecular orbitals of each electron (neglecting any interaction between the electrons)[8],

$$\Psi = \prod_i \psi_i \tag{2.2}$$

To move from a description of the multi-electron wavefunction to the energy of the multi-electron state, we must solve the Schrödinger equation,

$$\hat{H} \left|\psi\right\rangle = E \left|\psi\right\rangle \tag{2.3}$$

where $\hat{H}$ is the Hamiltonian operator and E is an eigenvalue that solve the equation. For the wavefunction describing the whole molecular state, the Hamiltonian includes

terms for the kinetic operator ($\hat{T}$) of the electrons and nuclei, and the Coulombic interactions ($\hat{V}$) between electrons, between nuclei, and between electrons and nuclei,

$$\hat{H}_{total} = \hat{T}_e(\boldsymbol{r}) + \hat{T}_n(\boldsymbol{R}) + \hat{V}_{e-e}(\boldsymbol{r}) + \hat{V}_{n-n}(\boldsymbol{R}) + \hat{V}_{e-n}(\boldsymbol{r};\boldsymbol{R}) \tag{2.4}$$

$\boldsymbol{r}$ and $\boldsymbol{R}$ are the electronic and nuclear coordinates respectively. Although the Schrödinger equation is solvable with this Hamiltonian for a single electron in a hydrogen atom, it is not for two electron systems, let alone the dozens of electrons in a typical organic molecule. To make progress, we follow the Born-Oppenheimer approximation, which separates the nuclear and electronic parts of the wavefunction based on their vastly different masses[14,15]. To the comparatively light and fast-moving electrons, the nuclei appear static, while the slow and comparatively heavy nuclei feel the effect of an averaged cloud of electrons[8]. The wavefunction can thus be factorised,

$$\Psi(\boldsymbol{r},\boldsymbol{R}) = \psi_e(\boldsymbol{r};\boldsymbol{R})\psi_n(\boldsymbol{R}) \tag{2.5}$$

The electronic wavefunction, ψ_e, depends on the positions of the electrons and nuclei, while the nuclei move in a potential defined by the electron cloud. Given that this potential is a function of the nuclei positions, the nuclear wavefunction, ψ_n, is a function only of the positions of the nuclei. We can now define a electronic Hamiltonian $\hat{H}_{el}$,

$$\begin{aligned}\hat{H}_{el}\left|\psi_e(\boldsymbol{r};\boldsymbol{R})\right\rangle &= \left[\hat{T}_e + \hat{V}_{e-e} + \hat{V}_{e-n}(\boldsymbol{R}) + \hat{V}_{n-n}(\boldsymbol{R})\right]\left|\psi_e(\boldsymbol{r},\boldsymbol{R})\right\rangle \\ &= E(\boldsymbol{R})\left|\psi_e(\boldsymbol{r};\boldsymbol{R})\right\rangle\end{aligned} \tag{2.6}$$

The eigenvalues, $E(\boldsymbol{R})$, are the sum of the electron kinetic energy and all of the Coulombic potential energy terms. This result can then be applied to simplify the Schrödinger equation for the total Hamiltonian, neglecting the "non-adiabatic" terms from the contribution of nuclear motion to ψ_e,

$$\begin{aligned}\hat{H}_{total}\left|\psi_e\right\rangle\left|\psi_n\right\rangle &= \left[\hat{H}_{el} + \hat{T}_n(\boldsymbol{R})\right]\left|\psi_e\right\rangle\left|\psi_n\right\rangle \\ &= \left|\psi_e\right\rangle\left[E(\boldsymbol{R}) + \hat{T}_n(\boldsymbol{R})\right]\left|\psi_n\right\rangle \\ &= \epsilon(\boldsymbol{r};\boldsymbol{R})\left|\psi_e\right\rangle\left|\psi_n\right\rangle\end{aligned} \tag{2.7}$$

$\epsilon(\boldsymbol{r};\boldsymbol{R})$ is the eigenvalue for the total system, including nuclear kinetic energy. An electronic state can be described by plotting $\epsilon(\boldsymbol{r};\boldsymbol{R})$ against the nuclear coordinates, giving the adiabatic potential energy surface (PES). For each electronic state the PES describes the position of the nuclei and the resulting energy of the molecule at these

geometries. As shown in Figure 2.4, in each electronic state the PES has a minimum at the most stabilised geometry, but this is not the same for different states. Consequently, exciting a molecule out of the ground state usually results in a reorganisation of the nuclear coordinates to reach the energetic minimum of the excited state. The shape of the PES can be understood intuitively - at very small $\boldsymbol{R}$, the repulsion of the nuclei would put the molecule in a very high energy state, while at large $\boldsymbol{R}$ the surface flattens as the nuclei dissociate. Between these extremes, close to the minimum, the PES is approximately a harmonic oscillator, where nuclei can oscillate about the position of the stable low-energy minimum.

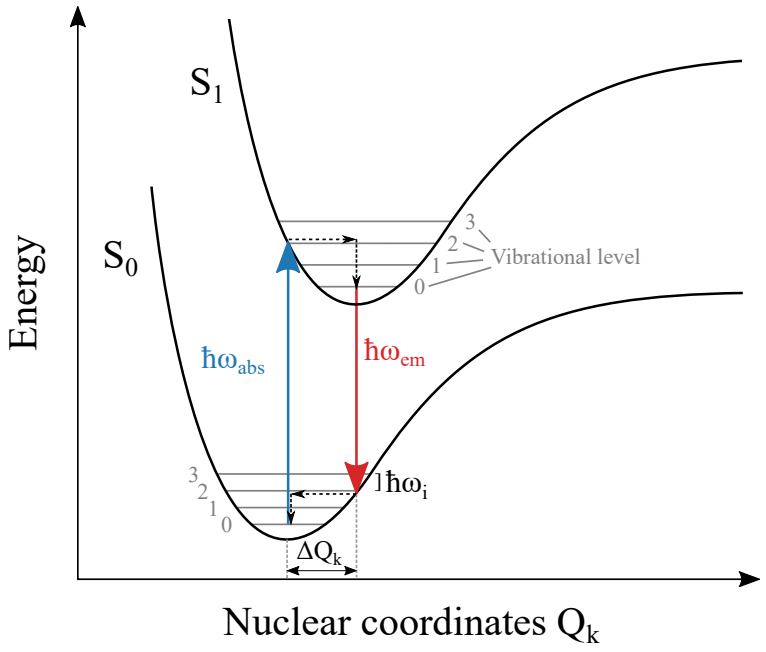

Fig. 2.4 Potential Energy Surfaces. Examples of possible potential energy surfaces as a function of nuclear coordinates $\mathbf{Q_k}$ for the ground and excited states. The minimum energy is at a different equilibrium nuclear geometry for the two states, meaning that the nuclei rearrange to different positions when in the excited state to minimise the energy of the state. Vibrational quanta are shown in grey. Absorption by a vertical transition from the ground state to a higher vibrational level of the S_1 state is shown in blue (0-2 transition), as well as fluorescence from the relaxed S_1 state to the second vibrational level of the ground state (2-0 transition). Non-radiative vibrational relaxation is shown by dashed black arrows.

The crucial assumption that underlies the Born-Oppenheimer approximation is that these states are adiabatic - that is, the change in nuclear coordinates occurs with no sudden change in electronic configuration, while electronic motion occurs within a

static nuclear arrangement. A consequence of this adiabatic assumption is that the PES of different electronic states cannot intersect. In reality, this is not always true and certain molecules experience a non-adiabatic coupling of nuclear and electronic motion known as vibronic coupling. This can result in conical intersections between two PES, allowing rapid transitions between electronic states at the same nuclear coordinates. These are cases where the Born-Oppenheimer approximation is not valid.

2.1.3 The Exciton

When a molecule transitions between electronic states, electrons are moving between molecular orbitals. For example, when a photon is absorbed and a molecule moves from the ground state to the first excited state, an electron is promoted from the HOMO to the LUMO, leaving a vacancy in the HOMO. This vacancy is in effect a positive particle, referred to as a hole. The electron and hole together form a charge-neutral quasi-particle called an exciton, and are held together by Coulomb forces. In organic molecules, the dielectric constant is low, limiting the screening of the Coulomb force, meaning that excitons are tightly bound together. This type of tightly bound exciton is known as a Frenkel exciton[20]. In materials with a high dielectric constant, typically inorganic semiconductors, we find the other exciton archetype - the Wannier-Mott exciton. In this case, the electronic screening of the Coulomb force reduces the attraction between electron and hole, allowing the exciton radius to become larger than the lattice spacing.

The exciton binding energy, due to the Coulombic attraction of electron and hole, reduces the energy of the exciton from the HOMO-LUMO gap. Frenkel excitons have significant binding energies, typically 0.1 to 1 eV, while Wannier-Mott excitons have a much smaller binding energy typically on the order of 10 meV[14,15]. Due to their stronger binding, the charges in a Frenkel exciton typically have a mean separation of less than 1 nm, much smaller than weakly-bound Wannier-Mott excitons[14,15]. The properties of excitons are crucial for understanding and utilising the properties of semiconductors, particularly organics. Low exciton binding energies, for example in silicon, result in easily separated and transported charges, important qualities for photovoltaic applications. In contrast to this, for organic semiconductors, a major challenge for photovoltaic applications is the separation of Frenkel excitons to produce free charges that can generate current.

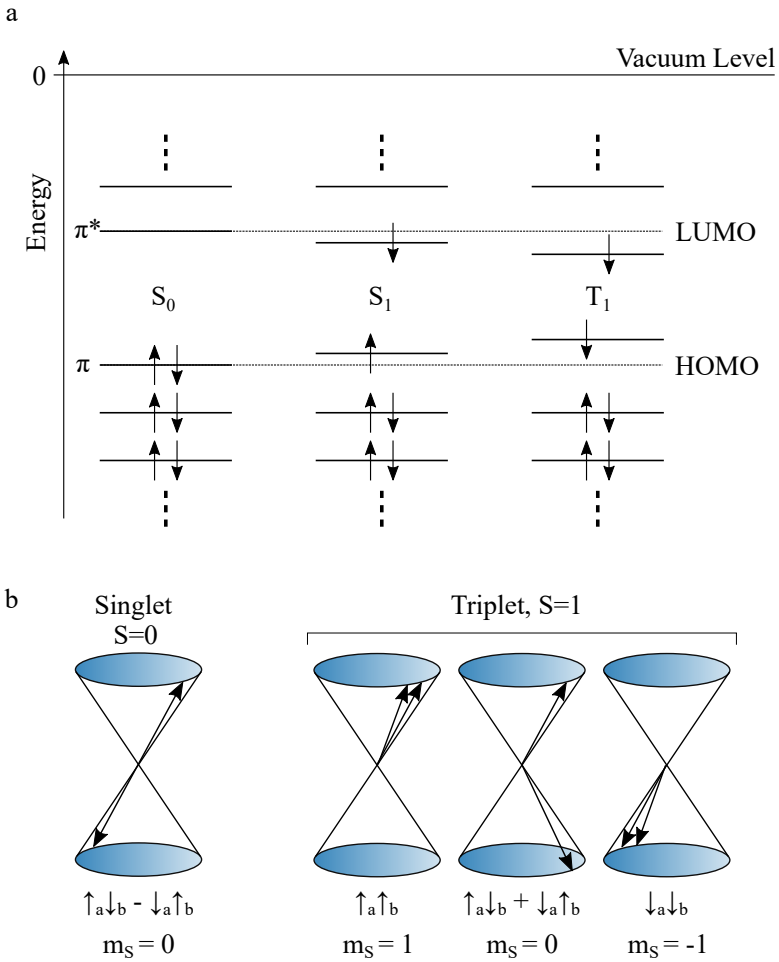

Fig. 2.5 Singlet and triplet excitons. a) Molecular orbital configuration scheme. In the ground state (S_0) and lowest singlet excited state (S_1) the electron spins are aligned anti-parallel and the total spin is zero. In the triplet excited state (T_1) the spins of the electrons in π and $\pi*$ orbitals are parallel. These frontier orbitals are shifted in S_1 and T_1 from their initial HOMO and LUMO energy levels by Coulomb and exchange interactions. b) Vector diagram of electron pair spins. The spins (arrows) precess about a magnetic field. Figure adapted from Köhler and Bässler[21]

2.1.4 Singlet and Triplet States

We have already discussed how Coulomb binding reduces the energy of the exciton from the ground state HOMO-LUMO gap. In addition to this, exchange interactions between the unpaired electrons in the HOMO and LUMO further perturb the energy of the exciton depending on the electron's relative spin states. In units of $\hbar$, electrons are spin-$\frac{1}{2}$ particles. They can have a spin quantum number of either $\frac{1}{2}$ (spin-up) or $-\frac{1}{2}$ (spin-down). Two spin-$\frac{1}{2}$ particles can be combined in four distinct states[22], labelled as $|S\, m_S\rangle$ where S is the total spin and m_S is the projection on the z-axis. One of these states has a total spin $S = 0$, and the other three have total spin $S = 1$. These states are commonly referred to by their multiplicity: singlets or triplets. The singlet and three triplet states are described in terms of the single electron spin states $|\uparrow_i\rangle$ and $|\downarrow_i\rangle$ as,

$$\text{Singlet} : |0\,0\rangle = \frac{1}{\sqrt{2}}\,|\uparrow_1\downarrow_2 - \downarrow_1\uparrow_2\rangle \tag{2.8}$$

$$\text{Triplets} : \begin{cases} |1\,1\rangle & = |\uparrow_1\uparrow_2\rangle \\ |1\,0\rangle & = \frac{1}{\sqrt{2}}\,|\uparrow_1\downarrow_2 + \downarrow_1\uparrow_2\rangle \\ |1\,{-1}\rangle & = |\downarrow_1\downarrow_2\rangle \end{cases} \tag{2.9}$$

In the ground state, with the π orbitals filled and $\pi*$ orbitals empty, the electrons in the HOMO are in the same electronic state so their spins must be antiparallel, as depicted in Figure 2.5a. Thus, there is only an S_0 state and no T_0 state. Figure 2.5b shows vector diagrams of the electron spins in singlet and triplet excitons precessing around a magnetic field in the z-direction, to visualise S and m_S. In the singlet, the spins are antiparallel and out-of-phase, giving an overall spin $S = 0$. The three triplet states have parallel spins such that total spin $S = 1$, but different projections on the z-axis.

The concept of exchange symmetry becomes important here. As fermionic states, the total wavefunction for an exciton, comprising spatial and spin terms, must be antisymmetric under particle exchange (switching of the indices). By inspection of Equations (2.8) and (2.9), we can see that the spin part of the singlet wavefunction is antisymmetric while the triplet spin wavefunction is symmetric under particle exchange. Therefore, to achieve an overall antisymmetric wavefunction, the spatial wavefunction must be symmetric for singlets and antisymmetric for triplets[21]. Additionally, the degeneracy of the singlet and triplet energies is split by the exchange interaction. This

stems from the requirement that fermions be antisymmetric under exchange, in the form of an additional term in the two-electron Hamiltonian,

$$K_{ij} = \iint \psi_i^*(r_1)\psi_j^*(r_2)V_{e-e}(r_1 - r_2)\psi_j(r_1)\psi_i(r_2)dr_1dr_2 \tag{2.10}$$

ψ_i is the wavefunction for the ith electron, and V_{e-e} is the effective interaction between electrons. K_{ij} is a positive term for fermions, meaning it is repulsive. Its magnitude scales with the overlap of the electrons' spatial wavefunctions, especially where they reside on the same atoms with significant amplitude. The net effect is to lower the energy of the triplet states relative to the singlet by the exchange energy $\Delta E_{ST} = 2K_{ij}$. The effect of the exchange interaction on the relative HOMO and LUMO energies for singlets and triplets is depicted in Figure 2.5a. Across a range of molecules and polymers, ΔE_{ST} tends to be around 0.6 to 1.0 eV[21,23]. For the oligoacenes, which will be an important class of molecules for this thesis, the exchange energy is on the higher end of this range, at ∼1.0 eV. The manipulation of this exchange energy by molecular design is of particular interest, in order to control the relative energies of singlet and triplet excitons to be useful in optoelectronic and spintronic devices[21].

2.2 Transitions within Molecules

Having established how atomic and molecular orbitals combine to form molecular states, and introduced the concept of excitons and their different spin configurations, we now move to the mechanisms involved in moving between these states. This thesis explores the photophysics of various organic molecules, and focuses on the dynamic evolution of photoexcited states in these systems. Therefore, it is helpful to review the theoretical rules of both radiative and non-radiative transitions in organic molecules.

2.2.1 Radiative Transitions

To understand in quantum mechanical terms how light interacts with matter, we begin with Fermi's Golden Rule[24], which describes the transition rate $\Gamma_{i\to f}$ between initial and final states $|\Psi_i\rangle$ and $|\Psi_f\rangle$, as a result of a weak perturbation $\hat{H}'$,

$$\begin{aligned}\Gamma_{i\to f} &= \frac{2\pi}{\hbar}|\langle f|\hat{H}'|i\rangle|^2\rho(E_f) \\ &= \frac{2\pi}{\hbar}|M_{i\to f}|^2\rho(E_f)\end{aligned} \tag{2.11}$$

where $\rho(E_f)$ is the density of states at the energy of the final state and $M_{i\to f}$ is the matrix element between the initial and final states coupled by $\hat{H}'$. For the case of absorption of light, $\hat{H}'$ is the oscillatory electromagnetic field of the incoming light,

$$\hat{H}'(t) = -q\sum_j \hat{r}_j \cdot \vec{E}cos(\omega t) = \hat{\mu}\cdot\vec{E}(t) \tag{2.12}$$

where $\hat{\mu}$ is the dipole operator. Remembering that the Born-Oppenheimer approximation from Section 2.1 allows us to separate the nuclear and electronic parts of the wavefunction, we factorise Ψ such that

$$\Psi_{total}(\boldsymbol{r};\boldsymbol{R}) = \Psi_{el}(\boldsymbol{r};\boldsymbol{R})\Psi_{vib}(\boldsymbol{R})\Psi_{spin} \tag{2.13}$$

Therefore the magnitude of the matrix element can be written as

$$|M_{i\to f}| = |\vec{E}|\,\langle\Psi_{el,f}\Psi_{vib,f}\Psi_{spin,f}|\hat{\mu}\cdot\epsilon|\Psi_{el,i}\Psi_{vib,i}\Psi_{spin,i}\rangle \tag{2.14}$$

where ϵ is a unit vector in the direction of the incoming electric field. As expected, the transition rate scales with the square of the electric field strength, i.e. the intensity of the incident light.

The dipole operator $\hat{\mu}$ only acts on the electronic wavefunction $\Psi_{el}(\boldsymbol{r};\boldsymbol{R})$ because it acts on the coordinates of the electrons with the position operator $\hat{r_j}$. The nuclei are heavy and do not react quickly enough to be perturbed by the oscillating electric field, so the vibrational wavefunction $\Psi_{vib}(\boldsymbol{R})$ describing nuclear motion is unaffected by the dipole operator[8]. Meanwhile, the spin wavefunction Ψ_{spin} is not affected by electric fields, but could be perturbed by a magnetic field. However, the magnetic field from a electromagnetic wave is too small in magnitude to have any effect[8]. Taking out the factor of the electric field strength from Equation (2.14) gives us the transition dipole moment $|\mu_{i\to f}|$.

$$|\mu_{i\to f}| = \langle\Psi_{el,f}|\hat{\mu}\cdot\epsilon|\Psi_{el,i}\rangle\,\langle\Psi_{vib,f}|\Psi_{vib,i}\rangle\,\langle\Psi_{spin,f}|\Psi_{spin,i}\rangle \tag{2.15}$$

We note that this derivation is perfectly valid also for the stimulated emission of photons (events which are measured by pump-probe spectroscopy later in this thesis), with the initial and final states reversed. Spontaneous emission (fluorescence or phosphorescence) occurs via interactions with the vacuum state of the quantized electromagnetic field. For a transition to be allowed, all three terms of the transition dipole moment in Equation (2.15) must be non-zero. We will now work through them one by one to obtain the selection rules for allowed transitions.

2.2.1.1 The Electronic Factor

The electronic term in the transition dipole moment is $\langle \Psi_{el,f} | \hat{\mu} \cdot \epsilon | \Psi_{el,i} \rangle$. The dipole operator $\hat{\mu}$ has odd parity under spatial inversion - that is, its sign is flipped if the spatial coordinate's sign is flipped. This means that for the integral of $\langle \Psi_{el,f} | \hat{\mu} \cdot \epsilon | \Psi_{el,i} \rangle$ over all space to be non-zero, $|\Psi_{el,f}\rangle$ and $|\Psi_{el,i}\rangle$ must have opposite parity. If they are both even or both odd, then the total integrand will be odd, and an integral over all space will be identically zero. In organic molecules, the ground state wavefunction is symmetric (it has even parity), which means that absorption of a photon must be into an antisymmetric (odd parity) state[8]. Molecular states are sometimes labelled with the German terms *gerade* or *g* when symmetric under inversion, and *ungerade* or *u* when antisymmetric.

This holds for one-photon absorption events, however two-photon absorption has an opposite symmetry requirement. In this case, the matrix element $|M_{i \to f}|$ is related to the the electric field strength squared. It can be shown that the transition dipole moment for two-photon absorption then depends on the square of the dipole operator[25], which has even parity. This leads to allowed transitions from the *gerade* ground state to other higher-lying *gerade* states.

Additionally to the symmetry requirements, this electronic part of the transition dipole moment scales with the overlap of the initial and final state wavefunctions, meaning that transitions will be stronger between orbitals in the same spatial region, such as $\pi \to \pi^*$ transitions. Weaker transitions occur between orbitals which occupy more separated locations such as charge transfer (CT) transitions in donor-acceptor type systems, which are designed with a spatially separated HOMO and LUMO, or $n \to \pi^*$ (n electrons are in non-bonding orbitals i.e. not σ or π orbitals)[8]. Stronger transitions also arise from wavefunctions with a greater spatial extent in the direction of the dipole moment, i.e. longer molecules or oligomers[8].

2.2.1.2 The Vibrational Factor

We have shown how the electronic wavefunction defines the intensity of particular radiative transitions. The product of the vibrational, or nuclear, wavefunction, $\langle \Psi_{vib,f} | \Psi_{vib,i} \rangle$, is known as the Franck-Condon overlap integral, and when squared (because the transition rate $\Gamma_{i \to f} \propto |\hat{\mu}_{i \to f}|^2$) is the Franck-Condon factor F. F has a defining effect on the shape of the absorption and emission spectra of organic molecules. Typical vibrational quanta are 100-300 meV, so at 300 K, where the typical thermal energy available is $k_B T = 26\,\text{meV}$, only the zeroth vibrational state is occupied in the ground

state. Therefore, absorption events from the ground state always originate in the zeroth vibrational state, and magnitude of F for the transition to each vibrational level in the excited state determines the relative strength of the different transitions. These transitions that simultaneously change the electronic and vibrational energy are known as 'vibronic' transitions, and the series of peaks to different vibrational levels seen in an absorption or emission spectrum are known as the 'vibronic progression'. In a stiff molecule with rigid bonds, the 0-0 transition will typically dominate due to minimal displacement of nuclear coordinates between ground and excited states, while the absorption spectra of more flexible molecules generally have a clear vibronic progression, and the 0-1 or 0-2 transitions may form the peak of these distributions of transitions.

The Franck-Condon principle is an extension of the Born-Oppenheimer approximation, that reorganisation of the electrons in a radiative transition occurs much faster than the nuclei can move, therefore electronic transitions must occur 'vertically', i.e. without a change in nuclear coordinates. The diagram of potential energy surfaces (PES) in Figure 2.4 is helpful to visualise this. Upon vertical excitation to a higher lying vibrational level of the excited state, within ∼1 ps the wavepacket moves horizontally as the nuclei reorganise, and then by the emission of phonons, vibrational energy dissipates and the exciton relaxes to the bottom of the S_1 PES. Another vertical transition can then occur, typical on a nanosecond timescale, to emit a photon and return to any of the vibrational levels on the S_0 PES, with the relative intensities governed by F. Finally, more vibrational relaxation by the emission of phonons brings the system to the zeroth vibrational level and the nuclei return to their ground state configuration.

For the case of a displaced oscillator, such as that depicted in Figure 2.4, relative intensities of the different vibrational transitions generally follow a Poisson distribution. The distribution is quantified by the Huang-Rhys parameter S,

$$I_{0-m} = \langle \Psi_{vib,f} | \Psi_{vib,i} \rangle = \frac{S^m}{m!} e^{-S} \tag{2.16}$$

An example of a molecule with only one dominant vibrational mode and $S = 1.2$ is shown in Figure 2.6. S can be a very useful parameter. Substituting $m = 0$ and $m = 1$ into Equation (2.16) shows that the ratio $I_{0-1}/I_{0-0} = S$. This can be experimentally measured as the ratio between 0-0 and 0-1 peaks in absorption or emission spectra. S represents the ratio between the potential energy associated with a vibrational excitation and the energy of the vibrational quanta of that mode, i.e. the average number of quanta involved in the vibrational excitation[8,26]. For the example PES shown in Figure 2.4, $S \sim 2$, while in Figure 2.6, S is close to 1 and we can see that 0-1

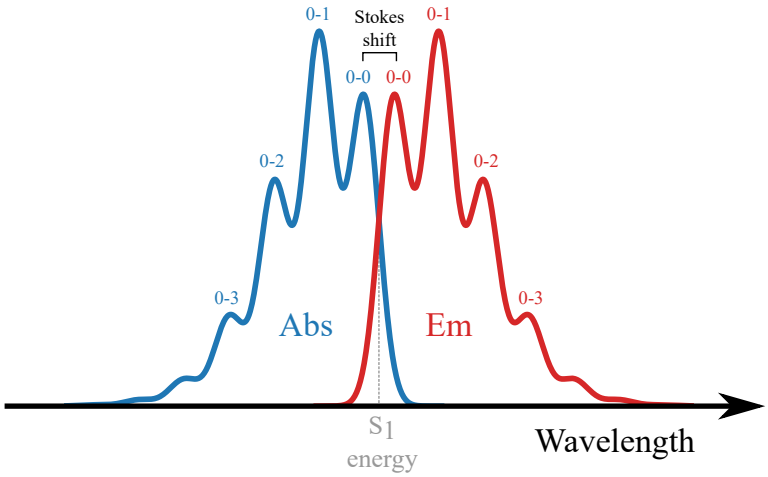

Fig. 2.6 Absorption and Emission Spectra showing vibronic progressions. Different vibrational transitions are labelled in blue/red, and the crossing point of the absorption and emission spectrum is marked as the energy of the S_1 exciton. The relative intensities of the different vibrational transitions were calculated for a Huang-Rhys factor of $S = 1.2$. The offset between 0-0 peaks in the absorption and emission is known as the Stokes shift. It is caused by vibrational relaxation and solvent reorganisation, and is a reflection of the level of disorder in the system.

is the strongest transition. Additionally, the energy associated with the reorganisation of the molecule in the excited state, the relaxation energy E_{rel}, is given by $S\hbar\omega$ for a single mode. In general, a larger Huang-Rhys factor implies a larger displacement between the ground and excited state PES.

In this treatment we have assumed that the molecule is dominated by one vibrational mode, however this is not always the case. For example benzene would have significant contributions from the ring breathing mode (stretching of all the C=C bonds) and the mode for in-plane 'wagging' of the C-H bonds[8]. In the absorption and emission spectra these modes superimpose. Each mode has its own Huang-Rhys parameter and the total relaxation energy becomes $\sum_i S_i\hbar\omega_i$.

Two important rules that apply to most organic molecules help us to clarify the fate of excitations to higher electronic states: Kasha's Rule states that emission occurs from the lowest excited singlet state; Vavilov's Rule states that the fluorescence quantum efficiency is independent of the excitation wavelength. This implies that there is efficient nonradiative interconversion to the lowest excited singlet state[15,27]. This will be discussed in Section 2.2.3, but the key point is that the vibrational relaxation

processes we have described outcompete radiative transitions from higher vibrational levels because the vibrational levels lie close in energy to each other.

2.2.1.3 The Spin Factor

Having addressed the electronic and vibrational contributions to the transition dipole moment, we are left with the integral $\langle \Psi_{spin,f} | \Psi_{spin,i} \rangle$. This evaluates to either 1 if the spins of the initial and final states are equal, or 0 if they are different. This effectively forbids radiative transitions between singlet and triplet states, but allows transitions within singlet or triplet manifolds, such as $S_0 \rightarrow S_1$ and $T_1 \rightarrow T_n$.

In reality, we do observe phosphorescence, which is the radiative transition $T_1 \rightarrow S_0$, although it is generally much weaker than fluorescence from the $S_1 \rightarrow S_0$ transition. Phosphorescence can only occur as a result of spin-orbit coupling, which mixes some singlet character into the triplet state, making the integral $\langle \Psi_{spin,S_0} | \Psi_{spin,T_1} \rangle$ non-zero.

2.2.2 Spin-Orbit Coupling

As we have shown, radiative decay of triplet excitons to the ground state are spin forbidden, unless there is some mixing of the states by spin-orbit coupling. This is an important concept as it has such a strong effect on the photophysics of triplet excitons, so it is worth exploring in some detail.

A transition between different spin states requires the change of an electron spin, known as a spin flip. In isolation, this would break the conservation of angular momentum, which is why such transitions are forbidden. However, if some angular momentum can be 'borrowed' from the orbital angular momentum of the system, l, then total angular momentum $j = l + s$ can still be conserved during a spin flip, as long as l changes to compensate for the change in s. This is what is meant by spin-orbit coupling. Given that this effect only mixes a small amount of singlet character into the triplet state, it can be treated using perturbation theory, where the perturbative Hamiltonian on the ith electron is

$$\hat{H}_{SOC} = \alpha^2 \sum_{j}^{N} \sum_{i}^{m} \frac{Z_j}{R_{ji}^3} \hat{L}_i \cdot \hat{S}_i \propto \frac{Z^4}{n^3(l+1)(l+0.5)l} \tag{2.17}$$

α is the fine structure constant, Z_j is the atomic charge of nucleus j, R_{ji} is the distance between the nucleus j and electron i, $\hat{L}_i$ and $\hat{S}_i$ are the orbital and spin angular momentum operators on electron i, and n and l are the principle and orbital angular momentum quantum numbers. The final expression is valid for a single atom

(N=1), and the important feature is that it scales with the fourth power of the atomic charge, Z. This result is similar in multi-atom molecules, between the fourth and fifth powers, and as a result $\hat{H}_{SOC}$ is much more significant if there are heavy heteroatoms in a molecule, such as transition metals Pt or Ir[8].

Now that we have the Hamiltonian, the mixing of the states follows perturbation theory:

$$|^3\Psi_1'\rangle = |^3\Psi_1\rangle + \sum_k \frac{\langle^1\Psi_k|\hat{H}_{SOC}|^3\Psi_1\rangle}{E(T_1) - E(S_k)} |^1\Psi_k\rangle \tag{2.18}$$

with the reverse expression mixing some amount of $|^3\Psi_1\rangle$ into $|^1\Psi_k\rangle$ also true. From the denominator, we can see that greater spin-orbit coupling occurs between states with similar energies - i.e. when the exchange energy which splits the singlet and triplet energies is small.

To obtain the rate of phosphorescence, we now input our new expression for the perturbed triplet and singlet states to Fermi's Golden Rule:

$$\Gamma_{i\to f} = \frac{2\pi}{\hbar} |\langle^3\Psi_1'|\hat{\mu}\cdot\epsilon|^1\Psi_0'\rangle|^2 \rho(E_f) \tag{2.19}$$

Knowing that these wavefunctions include the spin terms, when we expand the matrix element using Equation (2.18) we can immediately discard the terms which contain spin wavefunction integrals between pure singlet and triplet states. Then we are left with

$$M_{i\to f} = \sum_k \frac{\langle^1\Psi_k|\hat{H}_{SOC}|^3\Psi_1\rangle}{E(T_1) - E(S_k)} \langle^1\Psi_k|\hat{\mu}\cdot\epsilon|^1\Psi_0\rangle + \sum_k \frac{\langle^1\Psi_k|\hat{H}_{SOC}|^3\Psi_1\rangle}{E(S_0) - E(T_k)} \langle^3\Psi_1|\hat{\mu}\cdot\epsilon|^3\Psi_k\rangle \tag{2.20}$$

The second term will be small due to the large energy gap between S_0 and the higher triplet levels T_k, leaving us with the final expression for the rate as

$$\Gamma_{i\to f} \approx \frac{2\pi}{\hbar} \left| \sum_k \frac{\langle^1\Psi_k|\hat{H}_{SOC}|^3\Psi_1\rangle}{E(T_1) - E(S_k)} \langle^1\Psi_k|\hat{\mu}\cdot\epsilon|^1\Psi_0\rangle \right|^2 \rho(E_f) \tag{2.21}$$

This description of spin-orbit-coupling-enabled phosphorescence can be applied to other transitions between singlet and triplet manifolds, including the reverse process - absorption into the T_1 state, as well as non-radiative interconversion between excited singlets and triplets, known as intersystem crossing, which we will discuss further in Section 2.2.3.3.

2.2.3 Non-Radiative Transitions

2.2.3.1 Internal Conversion

Internal conversion is the category of non-radiative transitions between electronic states without involving a spin flip. Instead of being emitted as a photon, energy is dissipated in phonons and transformed into heat. We can still use Fermi's Golden Rule (Equation (2.11)) to describe the rate of internal conversion. In this case, rather than a perturbation from the dipole operator, instead we must use the nuclear kinetic energy operator $\hat{\mathcal{J}}_N$ for $\hat{H}'$:

$$\Gamma_{i\to f} = \frac{2\pi}{\hbar} |\left\langle \Psi_{el,f}\Psi_{vib,f}\Psi_{spin,f}|\hat{\mathcal{J}}_N|\Psi_{el,i}\Psi_{vib,i}\Psi_{spin,i}\right\rangle|^2\rho \tag{2.22}$$

By the derivation of Siebrand[28], this can be evaluated by taking the integral of the electronic and spin parts as J and remembered that the vibrational integral squared is the Franck-Condon Factor F,

$$\Gamma_{i\to f} = \frac{2\pi}{\hbar} J^2 F\rho \tag{2.23}$$

F depends exponentially on the energy difference between the initial and final states. J has no energy dependence, therefore

$$\Gamma_{i\to f} \propto \exp\Big(-\gamma\frac{\Delta E}{\hbar\omega_M}\Big) \tag{2.24}$$

This dependence is known as the Energy Gap Law. Non-radiative transitions are exponentially faster for smaller energy gaps[29]. This has the effect of lower photoluminescence quantum efficiencies for lower band gap molecules as internal conversion becomes more competitive with radiative decay. It also allows relatively fast internal conversion from higher singlet states such as S_2 to higher vibrational levels of S_1 to outcompete radiative transitions such as $S_2 \to S_0$, which is why Kasha's Rule holds.

2.2.3.2 Conical Intersections

Up to this point we have considered only cases where the Born-Oppenheimer approximation holds, where there is weak coupling between electronic and vibrational nuclear wavefunctions, so the displacement between the PES of different electronic states is small and they do not intersect. However, in the case of strong vibronic coupling, this breaks down and we can see large enough displacements between PES that they intersect[8]. The name comes from the conical shape of the intersecting PES,

and an example is shown in Figure 2.7. At the point of the intersection the adiabatic Born-Oppenheimer approximation is invalid and the surfaces are non-adiabatically coupled[30].

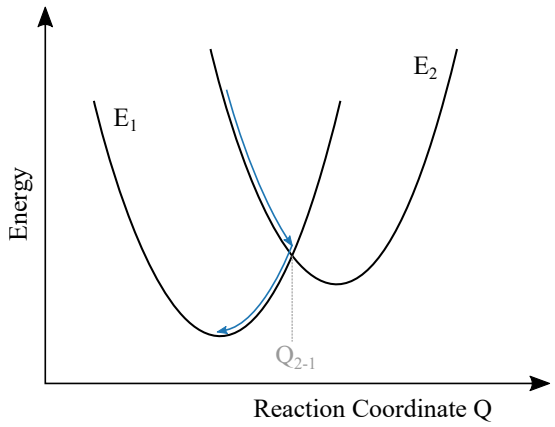

Fig. 2.7 Conical Intersection. Potential energy surfaces of two states that are strongly vibronically coupled are shown in black, plotted against the reaction coordinate Q, a combination of the nuclear coordinates for the vibrational modes that are involved in the intersection. The blue arrows indicate the movement of a wavepacket after excitation into the state described by E_2 to the intersection, where internal conversion to the E_1 state occurs, followed by relaxation to the E_1 equilibrium geometry.

The conical intersection is a special case of non-radiative transition where rather than the final state being a band of vibrational levels it is a single isoenergetic electronic state. The transfer from one PES to the other occurs instantaneously with no nuclear motion - it is purely a rearrangement of the electronic wavefunction. When at the point of the intersection, labelled by reaction coordinate Q_{2-1} (the reaction coordinate is a combination of the normal mode coordinates that are active in the transition), the system is in a superposition of the two states. From this point the lower equilibrium energy of the final state drives the system efficiently in this direction. The rapid internal conversion once at the point Q_{2-1} makes the vibrational relaxation to achieve this geometry the limiting step, and so conical intersections efficiently funnel energy between PES on the same timescale as vibrational relaxation[31].

A well studied example of a conical intersection is the photoisomerisation of rhodopsin, a key step in the process of turning photons to neurological signals in vision. It occurs rapidly in under 200 fs and at a high quantum yield, transforming the molecule from its original *cis* orientation to the *trans* photoproduct[32]. While challenging to observe directly, due to the short timescales available to observe the relevant vibrational

modes, a telltale sign of a conical intersection is an internal conversion event that seems to violate the energy gap law (Equation (2.24)) by proceeding too quickly.

2.2.3.3 Intersystem Crossing

Internal conversion describes non-radiative transitions between states that are possible without a spin flip, intersystem crossing (ISC) describes the non-radiative transitions between singlet and triplet manifolds. The most common and best-understood mechanism for the formation of triplets is spin-orbit coupling mediated intersystem crossing. This utilises the same mixing of states by spin-orbit coupling (Equation (2.18)) as the phosphorescence mechanism described in Section 2.2.2. As for phosphorescence, the rate of ISC is increased by the presence of heavy atoms, either within a molecule or even nearby, for instance in a brominated solvent or host matrix.

Other possible mechanisms of ISC include vibronic coupling to higher triplet levels and hyperfine coupling, which couples the electron spin to nuclear spins rather than to orbital angular momentum, however this is currently understood to be less significant than spin-orbit coupling mediated ISC. The energy gap law (Equation (2.24)) applies to ISC, and as such in materials designed to quickly populate the triplet state, ΔE_{ST} is often minimised by spatially separating the HOMO and LUMO with donor-acceptor structures.

A schematic summary of the various transitions discussed in this section is shown in Figure 2.8.

2.3 Excitons in the Solid-state

Our descriptions of properties and transitions thus far have been focused on the behaviour of single molecules, however in order to be useful in devices, organic semiconductors must also be understood in the condensed phase. With the introduction of intermolecular coupling and forces, we observe a range of important phenomena such as the delocalisation of excitons, energy transfer between molecules, and charge transfer and separation of charges.

2.3.1 Aggregation and Excimers

The effects of intermolecular coupling in aggregates of molecules can be readily observed in their absorption spectra. To understand the origins of this effect, we consider the simplest case of a pair of molecules brought together, which we will call a dimer (not

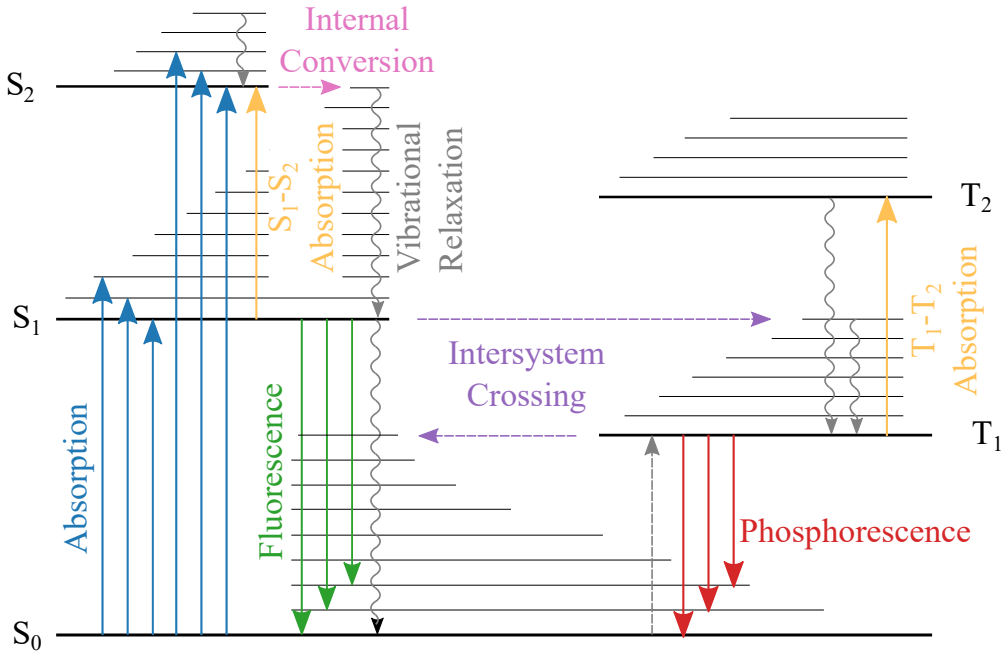

Fig. 2.8 Jablonski diagram of radiative and non-radiative transitions within organic molecules. Allowed absorption of photons into the singlet manifold are shown by blue arrows. Absorption into the triplet manifold, shown with a dashed grey arrow, is only weakly allowed through the mixing of states by spin-orbit coupling, and is usually negligible in the absence of heavy atoms. When a high energy photon is absorbed to create a higher excited state such as S_2, internal conversion to a higher vibrational level of S_1 occurs, by the emission of a phonon or a conical intersection (dashed pink arrow). This is followed by vibrational relaxation within the S_1 electronic state to the relaxed singlet (wavy grey arrow). Relaxed S_1 can decay radiatively by fluorescence, shown by green arrows, or non-radiatively by internal conversion to a higher vibrational level of S_0 followed by relaxation (shown as one wavy line for simplicity). Singlet states may also undergo intersystem crossing into the triplet manifold (dashed purple arrow). The relaxed triplet may decay radiatively, known as phosphorescence, shown by red arrows, but will generally undergo non-radiative decay via intersystem crossing to a vibrationally excited S_0 state as this is not an allowed optical transition. Photoinduced absorptions within the excited singlet and triplet manifolds (orange arrows) can be observed using transient absorption, as described in Chapter 3.

to be confused with a covalent dimer which is a single molecule consisting of two covalently connected monomers). The interaction between the molecules in the dimer breaks the degeneracy of their energy levels, resulting in a pair of energy levels lowered by the Coulomb interaction energy D' and then split by the resonance interaction energy $2I_{12}$[16],

$$\begin{aligned} D' &= \langle \psi_1^* \psi_2 | \hat{V}_{12} | \psi_1^* \psi_2 \rangle \\ I_{12} &= \langle \psi_1^* \psi_2 | \hat{V}_{12} | \psi_1 \psi_2^* \rangle \end{aligned} \tag{2.25}$$

$\hat{V}_{12}$ is the intermolecular perturbation potential. For two well-separated dipoles this is given by,

$$\hat{V}_{12} = \frac{1}{4\pi\epsilon_0} \frac{p_1 p_2 - 3(p_1 \hat{r})(p_2 \hat{r})}{r^3} \tag{2.26}$$

where p_1 and p_2 are the dipole moments and $\hat{r}$ is the unit vector between them. This leads to excited state energy levels given by

$$E_\pm = E_1 - D' \pm I_{12} \tag{2.27}$$

This phenomenon of the splitting of the S_1 energy by intermolecular interactions is known as Davydov splitting[33].

In the two limiting cases of side-by-side and head-to-tail arrangements, one combination of the dipoles cancels out the transition dipole moment completely for either the lower or the upper level[15,16]. For the parallel side-by-side arrangement, the dipole moment is cancelled out in the lower energy level, while the opposite is true for head-to-tail dipoles. The result is a blue-shifted absorption and emission in parallel dimers, known as H-aggregates, and a red-shift in head-to-tail J-aggregates[15,16,34]. In reality dimers are rarely totally J- or H-aggregates, and both the red- and blue-shifted transitions can be observed to some extent[34].

This concept scales up to larger aggregates and is used to described the nature of the intermolecular interactions in a given molecular morphology. Work by Spano *et al.* has developed more sophisticated descriptions to capture more of the physics of molecular aggregates[35–37]. However, the simple picture of H- and J- aggregates is still a useful concept. Spano has shown shown how comparing the 0-0 and 0-1 transition intensities in the vibronic progression is a good marker for whether the dominant intermolecular interactions are more like an H- or J-aggregate[35].

In certain intermolecular situations, a pair of molecules will rearrange themselves geometrically after excitation to reach a lower-energy nuclear configuration, to form

what is known as an excimer. Excimer formation leads to red-shifted emission, and a reduction in photoluminescence quantum yield thanks to a narrower transition to the ground state and the Energy Gap Law (Equation (2.24)). Good examples of excimer formation can be found in pyrene aggregates[38], where excimers by the overlap of the central π-conjugated region in a face-to-face orientation. The excimer, which can be observed only in concentrated solutions or solid-state, has a distinct, broad, emission band compared to the monomer emission which is seen from dilute solutions with no intermolecular interaction.

2.3.2 Energy Transfer

Exciton diffusion is crucial in basically any optoelectronic device, and is one of the most important dynamical processes to understand when investigating molecular semiconductors. Within an extended system, excitons generally diffuse to the lowest-energy sites. For example, in photosynthetic systems, energy is funnelled between organic molecules from absorbers, chlorophyll, to reaction centres where it is converted to chemical energy[39]. Energy transfer can be described in terms of site-to-site hopping. Once again, we apply Fermi's Golden Rule, this time labelling state by D for donor, the molecule the exciton originates on, and A for acceptor, the molecule the exciton is transferred to:

$$\Gamma_{D\to A} = \frac{2\pi}{\hbar}|\langle\Psi_{A,f}|\hat{H}'_{ET}|\Psi_{D,i}\rangle|^2\rho_A(E_f) \tag{2.28}$$

There are two independent mechanisms with different $\hat{H}'_{ET}$ which we will cover here: Förster resonance energy transfer (FRET), mediated by Coulombic interactions, and Dexter energy transfer, which is driven by the exchange interaction (Equation (2.10))[14,21,39].

2.3.2.1 Förster Resonance Energy Transfer

The perturbative Hamiltonian for FRET can be simplified by treating the donor and acceptor as a pair of dipoles, which is a valid approximation as long as they are well enough separated[15]. Thus the rate of FRET is then proportional to

$$\Gamma_{FRET} \propto \frac{|\hat{\mu}_D|^2|\hat{\mu}_A|^2}{|\mathbf{R}_{DA}|^6} \tag{2.29}$$

The dipole moments $\hat{\mu}_D$ and $\hat{\mu}_A$ are evaluated for the transition from the ground state to the excited state that is undergoing transfer. From Section 2.2.1, we know

then that this will rule out the transfer of triplet excitons by FRET, as they do not have an allowed transition dipole to the ground state. By relating the emission and absorption spectra to the transition moment, as detailed in Barford[15], we find that,

$$\Gamma_{FRET} \propto \frac{1}{|\mathbf{R}_{DA}|^6} \int_0^\infty \frac{I_D(\omega)\alpha_A(\omega)}{\omega^4} d\omega \equiv \frac{f_D f_A}{\omega^2 |\mathbf{R}_{DA}|^6} J_{DA} \tag{2.30}$$

where J_{DA} is the overlap of the normalised donor emission and acceptor absorption and f are the oscillator strengths. The dependence on the overlap of the emission spectrum of the donor and absorption spectrum of the acceptor indicates that this process can be thought of as the emission and absorption of a (strictly virtual) photon.

In Figure 2.9a we can see a schematic for the FRET and in Figure 2.9b the absorption/emission overlap integrals J_{DA} is shown for two arbitrary molecules. If donor and acceptor are the same type of molecule (either 1 or 2), the overlap integral is J_{11} or J_{22}. A large Stokes shift as in molecule 2 reduces the efficiency of homogeneous energy transfer. Heterogeneous energy transfer from molecule 2 to 1 would have overlap integral J_{21}. Transfer from 1 to 2 is impossible due to lack of overlap.

The FRET rate also depends strongly on distance between the dipoles, and the effective FRET radius R_F is usually defined as the radius at which the FRET rate is equal to the decay rate of the donor were there no acceptor molecules around. In organic semiconductors, R_F is typically around 3 nm[21].

2.3.2.2 Dexter Energy Transfer

Dexter transfer rate can also be derived from Fermi's Golden Rule, using the exchange interaction (Equation (2.10)) between donor and acceptor K_{DA} as the $\hat{H}'$[40].

$$\Gamma_{Dexter} \propto J_{DA}|K_{DA}|^2 \propto J_{DA}\exp\Big(-\frac{2R_{DA}}{L}\Big) \tag{2.31}$$

Notably, although the rate still depends on the spectral overlap J_{DA}, there is no dependence on oscillator strength, so states without allowed radiative transitions to the ground state, such as triplets, can be involved. L is the average exciton radius in the donor and acceptor states, and the exponential fall off of Dexter transfer rate with R_{DA} means that Dexter transfer operates over shorter distances than FRET. The Dexter radius is typically < 1 nm[21,39]. This effectively limits transfer to direct neighbouring molecules, because Dexter transfer involves simultaneous electron transfer from donor to acceptor and acceptor to donor[41], as shown in Figure 2.9a. Despite the limited range of Dexter transfer compared to FRET, triplets can still diffuse over significant

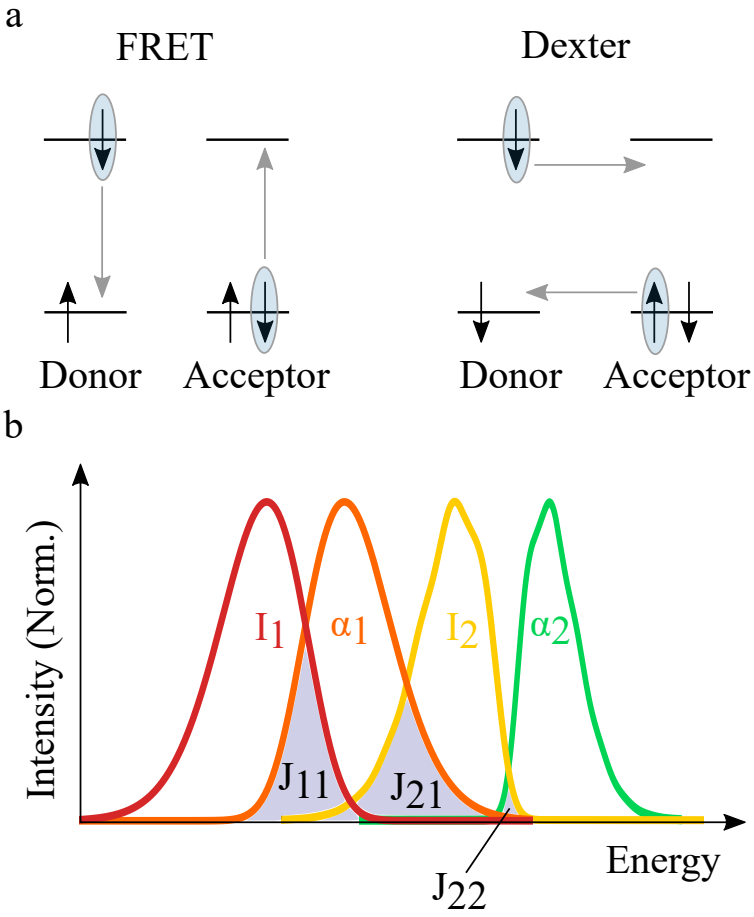

Fig. 2.9 a) Comparison of orbital schematics for FRET and Dexter transfer, where the horizontal lines are the HOMO and LUMO levels. In FRET, an excited electron transitions from LUMO to HOMO while in the ground state molecule an electron is promoted from HOMO to LUMO. In Dexter transfer, two-electron transfer occurs simultaneously from $\mathrm{LUMO_D}$ to $\mathrm{HOMO_A}$ and from $\mathrm{HOMO_A}$ to $\mathrm{HOMO_D}$. b) Normalised emission (I_i) and absorption (α_i) for two molecules 1 and 2, with their overlaps shaded and labelled as J_{DA}.

distances because of the long lifetime of triplets, allowing multiple Dexter transfer events before decaying to the ground state.

2.3.3 Charge Separation

In photovoltaics, excitons must be separated into electrons and holes that can travel to opposite electrodes and generate current. While this is simple in inorganic semiconductors where Wannier-Mott excitons are extremely weakly bound, in organics there is a significant binding energy to the Frenkel exciton that must be overcome. The most effective way of separating charges in OPV is with a type-II heterojunction of two different molecules or polymers with molecular orbitals that are offset in energy. In OPV, materials are typically categorised into electron donors and acceptors, according to their HOMO and LUMO levels. The energy offset at the heterojunction is then enough to overcome the binding energy of the exciton, and results in electron transfer if the exciton originates on the electron donor, or hole transfer is the exciton originates on the electron acceptor, as shown in Figure 2.10.

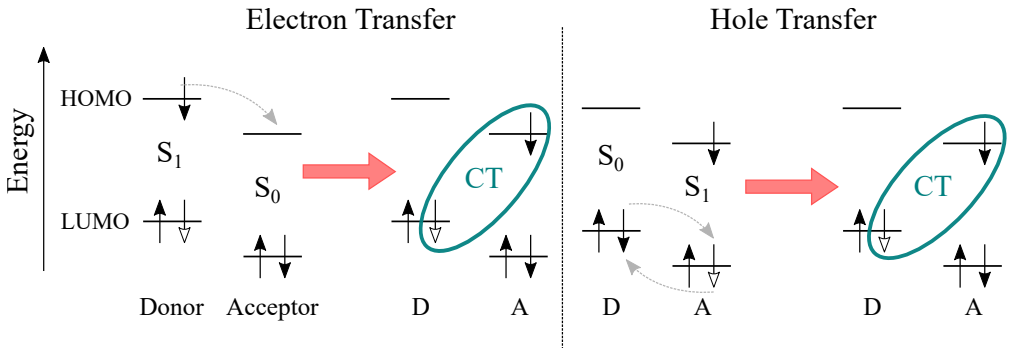

Fig. 2.10 Charge separation: Electron and hole transfer.

When charges separate by electron or hole transfer, they are typically still in a Coulomb-bound state, referred to as a charge transfer (CT) exciton or state, which must go on to separate into free, unbound charges. To maximise the power conversion efficiency (PCE) of an OPV system, there should be as high as possible quantum yield of free charges with the minimum energetic offset between donor and acceptor (i.e. the highest energy CT state) to minimise voltage loss. In recent years, after the long dominance of fullerene acceptors (NFA), there have been major improvements in the efficiency of non-fullerene acceptors. These acceptors can achieve high quantum yields with very low or zero energy offset between the donor and accepter frontier orbitals[42–45]. Clearly, the questions of why CT states form efficiently at these heterojunctions and

how the Coulomb binding energy of the CT state is overcome to form free charges are very important and various factors have been invoked to answer them. The morphology/crystallinity at the heterojunction, degree of delocalisation of CT states, and "hot states" that have not yet vibrationally relaxed have all been reported as facilitating efficient charge separation[46–52].

2.3.4 Exciton-Exciton Annihilation

In Section 2.3.2 we presented how excitons can move between molecules through a material. In the case of annihilation, we consider how rather than looking at an excitons moving from an excited molecule to one in the ground state, we can use the same formalism to now consider when two excited molecules interact[14,39]. In the case that at least one singlet exciton is involved, the following scenarios can result:

$$\begin{aligned} S_1 + S_1 &\rightarrow S_0 + S_n \rightarrow S_0 + S_1 + \text{phonons} \\ S_1 + T_1 &\rightarrow S_0 + T_n \rightarrow S_0 + T_1 + \text{phonons} \end{aligned} \tag{2.32}$$

where S_n and T_n are higher vibrational states which rapidly relax down to S_1 and T_1 respectively. Based on Equation (2.30), these transitions require an overlap between emission spectrum of the donor (in both cases $S_1 \rightarrow S_0$) and absorption of the acceptor (either $S_1 \rightarrow S_n$ or $T_1 \rightarrow T_n$, which we note has a good oscillator strength because it is wholly within the triplet manifold and requires no spin flip). The first transition in Equation (2.32) is known as singlet-singlet annihilation, and the second is singlet-triplet annihilation. Singlet-triplet annihilation cannot result in a singlet and the annihilation of the triplet, because this would require an oscillator strength for the emissive transition from $T_1 \rightarrow S_0$. Singlet-triplet annihilation results in a triplet, which persists for a long time compared to singlets, annihilating multiple singlets and providing a problematic loss pathway.

In the case that two triplet excitons meet, triplet transfer is mediated by Dexter transfer. Beginning with two spin-1 triplets, a triplet-triplet annihilation (TTA) event can result in a singlet, triplet or quintet (Q_n).

$$\begin{aligned} T_1 + T_1 &\rightarrow S_0 + S_n \rightarrow S_0 + S_1 + \text{phonons} \\ T_1 + T_1 &\rightarrow S_0 + T_n \rightarrow S_0 + T_1 + \text{phonons} \\ T_1 + T_1 &\rightarrow S_0 + Q_n \rightarrow S_0 + Q_1 + \text{phonons} \end{aligned} \tag{2.33}$$

Typically, the intramolecular quintet state, involving a doubly excited molecule, is at a higher energy than $2 \times E(T_1)$, and is thus the final pathway in Equation (2.33) is

energetically forbidden. The formation of a lone triplet from a TTA event is of little interest, and serves only to deplete the population of triplets, similarly to singlet-triplet annihilation in Equation (2.32). Notably, this does depend on the energy of the T_2 state - the condition being $E(T_2) < 2 \times E(T_1)$. However, the formation of a singlet from two triplets opens the door to some very interesting photophysics. Although it would seem to violate spin selection rules to move between triplet and singlet manifolds in this way, there is an important loophole in the form of an intermediate spin-singlet triplet-pair $^1(TT)$ state, which will be discussed in detail in this thesis.

$$T_1 + T_1 \rightleftharpoons {}^1(TT) \rightleftharpoons S_0 + S_n \tag{2.34}$$

The Merrifield model of an intermediate correlated triplet pair state, set out in Equation (2.34), was first proposed to explain the delayed fluorescence from anthracene and tetracene crystals[53]. In the 1960s, this behaviour was assigned to annihilation of triplet excitons due to its long lifetime, excitation density dependence, and temperature dependence[53–56]. Then, the discovery that delayed fluorescence in anthracene could be modulated by an external magnetic field was reported[57] and the Merrifield model of an intermediate correlated pair state emerged[58,59]. Suna also developed a more complex quantum mechanical description of the kinematics of the TTA process[60], which is beyond the scope of this thesis.

2.3.5 The Triplet-pair State

The combination of two triplets on neighbouring molecules involves four electrons, two on each molecule. Combining the spins of four electrons to form a single wavefunction gives 16 possible combinations, of which two are singlets ($S = 0$), nine are triplets ($S = 1$) and five are quintets ($S = 2$). The two $S = 0$ solutions for a 4 electron spin wavefunction across molecules A and B are:

$$|S_1^{(4)}\rangle = \frac{1}{\sqrt{2}}(|\uparrow\downarrow\rangle_A - |\downarrow\uparrow\rangle_A)\frac{1}{\sqrt{2}}(|\uparrow\downarrow\rangle_B - |\downarrow\uparrow\rangle_B) \tag{2.35}$$

$$|S_2^{(4)}\rangle = \frac{1}{\sqrt{3}}(|\uparrow\uparrow\rangle_A |\downarrow\downarrow\rangle_B + |\downarrow\downarrow\rangle_A |\uparrow\uparrow\rangle_B) - \frac{1}{2\sqrt{3}}(|\uparrow\downarrow\rangle_A + |\downarrow\uparrow\rangle_A)(|\uparrow\downarrow\rangle_B + |\downarrow\uparrow\rangle_B) \tag{2.36}$$

Equation (2.35) can clearly be separated into two singlets, one on each of the molecules A and B. However, Equation (2.36) is a superposition of triplet states which

add up to a total of $S = 0$. We can rewrite these states in the coupled spin basis of Equations (2.8) and (2.9):

$$|S_1^{(4)}\rangle = |0\,0\rangle_A\,|0\,0\rangle_B \tag{2.37}$$

$$|S_2^{(4)}\rangle = \frac{1}{\sqrt{3}}\Big(|1\,1\rangle_A\,|1\,{-1}\rangle_B + |1\,{-1}\rangle_A\,|1\,1\rangle_B - |1\,0\rangle_A\,|1\,0\rangle_B\Big) \tag{2.38}$$

The fact that Equation (2.38) cannot be separated in the molecular basis means that it is an entangled triplet-pair spin state[61]. Coupling between the $S_1^{(4)}$ and $S_2^{(4)}$ states allows TTA to produce a pair of singlet excitons (S_1 and S_0) without a spin flip. As can be seen by the reversible arrows in Equation (2.34), this also permits the reverse process without a spin flip, which is singlet exciton fission - the generation of a triplet pair from a singlet exciton.

2.4 Singlet Exciton Fission

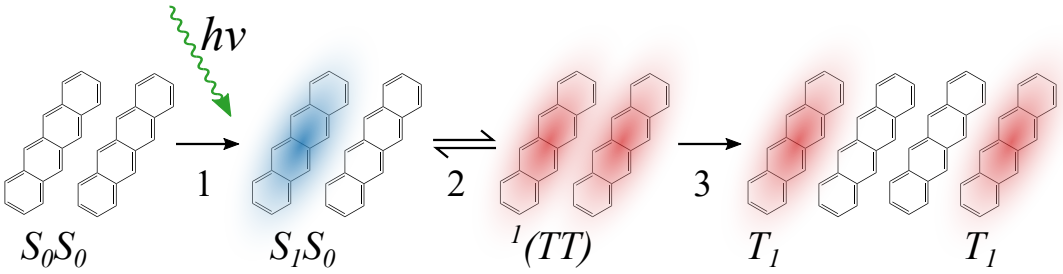

Fig. 2.11 Schematic of singlet exciton fission. Step 1: absorption of a photon creates an S_1 exciton on one molecule. Step 2: creation of a spin-singlet correlated triplet pair state. Step 3: Dissociation of the triplet-pair state to free triplets

When investigating the delayed fluorescence from TTA in anthracene and tetracene crystals in the 1960s, it soon became clear that the reverse process, singlet exciton fission, was also possible[53,62,63]. A simple schematic of this process is shown in Figure 2.11 - first a photon is absorbed to excite a single molecule to the singlet state. This state can then transition without the need for a spin flip to the correlated triplet pair that we have just discussed in the context of TTA, which can subsequently dissociate to form free triplets. The intermediate pair state $^1(TT)$ with overall spin $S = 0$ explains how fission can proceed so quickly when intersystem crossing of $S_1 \rightarrow T_1$ in organics without heavy

atoms is usually a slow process due to low spin-orbit coupling. This process comes with its own magnetic field effect (MFE) on the prompt photoluminescence[64–66]. Merrifield reported and modelled the different MFE for TTA and singlet fission in anthracene and tetracene[67]. Yarmus *et al.* used electron spin resonance (ESR) to probe the spin polarisation of triplets in tetracene generated by singlet fission, providing further evidence of fission via a spin-singlet pair state in the form of an preferential population of the $m_S = 0$ triplet level over $m_S = \pm 1$ (in the high field basis)[68]. These findings are all consistent with the Merrifield model used to explain TTA in Equation (2.34), and is now reversed:

$$S_0 + S_n \underset{k_{-}1}{\overset{k_1}{\rightleftharpoons}} {}^1(TT) \underset{k_{-}2}{\overset{k_2}{\rightleftharpoons}} T_1 + T_1 \tag{2.39}$$

After this initial flurry of reports following the discovery of singlet fission, in 1979, Dexter proposed that this quantum mechanical process that was unique to certain organic semiconductors could be useful for enhancing the PCE of photovoltaic cells[69]. He realised that if one could extract charge carriers from both triplet excitons generated in a fission event, photocurrent could be increased and losses to thermalisation reduced. This idea was revived by Hanna and Nozik in 2006[70], setting off a wave of singlet fission research that we will now review.

2.4.1 General Principles

In the simplest terms, the energetic condition for singlet fission is $E(S_1) \geq 2 \times E(T_1)$. However, while this approximately holds, singlet fission can definitely still proceed in slightly endothermic systems. The canonical singlet fission systems are the acenes, particularly pentacene and tetracene, which are exothermic and endothermic respectively. In pentacene, where singlet fission is exothermic by $\sim 110\,\mathrm{meV}$[71], the singlet state is totally quenched within 200 fs and a fission rate of $80\,\mathrm{fs}^{-1}$ has been measured with transient absorption[72,73]. In tetracene, the S_1 and T_1 energies are shifted such that $E(S_1) < 2 \times E(T_1)$, so singlet fission is endothermic. The final state of two triplets is at a higher energy than the initial photoexcited singlet, by $\sim 180\,\mathrm{meV}$[71]. Yet, in crystalline tetracene the formation of triplets still occurs, albeit on a slower $\sim 80\,\mathrm{ps}$ timescale[74,75]. The endothermicity of tetracene slows singlet fission down in comparison to pentacene, but it still proceeds with high yields (close to 200% of the initial singlet population) of triplets[74,76]. There are a number of factors that make this possible. There is an entropic effect, that the two triplet state has a higher entropy and so the process can increase overall entropy even when endothermic.

There is also evidence that for efficient endothermic fission systems like tetracene and TIPS-tetracene the energy of the TT state is lower or degenerate with the S_1 state, and the endothermic step is the separation of the TT state to $T_1 + T_1$[75,77,78]. This is deduced from the temperature independence of the formation of the pair and the temperature dependence of pair separation to free triplets. It has also been shown that this separation step is endothermic for a wider selection of materials, including overall-exothermic materials like pentacene and TIPS-pentacene, due to a binding energy associated with the correlated triplet pair[61,78].

In general, to compute the rate of fission, we need to consider the coupling V between the S_1S_0 state and the TT state.

$$V = \langle S_1S_0|\hat{H}|TT\rangle$$

To first order the rate of fission is proportional to this coupling[79]. However at higher orders we must also account for non-direct fission pathways, via virtual occupation of charge transfer (CT) states. The role of real and/or virtual CT states is contested. Some propose that CT states are vital in explaining the pathway from $S_1 + S_0$ to TT[79], while others calculate that the coupling between the $S_1 + S_0$ and TT states is strong enough for a direct formation of the TT state[80,81]. In Figure 2.12, the two proposed pathways are shown.

In a study by Yost *et al.*[80], the coupling, V, was calculated using a "bright" mixed state of S_1S_0 and CT states, but they found that the role of CT states varied significantly between molecules despite all the candidates they studied showing efficient fission. Although in some of the case studies, including pentacene, TIPS-pentacene and dithienyl-pentacene (DTP) there was a strong contribution to V from CT states, this was not a necessary criteria for rapid and efficient fission. Dibenzothiophene-pentacene (DBTP) showed sub-picosecond fission without significant CT character. This result implies that it is not required to reduce the energy gap to the CT states to make them accessible in order to design a molecule for singlet fission, however it does seem that CT states play a role in coupling the S_1 and TT states in certain systems.

2.4.1.1 Tetracene

Much of what we know about singlet fission has been learned from studying the archetypes of tetracene and pentacene. In tetracene, fission was first observed by the dependence of singlet and triplet populations on magnetic field by looking at singlet fluorescence[65]. As the magnetic field increases, the equilibrium between S_1S_0 and

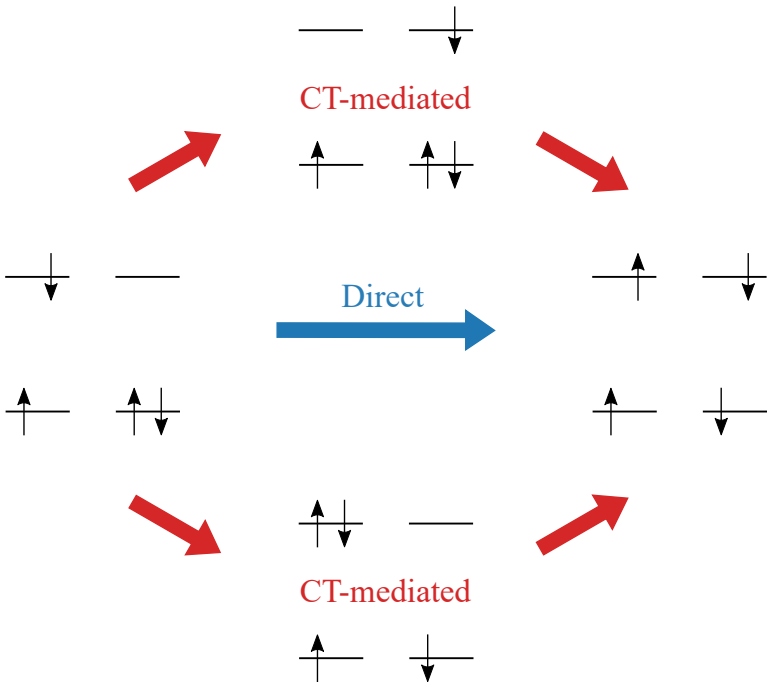

Fig. 2.12 Direct singlet fission (blue) and mediated singlet fission via a charge transfer state (red)

TT states shifts, changing the population of singlets and modulating the amount of fluorescence from the $S_1 \rightarrow S_0$ transition.

In more recent studies of tetracene, there has been a focus on explaining how it can proceed despite being endothermic by ~180 meV[65,71,82]. Cryogenic transient absorption measurements have shown temperature independence of the formation of the TT state, which suggests that TT is degenerate with S_1, and lower in energy than two free triplets[75,83]. It was reported in 2010 that fission in polycrystalline tetracene occurs within 10 ps (much faster than previously thought)[76]. However, this was based purely on the 9.2 ps decay of the stimulated emission signal from the S_1 state. There are other decay pathways for this state than singlet fission, and exciton-exciton annihilation had to be taken in to account due to high fluences. Later it was corrected and a new rate of 80 ± 3 ps was published for fission in solid tetracene, along with evidence of a dark TT state[74], and this rate has been verified by other studies[75,84].

Because the energy of two triplets is more than that of a singlet in tetracene, there is significant delayed fluorescence from TTA, the reverse of singlet fission. Quantum beats are seen in the intensity of the delayed fluorescence in single crystals of tetracene[85,86]. The oscillations arise because in singlet fission, the rapid decay of the singlet and

population of $^1(TT)$ provides the coherence required to see oscillations between the three zero-field triplet pair states $|xx\rangle$, $|yy\rangle$ and $|zz\rangle$ with overall singlet character. That is, the formation time of $^1(TT)$ is shorter than the period of the oscillations due to the energy gaps between the three triplet states[85]. The three dominant frequencies of the oscillations are a good match with the energy gaps between the $|xx\rangle$, $|yy\rangle$ and $|zz\rangle$ pair states, as calculated using the the zero-field splitting (ZFS) parameters D and E which can be measured using ESR. This was a significant finding, providing an independent verification of the pair-state mechanism from the magnetic field effect.

While there is clearly compelling evidence for a lower-energy pair state, an alternative explanation for the overall endothermicity of fission in tetracene is offered by Chan *et al.*[87]. They report that tetracene can overcome the endothermic barrier by coherent coupling and entropic gain, and that the intermediate multiexcitonic TT state is degenerate with $2 \times T_1$ not with S_1. This means that an $S_1 \rightleftharpoons TT$ superposition must be initially formed, and entropic gain is the driving force for the subsequent decay to $2 \times T_1$[87]. This assertion rests on data from time-resolved 2 photon photoemission spectroscopy (TR-2PPE). TR-2PPE is a two pulse experiment where after an initial pump pulse, usually resonant with the optical band gap, a high energy ionisation pulse (probe) causes the emission of photoelectrons with an energy corresponding to the difference between the probe energy and the ionisation energy of the state the electron was in. In the TR-2PPE experiment, a lower-energy state assigned to the triplet is seen within the rise time of the signal (20 fs), which Chan *et al.* assert confirms the coherent excitation of S_1 and a multiexcitonic TT state in an equilibrium. However, Yost *et al.* claim this experimental data is more likely explained by some CT character in the bright state that happens to be have a similar ionisation energy as the TT state[80].

Several studies have shown that there is a strong morphology dependence on fission in tetracene[88,89]. Single crystals have a slower S_1 decay of 130 to 300 ps (depending on the sample) and do show some thermal activation is required[85,89]. Polycrystalline samples tend to show faster singlet decays (70–90 ps) and show reduced or no temperature dependence to suggest thermal activation is a factor[74,75,89]. It seems likely that this is due to a greater density of defects or non-standard packing motifs that accelerate fission in more disordered morphologies[89]. These are often referred to as singlet fission "hot spots".

A study by Stern *et al.* on TIPS-tetracene in the solid state makes a comparison between polycrystalline and disordered films[77]. Here an initial rise of the TT state occurs within 300 fs and is matched by a rapid partial loss of the signal attributed to S_1. This is followed by a slower, morphology dependent phase of TT rise/S_1 decay

on a 6–20 ps timescale. The rapid initial rise of the TT state in TIPS-tetracene is much faster than previous studies of polycrystalline tetracene, and it is shown that it is vibrationally coherent. That is, vibrational modes induced by the shortness of the pump pulse but with a period too short to be generated impulsively by the TT formation itself (as in the oscillations in the delayed fluorescence of tetracene[85]), are preserved from the S_1 state to the TT state[77]. The vibrational coherence seen here is indicative of a breakdown of the Born-Oppenheimer approximation and strong coupling of vibrational and electronic degrees of freedom. A theoretical study of tetracene concluded that this vibronic coupling was in fact crucial for singlet fission to proceed[90].

Interestingly, when the Fourier transforms are taken of the oscillations in the TIPS-tetracene transient absorption data, it can be seen that different modes are present before and after this vibrationally coherent TT rise. Initially there is a strong 315 cm^{-1} vibrational mode in the S_1 signal, and this mode depletes simultaneously with the growth of a mode at 760 cm^{-1} in the TT signal[77]. This suggests that the 315 cm^{-1} mode is a tuning mode for the ultrafast TT formation and the 760 cm^{-1} mode is a product mode formed as the wavepacket crosses a conical intersection to the TT state. This model of vibrationally driven rapid singlet fission in TIPS-tetracene is at odds with the strong electronic coupling model offered for tetracene by Chan *et al.*[87]. In addition to the difference in the slower phase of the TT formation, the subsequent separation of TT to $T_1 + T_1$ is also shown to be morphology dependent in TIPS-tetracene, only occurring in the disordered samples and not in the polycrystalline sample, and is thermally activated[77].

The interplay between singlets, triplet pairs, and free triplets by singlet fission and TTA presents an interesting situation for exciton transport in tetracene. Transient absorption microscopy has shown triplet pairs diffusing in a singlet-like way by FRET, coining the term "cooperative transport". The singlet character of the triplet pair allows much greater diffusion via FRET than triplets can normally achieve via Dexter transfer alone[91,92].

2.4.1.2 Pentacene

In contrast to tetracene, pentacene offers a model system of exothermic fission. In polycrystalline pentacene, a fission rate of ∼80 fs has been observed[72,73,93]. Theoretical calculations confirm that pentacene also undergoes rapid fission via a dark multiexcitonic state that is energetically accessible from the optically allowed excited state[94].

Experiments on vibrational coherence in solid state TIPS-pentacene have been particularly successful. TIPS-pentacene also has a time constant of 80 fs for fission and has the added benefit of being solution processable[95]. Musser *et al.* find that in this case the coupling between vibrational and electronic degrees of freedom is strong enough to induce a conical intersection between the S_1 and TT potential energy surfaces[95]. Using a three pulse experiment with a long "dump" pulse tuned to the excited state absorption, it was possible to isolate the vibrations on the excited electronic state by removing residual signatures of vibrations in the ground-state. Unlike in tetracene[77], fission is much faster so coherence in the TT state could be caused impulsively by the rapid population transfer. However, even at 80 fs, the TT state still forms slower than the period of the fastest observed oscillations in the TT state. Vibrational coherence between the singlet and the explicitly intermolecular TT state implies that the singlet is delocalised over more than one molecule[95]. Another TIPS-pentacene report, from Bakulin *et al.*, used two-dimensional electronic spectroscopy (2DES), a four pulse experiment where both the electronic and coupled vibrational dynamics of singlet fission can be investigated[96]. Here, vibrational modes were observed that serve to couple the bright S_1 state to the dark TT multiexcitonic state through a "vibronic manifold of mixed states"[96].

2.4.2 Fission Beyond the Acenes

While the oligoacenes of tetracene and pentacene (and their derivatives) remain the canonical systems on which the majority of research has been focused, these molecules have some drawbacks when it comes to use in potential devices. The most important of these being their chemical stability - acenes readily react with oxygen and degrade, limiting the potential lifetime of the device[97,98]. The triplet energy in pentacene is too low to transfer to a silicon cell, while tetracene is possibly acceptable although lacking a large driving force which could limit the efficiency of triplet energy transfer[99]. Therefore, there is substantial interest in new classes of singlet fission material with greater chemical stability and the potential to tune their triplet energy level. Chapters 4 and 5 will explore work undertaken with this aim.

Singlet fission has now been experimentally observed in an array of organic molecules and polymers, depicted in Figure 2.13. As well as tetracene and pentacene, fission is reported in anthracene[53] and hexacene[100]. Modifications to these archetypal acenes have produced a large number of derivatives which are also fission-active, including the now widely studied Triisopropylsilylethynyl- (TIPS-) tetracene[77,82,101] and

TIPS-pentacene[95,96,102–107], and also biphenyl-ethynyl-anthracene (BPEA)[108], diphenyl-tetracene[109], and rubrene[110]

Beyond the acene derivatives, singlet fission has been observed in rylenes, a highly stable family of dyes, such as perylene[111], perylene diimide (PDI)[112–115], terrylene[116], terrylene diimide (TDI)[117] and quaterrylene diimide (QDI)[117,118]. Singlet fission has also been reported in carotenoids such as zeaxanthin[119], astaxanthin[120] and the carotenoid structures in peridin-chlorophyll-protein complexes in photosynthesis[121]. There are reports of fission in small molecules such as diketo-pyrrolopyrrole (DPP)[122–124], dipheynl-hexatriene (DPH)[125–127], diphenylisobenzofuran (DPBF)[128,129] and dipyrrolon-aphthyridinedione (DPND)[130]. Recent reports have established fission in zethrene diradicaloids[131] and carbene-derived diradicaloids[132]. Triplet pair-states also form in certain polymers, such as polydiacetylene (PDA)[133,134] and poly(thienylenevinylene)[135,136], and in some donor-acceptor co-poylmers like poly(benzodithiophene-n-thiophene-1,1-dioxide) (PBTDOn) and Isoindigo-di(methylthiophene) (IIDDT-Me)[137,138].

2.4.3 Singlet Fission in Solution

In solution, fission is diffusion limited. That is, once an isolated molecule has been excited, it must encounter another ground state molecule before fission can occur. The average timescale for these events depends on the concentration of the solution. Also, in solution, the molecules are free to arrange themselves in an optimal geometry and form an excimer. Fission has been observed in concentrated solutions of TIPS-pentacene[102] and TIPS-tetracene[82,139], the structures of which are shown in Figure 2.13.

In TIPS-tetracene and TIPS-pentacene, it was found that at high enough concentrations, singlet fission can occur in solution with a TT excimer state forming in under 100 ps in TIPS-tetracene, and 400-530 ps in TIPS-pentacene. They also see breaking up of the excimer to free triplets on a timescale of 10 ns[82] and 13 ns[102] respectively. Transient absorption was used to identify the TT excimer states which have a distinct spectral signatures compared to the initial S_1 spectra and the spectra assigned to free triplets. This was a significant finding, and another independent verification of the presence of a distinct intermediate pair state[82].

Triplet yields in solution were $197 \pm 3\%$ and 120% in TIPS-pentacene and TIPS-tetracene respectively[82,102]. The difference in yields of free triplets despite the similar kinetics (and actually a faster TT formation in the TIPS-tetracene) can be understood as a result of the endothermicity of the separation of the triplet pairs in TIPS-tetracene. The TT excimer is at a lower energy and so the separation is thermally activated and must compete with other decay pathways. In both molecules, red-shifted PL was

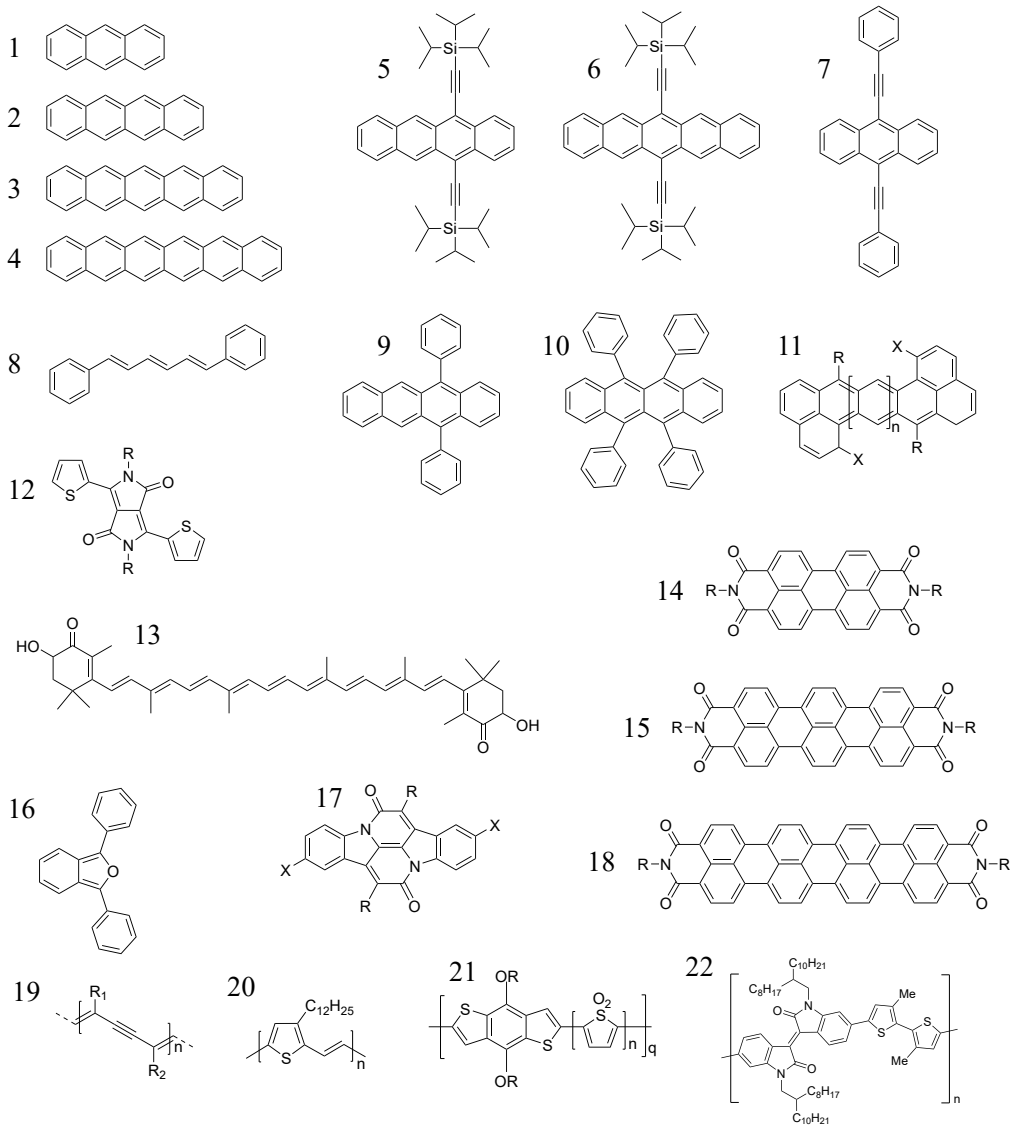

Fig. 2.13 Singlet fission chromophores that have been experimentally reported. 1. Anthracene, 2. Tetracene, 3. Pentacene, 4. Hexacene, 5. TIPS-tetracene, 6. TIPS-pentacene, 7. BPEA, 8. DPH, 9. Diphenyl-tetracene, 10. Rubrene, 11. Zethrene, 12. DPP, 13. Astaxanthin, 14. PDI, 15. TDI, 16. DPBF, 17. Cibalackrot, 18. QDI, 19. PDA 20. Poly(thienylenevinylene), 21. PBTDOn, 22. IIDDT-Me.

seen from the excimer when the concentrations was increased to above the threshold required for singlet fission.

There has been some disagreement on the specific role of the excimer in TIPS-tetracene fission in solution and how to make sense of the photoluminescence from this state. Dover *et al.* claim that the excimer state from which red-shifted PL is detected is not likely to break up into free triplets, and is in fact a significant loss pathway[139]. Their analysis is based on fitting the prompt and delayed PL to a reversible model. However, their interpretation is disputed by significant evidence from Stern *et al.* regarding the unique transient absorption signature and temperature-activated separation of the excimeric state[77,82]. It appears that the condition of reversibility is incorrectly invoked by Dover *et al.*, as the TTA process, which is exothermic, need not always proceed via the same excimer state as singlet fission.

Beyond TIPS-tetracene and TIPS-pentacene, fission in solution has also been verified by MFE in solutions of diphenyl-tetracene, diphenyl-pentacene, dithienyl-tetracene and rubrene[109]. Thompson *et al.* suggested that if the MFE was enhanced or reduced by altering the solvent polarity it would point toward a role for a real CT state in fission, however this was not seen in any of these solutions[109].

2.4.4 Intramolecular Fission

While fission can occur in highly concentrated solutions of TIPS-pentacene and TIPS-tetracene, many molecules are not soluble enough to reach the required concentrations. However, singlet fission can be seen in dilute solutions of certain molecules which are designed to host the whole triplet pair in one covalently bonded system, namely dimers, oligomers and polymers. Dimers especially offer the chance to reduce the complexity of singlet fission compared to the solid state, by investigating the smallest possible system capable of fission. However, initial attempts with covalently bonded tetracene dimers[140,141] and DPBF dimers[142] reported very low triplet yields, below 10%.

It has become clear that the nature of the covalent linker between the individual chromophores in a singlet fission dimer or oligomer is very important for improving on the low yields of the first iterations of singlet fission dimers. Various studies have investigated varying both the physical distance and the degree of conjugation/electronic coupling across the linker. Sanders *et al.* used a phenylene linker motif in a bipentacene dimer, and varied the number of phenylenes in the bridge from none (i.e. a direct link between carbons on the pentacene cores) to two phenylenes, and found that increasing the number of phenylenes slowed singlet fission[143]. However, the yield was $\sim 200\%$ for all of the linkers, showing the robustness of pentacene fission. Indeed, a pentacene

dimer with a totally non-conjugated linker still showed quantitative fission[144]. The same is not true for tetracene dimers, where different linkers have a large effect on the fission yield.

With a phenyl linker, significant differences have been demonstrated between connecting to the phenyl at the para, meta and ortho positions. In pentacene, the balance between tripet formation and decay rate varies between the three isomers and is optimal for a yield of 150% in the meta isomer[145]. Calculations comparing meta- and para-phenyl linked pentacene dimers show that the triplet pairs cannot dissociate in the para isomer whereas they can in the meta isomer[146]. In tetracene dimers with the same phenyl linkers, fission was shown to be favoured in the para isomer, which is wholly conjugated, while singlets decayed radiatively in the meta isomer which is cross-coupled rather than fully conjugated[147,148]. Additionally, while coupled triplets formed in both the ortho and para isomers, the lack of rotational freedom in the ortho isomer prevents the triplets from decoupling[148]. Calculations have shown that vibronic coupling in these dimers connects S_1S_0 to TT, and the strength of this coupling allows much faster pair formation in the para isomer than the meta isomer. The large vibronic coupling in the para isomer is a consequence of the rotational freedom around the phenyl[149]. Interestingly, in dimers of pyrene-fused azaacenes (dibenzodiazahexacene), the ortho isomer reported the highest triplet yield, due to the increased spatial contract between the monomers[150].

In systems where the energetics for singlet fission are finely balanced, unlike pentacene, it is important not to allow the dimerisation to lower the singlet energy significantly. Singlet fission was not seen in a DPP dimer where the singlet was stabilised by 400 meV relative to the monomer while the triplet was unchanged, such that the energetics of fission became unfavourable[151].

In order to maximise the yield of triplets and also prolong their lifetime such that they might be usefully observed or extracted, a fine balance must be struck to prevent recombination by triplet-triplet annihilation (TTA), while keeping the initial rate of triplet pair formation high. In a study of homo-conjugated and non-conjugated linkers for pentacene dimers, homo-conjugated linkers proved especially successful as they had even faster triplet pair formation times than conjugated analogues, while significantly slowing recombination and extending the triplet lifetime[152]. In the phenylene series of pentacene dimers, increasing the number of phenylene linkers extended the triplet lifetime by slowing TTA[143]. As well as modifying the linker to promote longer triplet lifetimes by better decoupling, trimers or larger oligomers allow triplets to migrate away from each other, increasing their lifetimes and the triplet yield relative to

dimers[111,153]. This effect is enhanced by using energetics to force apart the triplets, such as in pentacene-tetracene-pentacene structures, where the triplets are inclined to stay separated, concentrated on the terminal pentacenes with the lower triplet energy[154].

A useful variable to change when investigating intramolecular fission is the solvent polarity. Solvents with a higher polarity can stabilise CT states, and consequently the effect of the solvent polarity of fission rates and yields can be informative with regards to the role of CT states in the fission process. For example, in an orthogonal pentacene dimer, the singlet fission rate increases when moving from toluene to the more polar ortho-dichlorobenzene (o-DCB), showing that a more-accessible virtual CT state can increase the coupling between S_1 and $^1(TT)$[155]. Solvent polarity dependence has been seen in many intramolecular singlet fission systems, such as phenyl-linked pentacenes[145], DPBF dimers[142] and PDI dimers[156]. As well as by solvent polarity, the CT state of orthogonal pentacene dimers can also be tuned by side groups, further demonstrating the effects of coupling via a virtual CT state[157].

Pentacene dimers have also been used to investigate the heavy-atom effect on singlet fission. A set of platinum-bridged pentacene dimers demonstrated that the heavy atom effect does not affect TT formation but does serve to increase coupling from $^1(TT)$ to $^3(TT)$ and $^5(TT)$. The majority of these pairs still annihilate to form a singlet triplet, however a minority are able to decouple to free triplets, which is not the case without the effect of the spin-orbit coupling of the heavy Pt atom[158]. Enantiomerically pure versions of the Pt-bridged pentacenes showed no dependence on chirality, but triplet yields are affected by solvent polarity, again implying fission mediated by a CT state[159].

2.4.5 Influence of Morphology

As already alluded to for tetracene, sample morphology and crystal packing have significant effects on both the fission rate and triplet yield. This has been shown in samples of identical molecules arranged in different polymorphs, such as in tetracene[89,160], TIPS-tetracene[77], TIPS-anthracene[161] and DPH[125]. The packing of molecules can also be varied by adding different quantities of inert spacer molecules, as has been reported for rubrene[162], where an exponential dependence of fission yield on inter-molecule spacing was found, and pentacene[163], where quintets were observed by trESR only in an intermediate concentration regime where pentacene dimers were present. We can go further and modify the molecule itself to induce a different packing. Often this is achieved with inert side groups/alkyl chains, such as in a study by Pensack *et al.* of side group bulkiness in pentacene derivatives[164]. Bulkier side groups separate the molecules

and reduce coupling of the pair state to the ground state, extending triplet lifetimes and decoupling of the pair[164]. Similar findings are apparent from changing the groups on the imide position of PDI[115] and the side chains on DPP[123]. Substitution of carbons within the conjugated core can also disrupt packing and affect singlet fission, however it is harder to deconvolve the effects from packing and those from the change in electronic structure of the monomer. Nonetheless, fluorinated and brominated pentacenes have demonstrated that a more disrupted/amorphous packing can slow singlet fission which would otherwise occur rapidly when excitons can delocalise over long-range ordered crystals[165]. Amorphous TIPS-pentacene nanoparticles have shown frustrated TT pair separation compared to crystalline versions[104].

While long range order can sometimes promote faster fission, if the innate crystal structure does not contain a favourable geometry for fission, then it can only occur at defects or "hot spots", which occur at a greater density the more amorphous a sample is. The kinetic signatures of "hot spot" mediated fission, where excitons often have to migrate to these positions in the film after photoexcitation, have been seen in Diphenyl-tetracene[166] and verified by calculations[167]. Similar findings are reported for cyano-tetracene[168] and TIPS-pentacene[107].

2.4.6 Insights from Magnetic Resonance

The findings discussed thus far have been from optical experiments, measuring photoluminescence and transient optical absorption signatures of excitonic states. These are very powerful tools in singlet fission, however they lack sensitivity to different spin states which are separated by energies that are small relative to optical transitions. To probe the spin dynamics of singlet fission it is necessary to use ESR and optically detected magnetic resonance (ODMR). The experimental details of these techniques will be described in the next chapter.

Triplet signatures from singlet fission were first seen using ESR by Yarmus *et al.* in 1972[68]. ESR is uniquely able to distinguish between triplets formed by ISC and singlet fission, due to the different relative populations of the triplet sublevels associated with different formation mechanisms[169,170]. In crystalline tetracene, ESR was used to see the turning off of pair dissociation to free triplets below 200K, where triplets born from ISC domninate instead[171]. In 2017, for the first time the spin signature of a quintet multiexcitonic state, unambiguously a triplet pair, was observed in TIPS-tetracene films[172] and pentacene dimers[173]. There is now evidence in a variety of systems that through singlet-quintet mixing[61], quintet multiexcitons are present as an intermediate between $^1(TT)$ and free triplets, including in TDI dimers[174], in TDI and QDI films[117],

in pentacene and tetracene dimers with an aliphatic adamantane linker[144,175], and in diluted pentacene films where the concentration of pentacene is seen to modulate the coupling within triplet pairs[163].

There is ongoing work to establish a full theoretical framework for the formation of quintet states and the nature of the mixing between pair states in the singlet, triplet and quintet manifolds. The exchange interaction between triplets within a pair, J is a critical parameter. Collins *et al.* propose that exchange interactions must vary with time to explain the formation of quintets[176]. There is good evidence that J is dependent on the precise relative geometry of the pair of molecules on which the pair state is located. In TIPS-tetracene, in a high-field MFE experiment, level anticrossings at J, $3J/2$ and $3J$ were seen for four different values of J, matching the four unique molecular pair geometries in the crystal structure[177]. At low enough temperatures, each of these unique pairs has a distinguishable photoluminescence spectrum that is shifted according to the strength of interaction in the pair[171], and these different spectra have been related to specific pairs in the crystal structure[178,179]. A MFE modelled by multiple Js was also seen in DPH, where J decreased as the triplets dissociate and move apart[127].

2.4.7 Harvesting Triplets

Singlet fission can only be useful in a photovoltaic application if the triplet excitons can somehow be harvested. There are a number of strategies for this under investigation, which can broadly be grouped into three categories: 1. Charge transfer from a singlet fission material to an electron acceptor such as C_{60}, 2. Directly transferring excitons from a fission material to a lower-band gap cell (e.g. silicon), or 3. Transferring triplets to an acceptor which emits the energy as photons which can absorbed by a lower-band gap cell (e.g. silicon)[180].

2.4.7.1 Triplet Charge Transfer

In this architecture, triplets must be formed at or migrate to an interface with an acceptor, in the exact same way as for conventional OPV donors[181]. Early demonstrations with pentacene and C_{60} bilayers showed proof of the concept[182] and external quantum efficiency (EQE) over 100%[183]. In a TIPS-pentacene/C_{60} heterostructure, it was shown that ultrafast (<75 fs) electron transfer can occur from singlets can outcompete singlet fission, followed by slow (1.6 ps) triplet electron transfer[184]. This clearly shows that this strategy requires careful design against long range delocalised singlets that can

undergo electron transfer with the acceptor before singlet fission occurs. An alternative architecture has the singlet fission material (in the demonstration this was rubrene) between layers of donor and acceptor, so excitons on the donor can FRET to the singlet fission material before undergoing fission[185]. In a comparison of different electron acceptors to be paired with pentacene, MFE on photocurrent was measured and it was found that colloidal nanocrystal of PbSe were more promising than C_{60}[186]. Although more challenging to integrate into a device, intramolecular fission has been used to generate charges directly: two electron transfer was seen to anthraquinone from a dimer of Tetracyanomethylene quinoidal bithiophene[187].

2.4.7.2 Triplet Energy Transfer

A consensus has emerged that given the commercial success and technological maturity of silicon solar cells, singlet fission can be most usefully applied in sensitizing silicon. That is, transfer of the whole exciton to silicon to create an electron-hole pair. Tetracene has a promising triplet energy level, $\sim 150\,\text{meV}$ above the silicon band gap. This has been technologically very difficult to achieve, however a recent report from Einzinger *et al.* demonstrated triplet energy transfer from tetracene to silicon using an ultra-thin hafnium oxide interfacial layer[188]. The engineering of this interface is a significant challenge. A technique has been developed to use the triplet transfer as a function of height of tetracene islands to compare the effectiveness of different oxide/aromatic interlayers[189]. Triplets can only transfer by Dexter transfer, requiring direct wavefunction overlap. It has been shown that thermally annealing the tetracene layer can promote an inclined orientation at the interface which maximises wavefunction overlap[190].

2.4.7.3 Photon Multipliers

Perhaps the most promising and pursued architecture is the photon multiplier - transferring the triplets to an emissive system that emits photons above the band gap of silicon that are then absorbed by a silicon cell[191,192]. The key is to use an emitter with large spin-orbit coupling such that the triplet state can quickly evolve to an emissive state. For this reason, PbS or PbSe quantum dots/nanocrystals have been the most successful[193]. Triplet transfer has been demonstrated from tetracene to PbS nanocrystals[194], and from pentacene to PbSe nanocrystals[195]. An important recent development was singlet fission ligands - ligands based on tetracene/other conjugated organics with a comparable triplet level, that can funnel energy to the nanocrystal[196,197].

The native ligands that nanocrystals are synthesized with are typically long inert chains such as oleic acid, which block efficient triplet transfer.

Due to the promise of photon multipliers, the physics of triplet transfer across the organic/inorganic interface is subject to considerable interest. The nature of the binding and molecular orientation at the surface is crucial[198,199]. The mechanism in tetracene/pervoskite nanocrystals has been shown to include a CT state, as electron transfer is followed by hole transfer[200]. In tetracene and PbS quantum dots with tetracene ligands, triplet energy transfer trends are consistent with an electron exchange mechanism, where an electron is transferred from the tetracene ligand to the quantum dot and vice versa[99]. An energetic driving force is required to ensure quantitative triplet transfer both to the ligand and then from the ligand to the nanocrystal, meaning that a singlet fission with triplets at 1.4-1.5 eV, significantly above tetracene, is desired[99].

2.5 Enhancing Photovoltaics

The nature of single-junction solar cells sets a thermodynamic limit on their PCE. Next generation solar technologies must look outside of the simple single-junction architecture to circumvent this limit, through better harnessing the breadth of the solar spectrum.

2.5.1 The Single-junction Limit

The single-junction limit dates back to a calculation from 1961 of the maximum PCE for a single band gap cell operating perfectly under a solar spectrum[201]. Approximating the solar spectrum to a black body at temperature $T_{Sun} = 6000\,\mathrm{K}$, and assuming that the cell is an infinite absorber of all photons above its band gap $E_g = h\nu_g$, and that any excess energy is lost to heat as excitations cool to the band edge, the incident and output powers are given by P_{in} and P_{out}:

$$P_{in} \propto qh \int_0^\infty \nu n(\nu) d\nu \tag{2.40}$$

$$P_{out} \propto qh\nu_g \int_{\nu_g}^\infty n(\nu) d\nu \tag{2.41}$$

$$n(\nu) = \frac{2h\nu^3/c^2}{\exp(\frac{h\nu}{k_B T_{Sun}}) - 1} \tag{2.42}$$

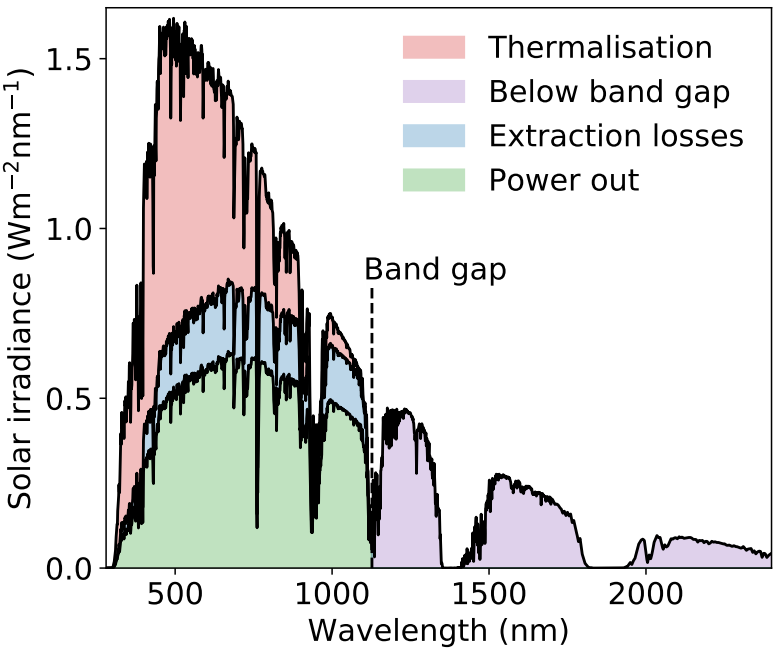

Fig. 2.14 Energy losses in a perfect single junction solar cell. AM1.5 spectrum, an approximation of the irradiance on the surface of the earth, is used. Photons below the band gap are not absorbed, shown in purple. Energy lost to thermalisation is red, and other extraction losses are in blue, with power output in green.

$n(\nu)$ is the Planck distribution[202]. The PCE is then the ratio of P_{out} to P_{in}. In this idealised single junction cell, energy is lost as photons with energy below $h\nu_g$ that are not absorbed, and photons with energy greater than $h\nu_g$ lose their excess energy to heat by thermalisation. With only these losses, a PCE of 44% is possible for $h\nu_g = 1.1\,\text{eV}$. However, when factoring in thermodynamic losses and energy lost in photon emission a detailed balance limit of 33% is found[201,203]. These extra losses are grouped together as extraction losses in Figure 2.14. Calculations using the most accurate simulated solar spectrum (AM1.5G) rather than the black body approximation indicate a limit of 33.77% for a band gap of $1.34\,\text{eV}$[3].

It can be seen from Figure 2.14 how the power from different parts of the sun's spectrum is utilised or lost in a single junction cell. An intuitive way to deal with this is to use multiple different materials with different band gaps that can each efficiently capture energy from different parts of the spectrum. For a tandem cell with two sub-cells the detailed balance limit increases by 12%, and three sub-cells would give a further 7%[204]. Taking this to the limit of an infinite stack of cells each with an infinitesimally different band gap, the limit becomes 68%. However, even two sub-cell tandems are very expensive and challenging to engineer, because the current must be

matched between all the sub-cells in series. This is difficult when the incident spectrum changes with cloud cover/time of day. There are alternative spectral management techniques that could circumvent the single-junction limit without the current matching issues of a multi-junction tandem cell: up-conversion and down-conversion.

2.5.2 Up-conversion

In an up-conversion solar cell, photons below the band gap are absorbed by a separate system which combines two photons to a higher energy state that is above the band gap. Triplet-triplet annihilation (TTA) can potentially fulfil this purpose. The general scheme typically involves a triplet sensitizer, which absorbs the low energy photons and quickly intersystem crosses to a triplet state, and must therefore usually involved a heavy metal to induce strong spin-orbit coupling. A typical sensitizer would be platinum octaethylporphyrin (PtOEP)[205]. The triplet on the sensitizer is transferred to a triplet annihilator, which should be a molecule with an exchange energy such that $E(S_1) \leq 2 \times E(T_1)$, for example diphenyl-anthracene (DPA)[205]. Two annihilators in the T_1 state can then undergo annihilation to produce a singlet which can fluoresce to produce a photon above the band gap of the solar cell, thus reducing sub-band gap losses.

TTA-up-conversion (TTA-UC) has been well characterised in solution[205–208], where the sensitizer-annihilator and annihilator-annihilator interactions are diffusion mediated and rely on high excitation densities, which limits the performance under solar excitation densities. Solid-state diffusion-limited systems have also been developed, for practical reasons for incorporating into a device[209–211]. Strategies to circumvent the limitations of diffusion include using dimers as intramolecular annihilators[212], and building supermolecular, macromolecular and self-assembled systems that funnel triplets towards annihilation centers[209].

TTA-UC is not the only possible up-conversion system. Lanthanide-doped nanocrystals can achieve up-conversion quantum efficiencies of 5% under monochromatic excitation, however they are limited by their narrow absorption spectrum[213,214]. Another form of up-conversion has been proposed that uses inorganic quantum well structures to produce anti-Stokes emission with the extra energy coming from the ambient thermal reservoir, and coupling to a second conventional solar cell[215], however TTA-UC is the most promising up-conversion strategy at present[216]. Up-conversion itself has other possible applications beyond photovoltaics, such as fluorescence labels for bio-imaging and drug-targeting[209]. For drug-targeting the idea is to use near infra-red (NIR) light, which can more easily pass through tissue, to excite up-conversion centers where higher

energy photons are produced that stimulate drug release at the location where the NIR light has been focused.

2.5.3 Down-conversion

While up-conversion addresses losses due to photons that are not absorbed below the band gap, down-conversion can reduce losses to thermalisation. High energy photons can be split by MEG in inorganic nanostructures[5,6] or singlet fission. As detailed in Section 2.4.7, following singlet fission, triplets can be harvested or transferred to a silicon sub-cell in order to double the amount of charge carriers produced compared to an ordinary silicon cell. Various estimates have been made of the efficiency limit increase from singlet fission, which vary based on their assumptions regarding the energy losses (or gains) from exothermic (or endothermic) fission. A PCE limit of 44.4% was calculated in 2006 by Hanna and Nozik[70] for a single junction cell with perfect carrier multiplication. In 2012, Tayebjee *et al.* calculated that by including the possible gains from endothermic fission, this could be improved to 45.9%, however when accounting for exciton binding energies inherent to organic semiconductors this may be reduced to 40%. An added benefit of reducing losses to thermalisation is the reduction in thermal degradation and resulting enhanced lifespan of the lower band gap sub-cell, as recently investigated by Jiang *et al.*[217].

2.6 Conclusions

In this chapter we have introduced the theoretical descriptions of singlet and triplet excitons in organic semiconductors, transitions between these states, and how excitons interact with each other. We then have covered the key theoretical concepts and experimental results relating to singlet exciton fission, and shown how fission has the potential to enhance the efficiency of solar energy conversion. In the next chapter we will describe the experimental techniques on which singlet fission research relies and which were used to produce the results which will be presented later in this thesis.

Chapter 3

Experimental Methods

In this chapter we will describe the experimental methods used in the following investigations. First, we will cover steady-state characterisation of absorption and luminescence. These simple techniques can reveal a lot about the properties of a material and are also important to enable interpretation of the spectral features in more complex techniques such as transient absorption (TA), the main technique used in this thesis. Next, we will describe the various methods of measuring time-resolved photoluminescence (PL) that we have used, before discussing the TA set-up and how to interpret a TA signal. After describing these optical techniques, we will outline the spin resonance techniques that were used. Finally, we will discuss the numerical methods that were used to analyse the data.

3.1 Steady-state Characterisation

3.1.1 Absorption

Steady state absorption (also known as UV-visible or UV-vis absorption) was measured using an Agilent 8453 UV-visible spectrometer. This combines the output from deuterium and tungsten lamp light sources, which is collimated into a single beam that passes through the sample. Transmitted light is focused with a lens and dispersed by a grating onto a 1024-element diode array. Absorption $A(\lambda)$ is calculated using Equation (3.1).

$$I(\lambda) = I_0(\lambda)10^{-A(\lambda)} \tag{3.1}$$

$I_0(\lambda)$ is measured using a blank substrate for solid samples or a cuvette filled with pure solvent for solutions. A small offset sometimes remains despite this correction to a blank, due to non-absorptive scattering by the sample itself and/or the difference in refractive index at the interface between sample and substrate. The concentration of a solution c can be related to the absorption A by the molar attenuation coefficient ε and the optical path length l in the Beer-Lambert law:

$$A(\lambda) = \varepsilon(\lambda)cl \tag{3.2}$$

Thus, absorption measurements can determine the concentration of a sample with a known ε.

3.1.2 Photoluminescence

A number of techniques were used to record steady-state photoluminescence spectra. For quasi-steady-state photoluminescence we used a 40 MHz pulsed excitation source at either 407 nm (PicoQuant LDH407) or 470 nm (PicoQuant LDH470) with a pulse length of around 100 ps. Photoluminescence was collimated with a lens and focused into a spectrometer (SpectraPro 2500i, Acton) with a grating with 150 grooves/mm. A CCD camera (PIXIS 100F, Princeton Instruments) measures the dispersed light.

An alternative set-up, used to gain extra sensitivity with a different camera, measured steady-state photoluminescence using an Andor iDus DU420A BVF Si detector. The excitation sources for this camera were temperature-stabilised Thorlabs continuous-wave (CW) lasers, at 405 nm or 520 nm. A lens focused the excitation beam onto the sample, and we used a further pair of lenses to project the photoluminescence emitted to a solid angle of 0.1π onto the detector.

For ease of changing the excitation wavelength or creating excitation scans over a series of excitation wavelengths, some photoluminescence measurements were recorded on an Edinburgh Instruments FLS980 fluorimeter. This uses a broadband light source (Xe1 Xenon Arc Lamp, 230–2600 nm) followed by a monochromator to select a single excitation wavelength. This is then focused on the sample, and luminescence is collected by a lens before another monochromator selects the detection wavelength. Finally, a photomultiplier tube counts the photons as the second monochromator steps across a range of wavelengths to record a full photoluminescence spectrum.

3.1.2.1 Photoluminescence Quantum Efficiency

Photoluminescence quantum efficiency (PLQE) was measured using a 405 nm or 520 nm CW laser and the sample inside an integrating sphere with a white inner surface that scatters light isotropically, with detection via a fibre optic cable to an Andor iDus DU420A BVF Si detector. PLQE was calculated by the de Mello method to account for secondary absorption of scattered light[218]. In this method, three measurements are taken:

- a - empty sphere, measuring the laser light scattered off the inside of the sphere
- b - sample is in the sphere but the excitation beam is not directly incident on the sample, and it is only excited by diffuse scattered light
- c - sample is directly excited

After correcting the spectra for the sensitivity as a function of wavelength, L_a is the integrated photons detected from the laser near the excitation wavelength, and P_c is the integrated photons detected over the range of wavelengths of the photoluminescence, with the subscripts referring to one of the three different measurements. The absorption A of the incident laser in c, not including subsequent absorption of scattered light, is calculated as:

$$A = 1 - \frac{L_c}{L_b} \tag{3.3}$$

The PLQE, η, is defined as photons emitted per photon absorbed. Hence the number of photons emitted in c from direct excitation is $\eta L_a A$. However, there are also photons emitted following the absorption of scattered laser light. The number of photons detected from scattered laser light and photons emitted after the absorption of scattered laser light is $L_b + P_b$ in b, and reduced by a factor of $(1 - A)$ in c to $(1 - A)(L_b + P_b)$. Thus, we can write that the total photons detected in c and rearrange for η (using Equation (3.3) to eliminate L_b and L_c).

$$\begin{aligned} L_c + P_c &= (1 - A)(L_b + P_b) + \eta L_a A \\ \eta &= \frac{P_c - (1 - A)P_b}{L_a A} \end{aligned} \tag{3.4}$$

This method relies on the assumption that the location from which laser light is scattered is unimportant, which has been proved experimentally to with a similar integrating sphere to an accuracy of ±2%

3.1.2.2 Magnetic Field Dependent Photoluminescence

For photoluminescence measurements in a magnetic field, we used Thorlabs CW 520 nm laser source with a focusing lens on to the sample. A pair of lenses project the photoluminescence emitted to a solid angle of 0.1π onto an Si detector, with the sample positioned in an electromagnet (GMW - Model 3470) with 3 cm distance between cylindrical poles. The magnetic field for a range of voltages supplied to the electromagnetic was first measured with a gauss meter mounted at the sample position, enabling measurements of the photoluminescence as a function of voltage to be calibrated to the magnetic field. Different field strengths were measured in a random, non-consecutive order, and every field strength was immediately followed by a zero-field measurement for normalisation, in order to rule out any effects of degradation that might bias the results.

3.1.2.3 Photostability

Photostability measurements were performed using the same set-up as the PLQE measurements, with the transmitted 520 nm laser signal T being measured as a function of time over which the sample was continually exposed to the excitation source. T is converted to absorption A by comparing to the incident photons I measured with no sample present using $A = I - T$.

In Chapter 5 stability measurements were performed by Kealan Fallon and consisted of daily measuring of the absorption spectra of films left out in air and natural light.

3.2 Time Resolved Photoluminescence

Time-resolved photoluminescence is an extremely useful tool for understanding the timescales of any photophysical process involving emissive states. We have studied processes that range from the ultrafast (< 1 ps), such as singlet fission and internal conversion, to the µs lifetimes of triplets involved in TTA. To observe time-resolved photoluminescence over such a range of timescales requires multiple different techniques, and which we will describe from slow to fast.

3.2.1 Intensified Charge-coupled Device

The intensified charge-couple device (ICCD) uses an electronic gate to time-resolve photoluminescence relative to an electronic trigger signal from the excitation source. The excitation comes from a 1 kHz Ti:sapphire amplifier (Spectra-Physics Solstice Ace).

The amplifier generates 100 fs pulses centred at 800 nm with an output of 7 W, and this output is split off into many experiments operating simultaneously using beam splitters. For the ICCD, the 800 nm pulses are frequency doubled in a BBO crystal to produce 400 nm pulses which can excite the sample. Alternatively, a non-collinear parametric amplifier (NOPA) can be used to generate narrow pulses at wavelengths from ∼480–700 nm.

The ICCD (Andor iStar DH740 CCI-010) contains a photocathode, a microchannel plate (MCP) and a phosphor screen in front of a charge-coupled device (CCD). The photocathode emits photoelectrons when it is struck by an incident photon. A time-dependent electric field accelerates the photoelectrons towards the MCP, and it is the control of this electric field which provides the time resolution. The electric field is switched on for a user-defined length of time, for example 10 ns, at a variable delay after the trigger that indicates the timing of the excitation, for example 100 ns. In this example only the PL emitted within 100-110 ns after excitation is recorded. By stepping delay for this electronic gate, we can build a kinetic picture of emission over time. The high potential of the MCP accelerates the electrons, leading to a cascade of secondary electrons from the channel walls and amplification of the signal. When the secondary electrons collide with the phosphor layer they are converted back into photons, where they can be read by the CCD. The ICCD is connected to a calibrated grating spectrometer (Andor SR303i) for spectral resolution. Due to the amplification by the MCP and phosphor, the ICCD is especially useful for resolving weakly emissive species with long lifetimes. Due to the limits of electronic gating, the time resolution of the ICCD is ~ 3 ns

3.2.2 Time-correlated Single Photon Counting

Time-correlated single photon counting is capable of recording photoluminescence kinetics at a time resolution roughly an order of magnitude faster than the ICCD, with an instrument response function of ~ 300 ps. The excitation source is a 40 MHz pulsed excitation source at either 407 nm (PicoQuant LDH407) or 470 nm (PicoQuant LDH470) with a pulse length of around 100 ps. A timer is started for every pulse generated, and this is stopped when a photon is detected by the photomultiplier tube (PMT), in this case a Hamamatsu R3809U-50. The photoluminescence is collimated and directed into a monochromator prior to the PMT, in order to select a single wavelength. A histogram is generated of the times between a laser pulse and a photon emitted from the sample being detected.

3.2.3 Transient Grating Photoluminescence

Transient grating photoluminescence has the fastest time resolution but involves using much greater pulse energies. Spectrally resolved measurements with a time resolution of 200 fs are possible. Ultrashort snapshots of the photoluminescence are sampled by diffraction from a transient grating formed by the interference of two ultrafast 800 nm gate pulses in a piece of fused silica which forms a grating of modulated refracted index by the optical Kerr effect[219]. The transient grating deflects the photoluminescence into the camera, an ICCD, and is only present for the duration of the gate pulses. Any photoluminescence which passes through the fused silica before or after the gate pulses is undeflected and misses the camera. The 800 nm gate pulses are generated at 1 kHz by a Ti:sapphire amplifier system (Spectra-Physics Solstice Ace), and the pump is either 800 nm pulses frequency doubled in a BBO crystal to produce 400 nm pulses or the output of a tuneable NOPA that can be used to generate narrow pulses at wavelengths from ∼480–700 nm. Two lenses collimate and focus the gated signal onto the spectrometer entrance (Princeton Instruments SP 2150) after long- and short-pass filters remove scattered pump and gate light respectively. Gated photoluminescence spectra are measured using an intensified CCD camera (Princeton Instruments, PI-MAX4). The (∼10 ns) electronic shutter of the intensified CCD camera was used to further suppress long-lived PL background. The time delay between pump and gate beams is controlled via a motorized optical delay line on the pump beam path.

3.3 Transient Absorption

3.3.1 General Principles

While time-resolved photoluminescence is a powerful technique for observing the emissive states (i.e. those optically coupled to the ground state) in a photophysical system, transient absorption (TA) has the advantage of probing all states which can optically couple to a higher lying state (known as photoinduced absorption) and depletion of the ground state. In its simplest description TA is the change, induced by the pump pulse, in absorption of the probe pulse, as a function of the pump-probe delay. The fundamentals of the pump, probe and delay can be mixed and matched from a variety of options. The probe can be generated by a custom-built NOPA, white light generation (WLG) in a yttrium aluminium garnet (YAG) crystal, or a ns pulse-length supercontinuum laser. The pump can be the 800 nm fundamental of the Ti:sapphire amplifier, the 400 nm second harmonic, the output of a custom-built NOPA, the output

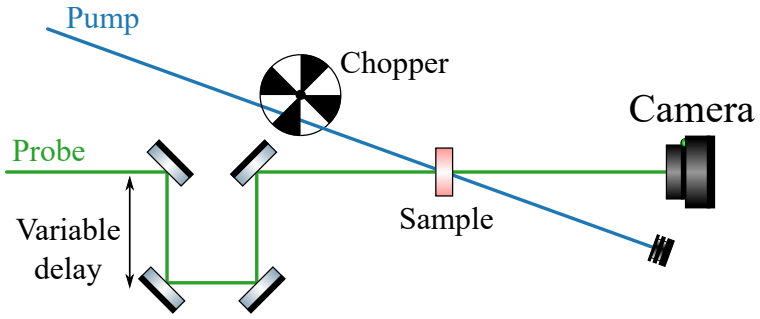

Fig. 3.1 Schematic of transient absorption

of a commercial optical parametric amplifier (OPA) (TOPAS, Light Conversion), or a ns pulse-length Q-switched Nd:YVO4 laser (AOT-YVO-25QSPX, Advanced Optical Technologies) with a 1064 nm fundamental, 532 nm second harmonic, and 355 nm third harmonic. The delay can be controlled by either mechanically adding to the optical path length of the pump or probe with a delay stage (fs-ps timescale) or by using an electronic delay generator (ns-µs timescales). The generic scheme of a TA experiment is shown in Figure 3.1.

The pump pulse creates a short-lived population of excited states with their own absorption features, which are monitored by the probe. In order to isolate only the absorptions due to the excited states, the transmission of the probe is compared with and without the pump to give the differential transmission $\Delta T/T$, defined as

$$\frac{\Delta T}{T} = \frac{T_{\text{on}} - T_{\text{off}}}{T_{\text{off}}} \tag{3.5}$$

T_{on} and T_{off} refer to the transmission of the probe with the pump on and off respectively. Each probe pulse is measured on a camera and is referred to as a "shot". In order to compare consecutive pump-on and pump-off shots, an optical chopper (Thorlabs MC2000B-EC) is used to halve the frequency of pump pulses compared to the probe in the case of a 1 kHz probe (and therefore a 500 Hz pump). Due to the limit of the optical chopper, the chopper operates at a quarter of the frequency of the high repetition rate system with a 38 kHz probe, such that the pulse sequence is pump-on, pump-on, pump-off, pump-off.

When using a broadband NOPA for the probe, to reduce the noise from shot-to-shot fluctuations in the probe spectrum, a reference is used. A 50:50 beam splitter divides the probe into two beams, which are both passed through the sample; one is overlapped with the pump (the probe) and the other passes through on an unperturbed part of

the sample (the reference). The reference is used to normalise the probe and correct for fluctuations that can otherwise reduce the signal to noise (S/N) to unmeasurable levels. Due to the multiple non-linear processes in the NOPA, very small shot-to-shot variations in the Ti:sapphire amplifier output can results in large fluctuations in the NOPA output. The referenced differential transmission then becomes

$$\frac{\Delta T}{T} = \frac{\frac{T_{\text{probe,on}}}{T_{\text{ref,on}}} - \frac{T_{\text{probe,off}}}{T_{\text{ref,off}}}}{\frac{T_{\text{probe,off}}}{T_{\text{ref,off}}}} \tag{3.6}$$

3.3.2 Transient Absorption Signals

There are three main types of signal that we seek to observe when measuring TA, which are pictured in Figure 3.2. Ground state bleach (GSB), shown in blue, is a positive $\Delta T/T$ signal, due to the pump-induced reduction in ground state molecules which, when there is no pump, would absorb the probe at the energies of the ground state absorption. The spectral shape of the GSB should match the steady-state absorption. Any excited state, including both singlets and triplets, should generate a GSB signal, as they all deplete the ground state.

Stimulated emission is also a positive $\Delta T/T$ signal, shown in green in Figure 3.2. The transmittance of the sample appears to increase when excited states that are radiatively coupled to the ground state interact with the probe to emit an extra photon at the same frequency as the probe. SE signals therefore allow the specific tracking of the population of emissive excited states.

Finally, a photoinduced absorption (PIA) is negative $\Delta T/T$ signal, shown in red in Figure 3.2. PIAs result from transitions from excited states to higher-lying excited states, e.g $S_1 \rightarrow S_n$ and $T_1 \rightarrow T_n$. The transmittance of the sample decreases at the energy of these transitions, due to the pump-induced population of excited states. By assigning the spectral locations of any PIAs to specific excited states, it is possible to track the population changes and interconversion of different excited states over time.

3.3.3 Non-collinear Optical Parametric Amplifier

NOPAs are used in TA to amplify broadband (or narrow, if required), ultrafast pulses for both pump and probe. A schematic of a typical NOPA, running off the Spectra Physics Solstice Ace Ti:sapphire amplifier is shown in Figure 3.3. The NOPA can provide tuneable broadband pulses in the visible (480 – 830 nm)[220], NIR (750 – 1150 nm)[220], and IR (1200 – 1650 nm)[221]. For each NOPA, $\sim 300 - 400\,\mu\text{W}$ of the 800 nm fundamental is

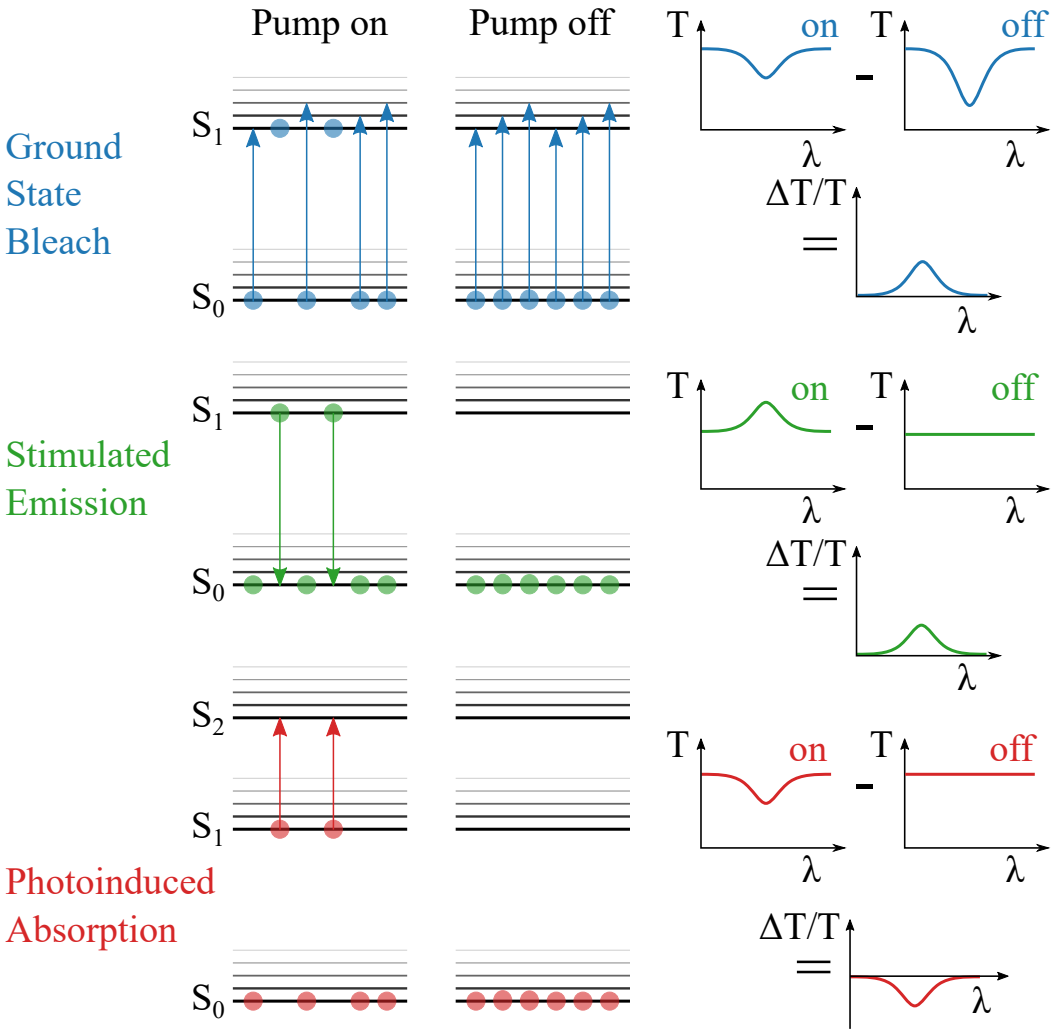

Fig. 3.2 Explanation of transient absorption signals from ground state bleach (blue), stimulated emissions (green) and photoinduced absorption (red). For each type of signal, schematics of the transitions that occur due to the interaction between the probe and sample are shown for "pump on" and "pump off". Also, for each type of signal, probe transmission (T) is plotted against wavelength (λ) for "pump on" and "pump off", as well as the differential transmission $\Delta T/T = (T_{\text{pump on}} - T_{\text{pump off}})/T_{\text{pump off}}$.

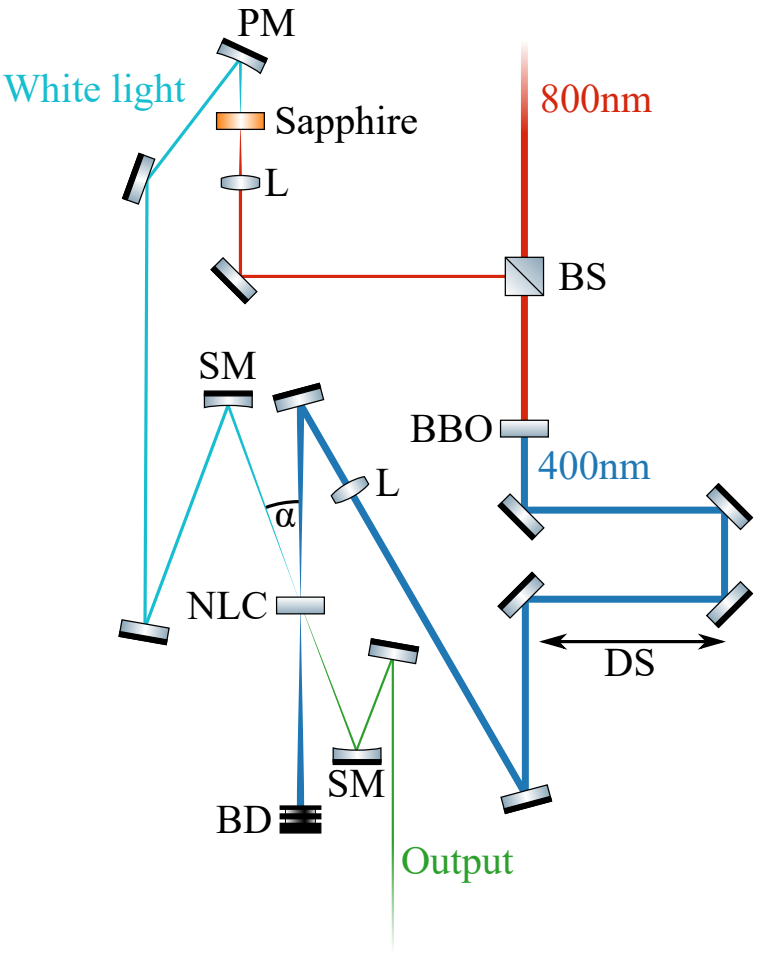

Fig. 3.3 Schematic of a custom-built broadband NOPA. BS: beam splitter, L: lens, PM: parabolic mirror, SM: spherical mirror, DS: delay stage, NLC: non-linear crystal, BD: beam dump. For visible and NIR amplification, the NLC is BBO.

split off using beam splitters. Within each NOPA, this is further split by a 90:10 beam splitter, with the 90% of the power being doubled to 400 nm in a β-barium borate (BBO) crystal for the visible and NIR NOPAs and left as 800 nm for IR amplification. Frequency doubling in a non-linear crystal is a second order effect that occurs at high intensities when the energy of two photons form a virtual energy level. From this virtual level, a photon of twice the initial frequency is emitted.

The 10% power beam is focused down and used for WLG in a sapphire crystal. The physics of WLG are still only partially understood, but we utilise the effect in both sapphire and YAG to create extremely broadband pulses for TA (in the case of the NOPA, WLG in sapphire is used for the seed). It is considered likely that WLG is a result of a combination of changes in the refractive index inducing self-focussing, and self-defocussing, due to the generation of an electron plasma by the extreme intensity of the photon's electric field in an ultrafast, highly focused pulse[222]. We filter out the residual 800 nm fundamental from the white light seed using a BG38 filter for the visible NOPA and an RG830 filter for the NIR and IR NOPAs. The WL seed is collimated using a parabolic mirror and pump pulses are then focussed into another non-linear crystal (NLC): BBO for the visible and NIR NOPAs and periodically poled stoichiometric lithium tantalite (PPSLT) for the IR NOPA.

When the pump and seed pulses are overlapped spatially and temporally in the NLC, with the correct pump-seed angle, labelled as α in Figure 3.3), and correct orientation of the NLC, the seed is amplified by difference frequency generation (DFG)[220]. When the angle is correct, the pump, with energy $\hbar\omega_1$, and seed, with energy $\hbar\omega_2$, are phase matched, resulting in amplification of the seed. The pump photon populates a virtual state with energy $\hbar\omega_1$, and the seed photon stimulates the emission of a second photon at energy $\hbar\omega_2$, the signal, as well as another photon with frequency $\omega_3 = \omega_1 - \omega_2$ such that energy is conserved. The photon at frequency ω_3 is known as the idler. The phase matching condition requires that the wave vectors $\mathbf{k}$ of initial and final photons are conserved, with $\mathbf{k}(\omega) = \frac{\mathbf{n}(\omega)\omega}{c}$, $\mathbf{n}(\omega)$ being the refractive index, which is anisotropic in the birefringent NLC.

In a collinear configuration, known simply as an OPA, the range of wavelengths that can be phase matched simultaneously is small and therefore results in narrow pulses. NOPAs are capable of phase matching across a wider range of frequencies at a given angle, allowing the amplification of broadband pulses, which we can use as the probe for TA. Broadband pulses must be used for ultrashort (sub-10 fs) pulse lengths, due to the Heisenberg uncertainty principle. In this case, chirped mirrors are used to

compress the pulses to close to the Heisenberg limit[220]. Without compression the pulse length will be the duration of the pump used for amplification, $\sim 100\,\text{fs}$.

3.3.4 Transient Absorption Artefacts

As well as the signals from transitions between states that we are interested in, there can be other contributions to the TA signal which we are not intending to measure, such as the coherent artefact and thermal artefacts. The coherent artefact occurs around time zero, when pump and probe are overlapped in the sample simultaneously, and results from non-linear optical effects in the sample substrate and/or solvent[223]. While the coherent artefact can make determining the very early-time signal difficult, it is useful for chirp correction, which is required because the probe pulse is typically chirped by the optics (and air) that it passes through. Therefore for a given path length, there will be an offset in pump-probe delay across the broadband spectrum of the probe, typically on the order of 1 ps. Data must be corrected for this effect before being analysed, which is known as chirp correction.

A sometimes more problematic artefact is thermal artefacts, resulting from temporary, pump-induced heating of the sample[73,224]. When the sample absorbs the pump, unless it is a high emissive sample, most of the energy will be dissipated as heat. While this will eventually be lost to the environment, there is often a temporary heating effect lasting on the ns timescale. Heating can change the ground state absorption of the sample, either in magnitude or by shifting it slightly, which would result in a false GSB-like signal or a derivative signal respectively. There can also be a change in refractive index associated with heating, which can alter the scattering at the air/sample and sample/substrate interfaces, leading to anomalous signals. These signals can be identified by comparing samples prepared on substrates with different heat capacities, which therefore dissipate heat from the sample at different rates. If the signal lifetime changes with the substrate, then it can be assumed to be associated with heating rather than an electronic state transition.

3.4 Transient Electron Spin Resonance

Electron spin resonance uses the combination of microwaves and a magnetic field to probe the spin physics of a sample. When the electron spins interact with an external field, the Zeeman term $\hat{H}_Z$ is included in the Hamiltonian.

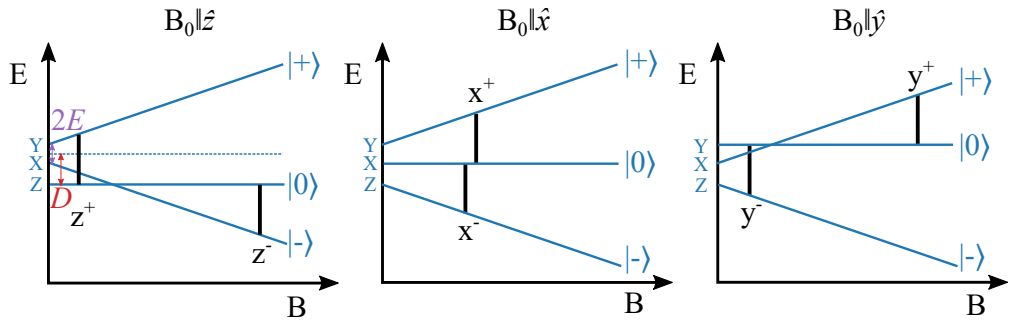

Fig. 3.4 Zeeman interaction in triplet excitons, with zero field splitting parameters $D, E \neq 0$, for magnetic field direction parallel to $\hat{z}$, $\hat{x}$, and $\hat{y}$. Resonances with the microwave frequency are indicated by the vertical black bars.

$$\hat{H}_Z = g\mu_B \mathbf{B} \cdot \mathbf{S} \tag{3.7}$$

This term splits the energies of states with a difference in spin projection quantum number of $|\Delta m_S| = 1$ by $|\Delta E| = g\mu_B B$. Electron spin resonance (ESR) uses microwaves to probe the transitions between spin states when they are split in this way by an external field $\mathbf{B_0}$. CW microwaves, are coupled into a resonator containing the sample, and the $\mathbf{B_0}$ field is swept, with the microwave output being measured. When $\mathbf{B_0}$ reaches a magnitude that induces an energy splitting which matches the energy of the microwaves, molecules transition between states by either the absorption or emission of microwaves, depending on whether there is a greater population of the lower or higher state respectively. The resulting change in microwave amplitude from the net absorption and emission as a function of $\mathbf{B_0}$ field gives the ESR spectrum. To specifically study the ESR signals of photoexcited states, we used a pulsed laser to excite the sample, and trigger an oscilloscope to measure the microwave output from the resonator as a function of time after the laser pulse. This is known as transient ESR (trESR).

Singlet excitons have spin $S = 0$ and therefore their Zeeman term is also zero, meaning they cannot be detected with ESR. However, in $S = 1$ triplet excitons, the three spin states are split by the Zeeman interaction in addition to the zero-field splitting (ZFS) as shown in Figure 3.4. At zero field, the triplet eigenstates are $|x\rangle$, $|y\rangle$, and $|z\rangle$, according to the molecular axes. For pentacene, the long axis of the molecule is assigned the x axis, the short axis y, and z is out of the plane of the molecule[163,225,226]. In the high field limit, the triplet eigenstates are now $|-1\rangle$, $|0\rangle$, and $|1\rangle$. The conversion between these two basis sets depends on the orientation of the molecule with respect

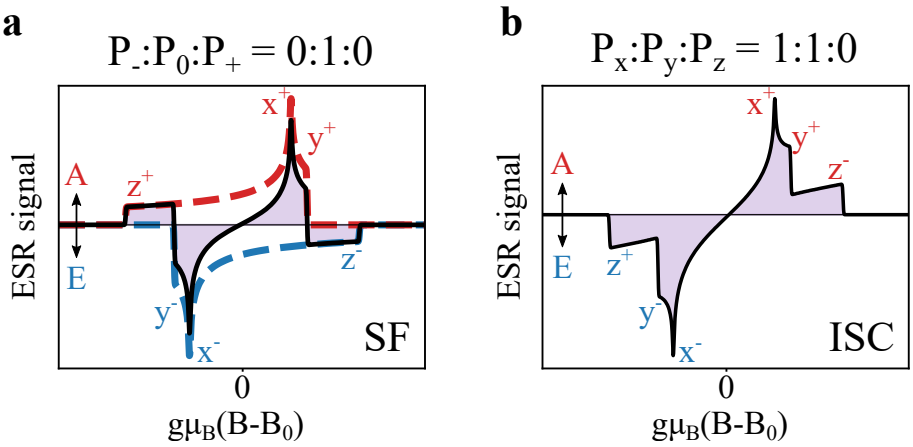

Fig. 3.5 ESR polarisation patterns for a) preferential population of $|0\rangle$ from singlet fission and b) preferential population of $|x\rangle$ and $|y\rangle$ from ISC.

to the magnetic field. For example, with $\mathbf{B_0} \parallel \hat{z}$, $|0\rangle = |z\rangle$ and $|\pm\rangle = \frac{1}{\sqrt{2}}(|x\rangle \pm |y\rangle)$. As a consequence, resonances with the microwave field occur at different $\mathbf{B_0}$ fields for different molecular orientations relative to the $\mathbf{B_0}$ direction, as shown by the black bars in Figure 3.4. For a sample made up of a randomly oriented powder, resonances occur at a distribution of magnetic field strengths, as shown in Figure 3.5.

The polarisation of the different peaks in the powder pattern is dictated by the relative population of the high field eigenstates, which depends on the triplet formation mechanism. For example, in triplets generated by singlet fission, typically the high field $|0\rangle$ eigenstate is preferentially populated over $|\pm\rangle$[68,86,169], leading to an ESR spectrum as shown in Figure 3.5a with polarisation AEEAAE where A refers to a positive absorptive peak and E refers to a negative emissive peak. By contrast, triplets formed by spin-orbit mediated ISC populate the zero field eigenstates according to their relative formation/relaxation rates, which are particular to the molecule. A common ISC population distribution is an overpopulation of $|x\rangle$ and $|y\rangle$ compared to $|z\rangle$, which leads to an EEEAAA spectrum, as shown in Figure 3.5.

The trESR in Chapter 4 was measured together with collaboration with Leah Weiss and Naitik Panjwani at Free University, Berlin. We performed the measurements using a Bruker MD5 dielectric ring resonator and an X-band ESR spectrometer. The precise frequency is kept in resonance with the cavity Pulsed 532 nm excitation was provided by a Nd:YAG laser (Atum Laser Titan AC compact 15 MM) with a 5 ns pulse length. A constant Helium flow was used to cool the sample to temperatures below 100 K, in order to extend the spin-lattice relaxation time T_1. The trESR in Chapter 6 was

measured by Leah Weiss alone at the same facility, while the trESR in Chapter 5 was measured by Enrico Salvadori at University College London.

3.5 Optically Detected Magnetic Resonance

Optically detected magnetic resonance (ODMR) probes the same triplet resonances as ESR, however rather than detecting changes in microwave intensity, microwave induced changes in photoluminescence intensity are detected. Photoexcitation is continuous rather than pulsed, so there is a steady population of photoexcited states. Instead of CW microwaves, the microwaves are modulated on and off in a square wave pattern. Changes in photoluminescence with microwaves on compared to microwaves off are then detected using a lock-in amplifier.

ODMR was performed in collaboration with Naitik Panjwani at Free University, Berlin using a home built optical resonator (based on a dielectric ring resonator) which allows for excitation of the sample and collection of photoluminescence in transmission mode). A 532 nm diode pumped solid state laser (DJ532-40 Thorlabs) was used for continuous excitation of the sample. The integrated photoluminescence was collected by a Silicon avalanche photodetector (APD120A Thorlabs), with a 532 nm notch filter (Semrock) to remove the laser. The ODMR was carried out at X-band and the microwaves were square wave modulated at frequencies between 17 Hz and 100 kHz. The change in photoluminescence due to microwave absorption was monitored at the microwave modulation frequency using lock-in detection (Stanford Research Systems SR830) as the static magnetic field was swept through resonance.

3.6 Grazing Incidence Wide Angle X-ray Scattering

X-ray scattering techniques, such as grazing incidence wide angle x-ray scattering (GIWAXS) can be used to understand the crystallinity and specific crystal structures present in a sample. GIWAXS, which is capable of resolving molecular length scales, was performed by Dr Andrew Pearson on the I07 beamline at the Diamond Light Source, Didcot, U.K. The X-ray beam energy was 10 keV and the angle of incidence was 0.4°. During measurement each sample was housed inside a custom-built sample chamber held under a continuous overpressure of dry He. Data was collected using a Pilatus 2M detector and analysed using the DAWN software package (www.dawnsci.org).

3.7 Genetic Algorithm

Frequently in this thesis, we encounter spectrally and temporally resolved experiments. From these 2-dimensional datasets, we ideally wish to extract the spectral signatures of the different species present, and their kinetic progression. The Genetic Algorithm (GA) is a useful tool for this purpose has been adapted by the Optoelectronics research group to deconvolve spectra from time-dependent data. Briefly, GA generates initial random guesses for the spectra of the desired number of species, and reconstructs the dataset using linear combinations of these spectra that minimise the residual error at each time point. The GA tries out a series of spectra and selects the most successful, makes small "mutations" to them, and then "breeds" (mixes) them together to generate a new set of spectra to test. This process is iterated until the GA converges on a solution that best reconstructs the experimental data. This method includes random processes and is not guaranteed to produce a model that represents the best approximation of the data. It has some particular weakness, such as when spectra gradually shift in time. GA should be run multiple times with different starting parameters to ensure that the results are reproducible.

Chapter 4

Singlet Fission in a Modified Acene with Enhanced Stability and High Photoluminescence Yield

In this chapter, we report a fully efficient singlet exciton fission material with high ambient chemical stability. Bis(triisopropylsilylethynyl)-tetrabenzo[a,c,l,n]pentacene (TTBP) combines an acene core with triphenylene "wings" that protect the formal pentacene from chemical degradation. In our investigations we have deduced that the electronic energy levels in TTBP are positioned such that singlet fission is endothermic, similar to tetracene despite the triphenylene "wings". In the solid-state, TTBP exhibits rapid early time singlet fission with quantitative yield of triplet pairs within 100 ps followed by thermally activated separation to free triplet excitons over ∼65 ns at 300 K. Perhaps the most striking property TTBP exhibits is its high photoluminescence quantum efficiency of 20% in solid films, predominantly arising from triplet-triplet annihilation. In using such a system for exciton multiplication in a solar cell, maximum thermodynamic performance requires radiative decay of the triplet population, observed here as emission from the singlet formed by recombination of triplet pairs. Combining chemical stabilisation with efficient endothermic singlet fission provides a promising avenue towards singlet fission materials for use in photovoltaics. The findings presented in this chapter are currently in peer review, as paper [2] in the List of Publications.

The project described in this chapter was led by the author, and all steady-state optical characterisation, transient absorption, and time-resolved photoluminescence were measured by the author alone. The author measured transient electron spin resonance and optically detected magnetic resonance at Freie Universität, Berlin, in collaboration with Naitik Panjwani. Matthias Müller synthesized the molecule. Simon Dowland measured the photoluminescence quantum efficiency and assisted with preparation of polystyrene samples.

4.1 Background and Motivation

Singlet fission, the evolution of one photoexcited singlet exciton to form a pair of triplet excitons that is described in detail in Section 2.4, occurs in a subset of organic semiconductors where the energy of a singlet is approximately twice the energy of a triplet. Initially reported in 1969 in crystalline tetracene[65], there has been a growing interest in singlet fission in recent years due to its demonstrated ability to increase the efficiency of photovoltaic devices[183,191]. In a traditional single-junction device, all photons with energy above the band gap will lose their excess energy to heat as the excitations relax to the band edge, before being extracted as charges. These thermalisation losses can be reduced by absorbing high-energy photons with a singlet fission chromophore and producing two triplet excitons with energy greater than or equal to the band gap of the device (i.e. 1.1 eV for silicon). The energy of both these triplet excitons must then be transferred to the main device, either via triplet energy transfer, electron transfer, or the emission and absorption of infra-red photons[188,195–197]. Calculations have shown that for an optimal band gap and singlet fission chromophore, the theoretical limit of a single-junction solar cell increases from 33% to 45% with singlet fission[7,201]. Recent experiments demonstrate that integration of tetracene with silicon enables triplet energy transfer into silicon following photon excitation in tetracene[188], affirming the potential impact of a chemically stable alternative. The possibility of increased efficiencies from silicon tandem systems, of which singlet fission is a contender, has led to projections from ITRPV that tandems will begin to take significant market share from single junction c-Si modules in the next decade, with 4% in 2030[227]. One of the biggest roadblocks for realising this potential from singlet fission tandems is the stability of the singlet fission materials.

Currently, the most thoroughly studied and highest yield singlet fissions systems are linear acenes and their derivatives[72,75–77,82,95,102,166,228], but as is described in Section 2.4.2, singlet fission has also been reported in other systems such as rylenes[111–118],

polyenes[119,120,125,126,135], diketopyrrolopyrrole[122,123], and 1,3-diphenylisobenzofuran[128]. Tetracene and TIPS-tetracene have been of particular interest due to the favourable triplet energy (∼1.25 eV) slightly above the band gap of silicon, and because for them fission is endothermic yet still efficient, maximising potential power output thanks to thermal energy. Here we study 10,21-bis(triisopropylsilylethynyl)tetrabenzo[a,c,l,n]pentacene (TTBP), a soluble acene derivative with improved ambient stability, which retains the characteristic acene behaviour of singlet fission, and also demonstrates reduced non-radiative loss pathways that would be parasitic in a solar cell. We note a recent theoretical study has shown the potential for pyrene-fused acenes for singlet fission[229], which while not identical is a similar structural motif, and intra-molecular singlet fission has been experimentally observed in dimers of pyrene-fused aza-acenes[150], demonstrating that adding off-linear fused rings does not preclude singlet fission.

As we develop in this chapter, in TTBP we find both efficient singlet fission, and also triplet fusion evident through delayed singlet emission. Thanks to the favourable energetics that make singlet fission reversible, and notably slow non-radiative decay, TTBP has a high photoluminescence quantum efficiency (PLQE) of 20%, despite singlet fission to the pair state proceeding at ∼200 times the radiative rate. It follows that if used in a singlet fission tandem where triplets could be efficiently transferred to a lower band gap solar cell (an engineering challenge yet to be solved), TTBP would have much lower non-radiative voltage losses, which limit the power conversion efficiency, than an equivalent low-PLQE singlet fission material. This thermodynamic argument is in it s essence identical to the detailed balance limit for single-junction cells[201], and will be addressed in more detail at the end of the chapter.

TTBP was synthesised in 2018 by Müller et al.[230], where it was found that the two- or fourfold benzannulation of heptacene, hexacene and pentacene improved their stability. The addition of the branched triphenylene "butterfly-wings" extends the π-conjugated system, but not as significantly as a lone linear benzene annulation would do, causing TTBP to have a similar energy levels as tetracene (Figure 4.1). There is also a similarity to the energetics of rubrene, another acene derivative capable of both singlet fission and triplet fusion, although unlike TTBP rubrene is highly unstable, and has not been reported to show the same high PLQE in the solid state, but can undergo highly efficient TTA on single rubrene molecules when in a dilute form[231]. Through a combination of optical and spin-resonance experiments, we show that singlet fission occurs quantitatively in solid samples that also have high PLQE. We propose that, as in a typical single-junction photovoltaic, a high PLQE is key to reducing voltage losses due to non-radiative decay in a potential singlet fission solar cell.

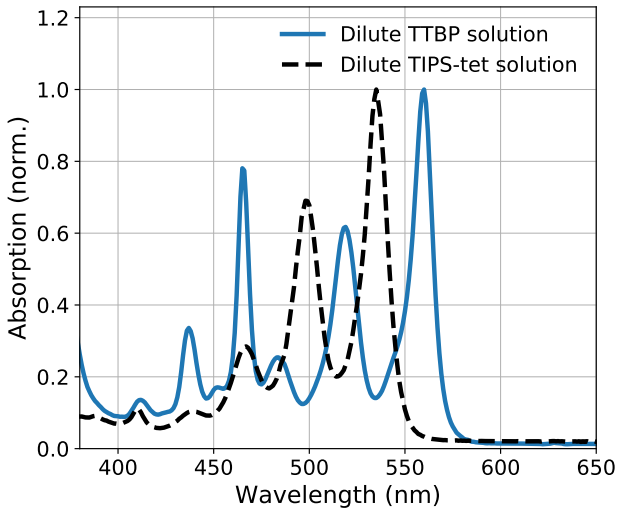

Fig. 4.1 UV-vis absorption spectra for TTBP (blue solid line) and TIPS-tetracene (black dashed line) in dilute solution, showing their similar band-gap/absorption onset.

4.2 Steady-state Characterisation of TTBP

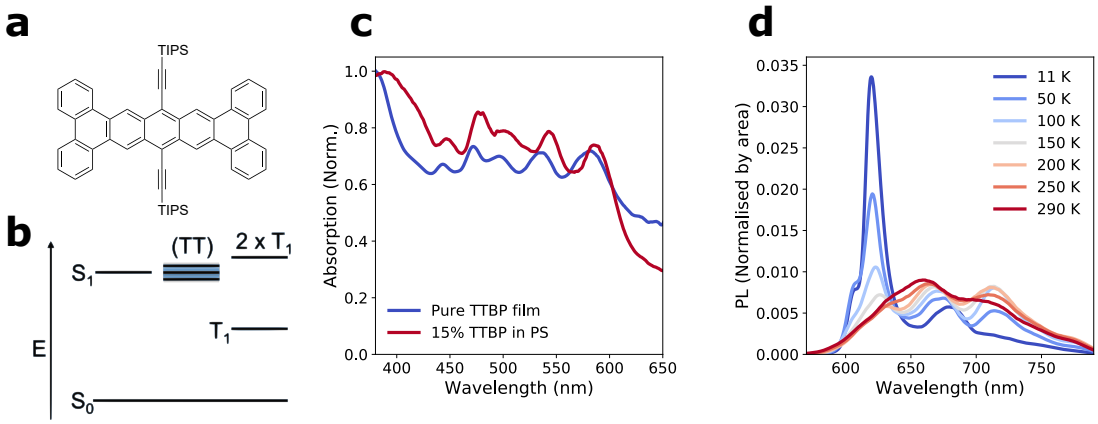

Fig. 4.2 a) Molecular structure of TIPS-tetrabenzo[a,c,l,n]pentacene (TTBP). b) Schematic energy level diagram for endothermic singlet fission in TTBP. c) Absorption spectrum of a pure TTBP film (blue) and a 15% blend of TTBP in polystyrene (red) at room temperature. The measured absorption at wavelengths longer than ∼600 nm is due to scattering and reflectance. d) Temperature-dependent time-integrated PL, using a pulsed excitation source at 500 nm, pulse duration 200 fs, 1 kHz repetition, from 11 K to room temperature

The molecular structure of TTBP is given in Figure 4.2a, with an energy level diagram showing ordering of singlet and triplet energy levels, where singlet fission to a

pair of uncorrelated triplets ($2 \times T_1$) is overall endothermic, and mediated by a pair-state manifold ((TT) state) that is approximately isoenergetic with the singlet (Figure 4.2b). Figure 4.2c shows continuous-wave (CW) optical absorption of 100% TTBP films and 15% TTBP in an inert host of polystyrene (PS). Both show some scattering, evident in the reduced transmission at longer wavelengths below the band gap. Solid-state films show a 25 nm red-shift in the absorption onset relative to solution (Figure 4.1), indicating significant intermolecular interaction in the solid state. In this work we use either 100% TTBP films or TTBP/PS blend films, which exhibit comparable optical properties (see Figure 4.2b), in order to reduce scattering. Figure 4.2d shows the temperature dependence of the steady-state photoluminescence (PL); we discuss the strong temperature dependence later, and note here that the sharper and stronger low temperature emission is similar to that of tetracene[75].

The level of aggregation in the TTBP/PS films can be inferred from their PL spectra, as shown in Figure 4.3. The strong majority of TTBP is aggregated at 5% concentration in polystyrene, with a minority of dispersed molecules, meaning that the transient absorption experiments for which the polystyrene blends were designed are dominated by the signal from aggregated TTBP.

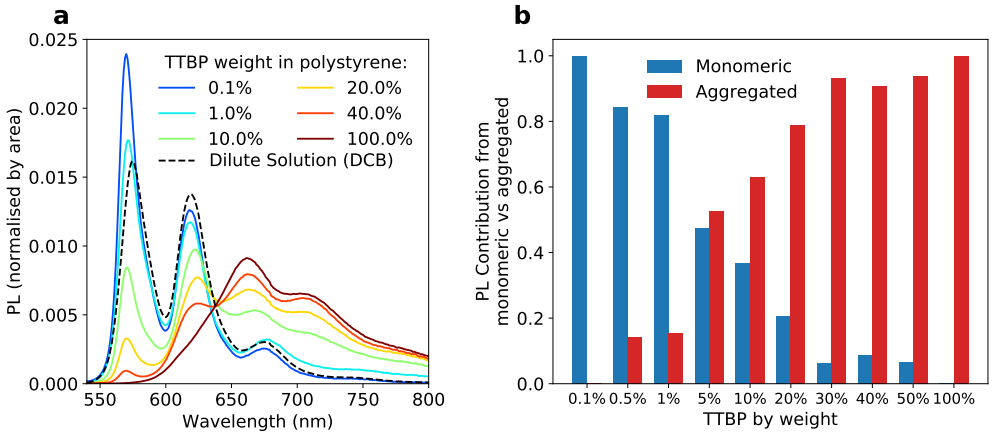

Fig. 4.3 a) Steady state PL of TTBP in PS at varying concentrations from 100% TTBP (dark red) to 0.1% (blue), with excitation from a Xenon lamp with a monochromator set to 530 nm. Dilute solution PL spectrum, with dichlorobenzene (DCB) as solvent, is shown in dashed black.b)

In Figure 4.3a, it is clear that there are contributions from two distinct spectra – the aggregated TTBP with broad peaks at ∼660 nm and ∼710 nm, and the monomer TTBP spectra which closely matches that of the dilute solution, characterised by narrower peaks at 570 nm, 620 nm, and 675 nm. Apart from some modulation of the relative intensities of the vibronic peaks in the monomer spectrum, the spectra of the

PS blends can be recovered from a linear combination of the 0.1% and 100% spectra. The relative contribution from these two spectra at each concentration, using a linear regression fit, is shown in Figure 4.3b. Importantly, as shown in Figure 4.4, the PLQE increases by a factor of 5 between the aggregate and the dispersed TTBP, implying that even in the 5% TTBP film where there is roughly even contributions to the PL, there is ∼5 times as much of the excitations are in the aggregated TTBP rather than the dispersed.

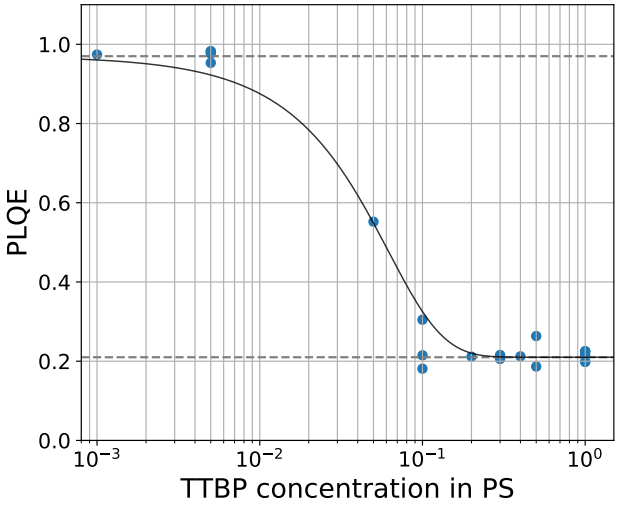

Fig. 4.4 PLQE for a range of concentrations in PS, showing that as TTBP aggregates, PLQE plateaus at 20%. Excitation with a CW 520 nm laser, PL collected using an integrating sphere and PLQE values calculated by the de Mello method[218]. These PLQE measurements were performed by Simon Dowland.

This analysis of the PL reveals a small fraction of monomeric molecules in the intermediate concentration blends that are not aggregated, but the majority have identical luminescence to the 100% film. This is as we expect due to the low affinity between PS and the strongly crystallising molecular material. At intermediate concentrations of TTBP, there will only be limited solubility for isolated TTBP molecules, beyond which we see phase separation and TTBP domains forming with the same optical properties as the 100% TTBP film.

4.2.1 Photostability of TTBP

The stability of TTBP in air is shown to be superior to TIPS-tetracene in Figure 4.5. Under CW 520 nm illumination, there is a small initial reduction of absorption, likely due to surface damage, after which there is no further degradation. In contrast, TIPS-

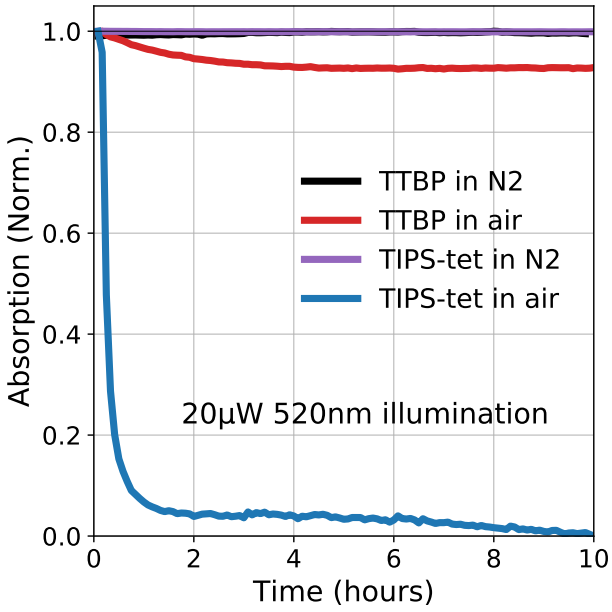

Fig. 4.5 Stability of TTBP compared to TIPS-tetracene. Drop-cast samples prepared from 50 mgml^{-1} solutions in DCB were illuminated by 20 µW CW 520 nm, with the absorption monitored over time. Black and purple lines show samples encapsulated in an O_2 and H_2O free environment, while red and purple lines show unencapsulated films in ambient conditions.

tetracene absorption falls by 90% within the first hour of illumination, and goes on to decay to 0 over 10 hours. As well as dropping by only 6% compared to 90%, the initial decay in TTBP is much slower, taking 4 hours compared to 1 hour.

Both light and the presence of O_2 and/or H_2O are required for the samples to degrade, as we observed little to no degradation of well-encapsulated samples in an inert N_2 atmosphere. For the stability test, the spot size was $\sim$0.8 mm in diameter, giving an irradiance of $\sim$1 mWcm^{-2}.

4.3 Triplet Pair Formation in TTBP

Transient absorption, where samples are excited with a narrow 500 nm, 200 fs pulse followed by a broadband probe with a controllable delay, allows the tracking of photoexcited states over time with femtosecond resolution. In TTBP/PS films, the photoexcited singlet, which has a photoinduced absorption (PIA) at 620 nm, is quenched to form a triplet-like species, which shows a strong PIA at 590 nm and a series of smaller PIAs in the near IR (Figure 4.6a-b). The peak at 590 nm after 1 ns is a close match to the solution triplet spectrum obtained by sensitisation (Figure 4.6b), although the NIR transitions are significantly red-shifted and broadened, a possible indication of strong coupling within the triplet pair[77,82].

Population kinetics in Figure 4.6c are extracted from the transient absorption data shown in Figure 4.6a using a Genetic Algorithm, with species associated spectra plotted in Figure 4.6d. Triplet pair formation occurs on a timescale of 100 ps or faster; the solid lines in Figure 4.6c show bi-exponential fits with time constants of 11 ps and 160 ps for the singlet decay, and 10 ps and 100 ps for the triplet rise. We note that the overall singlet population decay may be slower than the singlet fission rate due to a sub-population of isolated molecules in the polystyrene blend that do not undergo singlet fission and hence are expected to decay with a 22 ns lifetime (Figure 4.9). The apparent initial rise of the triplet pair signal to 0.4 within the instrument response function of the experiment could be coherent pair formation, as seen by Stern *et al.* for TIPS-tetracene[77].

Figure 4.7, measured on a 30% sample, shows good similarity to the 7% sample in Figure 4.6a. Within this intermediate range, we conclude that the concentration of TTBP in PS has little effect on the population dynamics, but does have a significant impact on the quality of measurements that are possible.

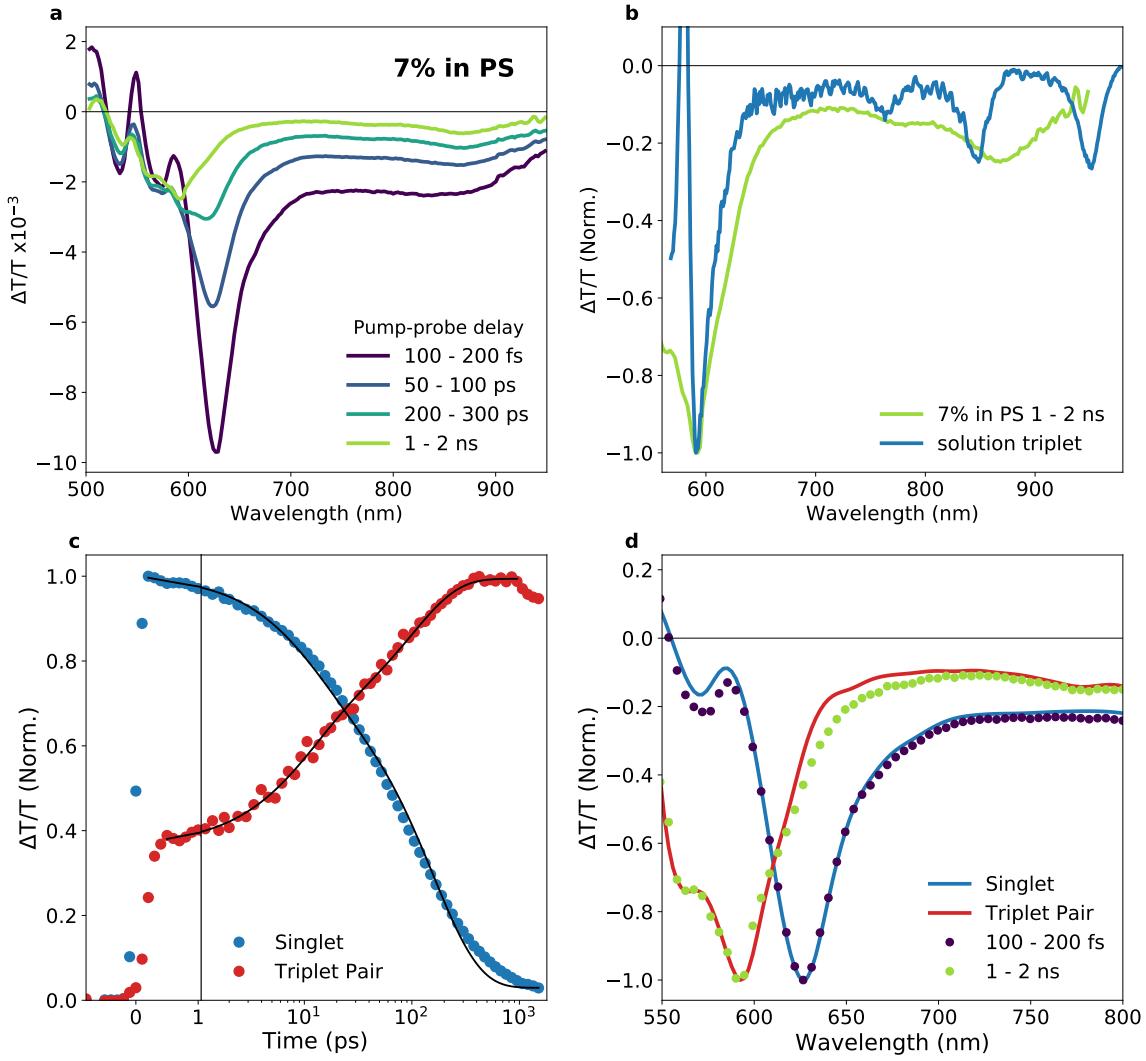

Fig. 4.6 a) Time-cuts from ultrafast, room-temperature transient absorption with a 250 fs, 38 kHz, 500 nm pump and a broadband probe generated in a YAG crystal for a 7% TTBP film. Pump fluence was 25 $\mathrm{Jcm^{-2}}$ per pulse. b) Comparison of the 1–2 ns time-cut with the solution triplet spectrum (using NMFP as sensitizer) showing a red shift and broadening in the near IR absorptions. c) Kinetics and d) spectra of the singlet and triplet pair, separated using a Genetic Algorithm (see Chapter 3 for details). Solid lines in c) are bi-exponential fits. Dots in d) are normalised transient absorption data from a).

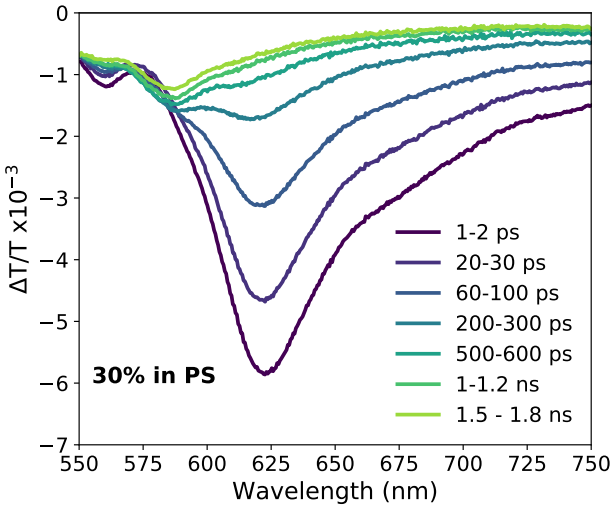

Fig. 4.7 Transient absorption of 30% TTBP in PS film with a 200 fs, 1 kHz, 400 nm pump and a visible NOPA probe, showing broadly similar behaviour to 7% in PS in Figure 4.6a. The pump fluence was 20 µJcm^{-2} per pulse.

4.3.1 Triplet Sensitisation

To reveal the absorption spectrum of the TTBP triplet exciton, a triplet sensitizer, N-methylfulleropyrrolidine (NMFP), was used. NMFP undergoes rapid intersystem crossing (ISC) from S_1 to T_1 and has a triplet energy higher than that of TTBP, ensuring that triplet energy transfer to TTBP is energetically favourable. From comparison of the UV-vis absorption of the mixed sensitization solution to the respective stock solutions at 1 mgml^{-1} we confirmed the relative concentrations of NMFP and TTBP to be 1.1 mgml^{-1} and 0.52 mgml^{-1} respectively (see Figure 4.8).

The mixed solution was measured with ns-resolution transient absorption, and the results compared to the pure solutions of dilute TTBP or NMFP. The singlet exciton of TTBP has a strong, sharp PIA at 630 nm. In a dilute solution, this decays with a lifetime of 22 ns (Figure 4.9) in agreement with the fluorescence lifetime in dilute solutions/films. NMFP, when excited at 400 nm, quickly undergoes intersystem crossing from the singlet, which has a broader PIA extending out into the near IR, to the triplet exciton, which has a PIA peaked at 700 nm and negligible absorption beyond 850 nm. In a pure solution of NMFP in tetrahydrofuran (THF), the lifetime of this triplet state was found to be 11.1 µs, implying a decay rate $k_{\mathrm{NMFP}} = 9$ x 10^4 s^{-1}. When mixed together and excited at 400 nm, TTBP singlets decay whilst the NMFP triplets transfer to the TTBP molecules when they collide, as the TTBP triplet is at lower energy than the NMFP triplet. This results in a quenching of the NMFP triplet

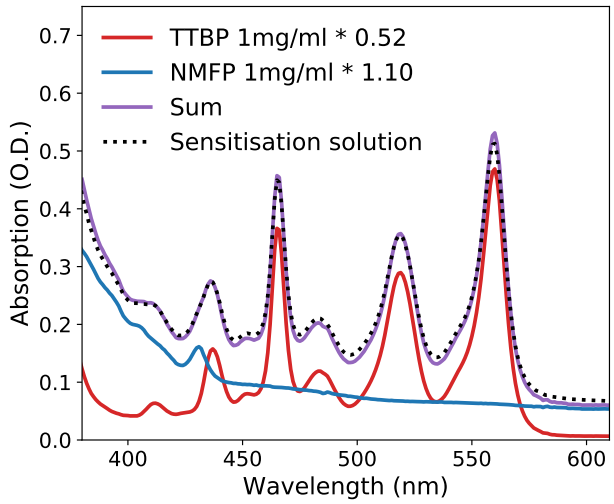

Fig. 4.8 UV-vis absorption for TTBP (red) and NMFP (blue) 1 mgml^{-1} solutions, and a mixed solution of both TTBP and NMFP (dotted black), all in THF. The TTBP and NMFP absorption spectra are scaled by factors of 0.52 and 1.10 respectively, such that their sum (purple) matches the absorption spectrum of the mixed solution, with the scaling factors optimised using a least-squares regression method.

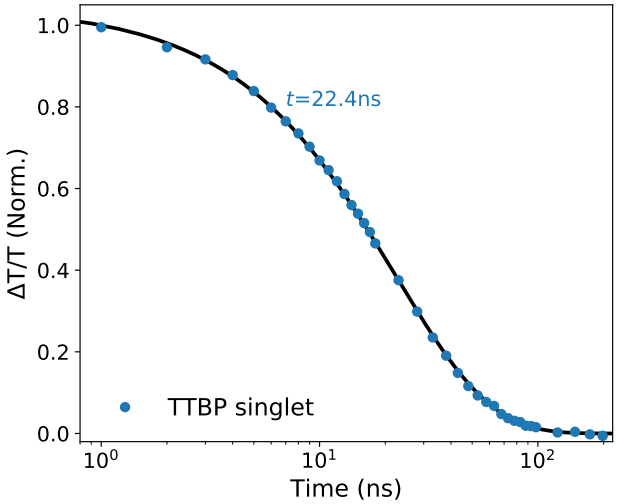

Fig. 4.9 Transient absorption kinetic at 630 nm for 1 mgml^{-1} solution of TTBP in THF, with a mono-exponential fit. Excitation was performed with a 500 Hz 200 fs 400 nm pulse with a fluence of 500 µJcm^{-2}. The probe was a ∼1 ns 1 kHz broadband probe from a supercontinuum laser, with the delay relative to the excitation pulse controlled electronically.

signal from a lifetime of 11.1 µs to 1.3 µs. The triplet energy transfer rate, k_{TET} can then be calculated as 6.8 x $10^5\,\mathrm{s}^{-1}$. Additionally, the lifetime of the triplets formed on TTBP is extracted as 9.4 µs, implying $k_{\mathrm{TTBP}} = 1.2$ x $10^5\,\mathrm{s}^{-1}$.

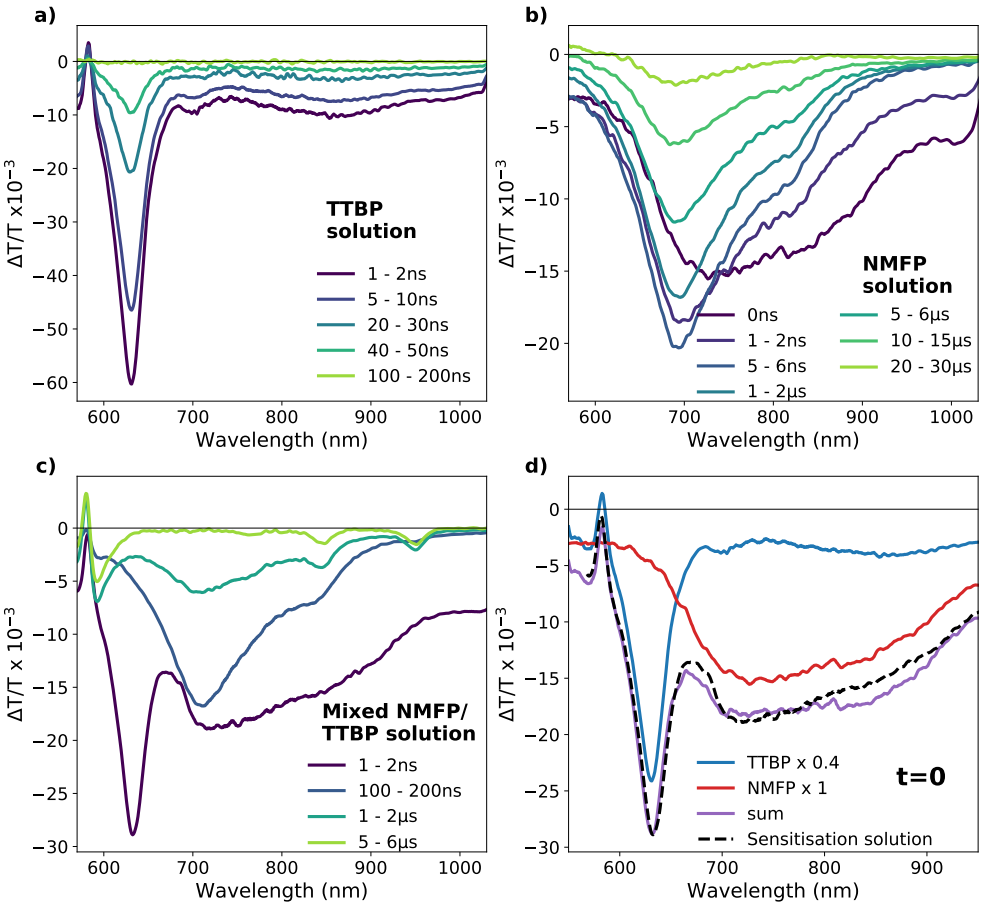

Fig. 4.10 Transient absorption of a) TTBP solution, b) NMFP solution, and c) mixed TTBP and NMFP solutions. d) Comparison of the spectra at $t = 0$ showing the relative contributions from TTBP and NMFP to the mixed solution spectrum. Excitation was performed with a 500 Hz 200 fs 400 nm pulse with a fluence of 500 µJcm^{-2}. The probe was a ∼1 ns 1 kHz broadband probe from a supercontinuum laser, with the delay relative to the excitation pulse controlled electronically.

4.3.2 Triplet Yield

To calculate a fission yield, we need to use the sensitisation experiment to quantify the relative magnitudes of the singlet and triplet PIAs in TTBP. Therefore we need to understand what the relative population of TTBP triplets is at its peak in the sensitisation experiment(∼3 µs). Using the following scheme, we recreated the sensitisation population dynamics based on the decay rates extracted from the transient absorption data in Figure 4.10.

$$\begin{array}{ccc} \mathrm{NMFP_{T1}} & \xrightarrow{k_{\mathrm{TET}}} & \mathrm{TTBP_{T1}} \\ \downarrow & & \downarrow \\ k_{\mathrm{NMFP}} & & k_{\mathrm{TTBP}} \end{array} \tag{4.1}$$

Solving the coupled differential equations for the population of NMFP triplets (N) and TTBP triplets (T), gives the following solutions:

$$N = A_0 e^{-(k_{\mathrm{TET}}+k_{\mathrm{NMFP}})t} \tag{4.2}$$

$$T = A_0 \frac{k_{\mathrm{TET}}}{k_{\mathrm{TET}} + k_{\mathrm{NMFP}}} (-e^{-(k_{\mathrm{TET}}+k_{\mathrm{NMFP}})t} + e^{-(k_{\mathrm{TTBP}})t}) \tag{4.3}$$

Inserting the rates from fitting the transient absorption kinetics in Figure 4.11a shows that the peak population of TTBP triplets is 53% of the initial population of NMFP triplets (Figure 4.11b). We must also take in to account the ISC efficiency of NMFP, which is reported elsewhere to be 90–100%[232]. In this case we will use 90% as a lower bound.

When excited at 400 nm, based on the summing of the absorption spectra in Figure 4.8, we create singlets in TTBP and NMFP in a ratio of $\frac{0.04}{0.21} = 0.21$. Then we must include a factor of 0.9 for the NMFP ISC efficiency, and 0.53 for the population dynamics, to get a ratio between initial TTBP singlet population and peak TTBP triplet population of 0.43. At $t = 0$ in the mixed sensitization solution, there is a small contribution at 630 nm from the NMFP (Figure 4.10d), which we subtract to leave a PIA of magnitude 2.4×10^{-3} from TTBP singlets. By comparison, the peak TTBP triplet PIA at 590 nm is 7.1×10^{-4}. Therefore, the relative magnitudes of the absorption cross-sections of the singlet 630 nm PIA to triplet 590 nm PIA is 7.8. It is not unusual to report much larger cross-sections for singlet PIAs than triplets, for example in TIPS-tetracene the ratio has been reported to be 26[77].

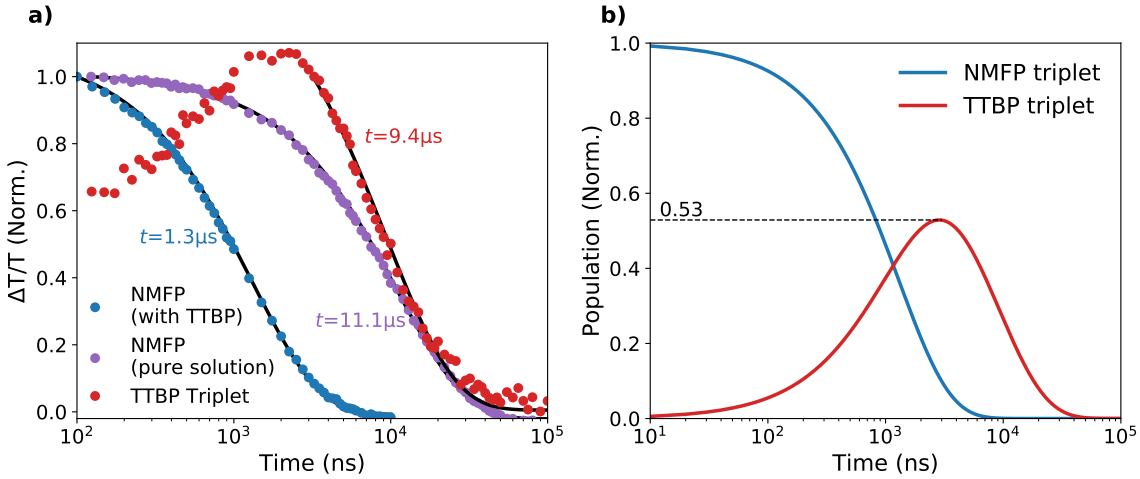

Fig. 4.11 a) Kinetics taken from the transient absorption spectra shown in Figure 4.10. Blue circles are NMFP kinetic taken at 700 nm in the mixed solution. Purple circles are NMFP pure solution kinetic taken at 700 nm. Red circles are TTBP triplet kinetic taken at 930 nm in the mixed solution. Mono-exponential decay fits are made to each kinetic, plotted in black. b) Population kinetics in the mixed solution recreated utilising the lifetimes and triplet transfer rate extracted from a).

Fluence (μJcm^{-2})	Singlet PIA (100 fs)	Triplet PIA (1 ns)	Triplet yield
25	-9.70×10^{-3}	-2.49×10^{-3}	201%
8	-3.09×10^{-3}	-1.04×10^{-3}	265%
4	-6.68×10^{-3}	-2.86×10^{-3}	335%

Table 4.1 Triplet yield calculated for the 3 fluences shown in Figure 4.12, using the relative absorption cross sections for singlet and triplet calculated from solution sensitisation.

Table 4.1 shows the magnitudes of the singlet and triplet PIAs and the resulting calculated triplet yield for a range of fluences in a 7% TTBP in PS film (Figure 4.12). We see that across a range of excitation densities the calculated triplet yield varies, with the highest yield at the lowest fluence. This is likely due to bimolecular annihilation events between singlets or triplet pairs. The calculated yield at lower fluences exceeds 200%, which implies a systematic error in the calculation, likely due to using the solution absorption cross sections in the solid state. However, we note that these figures are in the correct order of magnitude for quantitative generation of the triplet pair state, as expected from the fact that singlet fission to the pair is ∼100 times faster than the radiative rate, while in dilute (<1%) films in PS the PLQE is ∼97% indicating a lack of competitive non-radiative decay pathways for the singlet. This implies that with no annihilation the fission yield should be 198% with ∼1 in 100 singlets decaying radiatively and ∼99 out of 100 forming a triplet pair. Taking all of this into account, we think it likely that the initial fission process proceeds at approximately full efficiency (∼200%) at low fluences where bimolecular singlet-singlet annihilation is minimised.

4.4 Magnetic Field Effect in TTBP

The modulation of steady-state PL intensity under low magnetic field unequivocally confirms that singlet fission occurs in TTBP. A range of TTBP films, diluted to varying concentrations in polystyrene, display a clear magnetic field effect (MFE), as shown in Figure 4.13a. The observed MFE exhibits the singlet fission signature initial decrease in PL at low fields followed by an increase to a positive MFE, as originally observed in tetracene[65]. As shown in Figure 4.13b, the magnetic field effect on PL is approximately uniform across the whole spectrum, despite the differences in kinetics in different parts of the PL spectrum (Figures 4.23 and 4.24). This indicates that any emission from lower-energy geometries/defects also originates from excitons produced by or capable of singlet fission, and are not indicative of a singlet-trapping mechanism that is competitive with singlet fission, although it does not rule out a trap for triplet pairs. Lowering the concentration of TTBP in polystyrene reduces the magnitude of the effect, implying an increasing fraction of the total emission is from isolated molecules that do not exhibit singlet fission. However, there is a measurable MFE down to 5% by weight, indicating even these dilute samples contain aggregates exhibiting singlet fission.

We note that the B field of minimum PL and the zero crossing point where PL(B) = PL(0) are both at much higher fields than for other singlet fission materials such

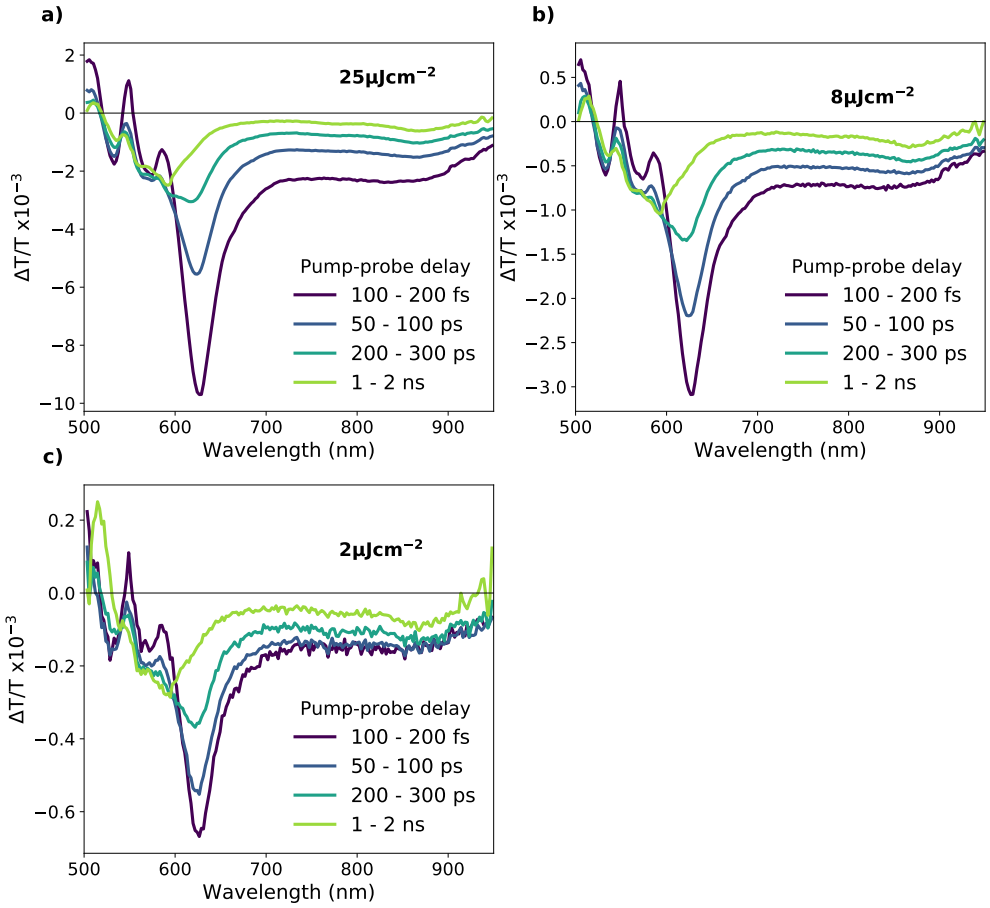

Fig. 4.12 Transient absorption spectra for 3 different excitation densities on a 7% TTBP in PS film. Excitation was performed with a 17 kHz 200 fs 550 nm pulse. The probe was a 34 kHz broadband probe generated in a YAG crystal, with the delay relative to the excitation pulse controlled mechanically.

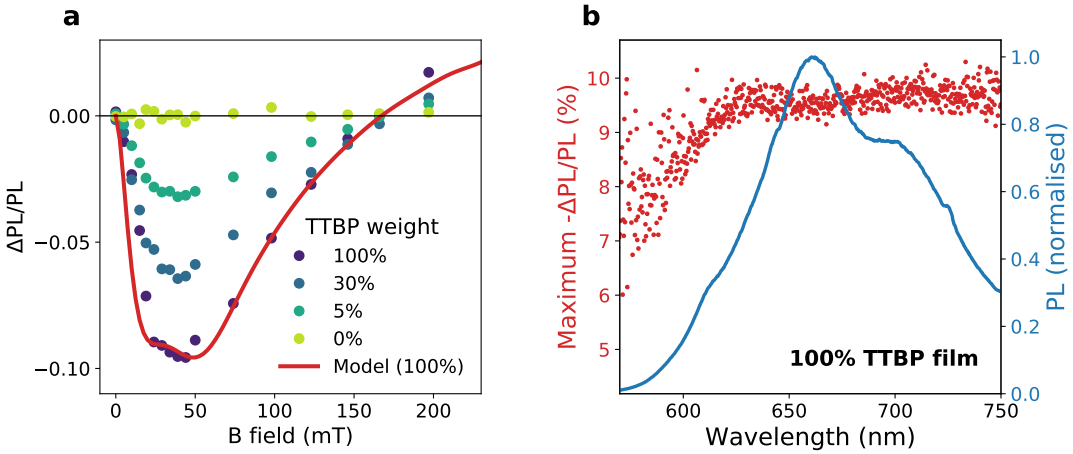

Fig. 4.13 a) Magnetic field effect on room-temperature steady-state PL using 520 nm CW excitation. Circles indicate relative change in integrated PL intensity in a magnetic field for films of varying weight % of TTBP in polystyrene, the solid red line shows a fit for the 100% TTBP film of the Merrifield model averaged over 10,000 random angles between B field and molecular orientation. b) Spectral dependence of the maximum magnitude of the MFE in 100% TTBP film (red, dots) compared to the steady state PL spectrum at B=0 (blue line).

as tetracene[65], rubrene[185], anthracene[67] and DPP[186]. The Merrifield model used to fit the magnetic field effect (MFE) in Figure 4.13 is described in Equation (4.4). When constrained to a steady state with constant populations of S and P_i, we obtain PL as a function of B shown in Equation (4.5). The PL depends on α_i, the singlet projection of the pair states P_i, calculated according to the pair Hamiltonian. This Hamiltonian includes the exchange interaction with coupling parameter J, the intra-triplet zero field splitting (ZFS) interaction parametrised by the zero-field splitting parameters D and E, and the Zeeman interaction with the external B field. The parameter $a = \frac{\gamma_+}{\gamma_r}$ is the ratio of singlet fission rate to radiative rate and $\epsilon = \frac{\gamma_-}{\gamma_d}$ is the ratio of the rate of triplet fusion (from pair-state back to singlet) to the rate of pair dissociation.

$$\begin{array}{ccccc} G & & & & \\ \downarrow & \gamma_+\alpha_i & & \gamma_d & \\ S & \rightleftharpoons & \{P_i\} & \rightarrow & T+T \\ \downarrow & \gamma_-\alpha_i & & & \\ \gamma_r & & & & \end{array} \tag{4.4}$$

$$PL(B) = \gamma_r S(B) = G\left(1 + a\sum_i \frac{\alpha_i}{1+\epsilon\alpha_i}\right)^{-1} \tag{4.5}$$

In addition to the kinetic parameters a and ϵ, the MFE is dependent on the strength of the inter-triplet exchange coupling J within the pair states. The low field MFE effect only occurs when J is small relative to D, the dipolar interaction[86,127]. The exchange value depends on inter-triplet wavefunction overlap between molecules[177,179]. We note that strongly coupled pairs give little or no effect in the range of 0–200 mT that was explored in this study and so this experiment highlights only weakly coupled triplet pairs, without ruling out the presence of other, more strongly coupled pairs.

The fitting process was as follows: D and E, the ZFS parameters which define the dipolar interaction, were fixed at the value extracted from transient electron spin resonance (trESR) simulations ($D = 1340$ MHz or 47.9 mT and $E = 28$ MHz or 1.0 mT). In order to fit to the line shape measured in films of TTBP, we had to increase ϵ from around 1 in tetracene to 10, which brought the zero crossing point to the correct range ($\sim$150 mT). Figure 4.14b shows how varying ϵ while keeping J low and a constant affects the MFE line shape. A fit with a large ϵ, such as that for TTBP in Figure 4.13a, is indicative of fast geminate triplet fusion and/or slower/impaired pair dissociation.

a can also be varied, however this has a negligible effect on the line shape and predominantly affects the magnitude of the effect. Figure 4.14a shows how increasing a increases the magnitude of MFE. We set a to 200 from the rates obtained from transient absorption – the radiative rate is 22 ns (Figure 4.9), while the formation time of the pair state is of the order of 100 ps (Figure 4.6c), giving a ratio of around 200. Finally, we come to J, for which we found the best fit at $J = 0.32D = 1.7$ µeV. Figure 4.14c shows the dramatic changes to line shape resulting from small changes in J. At $J > 0.5D$ the dips from the level anticrossings at J, $3J/2$ and $3J$ are visible in the simulation. At $J > 3D$ the level anticrossings occur outside the range of fields investigated and there is negligible MFE in 0–200 mT. Importantly, this means the the low field MFE measurement is selective for lower J pairs/sites - any high J pairs will not contribute any MFE and we are only sensitive to low J pairs. We do not rule out the presence of higher J pairs in addition to those measured in the MFE.

While the MFE results show clearly that singlet fission takes place in TTBP and TTBP/PS blends, and that all of the photoluminescence features are from fission-involved excited states, we note that the model used to simulate the line shape is overly simplistic. While we have fit to a single "average" exchange coupling strength and a singlet set of kinetic parameters, there is likely to be a distribution of both within any sample. This can be due to the presence of multiple structural polymorphs in the sample and differently geometrically-arranged pairs within a single polymorph, as seen in TIPS-tetracene[177] and DPH[127].

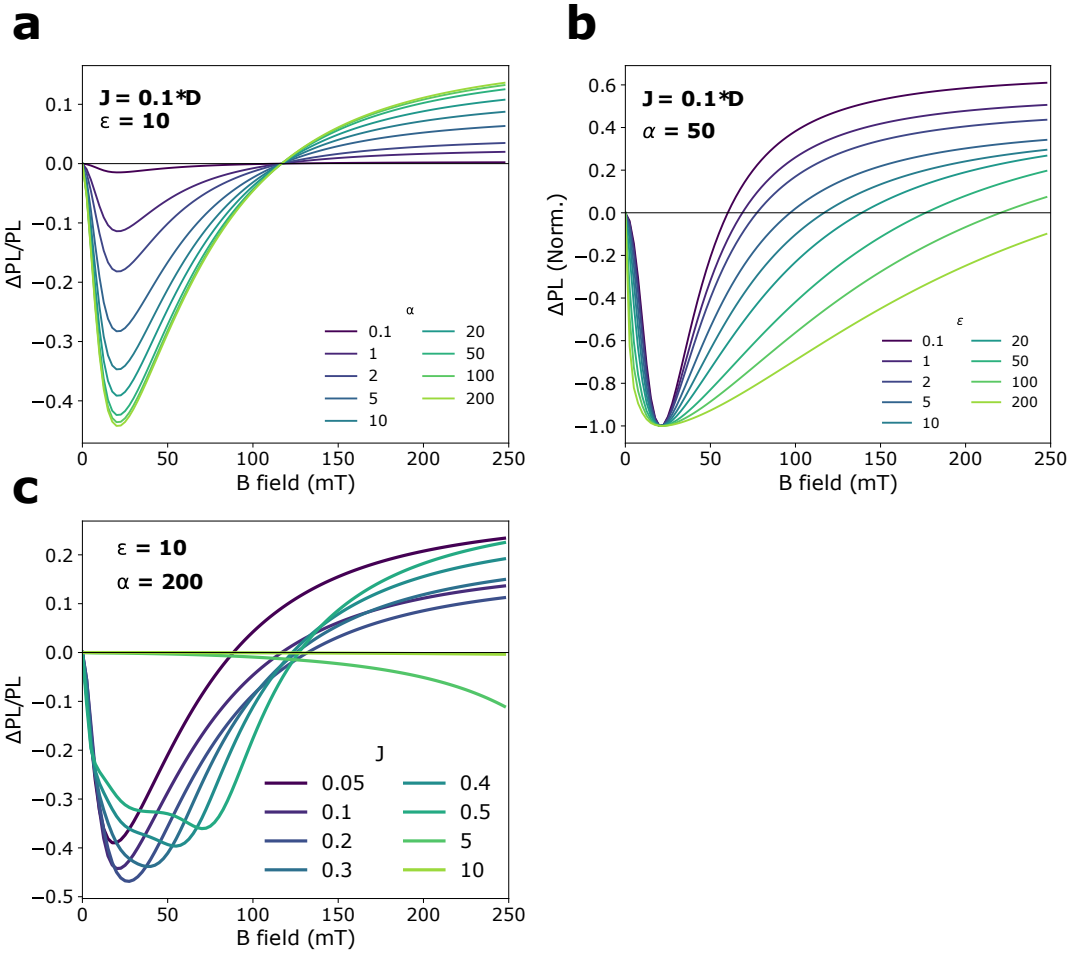

Fig. 4.14 Example MFEs calculated for at a single molecular orientation to the B field ($\theta = \frac{\pi}{4}$, $\phi = \frac{\pi}{2}$). a) Normalised MFEs for varying ϵ and low J ($0.1D$), showing how the line shape, particularly the zero crossing point, change with ϵ. b) Not-normalised MFEs for a range of α and low J ($0.1D$), showing how the line shape is unchanged with α, but the magnitude of the MFE increases with increasing α. c) Normalised MFEs for a range of J showing how the line shape changes with J.

4.5 Transient Electron Spin Resonance of TTBP

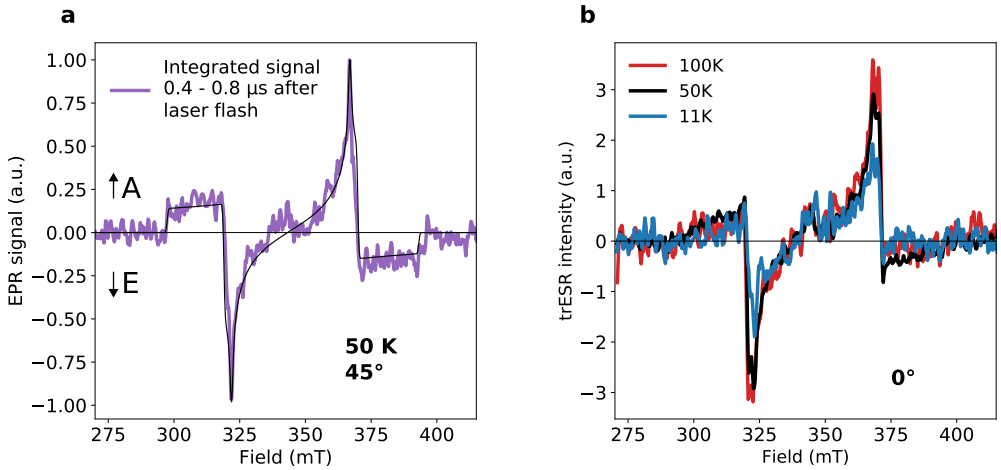

Fig. 4.15 a) trESR for a drop-cast film of 100% TTBP at 50 K, integrated from 0.4 – 0.8 µs after laser excitation at 532 nm. The sample substrate was oriented at approx. 45° to the B_0 direction. The polarisation pattern of AEEAAE is consistent with singlet fission which overpopulates the $m_s = 0$ sublevel. Black line is a simulation using EasySpin[233] for a triplet with zero-field splitting parameters $D = 47.9$ mT, $E = 1.0$ mT and $g = 2.000$, linewidth = 0.4 mT. b) trESR spectra at 11 K (blue), 50 K (black) and 100 K (red), for a pure TTBP drop-cast film, showing the higher population of free triplets at higher temperatures, due to temperature activated separation of the pair state. The sample orientated was at 0° to the B_0 field. Signal is integrated from 0.3–1.5 µs after laser excitation.

Electron spin resonance (ESR) uses microwaves to probe resonances of transitions between the sublevels of non-zero spin states such as doublets ($S = \frac{1}{2}$), triplets ($S = 1$) and quintets ($S = 2$). Time resolved ESR (trESR) couples this with a pulsed laser to observe the ESR signatures of photoexcited states, and their lifetimes. The relative sublevel populations (e.g. for a triplet state, the populations with spin projection quantum number along the magnetic field direction $m_s = \pm 1, 0$) of a state dictate the polarisation pattern of the ESR signal. This pattern of microwave emission and absorption across magnetic field therefore offers insights to its formation mechanism. In TTBP, we observe triplets in trESR with a polarisation pattern AEEAAE (Figure 4.15a), indicating an relative overpopulation of the $m_s = 0$ triplet sublevel relative to ± 1, a further unambiguous confirmation that the triplets are formed by singlet exciton fission to an overall spin-singlet pair-state which subsequently dissociates (triplets formed by intersystem crossing instead of singlet fission, as in dilute TTBP solution, would have an EEEAAA polarisation pattern, see Figure 4.17). In other acene derivatives

where a triplet pair-state is formed, trESR has been used to observe triplet pairs in spin-quintet states[163,172,173]. The absence of quintets in TTBP from 11 – 100 K suggests that either the triplet pairs in TTBP dissociate or decay faster than the time resolution of trESR (∼300 ns), and thus we only observe dissociated triplets, or J is very large, preventing mixing to the quintet manifold. The monomolecular decay of photoluminescence on a ∼65 ns timescale suggests that the pair-state is too short lived to be observed in trESR. The intensity of the ESR signal decreases by a factor of 2 from 100 K to 11 K (Figure 4.15), despite the fact that lower temperatures increase the Q-factor of the resonator and extend the lifetime of spin relaxation processes which should both increase the trESR signal intensity. We attribute the larger signal to the fact that at lower temperatures, there is less thermal energy to separate the triplet pair-state into free triplets. This interpretation is also consistent with the substantial increase in PL yield at lower temperatures (Figure 4.27).

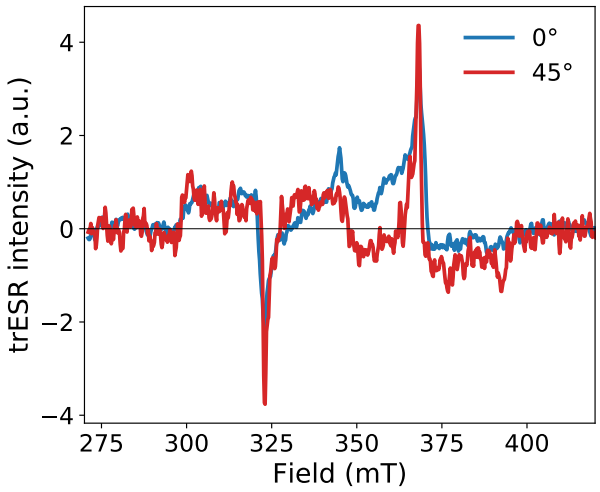

Fig. 4.16 trESR spectra for a sample of TTBP in polystyrene at 10% weight fraction, with the sample at angle at 0° (blue) and 45° (red) at 50 K. Signal is integrated from 0.4–0.8 µs after laser excitation.

To investigate the degree of aggregation and singlet fission activity in the TTBP/PS blends, trESR spectra were recorded for a sample of 10% TTBP in PS, of which two are shown in Figure 4.16. The polarisation pattern of AEEAAE is identical to the pure drop-cast TTBP sample, in Figure 4.15, while the difference between 0° and 45° is very similar to that of 225° and 270° in Figure 4.21a, indicating that there is still significant preferential alignment of the molecules relative to the substrate in the TTBP/PS blend.

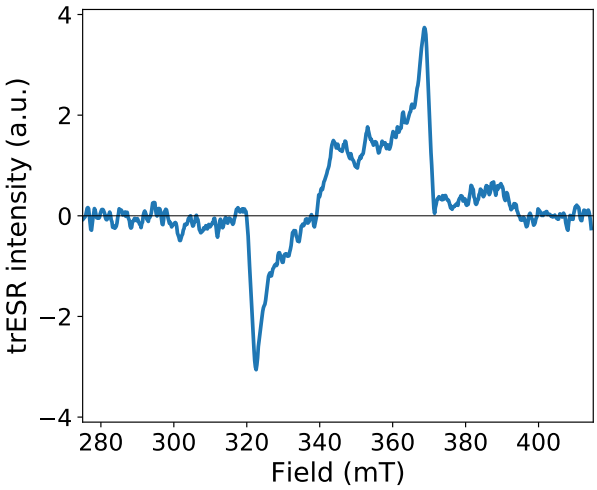

Fig. 4.17 trESR spectrum for a 1 mM frozen solution of TTBP in toluene at 50 K. Signal is integrated from 0.4–0.8 µs after laser excitation

In contrast to all the solid samples of TTBP studied, the frozen dilute solution of TTBP has an trESR polarisation pattern of EEEAAA, compatible with intersystem crossing. This is expected, as the solution is too dilute for any pair of molecules to be in close enough proximity to undergo fission.

4.5.1 Orientation Dependence

The trESR spectrum shows an orientation dependency with rotation of the substrate relative to the external magnetic field (B_0) direction, indicating orientationally selective crystallisation of molecules relative to the substrate (Figure 4.18). While we do not rule out a contribution to the rotational dependence from the presence of both of the two known polymorphs of TTBP, reported by Müller et al.[234], we were able to simulate the orientation-dependent trESR spectra using a model which represents partial ordering in our system (Figure 4.21). The simulations are consistent with the expected preferential alignment of the long axis of the conjugated core vertical to the substrate, as is typical for solution-processed small molecules that interact more strongly with each other than with the substrate. The trESR of a 10% TTBP in polystyrene sample, Figure 4.16, also shows the same orientation dependence, further indication of the similarity of the photophysics between the aggregated domains in the PS blends and the 100% TTBP samples.

Figure 4.18 and Figure 4.19 show a clear dependence on the angle of the sample substrate relative to the magnetic field. Considering the fact that two crystal structures,

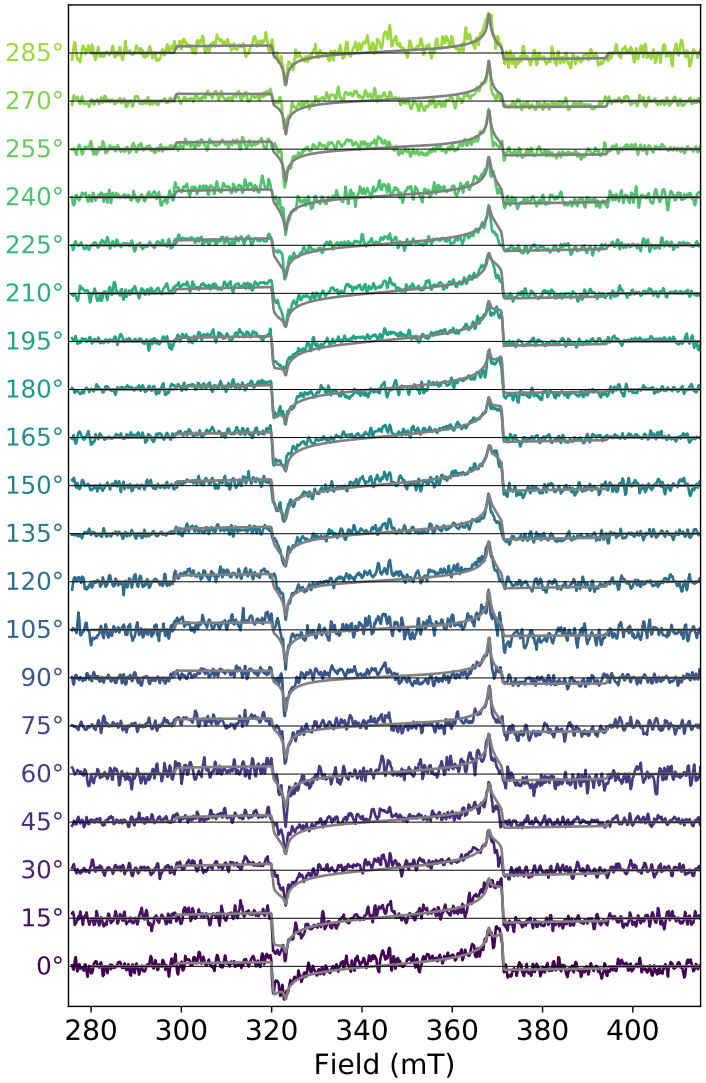

Fig. 4.18 Rotational dependence of trESR signal at 50 K integrated from 0.4–0.8 µs after laser flash, showing the preferential orientation of the crystalline domains to the substrate. Angles labelled are read out from the goniometer indicating angle of the substrate plane to the B_0 field. Simulations shown in grey using EasySpin[233], detailed below.

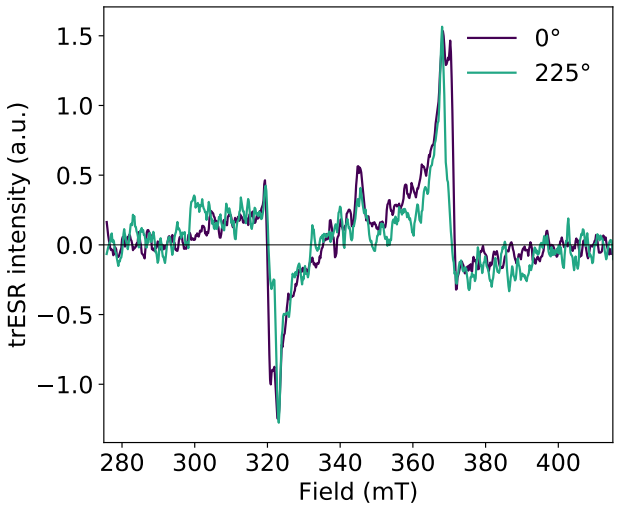

Fig. 4.19 Direct comparison of trESR spectra at 2 different sample orientations, 0° and 225°, at 50 K. Signal is integrated from 0.4–0.8 µs after laser excitation.

brick wall and leaning double stack, were reported for TTBP by Müller et al.[234], there are two scenarios could result in the observed orientation dependence. Firstly, the presence of the only one polymorph (likely the thermodynamically favoured: brick wall) in polycrystalline domains with partial ordering due to some orientation selective crystallization relative to the substrate. Secondly, the presence of both polymorphs (brick wall and leaning double stack) also with the presence of partial ordering due to orientation selective crystallisation. The crystal structure of the leaning double stack polymorph suggests that its presence alone would not lead to strong orientation dependent trESR spectra. While our partial ordering simulation does not explicitly account for multiple polymorphs, it does not rule them out.

We simulate the rotation dependent trESR spectra using EasySpin[233] and a custom model representing the partial ordering in the system, due to orientation selective crystallization relative to the substrate. The simulated spectra shown in Figures 4.18 and 4.21 are based on the ZFS parameters being $D = 1340\,\mathrm{MHz}$ (47.9 mT) and $E = 28\,\mathrm{MHz}$ (1.0 mT), with $g = 2.000$ and a linewidth of 0.4 mT.

The ZFS axes are assumed to be the same as for pentacene, where the molecular X axis is along the long axis of the conjugated core[163,225,226]. We expect the TTBP molecules to preferentially align this molecular X axis normal to the substrate plane. At a sample orientation of 0°, the substrate normal is perpendicular to the B_0 direction and parallel to the incident laser beam. In this sample orientation the molecular X axis will also be preferentially aligned perpendicular to the B_0 direction (parallel to

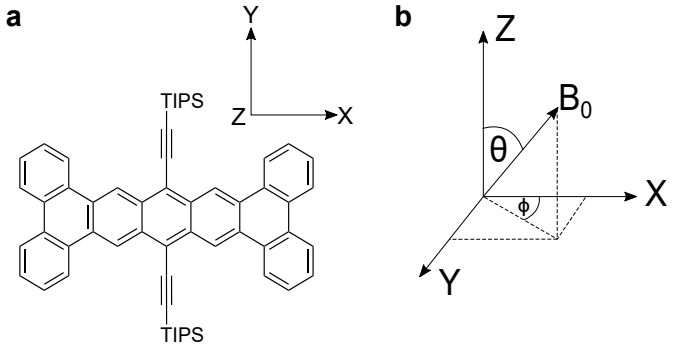

Fig. 4.20 a) Molecular axes of TTBP, with the x axis along the long axis of the molecule. b) shows the definitions of θ and ϕ which describe the angle between the B_0 direction and the molecular axes.

the substrate normal). As defined by EasySpin and shown in Figure 4.20b, θ is the angle between the molecular Z axis and the magnetic field vector, while ϕ is the angle between the molecular X axis and the projection of the magnetic field vector on the XY plane of the molecular frame.

Due to the preferential alignment, rotation of the sample in our setup (around the axis of the ESR tube) leads to rotation in both the molecular XZ and XY planes depending on the initial crystallisation orientation of each crystallite. Hence, we created a custom function for each sample orientation based on Gaussian curves which represent the distribution of the partially ordered system relative to the B_0 direction. The distributions at different sample orientations are shown in Figure 4.21, where panels b) and c) show the distributions used for sample rotation from 180° to 270° (blue to red curves). At each sample orientation, we generate a 2-dimensional distribution in θ and ϕ. Figure 4.21b,c show 1-dimensional cuts of this distribution in the θ and ϕ directions, with cuts taken at the peak of the ϕ and θ distributions respectively.

First, considering the distributions in θ shown in Figure 4.21b, partial ordering in the system means that when the sample orientation is at 180°, the distribution peaks at $\theta = 90°$ (dark blue line in Figure 4.21b). This means there is a larger probability of having molecules with their molecular Z axis perpendicular to B_0 and their molecular X axis parallel to B_0. When the sample is rotated to 270°, the distribution then peaks at $\theta = 0°$. This means it is more probable for molecules to have Z parallel to B_0 than X parallel to B_0. This can be visualised by looking at the higher signal at the Z and Z' transitions (the outer peaks) in the dark red line (sample orientation 270°) compared to the dark blue line (sample orientation 180°) in Figure 4.21a.

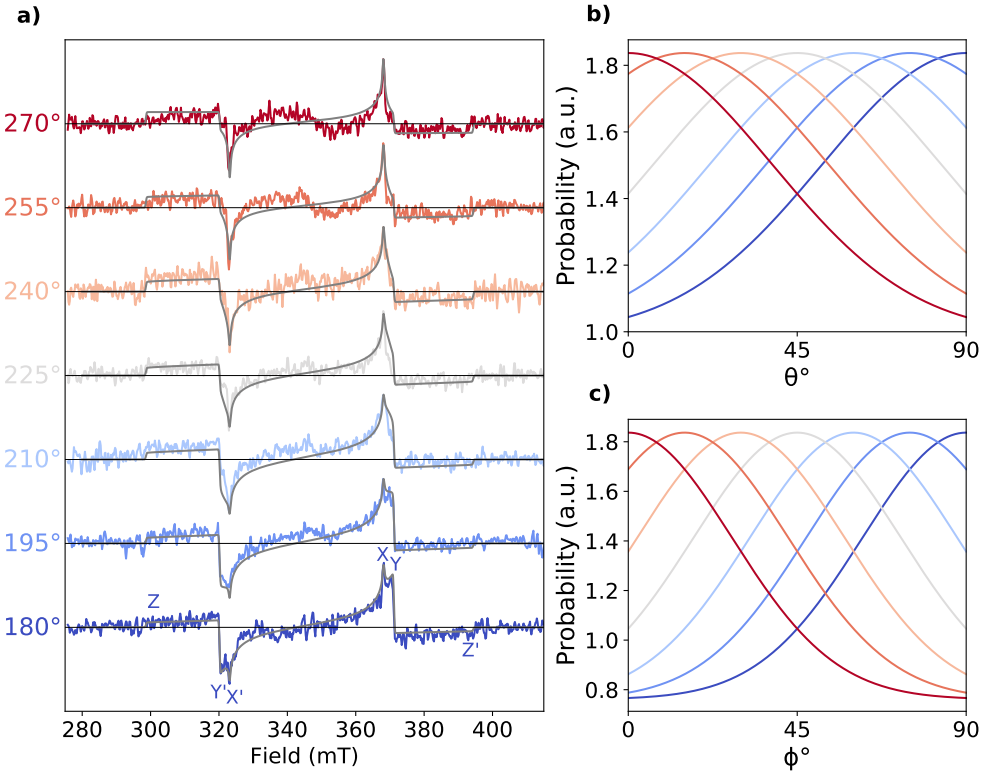

Fig. 4.21 a) trESR spectra from sample angle 180° to 270° with simulated spectra using EasySpin[233] in grey. For the sample orientation of 180°, the transitions for different molecular orientations are labelled in the X, X' notation, where X/X' indicates the absorptive/emissive transition for molecules with X axis parallel to B_0. b) θ is the angle between the Z axis of the molecular frame and the magnetic field vector. The different curves represent the distribution in θ as the sample is rotated, each plotted at $\phi = \phi_{max}$ where the distribution is maximised. c) ϕ is the angle between X axis and the projection of the magnetic field vector on the XY plane of the molecular frame. The different curves represent the distribution in ϕ as the sample is rotated, each plotted at $\theta = \theta_{max}$ where the distribution is maximised.

Microwave attenuation (dB)	Decay time (µs)
24	5.0
30	6.8
36	7.7

Table 4.2 Exponential decay times for different microwave attenuations, plotted in Figure 4.22

Similarly, when considering the distributions in ϕ shown in Figure 4.21c, at a sample orientation of 180°, the distribution is peaked for molecules oriented at $\phi = 90°$. There is a larger probability of having molecules with their molecular X axis perpendicular and their molecular Y axis parallel to B_0. When the sample is rotated to 270°, the distribution peaks at $\phi = 0°$, meaning there is a larger probability of molecules having their X axis parallel/antiparallel to the B_0 direction and their Y axis perpendicular. This can be seen in the change in strength of the Y and Y' transitions in Figure 4.21a – stronger at sample orientation of 180° (dark blue), where more molecules are aligned with Y axis parallel to B_0.

The simulations are calculated using the pepper function in EasySpin[233] and our custom distribution is accounted for by using the Exp.Ordering command. The peak positions of the distributions in θ go from 90° to 0° and in ϕ from 90° to 0° in steps of 15°, representing rotation of the sample about 90° from e.g. 180° to 270° (see Figure 4.21). The FWHM for the Gaussians used in the θ distribution is 90° and in ϕ distribution it is 65°. To simulate the full rotation study from the goniometer angles of 180° to 270°, the simulations are repeated every 90°, i.e. the simulation for angles 0° to 90° and 180° to 270° are the same.

4.5.2 Spin Relaxation Timescales

The trESR signal decay times are all in the 5–8 µs range. Since the decay times do not change by more than a factor of 1.6 going from 24 dB to 36 dB (Table 4.2), we know the spin-lattice relaxation time, T_1, is at least 8 µs but cannot be much larger than ∼10 µs. T_1 is an order of magnitude faster than the 100 µs ODMR component and therefore it is valid to assume that the 100 µs signal is from thermalised triplets.

4.6 Time-resolved Photoluminescence of TTBP

For a material where singlet fission comprehensively outcompetes the radiative lifetime, the photoluminescence yield of TTBP is unusually high, and we turn to time-resolved

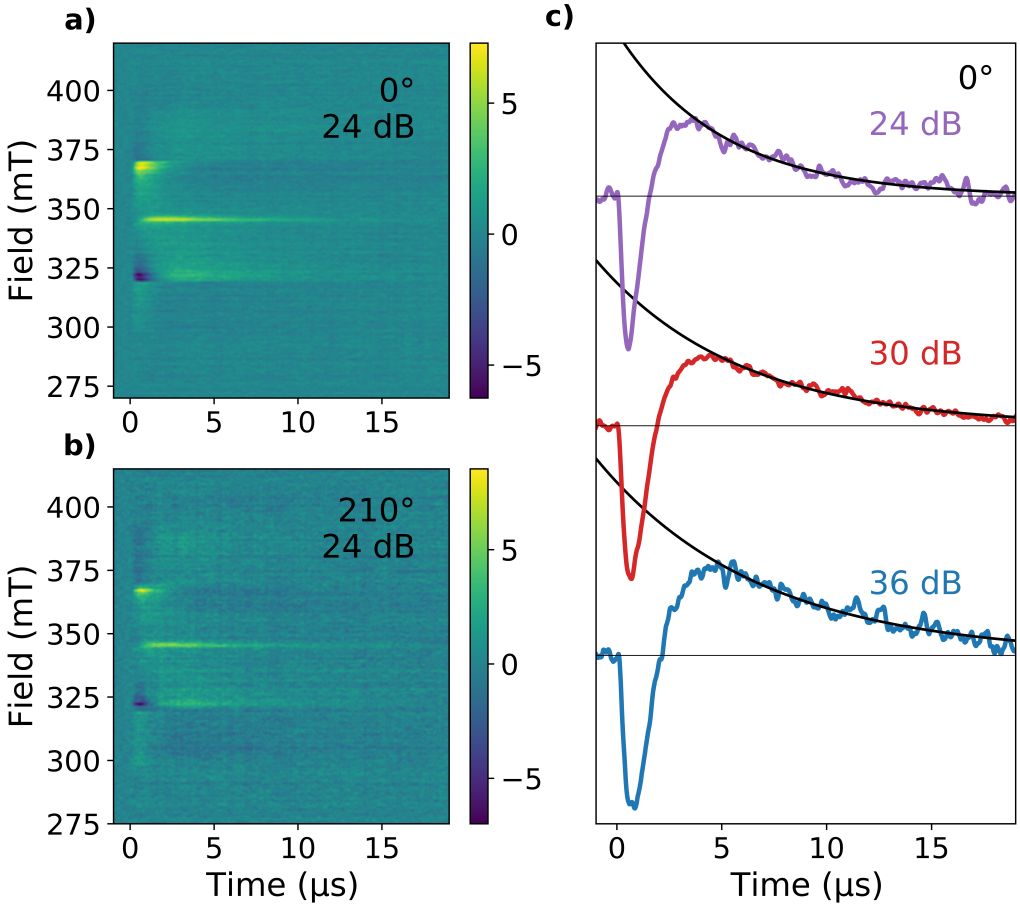

Fig. 4.22 a) Colourmap showing evolution of trESR signal over time at 50 K with sample at 0° relative to the B_0 field and microwave attenuation of 24 dB b) Colourmap showing evolution of trESR signal over time at 50 K with sample at 210° relative to the B_0 field and microwave attenuation of 24 dB. c) Kinetics of the main emissive peak averaged over 321-323 mT in a) at 24 dB microwave attenuation compared to the same orientation and temperature with lower microwave powers of 30 dB and 36 dB. Black lines are exponential decays fitted to the transients after the inversion of the signal.

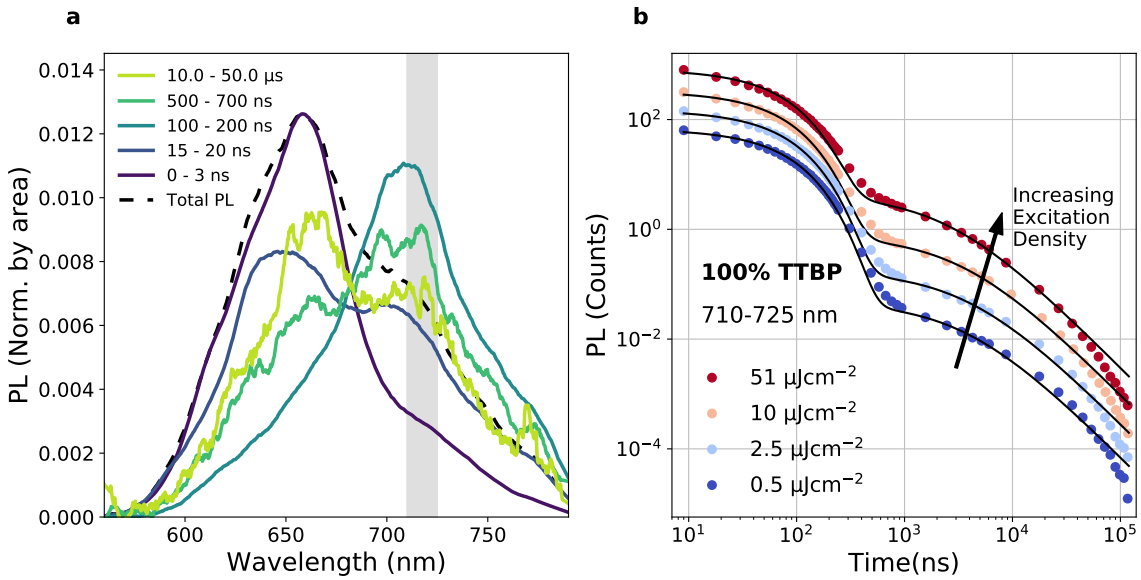

Fig. 4.23 a) Time-cuts of time-resolved photoluminescence for a 100% TTBP drop-cast film at room temperature with an excitation fluence of 25 µJcm^{-2}, showing the early dominance of the 660 nm peak, followed by a red-shift to 720 nm over ∼30 ns, followed by a shift back to 660 nm after ∼500 ns. Grey bar indicates wavelength range in panel b). b) Filled circles indicate PL signal integrated over the wavelength range indicated in grey in a) with varied fluence. A relative increase in the delayed photoluminescence (after 500 ns) is seen as excitation density increases. Solid lines are fits consisting of the sum of a monomolecular decay (τ∼65 ns) and a bimolecular decay at later times.

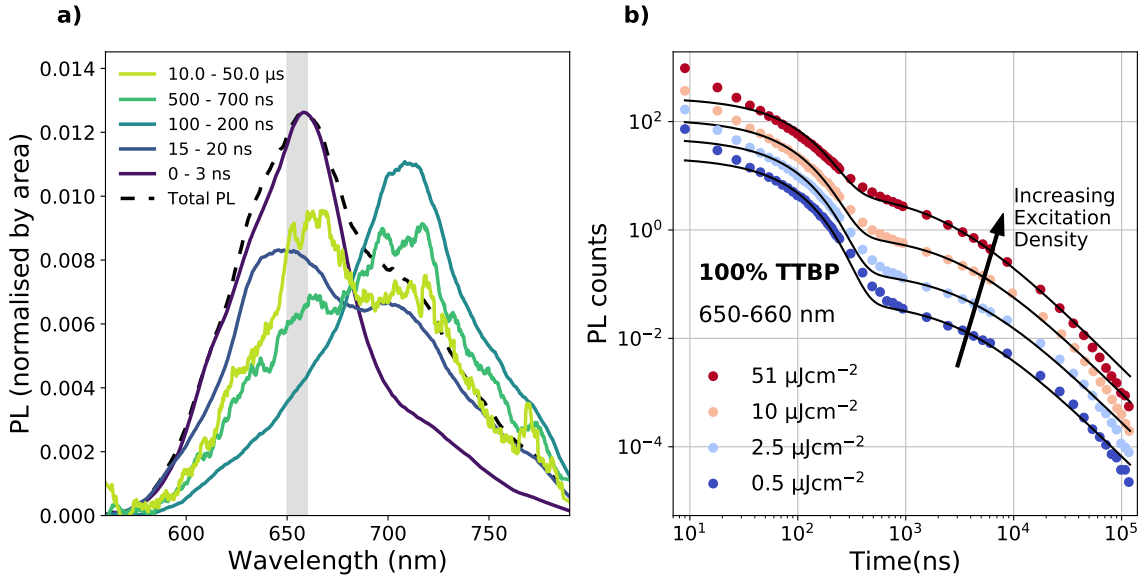

Fig. 4.24 PL kinetics at 650–660 nm, presented as in Figure 4.23 where 710–725 nm is highlighted. Before ∼20 ns, there is some prompt singlet PL which causes the fit to the geminate/non-geminate TTA model to under-predict the actual signal.

PL to understand how that can be possible. The PLQE is 20% in the solid state at room temperature, rising to 97% in increasingly dilute PS blends (Figure 4.4). In pure TTBP, there are two dominant spectral features, with distinct kinetics, shown in Figure 4.23a. Immediately after photoexcitation, emission is dominated by a feature which peaks at 660 nm with a shoulder at 600–620 nm. After delays of 100–500 ns, the 660 nm peak reduces in intensity to reveal a feature at 720 nm. When the time-cut spectra are normalised by area in Figure 4.23a, there is an isoemissive point at 685 nm, indicating that these are two distinct species. The spectrum continues to shift until 1 µs after excitation, beyond which the spectrum is a constant mixture of the initial 660 nm peak and the 720 nm peak that dominates in the intermediate regime.

While there is some early time singlet-singlet annihilation (evident from the sub-linear increase in total PL with excitation density and the difference in the initial PL decay kinetics with excitation density shown in Figure 4.25), by 10 ns this effect is negligible. Therefore, the PL emission rate at 10 ns can be used to benchmark the population of triplet pairs. From 10–500 ns the photoluminescence decay is monomolecular, with a lifetime of ∼65 ns and negligible excitation density dependence. Subsequently, as the pairs dissociate or decay radiatively, by 1 µs the photoluminescence is dominated by non-geminate triplet-triplet annihilation (TTA). The emission rate for non-geminate TTA is proportional to the square of the triplet population, and the decay is bimolecu-

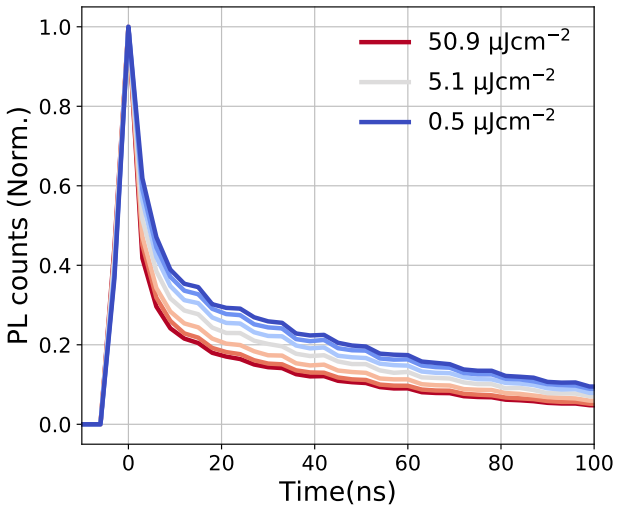

Fig. 4.25 Early time kinetics of the photoluminescence of 100% TTBP at room temperature at 710–725 nm. Excitation is by a 200 fs, 500 nm pulse at 1 kHz, while the smallest time step and instrument response function is ∼3 ns.

lar. The delayed contribution is excitation density dependent, with a stronger delayed component at higher excitation densities relative to the intensity of the early photoluminescence, characteristic of non-geminate, bimolecular TTA (Figure 4.23b). Solid lines in Figure 4.23b are the sum of a monomolecular decay (geminate TTA from triplet pairs) and a bimolecular decay (non-geminate TTA). Beyond ∼50 µs, the PL response falls below this bimolecular fit, likely due to time-dependent triplet mobility, with lower mobility triplets dominating at very long delays. The blue shift to the spectrum at late times can be understood as lower mobility triplets undergoing TTA with weak inter-triplet exchange coupling. We verify the linear and quadratic dependence of the integrated counts from each part of the fits with respect to the population density at 10 ns. Confirming this assignment, the delayed, bimolecular component scales with a power of 1.6 to the counts at 10 ns, while the monomolecular component scales with a power of 0.9 (Figure 4.26).

The delayed components of the kinetics are fitted using a non-geminate TTA model. This begins with the model for the time evolution of triplet population, $[T]$, from Poletayev *et al.*[235], Equation (4.6), where $G(t)$ is the generation of triplets over time, τ is the monomolecular decay lifetime and γ is the bimolecular decay constant.

$$\frac{d[T]}{dt} = G(t) - \frac{[T]}{\tau} - \gamma[T]^2 \tag{4.6}$$

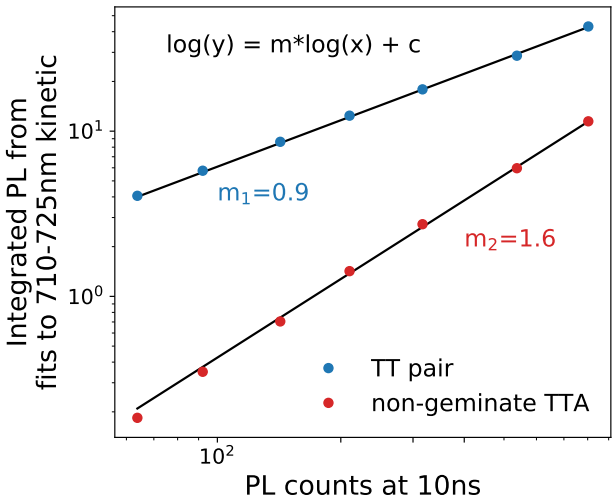

Fig. 4.26 Dependence of the integrated intensity of the two temporal components of the 710–725 nm PL kinetic on excitation density. Excitation density of triplet pairs at 10 ns is proportional to the PL signal at 10 ns. PL from triplet pairs, the monomolecular part of the decay, increases approximately linearly with density of triplet pairs at 10 ns ($m = 0.9$). The bimolecular part of the decay, from non-geminate TTA, increases super linearly ($m = 1.6$).

At long delays, we assume the generation of triplets, $G(t)$, is zero. Then, solving the differential equation for $[T]$ gives the solution in Equation (4.7).

$$[T] = \frac{\left(\frac{1}{\tau}\right)e^{\frac{c_1}{\tau}}}{e^{\frac{t}{\tau}} - \gamma e^{\frac{c_1}{\tau}}} \tag{4.7}$$

Setting PL $\propto$[T]^2, and allowing both τ and γ to vary in this model, we found that τ was always very large, and hence the contribution from monomolecular decay in our fit was negligible in comparison to bimolecular decay. This further simplifies the model to Equation (4.8), for which the solution is given in Equation (4.9).

$$\frac{d[T]}{dt} = -\gamma[T]^2 \tag{4.8}$$

$$[T] = \frac{1}{\gamma t + c} \tag{4.9}$$

4.6.1 Low Temperature Photoluminescence

The photoluminescence yield increases as temperature decreases (Figure 4.27). We consider that this occurs due to the suppression of pair separation as evidenced by the

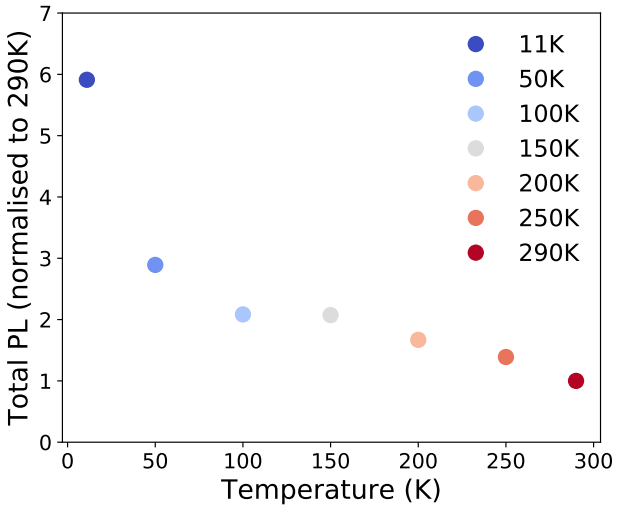

Fig. 4.27 Temperature dependence of the time-integrated and wavelength-integrated photoluminescence of 100% TTBP, excited at 500 nm with 200 fs pulses at 1 kHz, normalised to the value for 290 K. The sample spot may change slightly between different temperatures.

trESR, where fewer free triplets are observed at lower temperatures (Figure 4.15). The temperature dependence of photoluminescence (Figure 4.2d) in TTBP is strikingly similar to tetracene[75], an indicator that the relative energy of the singlet and the triplet pair is similar in both materials: isoenergetic or narrowly exothermic to reach the intermediate pair-state, while separation of the pair state to free triplets is a slower endothermic step. At low temperatures, the photoluminescence yield increases and the spectrum blue shifts and narrows. Below 50 K, we see superradiance, as in tetracene[75]. At 11 K, the 720 nm peak is greatly reduced. This part of the spectrum has the strongest non-geminate TTA (as discussed in Figures 4.33 to 4.35). We therefore attribute the relatively low emission at 720 nm at 11 K to a lower population of free triplets available to annihilate, in combination with superradiant enhancement of radiative rate from the singlet state. We note that it is also possible that at lower temperatures, the suppression of triplet hopping prevents the evolution of the pairs to geometries that emit at this low energy peak.

Figure 4.28 shows PL kinetics at different temperatures at 710-725 nm. At 100 K, the geminate triplet pair PL, which dominates from 10 – 500 ns, decays slower than at room temperature ($\langle\tau\rangle$= 73 vs 58 ns). The triplet pairs dissociate more slowly at lower temperatures. At 11 K, the superradiance effect accelerates the radiative rate of the singlet and/or geminate pair, leading to a faster geminate decay. Beyond 1 µs, at lower temperatures there are fewer free triplets and consequently less non-geminate TTA.

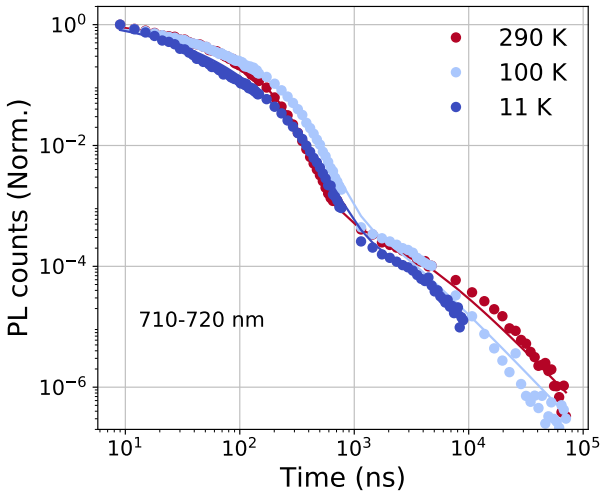

Fig. 4.28 PL kinetics for 100% TTBP, excited at 500 nm with 200 fs pulses, at 710–725 nm, for a range of temperatures. Kinetics are normalised to counts at 3 ns. Solid lines are fits to a stretch exponential plus bimolecular decay model, detailed below. 11 K measurement was not extended beyond 10 µs due to low signal/noise.

Temperature (K)	$\langle\tau\rangle$ (ns)
290	58
100	73
11	34

Table 4.3 Mean relaxation times for a stretch exponential fit to the geminate triplet pair emission decay at different temperatures.

Similarly as for the room-temperature fluence-dependent fits in Figures 4.24 and 4.35, the fits in Figure 4.28 comprise two components, one for the geminate triplet pair emission and a second for delayed, non-geminate TTA. While at room temperature, a single exponential adequately fits the triplet pair emission kinetic, with a lifetime of 65 ns, this does not accurately describe the behaviour at low temperatures. Instead, we use a stretch exponential, Equation (4.10), which approximates a distribution of decay timescales across the population.

$$PL(t) = PL(0)e^{-\left(\frac{t}{\tau_K}\right)^{\beta}} \tag{4.10}$$

The area under a stretched exponential can be interpreted as the mean relaxation time, $\langle\tau\rangle$, expressed in Equation (4.11) in terms of the Γ function, Equation (4.12).

$$\langle\tau\rangle = \int_0^{\infty} dt\, e^{-\left(\frac{t}{\tau_K}\right)^{\beta}} = \frac{\tau_K}{\beta}\Gamma\left(\frac{1}{\beta}\right) \tag{4.11}$$

$$\Gamma(z) = \int_0^{\infty} t^{z-1}e^{-t}dt \tag{4.12}$$

A table of $\langle\tau\rangle$ values for different temperatures is shown in Table 4.3.

4.7 Triplet Lifetimes in TTBP

We used fs-resolution transient absorption with a mechanical delay between pump and probe to monitor pair formation in Section 4.3. Figure 4.29 uses ns-resolution transient absorption with an electronic delay between pump and probe to monitor how the population of triplets evolves beyond the limits of the mechanical delay (2 ns). Figure 4.29a exhibits the same absorption S_1 and T_1 features that we identified in Figure 4.6. We see that the S_1 absorption at 620 nm is only dominant in the 0 ns and 1 ns spectra, within the envelope of the instrument response function. The triplet peak at 590 nm rises to a peak in the 1 ns spectra, and then decays biexponentially, as shown in Figure 4.29b.

The two lifetimes, 80 ns and 6.5 µs, are well matched to the two timescales of the time-resolved photoluminescence from geminate and non-geminate triplet-triplet annihilation (see Figure 4.23). The PL from geminate TTA decays exponentially with a lifetime of 65 ns, while the non-geminate part does not follow a simple exponential but does decay over ∼10 µs, confirming the role of triplets in the delayed PL. In addition, the kinetic of the triplet population shown in Figure 4.29b also affirms the interpretation of the lack of quintets seen in the trESR measurements being an issue

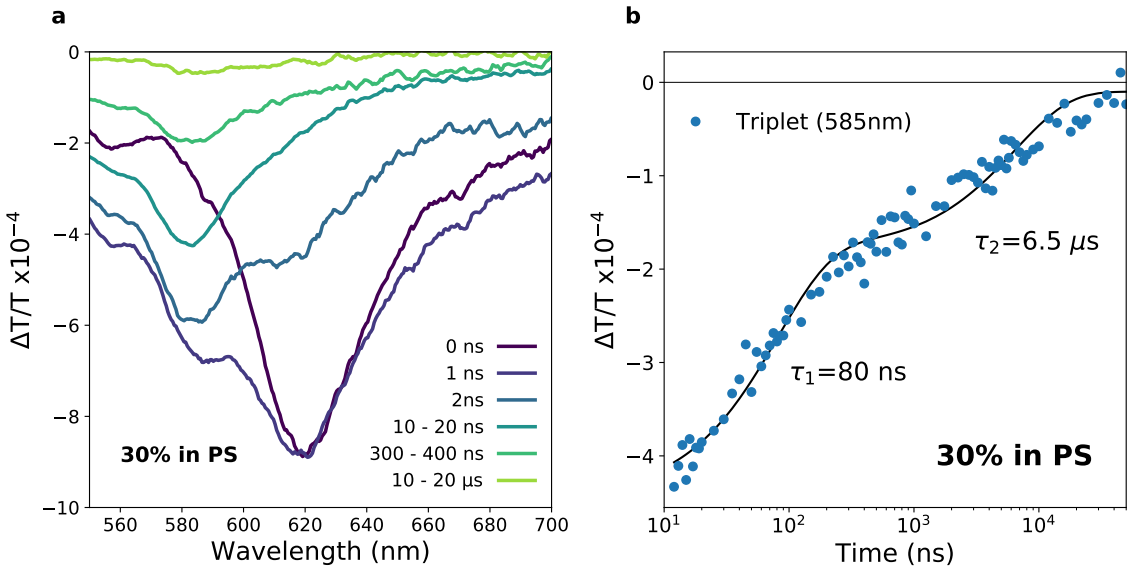

Fig. 4.29 ns-resolution transient absorption of a 30% TTBP in polystyrene film at room temperature, using a 1 ns, 500 Hz, 532 nm pump at a fluence of 7 µJcm^{-2} per pulse and a visible NOPA probe. a) Spectra at given pump-probe delays and b) Triplet decay kinetics taken at 585 nm. An approximately bi-exponential decay is observed with time constants of 80 ns and 6.5 µs, attributable to geminate and non-geminate triplet decay respectively.

of timing - the pair state decaying over 80 ns is faster than the instrument response of the measurement.

4.8 Optically Detected Magnetic Resonance of TTBP

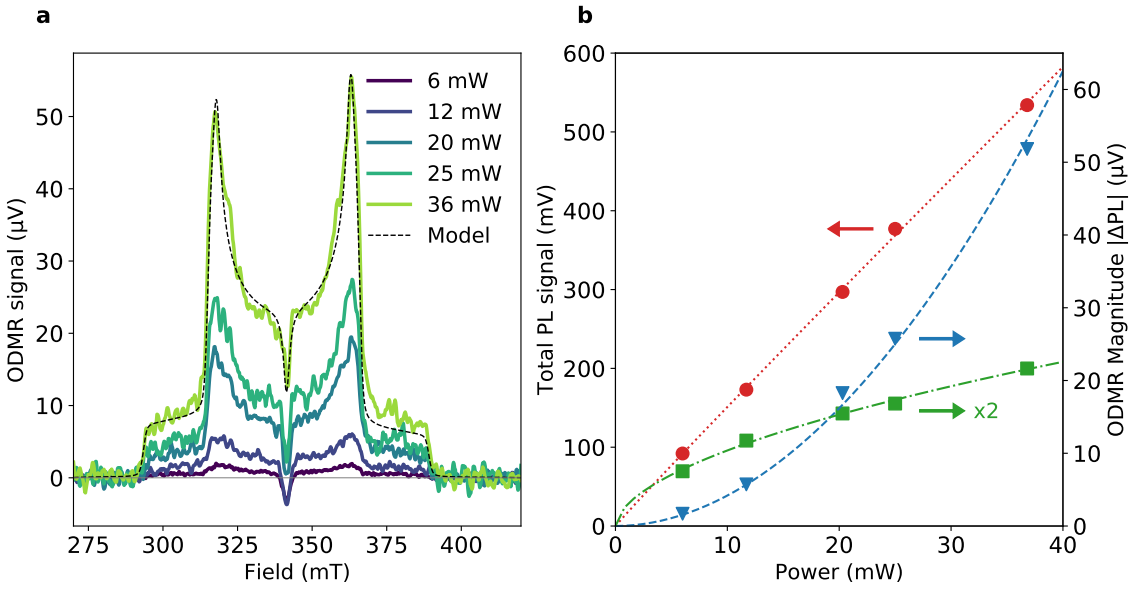

Fig. 4.30 a) ODMR of 100% TTBP film at 50 K using a 523 nm CW laser excitation at a range of excitation densities, labelled by the total laser power incident on the microwave cavity. The microwaves were modulated in a square wave at $f_M = 315$ Hz and data collected using an avalanche photodiode and lock-in amplifier. The "in-phase" signal is shown, and the "out-of-phase" signal was negligible in comparison. Black dotted line shows a simulation for a triplet signal performed with EasySpin[233] with an additional Lorentzian radical signal, with the same ZFS parameters for the triplet as used for the trESR simulation ($D = 47.9$ mT, $E = 1.0$ mT) and a line width of 1.3 mT. b) Power dependence of total PL and ODMR (triplet and doublet features) for the same powers as used in a). Total PL is in red, left axis, circles; ODMR triplet peak ΔPL (366 mT) is in blue, right axis, triangles; Doublet due to radicals (342 mT) is in green, right axis, squares. The lines are fits of PL or ΔPL $\propto$ (incidentpower)^m with m=0.97 for the total PL (red dotted line), m=1.95 for the triplet ODMR peak (blue dashed line), and m=0.56 for the ODMR doublet signal (green dash-dot line). The fits demonstrate that they are in the linear, quadratic, and sub-linear regimes respectively.

Figure 4.30 reports optically detected magnetic resonance (ODMR) with the effect of microwave absorption/emission detected via changes to the photoluminescence. This gives a very sensitive handle to explore the photoluminescence that results from paramagnetic species, especially triplets[236]. At 50 K, we observe a characteristic triplet

spectrum in phase with the microwaves, which matches the magnetic field positions of the trESR signal. The signal is positive, indicating an increase in photoluminescence with microwaves on relative to microwaves off. This polarisation is consistent with thermalisation of the populations in the triplet sublevels, i.e. a Boltzmann distribution, as observed in ODMR of non-geminate triplet-triplet annihilation (TTA) in TIPS-tetracene[237].

ODMR was carried out with a different resonator to trESR, which required re-mounting the sample. Care was taken to orientate the sample as close to the same angle relative to the B_0 field as possible, and the ODMR measurements were intended to be taken with the sample at 0° to the B_0 field. However, the shape of the ODMR spectrum, especially the sharp edge to the Z/Z' outer wings, indicates that the sample was likely to be closer to the orientation of 45° shown in Figure 4.15a.

The main peaks scale quadratically with excitation density, indicating that they arise from a bimolecular process – i.e. non-geminate TTA. This power dependence demonstrates that there is a radiative bimolecular decay pathway. We note that the central negative transition is consistent with a sub-population of radical doublets undergoing triplet-radical annihilation (TRA), scaling sub-linearly with excitation density, indicating that TRA is not the dominant loss process. The observed doublet signal is consistent with a small degree of charge formation and accumulation. The doublet peak has a small integrated area in comparison to the main peaks – indicating only a minor contribution from TRA relative to TTA.

The central doublet peak in the ODMR changed over time as the sample was irradiated with a 532 nm CW laser. Initially it was a positive peak, which quickly turned negative and then remained approximately constant. The power series data shown in Figure 4.30 was taken between the 22 hours purple spectrum and the 26 hours green spectrum in Figure 4.31, when there is only a modest increase in the magnitude of the doublet signal. The triplet peaks were unchanged throughout, so we attribute the doublet peak to a low density of light-induced, persistent charges which can undergo TRA.

By varying the microwave modulation frequency f_M we can learn about the characteristic timescale of triplet-triplet annihilation (Figure 4.32). As the modulation frequency f_M was increased to 100 kHz, the limit of the lock-in amplifier, we observed a decrease in signal strength of around 40%. At $f_M^* = 3$ kHz, half of this 40% drop has occurred. Using the equation $\tau = \sqrt{3}/(2\pi f_M^*)$, we calculated a timescale of ∼100 µs for 40% of the non-geminate TTA[237]. The remaining 60% occurs on a timescale faster than 3 µs, which we could not resolve due to the frequency limitations of the lock-in

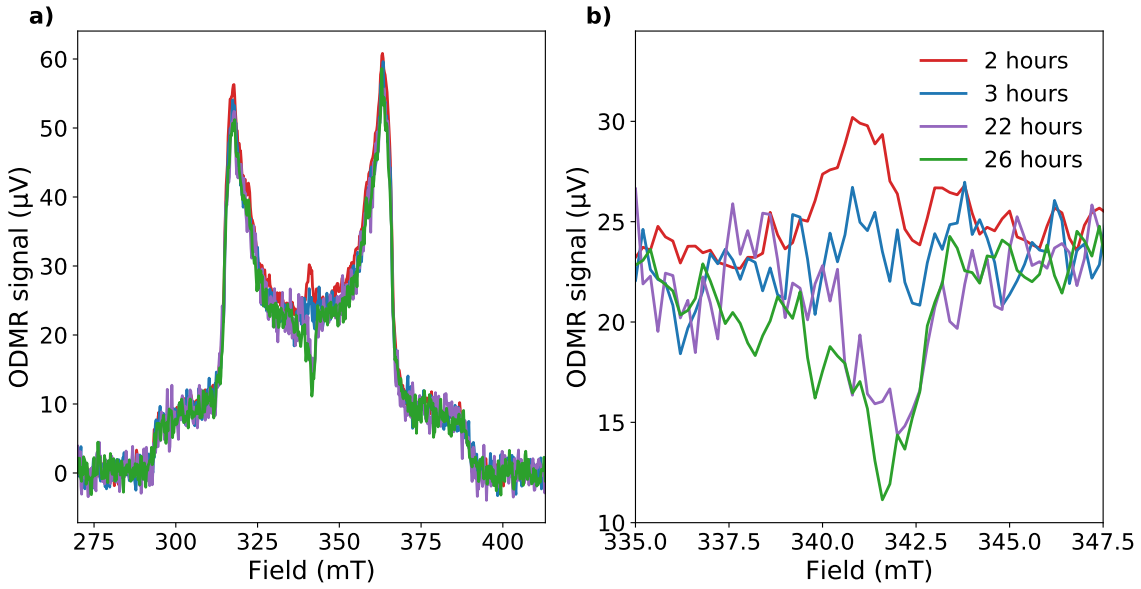

Fig. 4.31 Evolution of ODMR spectrum over time with 36 mW 532 nm CW excitation. Light-induced accumulation of persistent charges affects the central doublet peak.

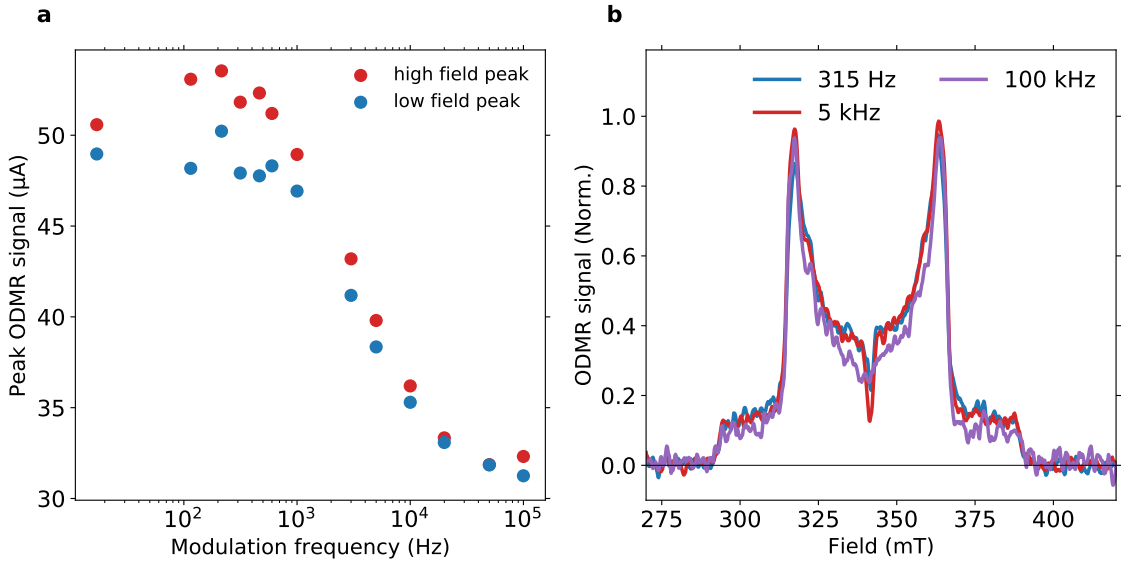

Fig. 4.32 a) Dependence of the intensity of low field (317.5 mT) and high field (363.5 mT) ODMR peaks on modulation frequency, at 36 mW CW 532 nm excitation. b) Comparison of ODMR spectra at different modulation frequencies, showing no change in polarisation of the signal at different timescales.

amplifier. The 100 µs component occurs on a timescale that we assume, from the trESR (Figure 4.22), is longer than the spin-lattice relaxation time, T_1, meaning the spin populations have depolarised and the sublevels will be occupied in a Boltzmann distribution, giving a positive ODMR signal from non-geminate TTA. However, the contribution from a timescale faster than 3 µs, which is faster than the estimated T_1 (on the order of 10 µs - Table 4.2), should originate from a non-Boltzmann population of the triplet sublevels because in the trESR we observe a spin polarised triplet up to 15 µs in time (Figure 4.22). Nevertheless, the ODMR spectrum and its polarization do not change with modulation frequency. The mechanism by which non-geminate TTA can generate this signal when not in a Boltzmann distribution remains an open question.

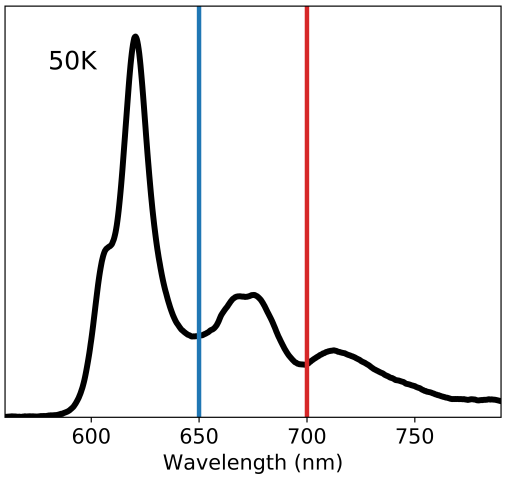

Fig. 4.33 100% TTBP photoluminescence spectrum at 50 K with the positions of the short pass (blue line) and long pass (red line) filters shown.

Long pass and short pass filters allowed coarse spectral resolution, and we confirmed that the lowest energy peak has a stronger contribution from triplet-triplet annihilation than the higher-energy peak (see Figures 4.33 to 4.35). This is in agreement with the time-resolved photoluminescence, where the delayed spectrum is more red-shifted than the prompt photoluminescence. We consider that the distinct spectral feature at 720 nm could be due to a specific geometric orientation of a pair of TTBP molecules. It has been shown in TIPS-tetracene that emission from triplet pairs with strong exchange coupling is red-shifted relative to that of weak coupling[177], so this feature could be attributed to very strongly coupled pairs. This would likely originate in pairs of molecules that

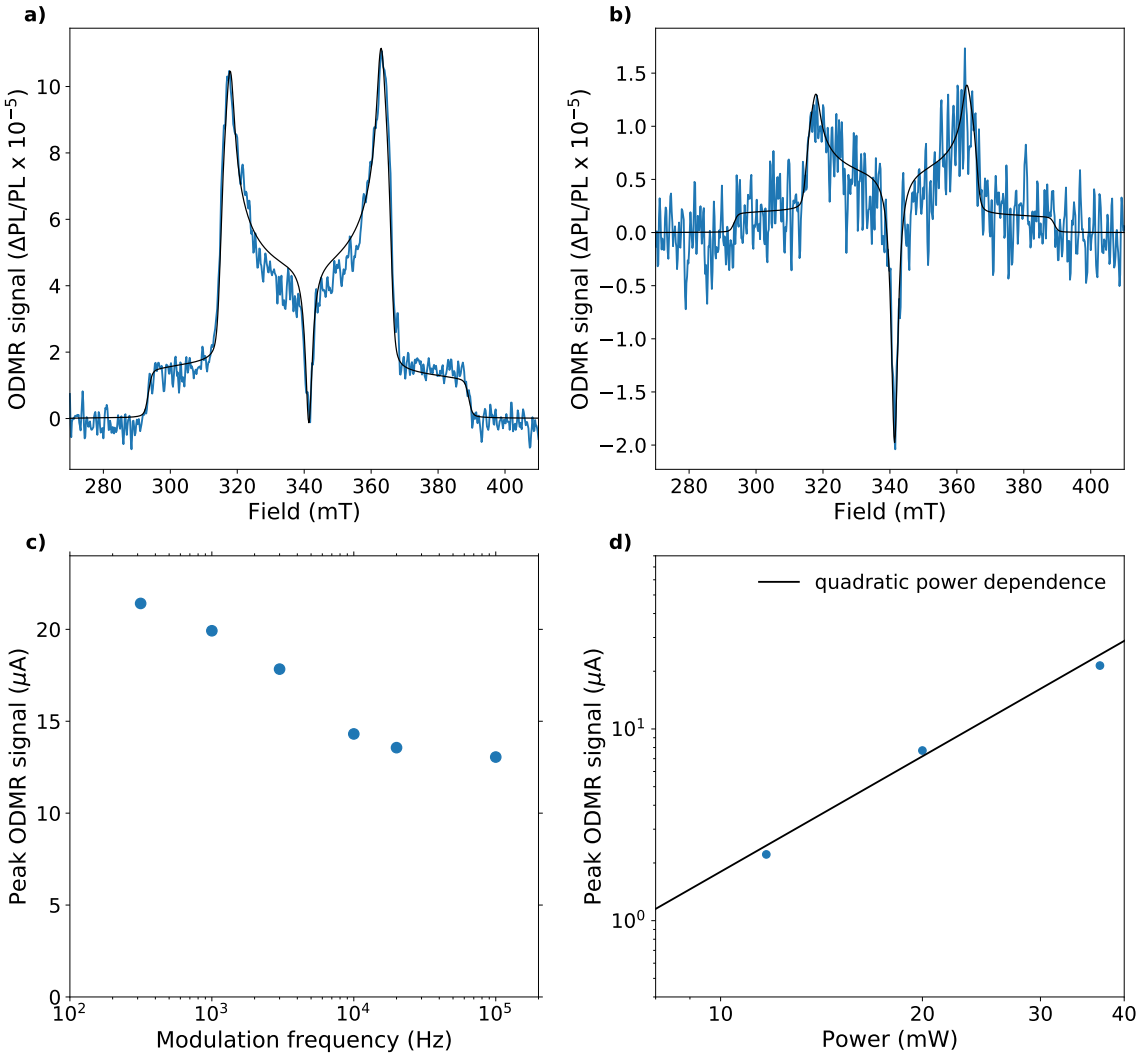

Fig. 4.34 ODMR using 650 nm short pass filter. a) ODMR signal at 36 mW CW 532 nm excitation, with simulation shown in black using EasySpin[233], with a thermal population at 50 K, the same D and E as for the trESR simulations ($D = 47.9$ mT, $E = 1.0$ mT) and linewidth = 1.3 mT. b) ODMR signal at 12 mW CW 532 nm excitation, with simulation shown in black. c) Dependence of peak ODMR signal on modulation frequency of the microwaves. d) Power dependence of the peak signal with a quadratic fit shown in black.

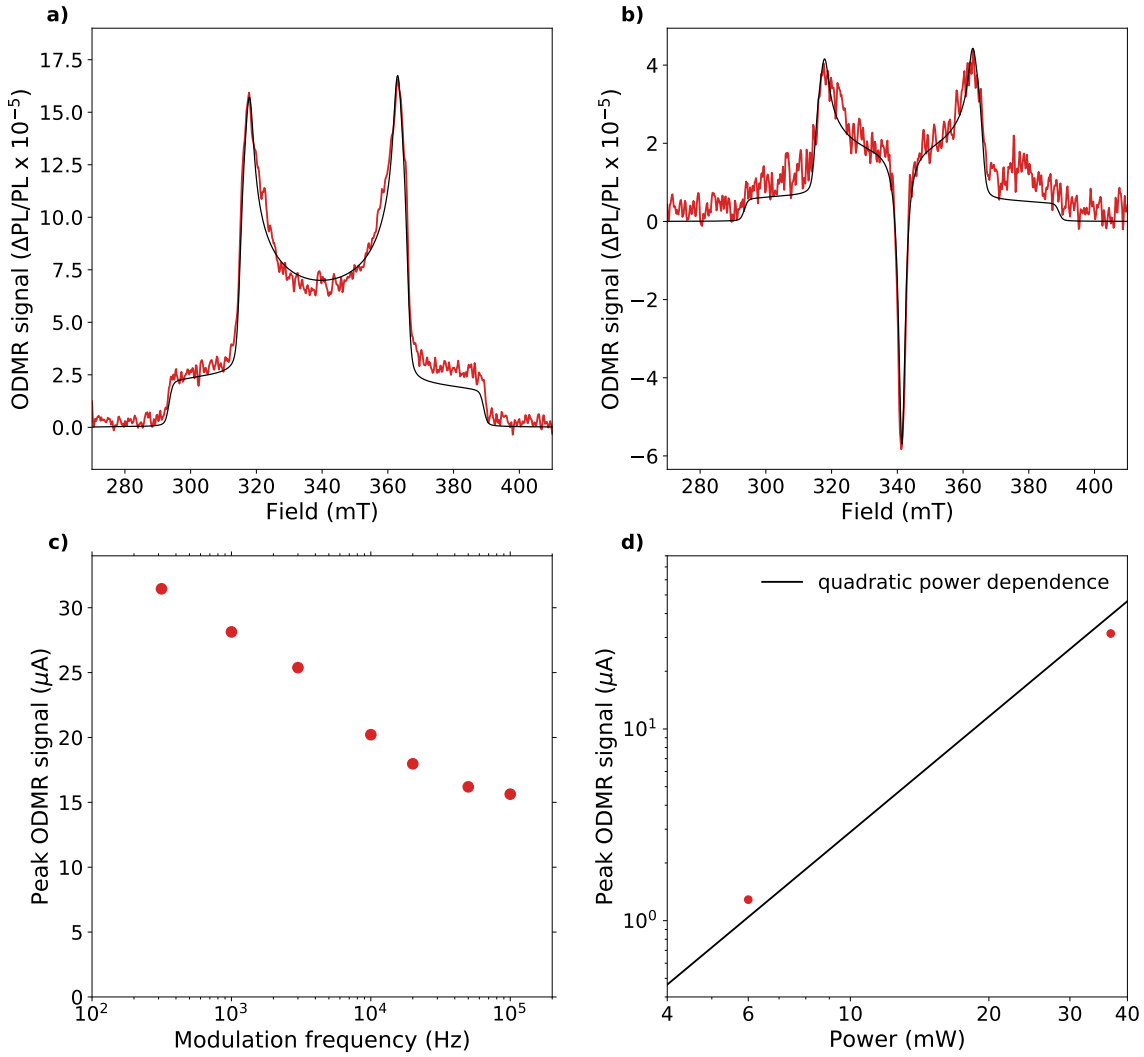

Fig. 4.35 ODMR using 700 nm long pass filter. a) ODMR signal at 36 mW CW 532 nm excitation, with simulation shown in black using EasySpin[233] with a thermal population at 50 K, the same D and E as for the trESR simulations ($D = 47.9$ mT, $E = 1.0$ mT) and linewidth = 1.3 mT. b) ODMR signal at 12 mW CW 532 nm excitation, with simulation shown in black. c) Dependence of peak ODMR signal on modulation frequency of the microwaves. d) Power dependence of the peak signal with a quadratic fit shown in black.

are slip-stacked face-to-face at 3.5 Å, consistent with the crystal structures reported by Müller et al.[230], notably closer than any pair in the TIPS-tetracene crystal structure[177].

4.9 Discussion

The unique photo-physics of TTBP are particularly well-suited for the thermodynamic requirements of enhancing photovoltaics by singlet exciton fission. The general scheme for such an enhancement is to arrange that triplet exciton pairs photogenerated in a wider gap organic semiconductor can be transferred to a lower gap inorganic semiconductor solar cell, where they each generate electron-hole pairs. Schemes developed in the literature include triplet transfer to luminescent PbS quantum dots that generate photons that can be absorbed by a silicon cell[191] or by direct energy transfer of the triplet exciton through an interface with silicon[188]. Endothermic fission maximises the energy of the triplets produced, and also ensures that interconversion of singlet excitons and triplet exciton pairs is reversible.

In a single film, as studied in this work, where triplets are not extracted to a lower gap solar cell (equivalent to "open circuit" conditions), the only available radiative decay channel will be through TTA (noting that phosphorescence is strongly forbidden). We think of the singlet fission system as a "black box": photons enter the system, and either triplets are extracted, photons are extracted, or the excitations are lost. In a single film ("open circuit" operation) where no triplet excitons are extracted, we can observe what the decay pathways are for triplets and therefore what the loss pathways will be where voltage would be lost when the material is operating in a device. 100% efficiency of photons being re-emitted would indicate the highest possible operating efficiency with zero non-radiative losses[238]. The material property of zero (in the ideal case) or low (in the case of TTBP) non-radiative losses applies whether in a single film ("open circuit") or under PV operating conditions in a working device. In the analogous situation for charges in silicon or GaAs, non-radiative voltage loss is described by Ross as $-\frac{kT}{q}ln(\phi)$, where ϕ is the electro- or photo-luminescence quantum efficiency[239–241]. ϕ must be maximised to eliminate non-radiative charge recombination in a single-junction solar cell. For singlet fission, ϕ must be maximised to eliminate non-radiative triplet decay pathways. We propose that the high PLQE of TTBP provides an important direction for the future development of singlet fission solar cells.

A further virtue of the TTBP system is a remarkable improvement in stability we find under illumination in ambient conditions compared to standard linear acenes (Figure 4.5 shows the degradation relative to that of a representative solution-processable acene

derivative, TIPS-tetracene). In combination with the high luminescence yield, this provides a very attractive route to enhance the efficiency of solar cells.

4.10 Conclusion

In this chapter we have used the molecule TTBP to show that benzannulation of acenes is a viable route to more stable singlet fission materials, as TTBP is much more stable than pentacene or tetracene and still undergoes fission. Through a combined analysis of the transient absorption, time-resolved photoluminescence, trESR and ODMR, we have built a detailed picture of the photophysics of TTBP, where triplet pairs are formed rapidly in quantitative yield and later separate by a temperature-activated process. We have shown efficient radiative decay of triplet pairs as singlet excitons through geminate TTA of bound pairs, or through non-geminate TTA of free triplets. In addition, we have used transient absorption to show that in the solid state, singlet fission is rapid and occurs at approximately quantitative yields.

We used trESR to probe the spin-physics of the TTBP system, and discovered that the films we measured have a preferential orientation that must be accounted for. We observed the temperature-dependence of triplet pair separation, and using ODMR, the non-geminate TTA of dissociated triplets. We also characterised the time-resolved photoluminescence, which through its red-shifting then blue-shifting peak illustrated the process of pair formation, dissociation, and annihilation.

TTBP is unique among efficient endothermic fission systems to have a high PLQE of 20% in the solid state. We demonstrate that this is a result of TTA, and indicates an unusually suppressed non-radiative decay of triplets. Non-radiative decay pathways are parasitic in a working solar cell, and so we argue that the PLQE, as a proxy for the contribution of non-radiative decay, should be considered when assessing potential singlet fission materials. While TTBP itself does have drawbacks, such as the inhibited dissociation of triplet pairs, the benzannulation of acenes shows much promise as a route to using singlet fission to surpass the single-junction limit in solar cells.

Chapter 5

Exploiting Excited-State Aromaticity to Design Stable Singlet Fission Materials

Singlet fission is a characteristic reserved for only a handful of organic molecules due to the requirement for the lowest excited triplet state to have approximately half the energy of the lowest excited singlet state. Of known examples, this is typically achieved by increasing ground state diradical character with the undesirable consequence of reducing ambient stability. In this chapter, we exploit Baird's rule of excited state aromaticity to manipulate the singlet-triplet energy gap and create novel singlet fission candidates. Inclusion of a [4n] 5-membered heterocycle in the resonance structures promotes triplet aromaticity, which stabilises its energy relative to the singlet excited state. We report a family of derivatives of indolonaphthyridine with highly tuneable excited state energies that undergo singlet fission whilst exhibiting excellent ambient stability due to the delocalised nature of the triplet excited state. We also report a strong morphology dependence for singlet fission in these materials, with fission only occurring at geometrical hot spots. We extend our study to show evidence of intramolecular fission in covalent dimers of indolonaphthyridine when the coupling strength across the linker is large enough and the solvent environment is sufficiently polar. Wider theoretical analysis reveals a clear relationship between triplet aromaticity and a widening singlet-triplet energy gap, demonstrating a novel strategy for manipulating the exchange

energy in organic materials. Some of the findings presented in this chapter are published in paper [1] in the List of Publications.

The photophysical investigation described in this chapter were led by the author, and all transient absorption and time-resolved photoluminescence data were measured by the author. Kealan Fallon synthesized the molecules and characterised the crystal structures. Enrico Salvadori and Leah Weiss performed the transient electron spin resonance. Lissa Eyre measured the transient grating photoluminescence. Simon Dowland measured the photoluminescence quantum yields. The quantum chemical calculations of energy levels and NICS(1) aromaticity were performed by Alex Ganose, Chris Savory and Kealan Fallon.

5.1 Background and Motivation

Recent advancements in singlet fission have been materials-limited due to the rarity of molecules that meet the essential energetic requirement for the process, that the energy of the lowest triplet excited state, T_1, be approximately half the energy of the lowest singlet excited state S_1. Known systems include rylene dyes[112,113,116,242], polyenes[119,120,135], donor-acceptor polymers[138,243,244], and derivatives of the linear acenes, particularly tetracene and pentacene, which have become the focus of the field and are explored elsewhere in this thesis[72,75,77,80,83,95,96,102,103,165,166,228,245–247]. The low triplet energies of the acenes relative to the singlet are a function of their large diradical character, which compromises their chemical stability (e.g. pentacene must be stored in the dark under inert gas to avoid photocatalyzed dimerization[97] or oxidation[98]). Unfortunately, all established rationales behind synthesising organic molecules with large singlet-triplet energy gaps – such as migrating Clar's sextets or forcing open shell character – also involve cost to chemical stability as they result in highly reactive localised unpaired electrons. This can potentially be addressed with careful protection of the radical sites[131,248], but the synthetic difficulty remains a major barrier to exploring new design motifs. There is an urgent need for a simple design approach for materials that undergo singlet fission at no expense to stability.

In the ground state, Hückel's Rule rationalises the enhanced stability of cyclic systems with [4n+2] electrons and this concept of aromaticity is a fundamental pillar of chemistry[249]. Lesser known is Baird's Rule, which states that in an excited state (for example, T_1), cyclic systems with [4n] are aromatic and hence stablised[250,251], and has since been verified with modern quantum chemical calculations[252–254]. Here, we demonstrate the synthesis and characterisation of highly stable, tunable organic

materials which undergo singlet fission through exploitation of Baird's aromaticity of the triplet excited state.

5.2 Materials and Steady-state Characterisation

In our investigation into designing fission materials using excited-state aromaticity, we focus in particular on derivatives of indolonaphthyridine benzene or *Cibalackrot*[255] (Figure 5.1a), which has previously been proposed as a singlet fission candidate[79]. Density functional theory (DFT) calculations (B3LYP/6-311G**) reveal *Cibalackrot* to possess a low-lying triplet state with $E(T_1)/E(S_1) \approx 0.5$, affirming its potential for singlet fission. This stabilised triplet state has been previously explained through the stabilised diradical nature of the indigo core[79,256]. It can likewise be rationalised using Baird aromaticity, due to the presence of [4n] contribution in its resonance structure (Figure 5.1a). The family of materials investigated below (Figure 5.1b) has been designed to investigate whether the indolonaphthyridine chromophore does indeed undergo singlet fission and whether contributions from an aromatic triplet state enhance chemical stability. These indolonaphthyridine thiophenes (INDTs) were synthesized by Kealan Fallon. Hereafter, we will refer to them as X-INDT where X is the atom or functional group installed at the 6,6'–positions of the INDT C6 ring (see Figure 5.1b).

The solution steady-state absorbance spectra (Figure 5.1c) demonstrate the optical tuneability of this family. H-INDT and F-INDT display comparable absorbance with λ_{max} of 602 nm. Both Cl-INDT and Br-INDT exhibit red-shifted but otherwise identical line shapes with λ_{max} of 615 nm. The addition of each carbonitrile group narrows the optical band gap of the material significantly, yielding λ_{max} of 635 nm for the mono- and λ_{max} of 650 nm for the di-carbonitrile compound. The energies of the S_1 and T_1 states of these materials were calculated using time-dependant density functional theory (TD-DFT) by Alex Ganose, Chris Savory and Kealan Fallon. The results suggest that they all possess the relationship of $2T_1 < S_1$ required for singlet fission (Figure 5.1d). These calculations reproduce the observed tuneability of the optical energy gap. Moreover, the calculated ratios of $E(T_1)/E(S_1)$ reveal that this parameter, and thus suitability for singlet fission, can be tuned through chemical substitution. The aromaticity of the five-membered (C5) ring in the triplet state was also assessed using nucleus-independent chemical shift (NICS(1)) calculations 1 Å above the plane of the ring[257]. The NICS(1) results for CN-INDT are shown in Figure 5.1e and demonstrate how the aromaticity in the C5 ring is significantly increased in the triplet state in

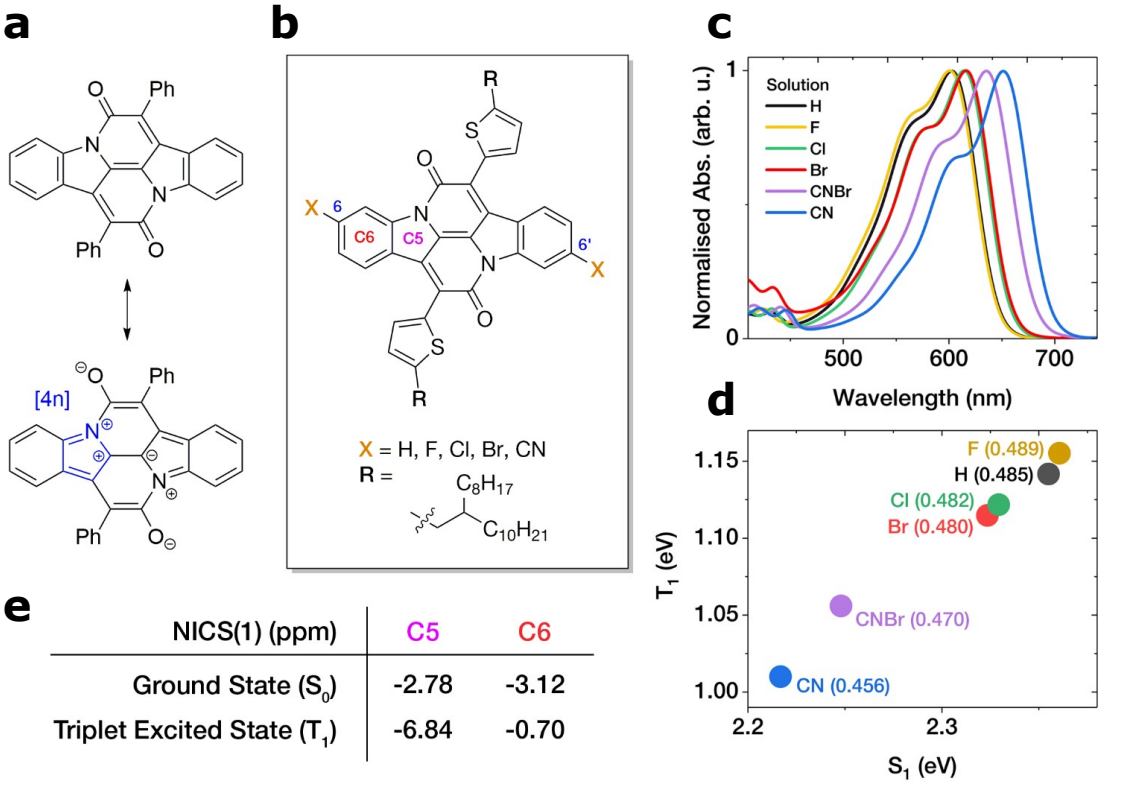

Fig. 5.1 Properties of indolonaphthyridine thiophenes. a) Cibalackrot (top) and its resonance form (bottom) showing a [4n] cyclic component (blue). b) The chromophore indolonaphthyridine thiophene (INDT) with labelling of the five (C5) and six (C6) membered rings, the substitution at the 6,6' positions and the species of solubilising alkyl chain (R, 2-octyl-1-dodecanyl). c) Solution steady-state absorbance spectra of the synthesised materials recorded in chloroform. d) Theoretical energies (eV, TD-DFT/TDA at B3LYP/6-311++G**) of S_1 and T_1 relative to the ground state with the ratio of these values given in brackets. e, Nucleus independent chemical shift calculations 1 Å above the molecular plane (NICS(1)) for CN-INDT, where a more negative value denotes a greater degree of aromaticity. The TD-DFT and

accordance with Baird's rules. We note that the use of TD-DFT for the prediction of triplet state energies is often problematic[258]. However, whether the predicted values for the $E(T_1)/E(S_1)$ ratio may be over- or underestimated as a whole, the key trends – tuneability of the ratio and its relation to triplet-state aromaticity – should remain robust. Indeed, these values are best taken as a guideline, since incorporation into the solid state inevitably alters the energetic structure to some degree.

In thin films (Figure 5.2), which are prepared by spin-coating from 50°C solutions in chloroform or chlorobenzene (the latter generally favoured for transient absorption measurements as it creates smoother films), all materials except H-INDT exhibit broader absorption and blue-shifted λ_{max} over 500–550 nm. These shifts indicate significant intermolecular interactions between chromophores, here consistent with predominantly H-type exciton coupling[35]. Large planar molecules such as these exhibit a propensity to aggregate through strong π-stacking[8]. The large branched alkyl side chains attached to the out-of-plane thiophene moieties suppress this coupling to a degree and minimise the stabilisation of S_1 in the solid state, which can unfavourably disrupt the energetic balance for singlet fission[79,256]. Despite the broad and variable lineshapes, we note that the thin-film absorption onsets display similar trends to the solution measurements.

H-INDT behaves differently than the rest of the materials in two ways. Firstly, when spin-coated, particularly at high spin speeds (>2000 rpm), it does not immediately form the thermodynamically favoured morphology. The absorption blue-shifts over a period of weeks, as shown in Figure 5.3. Secondly, the absorption peak of the day 0 spectrum is red-shifted with respect to the solution, while the other materials are all blue-shifted. This indicates J-type exciton coupling is present in H-INDT. Despite the apparent differences in absorption lineshape between old spin-coated or drop-cast films, we did not detect any difference to the photophysics via transient absorption or time resolved photoluminescence (PL).

5.3 Evidence for Singlet Fission

5.3.1 Long-time Transient Absorption

We investigated the ability of INDT films to undergo singlet fission using time-resolved optical and spin-resonance techniques. In transient absorption spectroscopy, the sample is excited with a short laser pulse and then interrogated with a broadband probe pulse at a controllable time delay (100 fs to 1 ms). Transient absorption spectra acquired

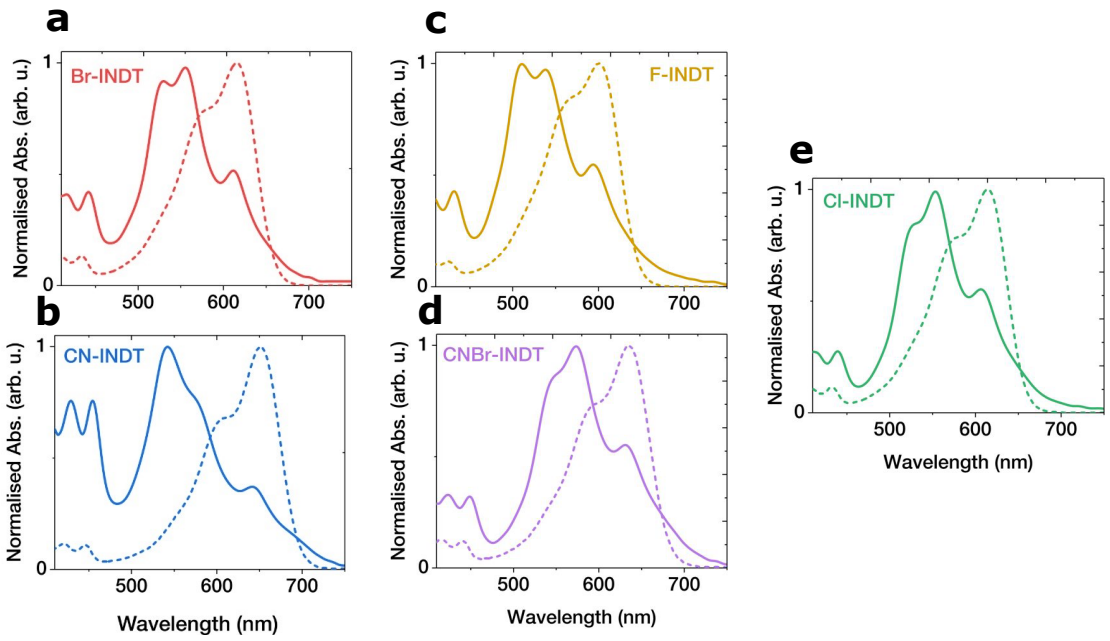

Fig. 5.2 Steady-state absorption spectra of a) Br-INDT (red), b) CN-INDT (blue), c) F-INDT (yellow), d) CNBr-INDT (purple), and e) Cl-INDT (green). Thin-film spectra shown in solid lines (spin-coated from 5 mgml^{-1} solutions from chloroform) and dilute solution (chloroform) spectra shown in dashed lines.

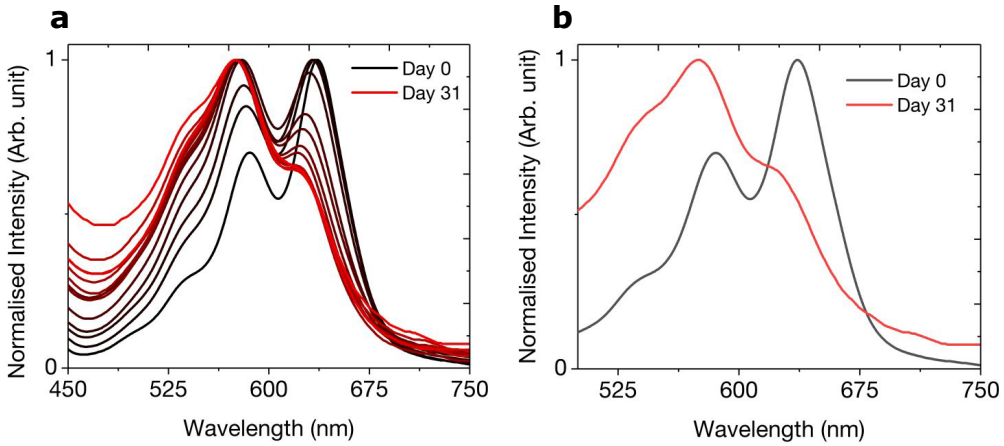

Fig. 5.3 Normalised steady-state absorption spectra of H-INDT showing the change in film morphology from as spun (black) to after 31 days (red). The two morphologies could be isolated by controlling spin coating film formation speeds - with slower speeds or drop-casting producing the thermodynamically favoured red spectrum. Both morphologies behaved identically with regards to their transient absorption spectra.

using a ns-resolution set-up ($\lambda_{exc} = 532\,\text{nm}$) are shown in Figure 5.4 for thin films of the six X-INDT candidates.

As shown in Figure 5.4, we observe a distinct, persistent photoinduced absorption (PIA) band in all of the X-INDTs except H-INDT, at ∼640 nm in F-INDT, ∼680 nm in Cl- and Br-INDT, ∼715 nm in CN/Br-INDT, and ∼740 nm in CN-INDT. This species, which persists out to the µs time scale with little spectral evolution, could only originate from charges or triplet excitons due its long lifetime. Triplet sensitization in solution (green dashed) yields a similar spectral signature, after taking into consideration the difference in underlying ground-state bleach (GSB) and a slight red-shift of the $T_1 \rightarrow T_n$ transition in the solid state which is consistent with other organic systems[120,135,259]. Thus, we assign this µs excited-state absorption to triplet excitons. This is further confirmed via electron spin resonance (ESR), discussed below. Figure 5.5 shows the kinetic evolution of the triplet PIA, with a lifetime of 3–6 µs in Br-, CN-, Cl- and CNBr-INDT, while in F-INDT the spectral signature we attribute to triplets decays faster, with a lifetime of 300 ns. There is also a shorter lived component to the triplet signature in CN-INDT, of 250 ns in addition to a 3 µs component.

In contrast to the rest of the materials, we do not find any evidence for triplets in H-INDT. The primary signature we observe in H-INDT after ∼3 ns is a set of positive peaks that match the ground-state absorption and can be assigned to bleaching of the ground state. These are accompanied by a weak photoinduced absorption ($\Delta T/T < 0$) from 650 nm to the near-infrared which decays on an instrument-limited time scale (in the ns-resolution set-up) and is assigned to the singlet state. There is no triplet-like absorption in this film, nor any significant long-lived electronic states in this film. The positive features that outlive the photoinduced absorption are instead an artefact due to thermal modulation of the absorption and reflectivity and are commonly observed in measurements in the ground-state absorption region[73,112,131,224]. In Section A.1 of Appendix A we go in to more detail on the thermal artefacts present in these materials.

5.3.1.1 Triplet Sensitisation

Triplet sensitisation in solution was performed, also using the ns-resolution transient absorption set up. We measured mixed solutions of the triplet sensitiser N-Methylfulleropyrrolidine ($0.3\,\text{mgml}^{-1}$) and X-INDT ($0.1\,\text{mgml}^{-1}$) in 1 mm path length cuvettes, following the same method as Chapter 4. The solutions were excited using ∼1 ns pulses at 355 nm to excite the sensitiser, which quickly undergoes intersystem crossing from singlet to triplet. The triplets then transfer from sensitiser to X-INDT mediated by molecular diffusion over 5-10 µs, after which the transient absorption

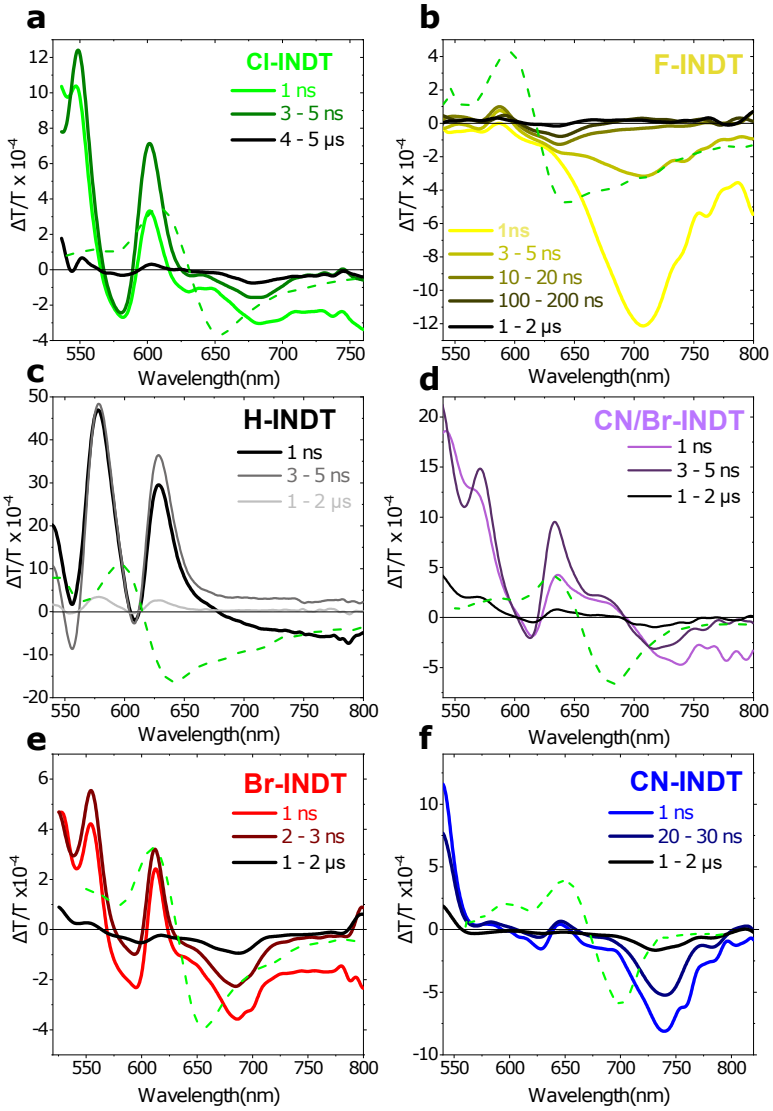

Fig. 5.4 Long-lived triplet excitations in INDT films. Transient absorption spectra acquired on ns-µs timescale following 1 ns excitation pulses at 532 nm of spin-coated films of a) Cl-, b) F-, c) H-, d) CN/Br-, e) Br- and f) CN-INDT. Corresponding decay kinetics and spectra acquired over a broader probe range are presented in Figure 5.5. Solution triplet signatures shown as green dashed line obtained by sensitisation experiments (Figure 5.6).

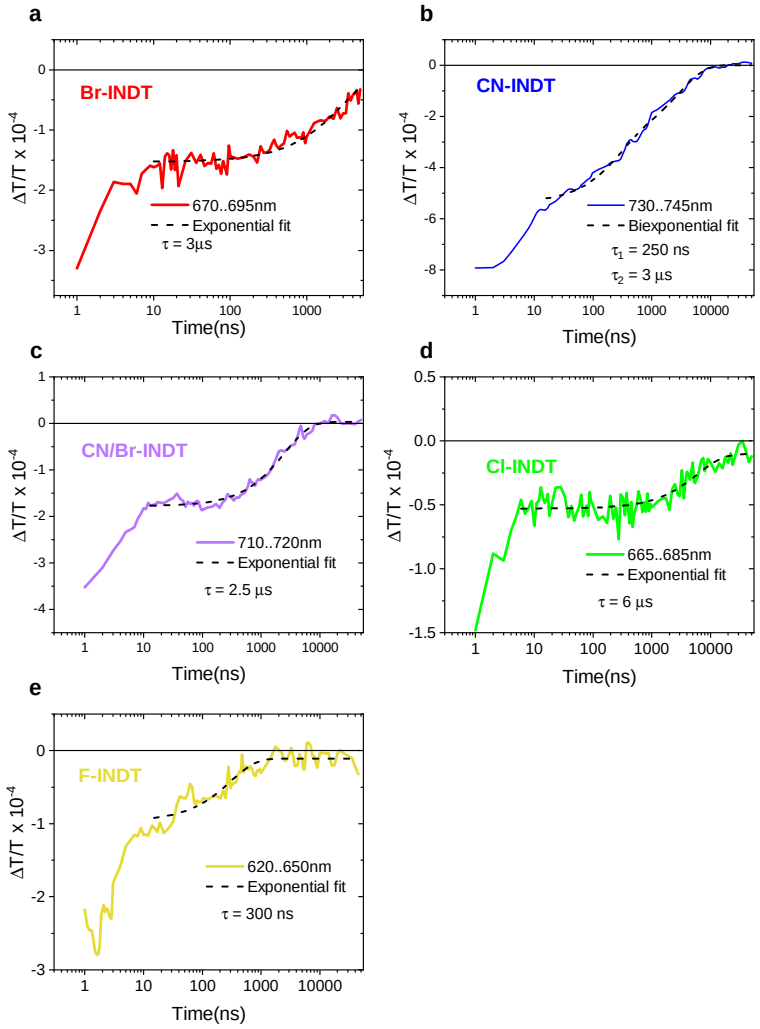

Fig. 5.5 Kinetics for triplet photoinduced absorptions in transient absorption experiments on spin-coated films of a) Br-, b) CN-, c) CN/Br-, d) Cl- and e) F-INDT. Monoexponential fits are shown for all but CN-INDT, which is best described with a biexponential kinetic.

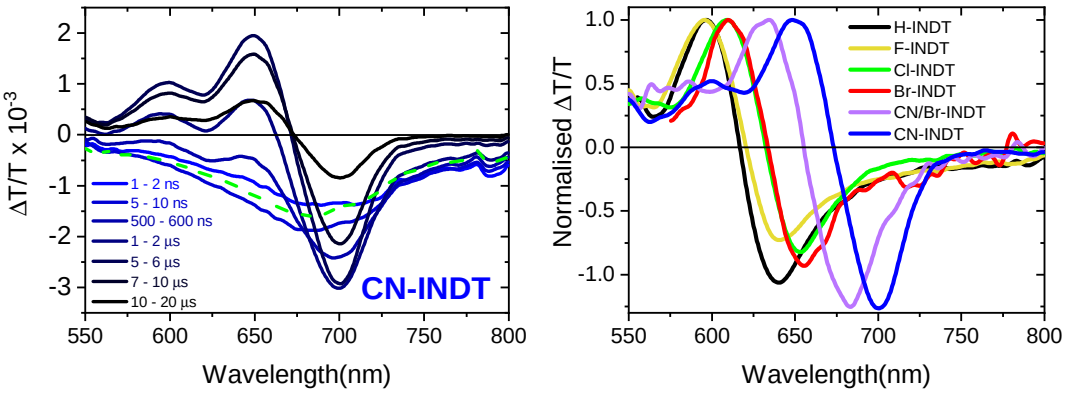

Fig. 5.6 a) Spectral slices of the solution triplet sensitisation of CN-INDT using a fullerene sensitiser (NMFP), showing time evolution (blue to black) from fullerene triplet to CN-INDT triplet and then decay of CN-INDT triplet. Green dotted line shows the pure fullerene solution triplet spectrum for reference. b) Triplet spectra for each of the X-INDT, taken at 10–20 µs after excitation of the fullerene.

spectrum shows purely X-INDT triplets on isolated molecules. The zero-field splitting parameters extracted from trESR (Table A.1) do not change from solution to film, confirming that triplets are not delocalised on multiple molecules in films, which is an encouraging sign that this reference spectrum should be close to that in the film. However, the triplet absorptions seen in sensitisation are blue-shifted compared to the film, which we attribute to overlap with a different underlying ground-state absorption line shape and possible aggregation effects in the solid state (e.g. shifting of the higher-lying T_n state involved in the PIA transition)[120].

5.3.2 Transient Electron Spin Resonance

The ns-transient absorption measurements provide clear evidence of triplet formation, but it can be difficult to distinguish the formation mechanism – intersystem crossing or singlet fission – from these results alone. We therefore used transient electron spin resonance (trESR), which has been a powerful tool for investigating singlet fission materials[144,152,163,172,173], to characterise the sublevel populations of the triplet states. In frozen dilute solution, fission is inactive, so the zero-field sublevel populations of triplet states and the corresponding ESR polarisation pattern are attributed to intersystem crossing (ISC). The frozen solution trESR spectra of all of the X-INDTs exhibit emission/absorption polarisation patterns of EEEAAA, which is typical for ISC-generated triplets which preferentially populate T_x and T_y over T_z. In thin film,

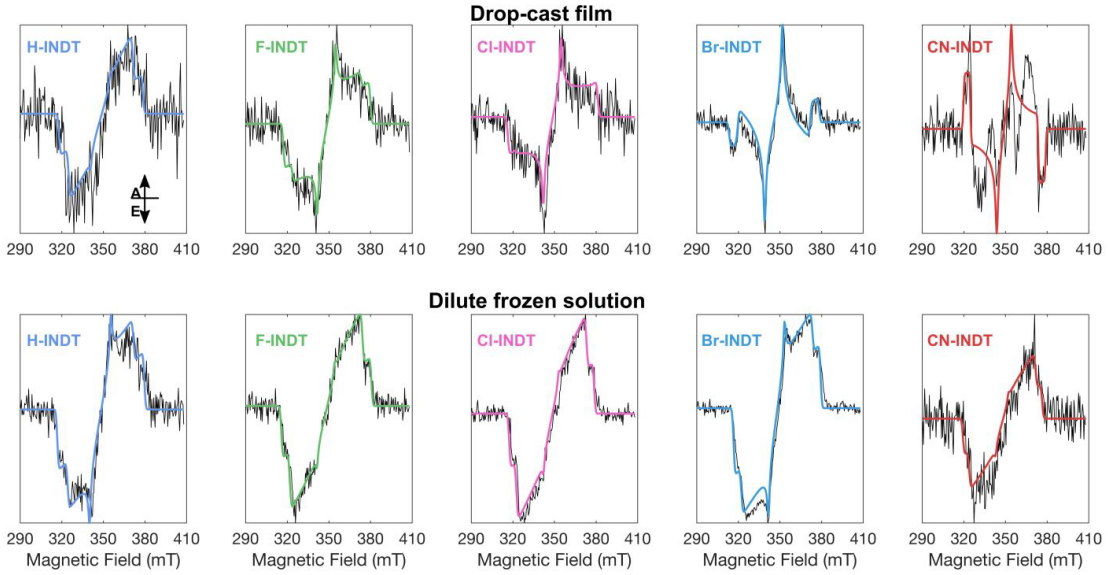

Fig. 5.7 10 K experimental trESR spectra of the INDT derivatives recorded in dilute frozen solution (bottom row) and drop-casted films (top row), black lines. The corresponding simulations are reported as coloured lines and the simulation parameters are summarized in the appendix in Table A.1. All simulations use an isotropic g-value (2.0023). Measurements and simulations by Enrico Salvadori.

singlet fission becomes possible and may out-compete ISC, in which case we expect to see changes in the polarisation pattern as a different formation pathway will populate the triplet sublevels differently.

The trESR measurements and simulations presented here were performed by Enrico Salvadori. There is a more detailed analysis in Appendix Section A.2, but we will summarise the important results here. The polarisation pattern of Br-INDT films is EAEAEA, which cannot be caused by the same intersystem crossing pathway as is active in dilute solution, but is also not characteristic of the overpopulation of T_0 high-field sublevel typically seen in fission-generated triplets[68,169]. We consider it likely that this is the result of the selective population of triplet sublevels in a triplet transfer process following the initial fission event. Given the ultrafast formation of the triplet PIA in Br-INDT shown below (Figure 5.9) and the absence of other potential mechanisms (for example we rule out a different ISC mechanism due to the effects of aggregation because the D parameter does not change), we attribute triplet formation in these films to singlet fission.

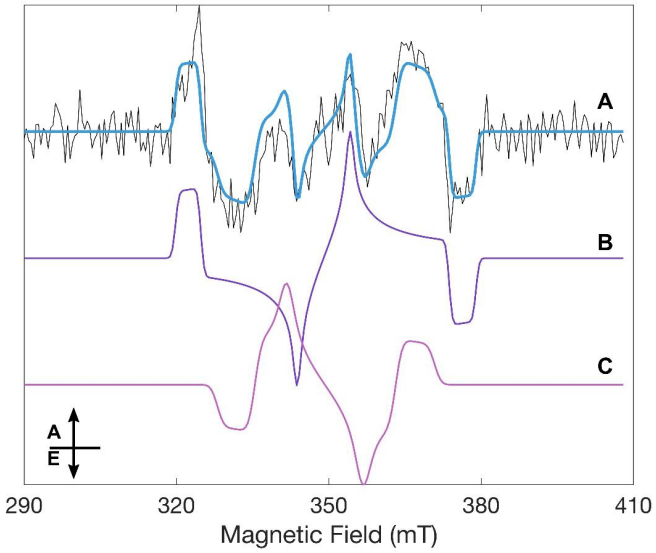

Fig. 5.8 10 K experimental trESR spectrum of CN-INDT film, with a two component simulation, measured and simulated by Enrico Salvadori. Simulation is a sum of components A and B, both of which show the T_0 sublevel is preferentially populated in high-field, compatible with singlet fission and incompatible with ISC (component A: D = +830 MHz, |E| = 180 MHz; component B: D = –600 MHz, |E| = 60 MHz, see Appendix Section A.2 for more discussion)

The spectrum of CN-INDT, shown in Figure 5.8 is more complex – two components with different zero-field splitting parameters appear to be present. One component has zero-field splitting parameters similar to those observed in solution but with AEEAAE polarisation. The second has a smaller magnitude and negative D, and the inverse polarisation of the first component: EAAEEA (the inversion being a consequence of the negative D). Importantly, the AEEAAE polarisation pattern is a signature of triplet pairs formed via singlet fission, with an overpopulation of the T_0 sublevel[68,169,172,173]. We speculate that the second component could arise from ordered aggregates, as the smaller magnitude of D (-600 MHz compared to 830 MHz) indicates that the triplet can delocalise over more than one molecule[260]. It was not possible to simulate the signal with the presence of quintets.

In Cl- and F-INDT, although we have evidence from transient absorption of similar photophysics to CN- and Br-INDT, we were not able to observe any change in ESR polarisation from solution to film. We suspect that the cryogenic temperatures necessary to slow down spin-lattice relaxation for trESR measurements have suppressed singlet fission in these materials. TD-DFT calculations showed that CN- and Br-INDT were more exothermic for fission than Cl- and F-INDT, and if there was some systematic error present in those calculations, as there often is with TD-DFT, then Cl- and F-INDT could be narrowly endothermic.

On the basis of the direct trESR evidence of fission in Br-INDT and CN-INDT and the similar sub-ns triplet formation observed in Figures 5.9 and 5.12, we conclude that singlet fission is active in all of the reported X-INDT derivatives except H-INDT. In H-INDT, we see no evidence of fission in transient absorption or trESR, and given that this is the derivative with the lowest predicted energetic driving force for fission, except for F-INDT, this is not unexpected. In addition to less favourable energetics, H-INDT appears to form a different morphology to the other materials (Figures 5.2 and 5.3), which we consider is likely also a contributing factor to the absence of triplets seen in H-INDT.

5.4 Ultrafast Triplet Formation

For further insight into the mechanism of singlet fission, we examine the initial decay of S_1 in Br-INDT and CN-INDT using fs-ps transient absorption spectroscopy (λ_{exc}= 530 nm, 250 fs, 37 kHz repetition rate). Representative transient absorption spectra at a higher and lower excitation density are shown in Figure 5.9. At early times there is a broad PIA (ΔT/T<0) spectrally overlapped with the ground state absorption

(making the spectra highly congested in this region) and also extending into the NIR. From comparison of the steady-state absorption and photoluminescence spectra, we can attribute much of the complex structure of this spectrum to overlapping $\Delta T/T>0$ signatures from bleaching of the ground-state absorption and stimulated emission from S_1.

The dynamics of the loss of PIA that peaks at 850 nm are strongly dependent on excitation density. At high laser powers comparable with those used to measure ultrafast transient-grating photoluminescence[219] (Figure 5.10), the PIA decay is ∼7 ps. This rapid decay is likely due to singlet-singlet annihilation. This effect is not significant at the lowest excitation densities, where the later timescales agree well with the results from time-correlated single-photon counting (Figure 5.10). This agreement with photoluminescence measurements firmly establishes the initially decaying spectral features as signatures of S_1 and indicates that X-INDTs are similarly sensitive to singlet-singlet annihilation as perylenediimides[112].

As the strong S_1 PIA decays, the underlying triplet signal is revealed (685 nm in Br-INDT, 745 nm in CN-INDT), corresponding well with the ns-transient absorption experiment (Figure 5.4). Due to the overlapping signals, it is not possible to definitively distinguish the formation time of this signal, however, it is certainly present by 2-3 ps in CN-INDT, effectively ruling out the formation of these triplets from ISC. We calculate that the yield of triplets at 1 ns in CN-INDT, based on the solution cross sections of the $S_1 \rightarrow S_n$ and $T_1 \rightarrow T_n$ transitions, is approximately 60% (see Section 5.4.1 below on yield calculations).

Curiously, the triplet yield is not strongly affected by excitation density, despite the clear excitation density dependence of the S_1 lifetime. This is illustrated in Figure 5.11, where the ratio of the initial S_1 signal to 1 ns T_1 signal is unchanged from 9 to 180 $\mu J cm^{-2}$ per pulse. Based on this evidence, we propose a branching on very early timescales between populations capable and incapable of singlet fission. This is likely due to morphology, with a subset of 'hot spots' where triplets can be formed rapidly via singlet fission[166], and the resulting triplets are much less susceptible to annihilation due to their lower mobility. Importantly, singlet fission at hot spots in this system is completely outcompeting the singlet annihilation events that occur from Förster transfer on a ps timescale, and singlet fission is therefore likely to be occurring on sub-ps timescales. Meanwhile, a parallel population of singlets formed far from the hot spots cannot undergo singlet fission, but are mobile enough to show a strong excitation density dependence due to singlet-singlet annihilation. Indeed, preliminary measurements using different solvents or film-forming conditions reveal considerable

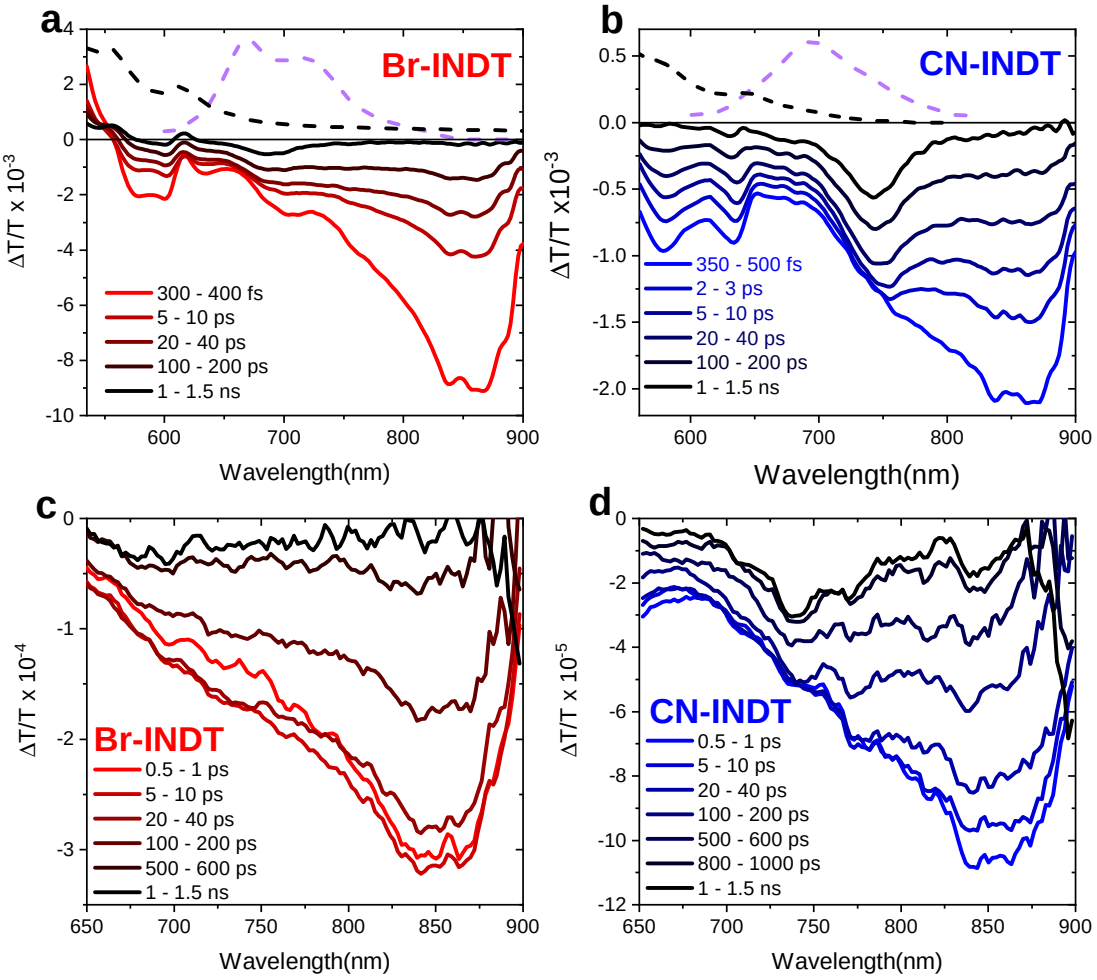

Fig. 5.9 Transient absorption spectra acquired on fs-ps timescale following 250 fs excitation for thin films of a),c) Br-INDT and b),d) CN-INDT. Dashed spectra show steady-state absorption (black) and photoluminescence (purple). a) and b) excitation fluence was 180 µJcm^{-2} and c) and d) excitation fluence was 9 µJcm^{-2}.

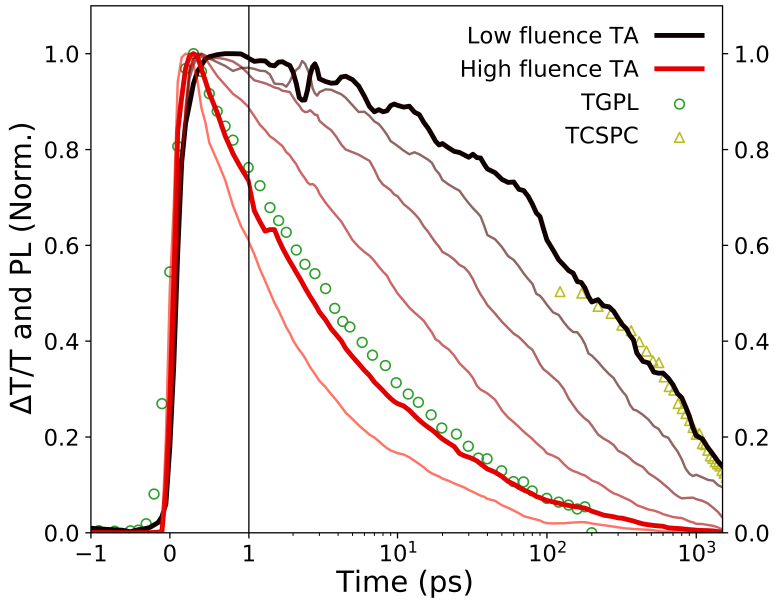

Fig. 5.10 Excitation-density-dependent transient absorption kinetics (lines) tracking S_1 features (860–880 nm), compared with transient grating photoluminescence[219] kinetics acquired at high excitation fluence (255 µJcm^{-2} per pulse, green open circles), and time-correlated single-photon counting kinetics acquired at low fluence (2 nJcm^{-2} per pulse, yellow open triangles). The rapid depletion of S_1 at high powers is due to significant singlet-singlet annihilation, and can be reproduced in transient absorption at the equivalent excitation density. S_1 decay measured by transient absorption at the lowest laser powers (biexponential: 58 ps and 990 ps) converges to the intrinsic lifetime observed in the low-power PL kinetics (1 ns). N.B. the instrument response for the low-fluence PL measurement is 300 ps and thus cannot capture the faster process. Transient-grating photoluminescence was measured by Lissa Eyre.

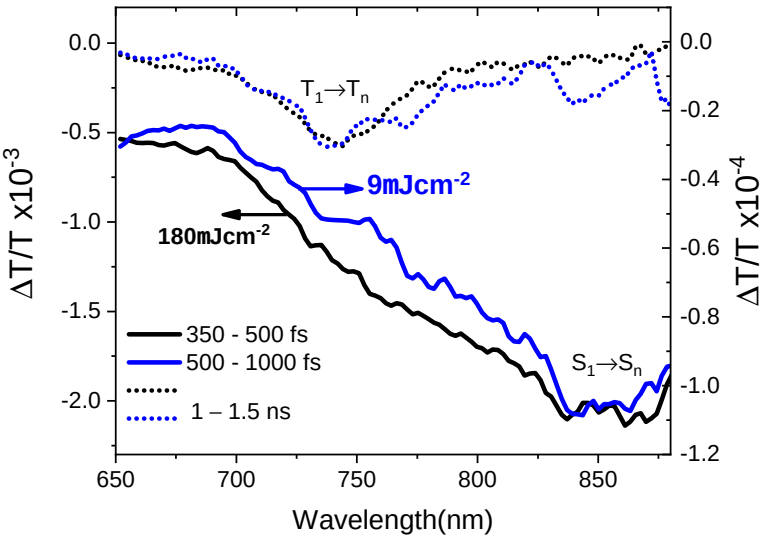

Fig. 5.11 Comparison of initial transient absorption signal, taken at the peak in time of the S_1 PIA at 850 nm, with the triplet signal at 1–1.5 ns for two different fluences: 180 µJcm^{-2} per pulse (black, left axis) and 9 µJcm^{-2} per pulse (blue, right axis), demonstrating that excitation density does not affect triplet yield in CN-INDT.

changes in photoluminescence quantum yield, suggesting the density of hot spots can be tuned through processing (Figure 5.20).

In Figure 5.9, short-time transient absorption spectra for Br- and CN-INDT are presented showing the decay of singlet PIAs and persistence of triplet PIAs. Figure 5.12 shows equivalent measurements for the remaining four molecules studied, H-, Cl-, CN/Br- and F-INDT. Cl-INDT shows similar evidence of singlet fission to Br- and CN-INDT, namely the appearance of the triplet PIA on very early timescales in coexistence with S_1. We see rapid evolution of the initial spectrum leading to a prominent PIA at 675 nm identical to the long-lived species (triplets) in ns-ms measurements. In this film the spectral signatures are sufficiently distinct that we can unambiguously confirm triplet formation is by singlet fission, occurring at a comparable rate to that in the CN- and Br-INDT samples.

In F-INDT, while we observed a small triplet signature closely matching the solution sensitisation in the long-time transient absorption (Figure 5.4b), this was much weaker than the triplet signals in the other materials. In the short-time transient absorption experiment we are unable to distinguish the triplet PIA at all, suggesting the triplet formation process is slower and/or less efficient. However, we note that F-INDT yielded the lowest quality films, with significant scattering and spatial variation. In films made

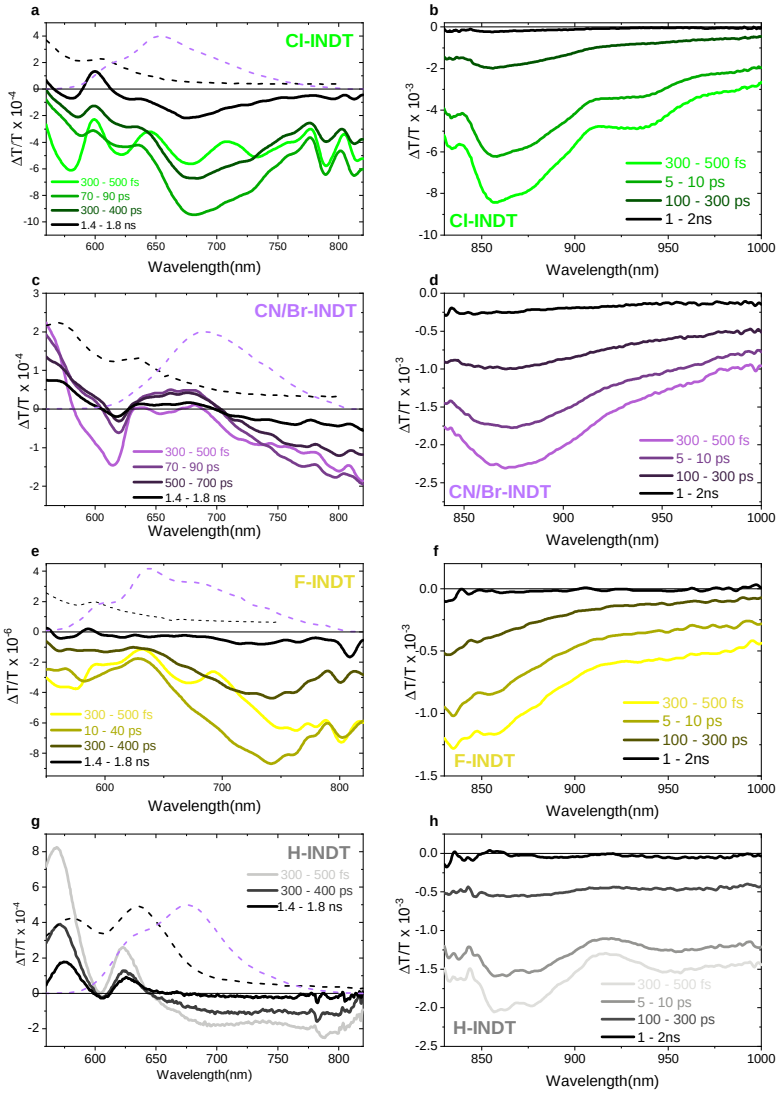

Fig. 5.12 Short-time transient absorption of Cl-INDT (a) and b)), CN/Br-INDT (c) and d)), F-INDT (e) and f)) and H-INDT (g) and h)), using a 530 nm pump and broadband NOPA probe in the visible region for a), c), e) and g), and the NIR region for b), d), f) and h).

using identical preparation protocols, F-INDT had the lowest optical density, meaning that the signal-to-noise ratio in transient absorption was poorest. We suspect that these factors contributed to our inability to detect triplet signatures in short-time transient absorption.

We also cannot unambiguously detect triplet formation in short-time measurements on CN/Br-INDT, due to the small signal strength and large amount of noise. However, the long-time transient absorption shows long-lived triplets which are formed within the time resolution (1 ns) of that measurement and so we interpret the broad residual signal in the short-time transient absorption to be triplets.

5.4.1 Triplet Yield in CN-INDT

As CN-INDT is the best-performing fission candidate according to our analysis, we will now look in more detail at estimating the triplet quantum yield in this material. Calculating the triplet yield in solid state is in general challenging, more so than when observing fission in solution[82,261], where reference sensitisation measurements are more accurate. One common technique is to analyse the kinetics of the PL in the presence (thin film) and absence (dilute solution) of singlet fission[112]. The critical assumption in this method is that the other underlying radiative and non-radiative decay rates do not change between film and solution, such that any difference in kinetics can be attributed to the presence of the new decay channel, singlet fission. In the case of CN-INDT films (and by extension, the other X-INDT derivatives), the parallel populations we describe between hot spots and other geometries means this approach is not suitable: the PL is dominated by a population of singlets which never undergo singlet fission, and hence cannot be used to calculate yield. Similarly, in some materials yields can be calculated by a kinetic model of transient absorption spectra rather than PL, by deconvolution of the singlet, triplet-pair, and free triplet spectra. Fitting the populations of these spectra to a kinetic model then provides a triplet yield. In systems like the X-INDTs with heavily congested excited-state absorption spectra, the deconvolution cannot be unambiguously performed and once again, the branching of the singlet population makes a kinetic-based method unsuitable.

With the limitations outlined above in mind, we present here a method for calculating triplet yield using the relative absorptions of the singlet photoinduced absorption (PIA) immediately upon photoexcitation, compared with the triplet PIA after approximately 2 ns, as utilized by many others previously[77,82,102,128,138,166,168,242,259]. To calculate triplet yield from these PIAs, we require the relative magnitude of the molar extinction coefficients for PIAs of the two states. First, to find the relative extinction

coefficient for the S_1 PIA at ∼850 nm, we measured the transient absorption of CN-INDT in dilute solution (0.09 mM), where the only excited state population present is singlets. In this measurement, shown in black in Figure 5.13, we can see the relative strength of the S_1 PIA at 850 nm and the GSB, which is indicative of excited state population.

As described earlier in Section 5.3.1.1, we also performed the same measurement for mixed solutions of N-methylfulleropyrrolidine (NMFP) and CN-INDT. NMFP undergoes quantitative ISC in a few nanoseconds, after which the triplets on NMFP transfer to CN-INDT, and therefore after approximately 1 µs we can observe the triplet transient absorption spectrum on isolated molecules in solution, which persists for ∼20 µs. Again, we can see that there is a GSB signal, proportional to the population of excited CN-INDT molecules. We take the CN-INDT triplet spectrum at 12–14 µs in order to avoid contributions from the overlapping NMFP triplet signature.

Solution singlet and triplet transient absorption spectra are shown in Figure 5.13, scaled to have equal GSB at the 0-1 absorption shoulder at 600 nm, such that they represent the signals for an equal concentration of singlets or triplets. The similarity of the shape of the GSB in this region suggests there are no major overlapping signatures (e.g. PIA or stimulated emission). By contrast, the very strong stimulated emission in the singlet state results in a markedly stronger, broader and red-shifted positive peak at the 0-0 position, meaning we cannot scale to this peak for this analysis. The ratio of the singlet PIA peak/triplet PIA peak from this figure is 2.18, and this ratio represents the relative magnitude of the molar extinction coefficients, ε, for singlet and triplet excitons on CN-INDT in dilute solutions.

As we discussed earlier, our measurements at different excitation fluences indicate there must be a branching on very early timescales between singlet excitons that are capable of very rapid fission and those that are not and are instead susceptible to singlet-singlet annihilation. Thus, the relative intensities of initial singlet and 1 ns-delay triplet PIA do not change over the full power range investigated, despite a substantial increase in singlet-singlet annihilation at high power. Taking the lowest fluence measurement where annihilation is minimized (9 µJcm^{-2} in Figure 5.9d), the 850 nm S_1 PIA at 0.5–1 ps has a magnitude of 1.08×10^{-4}, while the 740 nm T_1 PIA at 1–1.5 ns has a magnitude of 3.1×10^{-5}. The ratio of T_1/S_1 PIA intensity is 0.29, and this ratio was constant up to the highest fluence measured, 180 µJcm^{-2} (shown in Figure 5.11).

$$\eta = \frac{\mathrm{PIA}(T_1)}{\mathrm{PIA}(S_1)} \times \frac{\varepsilon(S_1)}{\varepsilon(T_1)} = 0.29 \times 2.18 = 63\% \tag{5.1}$$

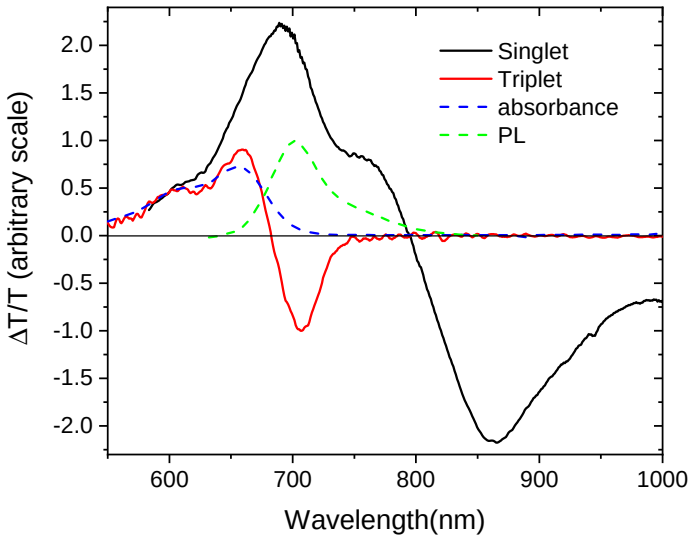

Fig. 5.13 CN-INDT solution singlet and triplet transient absorption spectra, scaled so the 0-1 ground state absorption bleach at 600 nm is equal. Dashed lines show the steady state absorption and photoluminescence of CN-INDT.

Applying the relative strength of the extinction coefficients (Equation (5.1)) results in a triplet yield, η, of 63%, or approximately 32% of singlets undergoing fission. It is then assumed that the remaining 68% of singlets must be too far from a fission hot spot.

5.4.2 Alternative Yield Calculation

Rather than benchmarking the triplet population in the solution sensitization experiment using the shoulder of the GSB, we can instead use a kinetic analysis of the NMFP signal to estimate the proportion of NMFP triplets that transfer to the CN-INDT[82,143,145]. In a series of solutions with varying concentration of CN-INDT but a constant concentration of NMFP, we see that the rate of quenching of the NMFP triplet signal increases with the concentration of CN-INDT, as shown in Figure 5.14.

We can use the lifetime of the NMFP triplet when mixed with different concentrations of CN-INDT to calculate the efficiency of triplet transfer. As seen in Figure 5.14, the pure NMFP triplet with no CN-INDT (red squares) has a mono-exponential lifetime of 12 µs, whilst in the mixed solution with 0.15 $\mathrm{mgml^{-1}}$ CN-INDT (dark red diamonds) it has a lifetime of 3 µs, indicating a triplet transfer efficiency of 75%. Therefore, assuming a minimum 90% intersystem crossing efficiency for the NMFP[232] we find that

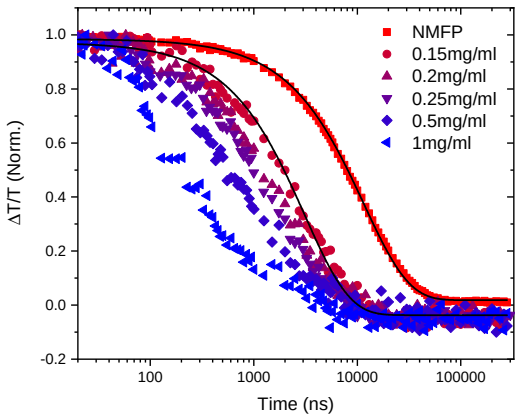

Fig. 5.14 Kinetics at 800–820 nm, where there is NMFP triplet PIA but no CN-INDT triplet PIA, for a series of mixed solutions with constant concentration of NMFP and a varying concentration of CN-INDT as labelled in the legend. The red squares are for a solution of pure NMFP with no CN-INDT. Black lines indicate exponential decays of 3 and 12 µs.

at least 67.5% of photons absorbed by the NMFP result in a triplet on a CN-INDT molecule at this concentration.

We calculate from the steady state absorption and the pump fluence that the initial excitation density on NMFP should be $9.4 \times 10^{14}\text{cm}^{-3}$. Therefore, the concentration of triplets transferred to CN-INDT should be $6.4 \times 10^{14}\text{cm}^{-3}$, or 1.1 µM. Converting ΔT/T to ΔOD and using Beer's Law, $A = \varepsilon cl$ ($l = 1$ mm, the cuvette path-length), we determine the triplet extinction coefficient $\varepsilon_{T1}(705\,\text{nm}) = 6.1 \times 10^4\,\text{Lmol}^{-1}\text{cm}^{-1}$.

From steady state absorption measurements of dilute solutions of CN-INDT, we have determined that the ground state absorption has the following extinction coefficients at the 0-1 shoulder and 0-0 peak: $\varepsilon_{S0}(600\,\text{nm}) = 3.9 \times 10^4\,\text{Lmol}^{-1}\text{cm}^{-1}$; $\varepsilon_{S0}(650\,\text{nm}) = 5.6 \times 10^4\,\text{Lmol}^{-1}\text{cm}^{-1}$. Using the strength of the GSB at 600 nm in the dilute solution at 1 ns ($\Delta\text{T/T} = 5 \times 10^{-3}$), we can calculate the molar concentration of excited molecules, which in the dilute solution case we assume to all be in the S_1 state, to be 0.55 µM. Again using Beer's Law, this gives $\varepsilon_{S1}(850\,\text{nm}) = 19 \times 10^4\,\text{Lmol}^{-1}\text{cm}^{-1}$. This gives a ratio of 3.11 between S_1 and T_1 PIA extinction coefficients, which follows through Equation (5.1) to a total triplet yield of 90%, significantly higher than the 63% calculated in the first method.

There are substantial unknowns involved in both methods detailed here. The most important caveat for both is that we are forced to assume the relative extinction coefficients in solution are the same as in the solid state, which is a significant assumption

given the differences in the ground state absorption (Figure 5.2). The second is that when we use the bleach to gauge the excited state concentration in solution, we assume there is no underlying PIA which would reduce the magnitude of the bleach signal. We have observed that this does occur in the solid state and the effect is so strong as to eliminate the bleach almost entirely in the region which we probe (Figure 5.9). Having said this, we believe the most reliable method to be the first presented here, comparing the relative strength of the PIAs to the strength of the 600 nm bleach, which gives a triplet yield of 63%. We are satisfied that this is far higher than a conceivable ISC efficiency for molecules of this type, and that it appears that if the morphology and intermolecular coupling could be tuned correctly then the singlet fission yield would be much higher, if not quantitative (quantitative fission meaning a 200% yield, or 2 triplets for every singlet).

5.5 Time-correlated Single Photon Counting

Time-correlated single photon counting (TCSPC) is performed at a much higher repetition rate, and consequently much lower fluence per pulse, than transient absorption and transient grating photoluminescence, meaning that TCSPC kinetics are unaffected by singlet-singlet annihilation and instead reflect the intrinsic mono-molecular rates. As exhibited in the near-infrared transient absorption (Figure 5.10), there is significant singlet-singlet annihilation at normal transient absorption pump intensities, however at the lowest intensities for Br-INDT we achieved the same decay kinetics as with TCSPC.

In a comparison of the different X-INDT films in Figure 5.15, we find significant variation in the decay kinetics through the series. All except H-INDT (i.e. all those that produce triplets through singlet fission) have a fast, almost instrument-response-limited, component, followed by a slower component. CN-INDT, which in calculations has the most exothermic energetics for singlet fission and has the highest yield of triplets in transient absorption, is dominated by the fast early decay. From CN- to H-INDT we can see a gradual shift of decay kinetics towards slower overall decay with a less dominant and slower early component. This trend broadly fits our calculations of exothermicity of singlet fission and our estimation of relative triplet yields from transient absorption (Figure 5.17), with the exception of F-INDT which would be expected to be slowest barring H-INDT. However, the branching mechanism we propose based on transient absorption measurements suggests that the longer-lived singlet states that contribute to the TCSPC signal have relatively little relationship to the sub-ps singlet fission

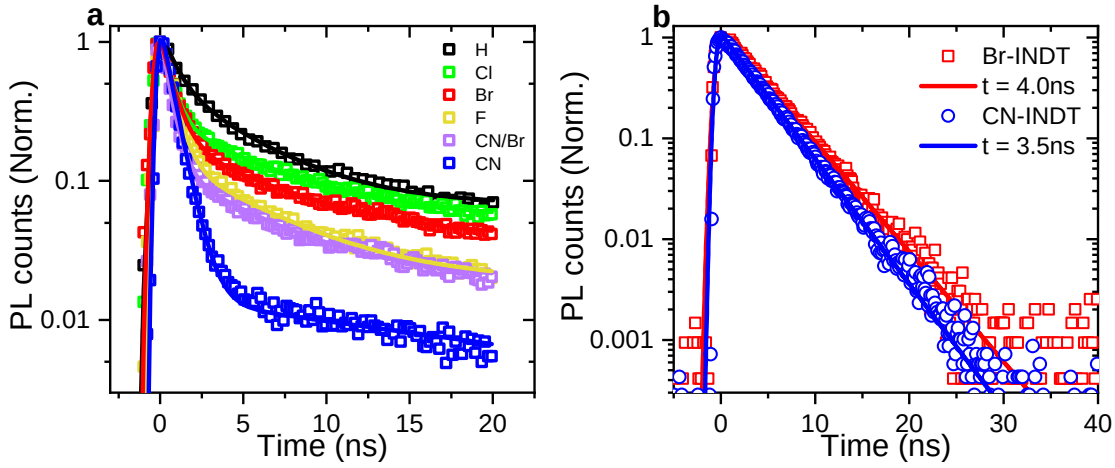

Fig. 5.15 Time-correlated single photon counting for (a) spin coated films and (b) dilute solutions of X-INDT excited by a pulsed 470 nm laser. The instrument response was 300 ps and modelled as a Gaussian. Solid lines are biexponential fits for the films and monoexponential for the solutions, convolved with the instrument response function.

dynamics. Given the important role of morphology we have uncovered and other non-radiative quenching pathways, which can vary between materials, we do not put significant weight on the observed TCSPC trends as a predictor of fission performance.

5.6 Dilute Solution Intersystem Crossing

Using ns-transient absorption with a visible NOPA probe, we measured dilute solutions ($0.1\,\mathrm{mgml^{-1}}$) of each X-INDT in 1 mm optical path cuvettes, as a control for the triplet sensitisation by NMFP described in Section 5.3.1.1. We observed ISC to the familiar triplet absorption lineshape, most significantly in the Br-INDT, due to the heavy Br atom. We fit the singlet decay to a monoexponential decay and used the shoulder of the GSB to calculate the ISC yield. There was no observable triplets in the CN- or BrCN-INDT, the second of which is curious seeing as there is still one Br atom per molecule. The dilute solution singlet decay lifetimes measured are comparable to those seen in TCSPC (Figure 5.15b).

5.7 Trends in the X-INDT Derivatives

Relative triplet yields of the X-INDT family of films at 500 ns can be estimated from the strength of the triplet absorption in the 630–760 nm range, shown in Figure 5.17. These spectra are scaled to roughly account for several factors. We accounted for variations of

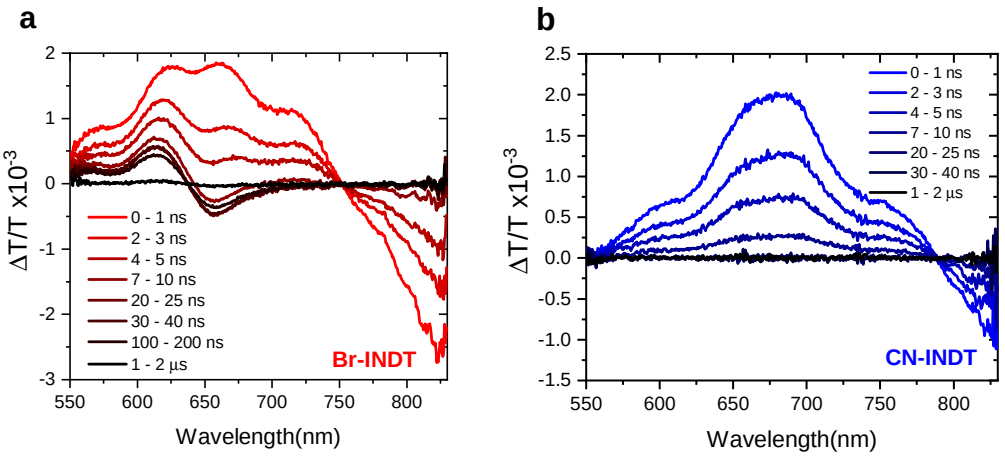

Fig. 5.16 Ns transient absorption spectra for a) Br-INDT and b) CN-INDT showing decay of singlet. Triplets are produced by ISC in Br-INDT but not in CN-INDT.

Molecule	S_1 lifetime (ns)	ISC yield (%)
Br-INDT	3.8	24
Cl-INDT	4.5	5
H-INDT	3.9	2
CN/Br-INDT	4.8	0
F-INDT	5.1	9
CN-INDT	4.3	0

Table 5.1 S_1 lifetimes (from TCSPC shown in Figure 5.15b for Br- and CN-INDT) and ISC yields (from transient absorption shown in Figure 5.16 for Br- and CN-INDT) in dilute solutions of X-INDT in chloroform.

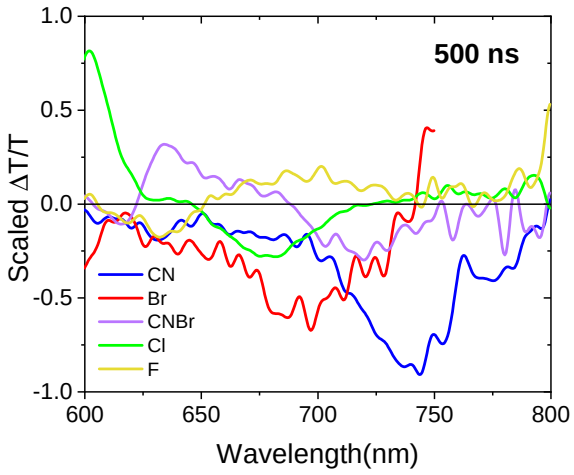

Fig. 5.17 Scaled triplet spectra demonstrating relative yields of triplets in spin coated films of X-INDT 500 ns after excitation in the ns-transient absorption experiment. Spectra have been scaled to account for differences in initial excitation density and triplet absorption cross-section, and as such their magnitude represents the best estimate of relative triplet population between the X-INDT films.

triplet PIA cross-section by comparing solution sensitisation spectra (Figure 5.6), which are normalised to the GSB peak to account for variations in total triplet population in this experiment (assuming similar ground state extinction coefficients for all the materials). The relative strength of triplet PIA to GSB was used as the first correction factor. The thin-film data were further scaled to correct for slight differences in excitation fluence and optical density between films. We note that the latter correction is somewhat imprecise, due to inhomogeneity which differently affects the steady-state (∼8 mm spot) and transient (∼200 µm probe spot) absorption measurements. This effect was most pronounced for films of F-INDT as these were most inhomogeneous. Moreover, the triplets formed by singlet fission exhibit different decay kinetics in the different materials (Figure 5.5), and the films probably have different underlying rates for geminate and bimolecular annihilation processes. Due to these inherent limitations in determining the final population of triplets, we present these scaled triplet transient absorption signatures as an indication of the trend rather than precise yields of triplets.

Figure 5.17 shows relative triplet yields of H < F < CN/Br ≈ Cl < Br < CN, which broadly follows a trend of increasing yield with increasing exothermicity of singlet fission calculated by TD-DFT. We recover a similar behaviour from the PL lifetimes observed using TCSPC (Figure 5.15), where the loss of singlet population is fastest for CN, and the relative lifetimes are CN < CNBr < F < Br < Cl < H. There is also a

possible connection to the strength of intermolecular coupling[80], as we observe that the CN-INDT film absorption is most blue-shifted from the solution spectrum and has the most suppressed 0-0 peak (characteristic of H-aggregation), while that of H-INDT is the least H-aggregate-like (Figures 5.2 and 5.3).

5.8 Stability and Aromaticity

The ultimate goal of exploiting excited state aromaticity to generate singlet fission-capable materials is to access triplet states without cost to the chemical stability. The ambient stability of each INDT material was compared to TIPS-pentacene, with results summarised in Figure 5.18. Thin films were identically prepared and stored in individual clear Perspex boxes on a shelf, in air, in a well-lit area, but out of direct sunlight, and the steady state absorption was measured periodically over 31 days by Kealan Fallon. Under these ambient conditions TIPS-pentacene showed total degradation after 4 days, whilst the INDT materials exhibited excellent ambient stability, with CN-INDT maintaining over 80% of its original absorbance after 31 days Figure 5.18h. The high chemical stability of the INDTs showcases their robustness despite SF occurring readily (and hence a high concentration of triplets being present) in the material. By exploiting triplet aromaticity, not only is the energy of the triplet state lowered such that it can undergo singlet fission, but the delocalised nature of the unpaired electrons means they are less susceptible to degradation reactions, in an analogous way that ground state aromaticity increases the stability of organic compounds.

The experimental proof of singlet fission in INDT-based materials and their photochemical stability benchmarks the essential validity of our approach: increasing triplet aromaticity through chemical functionalisation results in more energetically favourable singlet fission, into more stable triplet states. We now aim to show the link between excited-state energetics and triplet aromaticity applies to a wider range of compounds. Theoretical energies of S_1 and T_1 and NICS(1) aromaticity for 9920 indolonaphthyridine (IND) candidates were calculated using TD-DFT incorporating the Tamm–Dancoff approximation (TDA) at the B3LYP/6-311++G** level of theory by Alex Ganose, Chris Savory and Kealan Fallon.

In the wider sample group studied using TD-DFT, the correlation of increased excited state aromaticity and reduced $E(T_1)/E(S_1)$ is unequivocally clear (Figure 5.19a). It demonstrates that, through appropriate chemical substitution to increase the aromaticity of the triplet state, the triplet energy can be lowered without affecting the energy of the singlet (i.e. by moving down the black arrow in Figure 5.19a). We can

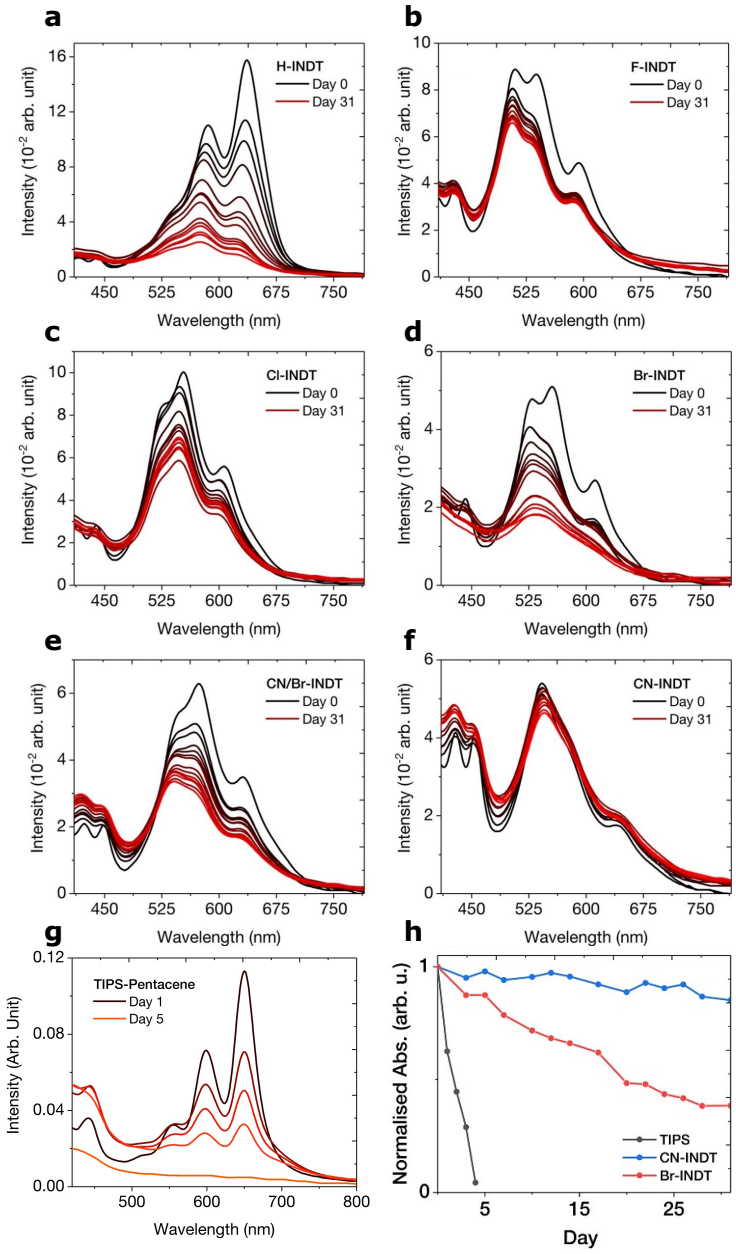

Fig. 5.18 a)-f) Steady-state absorption spectra of thin-films of INDT compounds over 31 days. Films were spin-cast from 5 mg/mL solutions in chloroform and stored in individual Perspex boxes on a shelf in a well lit area but out of direct sunlight. g) The same protocol for TIPS-pentacne, where sample was completely degraded within 5 days. h) Normalised intensity of the λ_{max} of the steady-state absorbance spectra of thin-films of TIPS-pentacene (TIPS), Br-INDT and CN-INDT. Measurements by Kealan Fallon.

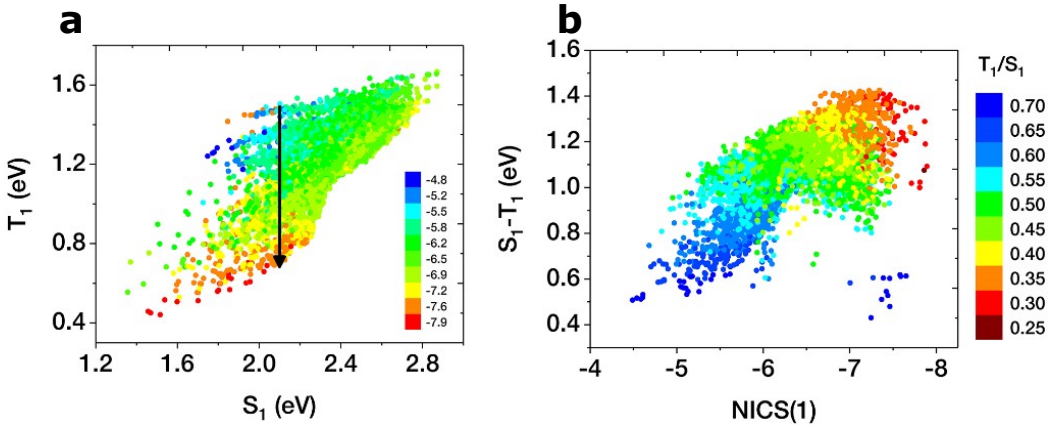

Fig. 5.19 a) Calculated energies of S_1 and T_1 for over 9920 IND derivatives with the corresponding C5 NICS(1) shown in colormap. b), The relationship between the singlet-triplet gap and triplet state aromaticity with the corresponding $E(T_1)/E(S_1)$ ratio shown in colour map. Calculations by Alex Ganose, Chris Savory and Kealan Fallon.

directly visualise this tuning by plotting the calculated singlet-triplet energy gap as a function of triplet-state aromaticity (Figure 5.19b). These results directly demonstrate that exploiting Baird-type aromaticity is a powerful approach for manipulating the singlet-triplet energy gap. Manipulation of the singlet and triplet energies in such a manner has never been demonstrated and has implications across many areas of science such as light emitting diodes, photovoltaics, photocatalysis, photochemistry, spintronics and magnetism. In the context of singlet fission, this data has identified 2616 new singlet fission candidates with a wide range of optical band-gaps and $E(T_1)/E(S_1)$ ratios. These are all based on straightforward substitution of the IND central chromophore, which is itself well known for photochemical robustness and large oscillator strength – both ideal properties for applications of singlet fission.

5.9 Photoluminescence Yield and Morphology Relationship

To investigate how the density of hot spots, and therefore the branching ratio between singlet fission and non-singlet fission decay pathways, changes with film preparation, we measured the photoluminescence quantum efficiency (PLQE) of a range of CN-INDT

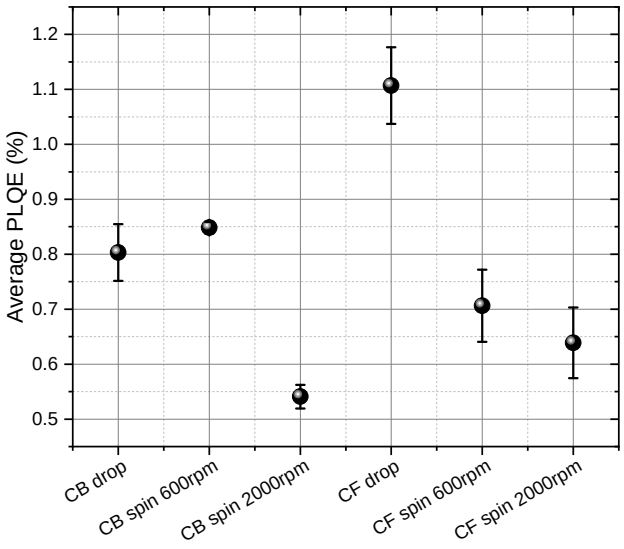

Fig. 5.20 Average PLQE values of four randomly selected spots on each film of CN-INDT, which were prepared from 10 mgml^{-1} solutions in either chlorobenzene (CB) or chloroform (CF) by drop-casting or spin-coating at 600 or 2000rpm. Error bars show $\pm\sigma$ range. These PLQE measurements were performed by Simon Dowland.

films, listed in Figure 5.20. Given that excitations that have undergone fission cannot decay radiatively (unless via TTA, which we have not observed to be significant in these materials), we propose that films with a higher PLQE have a lower density of hot spots, and therefore a larger portion of excitations can decay radiatively. We consider that the large difference in PLQE between sample types suggests that film preparation has an important impact on morphology and particularly the density of singlet fission hot spots.

Looking simply at the preparation dependent PLQE results for the films prepared from chloroform (CF) solution, a kinetic trapping argument emerges for the formation of the hot spots. The drop-cast film, where the solvent dries slowest, has a higher PLQE, therefore we deduce a lower density of hot spots, while spin-coating the film leads to a higher density of hot spots, and this density increases further as spin speed (and correspondingly, drying speed) is increased from 600 to 2000 rpm. The same pattern fits the spin-coated films from chlorobenzene (CB), with high spin speed leading to greater density of hot spots due to kinetic trapping and therefore a lower PLQE. The drop-cast CB film does not fully agree with this simple kinetic trapping model. However, as CB has such a high boiling point, it is possible there is little difference

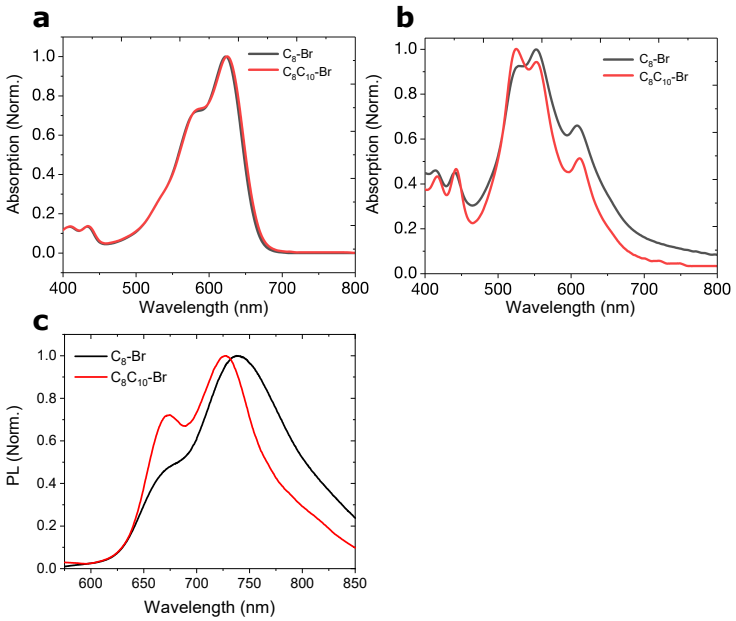

Fig. 5.21 Comparison between C_8- (black) and C_8C_{10}-Br-INDT (red). a) Solution UV-vis, b) Film UV-vis, and c) Film steady-state PL

between packing times for slow spin-coating and drop-casting, and the PLQEs are within 1σ of each other.

5.10 Side Chain Engineering

To further investigate the influence of morphology and crystallinity on fission in the INDTs, we replaced the octyl-decyl (C_8C_{10}) branched solubilising side chains with linear octyl C_8 side chains. This substitution does not affect the molecular behaviour in isolation but results in a different morphology, where we presume the conjugated IND cores are capable of packing more closely. Steady state absorption shows a significant difference in two films spin-coated from C_8- and C_8C_{10}-Br-INDT, see Figure 5.21. There is also a red shift, and broadening of the PL peaks, indicating that there is more intermolecular coupling in the C_8 film than in the branched chain version that we have been studying more generally.

From short-time transient absorption in Figure 5.22b we can see that the C_8-Br-INDT film undergoes fission - the triplet signal is present within the 200 fs instrument response and grows to a peak at 5 ps, which we interpret as singlets close by to hot spots transporting by FRET to a hot spot before forming triplets. To compare if

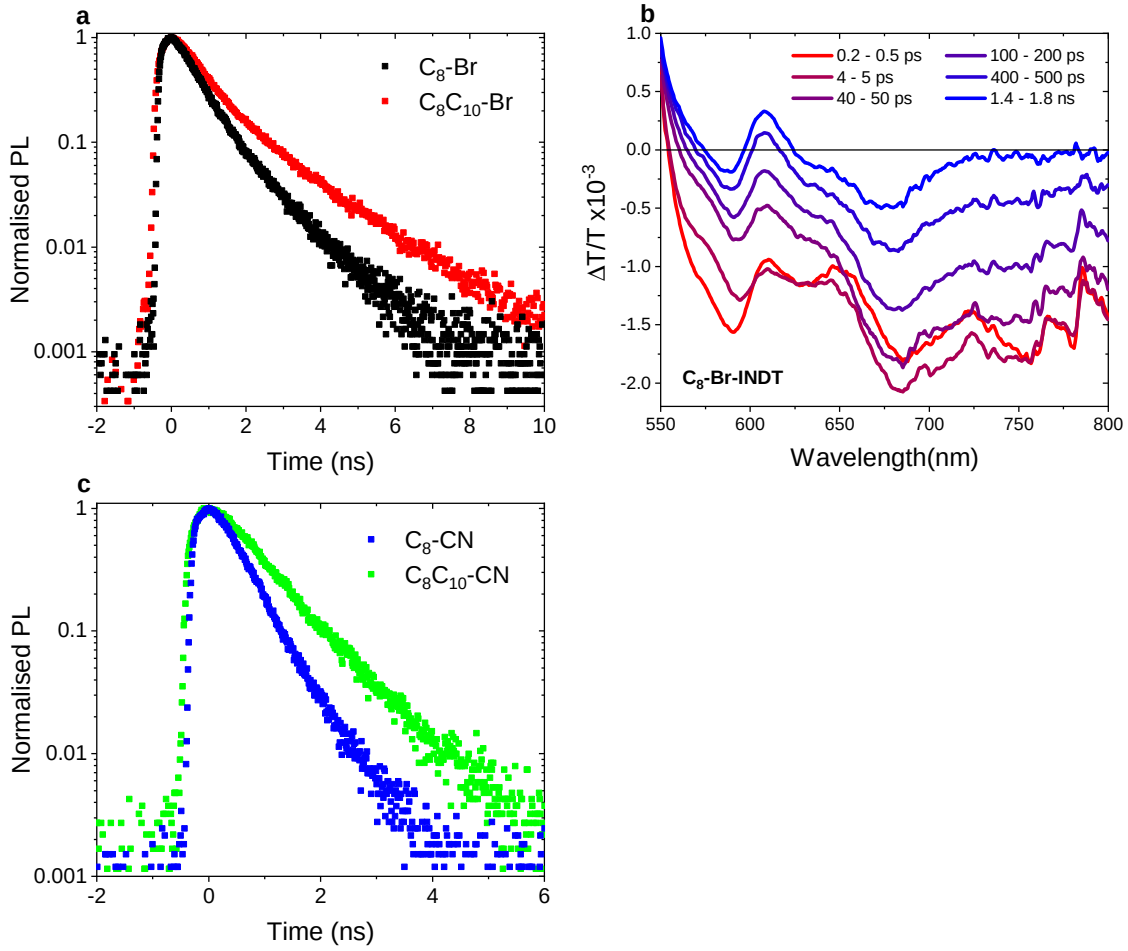

Fig. 5.22 a) TCSPC of C_8- (black) and C_8C_{10}-Br-INDT (red) films, showing faster decay of singlet PL in C_8-Br-INDT. b) Short-time transient absorption showing sub-ps triplet formation by singlet fission in a C_8-Br-INDT film. c) TCSPC of C_8- (blue) and C_8C_{10}-CN-INDT (green) films, showing faster decay of singlet PL in C_8-CN-INDT.

this new morphology has a higher density of singlet fission hot spots, we look at the PL decay (Figure 5.22a), where we can see that the singlet is quenched faster in the C_8-Br-INDT film than in the equivalent C_8C_{10}-Br-INDT film.

In addition, we investigated if the faster trend with the C_8- substitution continued with CN-INDT in the same way as Br-INDT. While the highly scattering nature of C_8-CN-INDT films meant that it was not possible to adequately measure decent UV-vis or transient absorption, we did confirm that the PL lifetime decreased (Figure 5.22c). In addition, the PLQE, which ranged from 0.5 to 1.1% for C_8C_{10}-CN-INDT based on preparation technique (Figure 5.20), ranged from 0.2% if spin-coated at 2000 rpm to 0.4% if spin-coated at 600 rpm in C_8-CN-INDT.

These results confirm our assessment that sample morphology defines the fission yield in these materials by way of changing hot spot density, and the length and bulkiness of side chains is a handle that can be adjusted to disrupt this. We have shown that less bulky side-chains, which lead to more closely packed chromophores, lead to samples with a higher density of hot spots. We speculate that this could mean that the hot spots involve π-stacked chromophores.

5.11 INDT Dimers

Clearly, morphology is critical for enabling fission in these materials. However, changing the side-groups or the "X" substitution are not particularly precise interventions. They evidently change the packing, but we are not able to use these variables to precisely control the intermolecular coupling. On top of this, in the films shown so far we have deduced that we are measuring mixed-morphology films with hot spot geometries alongside non-hot spot geometries. In order to address this and have greater control over the intermolecular coupling, we created INDT dimers, which we measured in solution to see if *intra*molecular fission is also possible using the aromaticity-informed INDT motif.

Three dimers were measured, which we have named meta-, para- and CN-dimer. For the meta- and para-dimers, the monomer is C_8-H-INDT, with an extra hexyl solubilising group at the 6,6' positions on the INDT C6 ring. They are bridged at the thiophene groups by a phenyl linker, either at the meta or para positions on the phenyl ring. This should alter the amount of conjugation across the bridge, with less conjugation in the meta-dimer expected due to destructive quantum interference (DQI)[262–266]. Although we did not see fission in H-INDT films, we suspect that this could be a result of the morphology (a lack of hot spots) rather than just energetics. From TD-DFT, we expected fission to be less exothermic in F-INDT than H-INDT, and we did observe fission in F-INDT films. In addition, the H-INDT morphology was the outlier in that it evolved significantly over periods of days (Figure 5.3). Even when drop-cast or spin-coated slowly such that the more blue-shifted spectrum is formed, it was less "H-aggregate"-like than the other X-INDTs (i.e. the 0-0 transition was less clearly suppressed).

Studies of intramolecular fission in phenyl-linked dimers have shown differences between para, meta and ortho linkers, but there is not a consistent behaviour for which will best promote fission nor a developed theory to predict why. In a study of pentacene dimers, meta was the best performing[145], and calculations have suggested that triplet

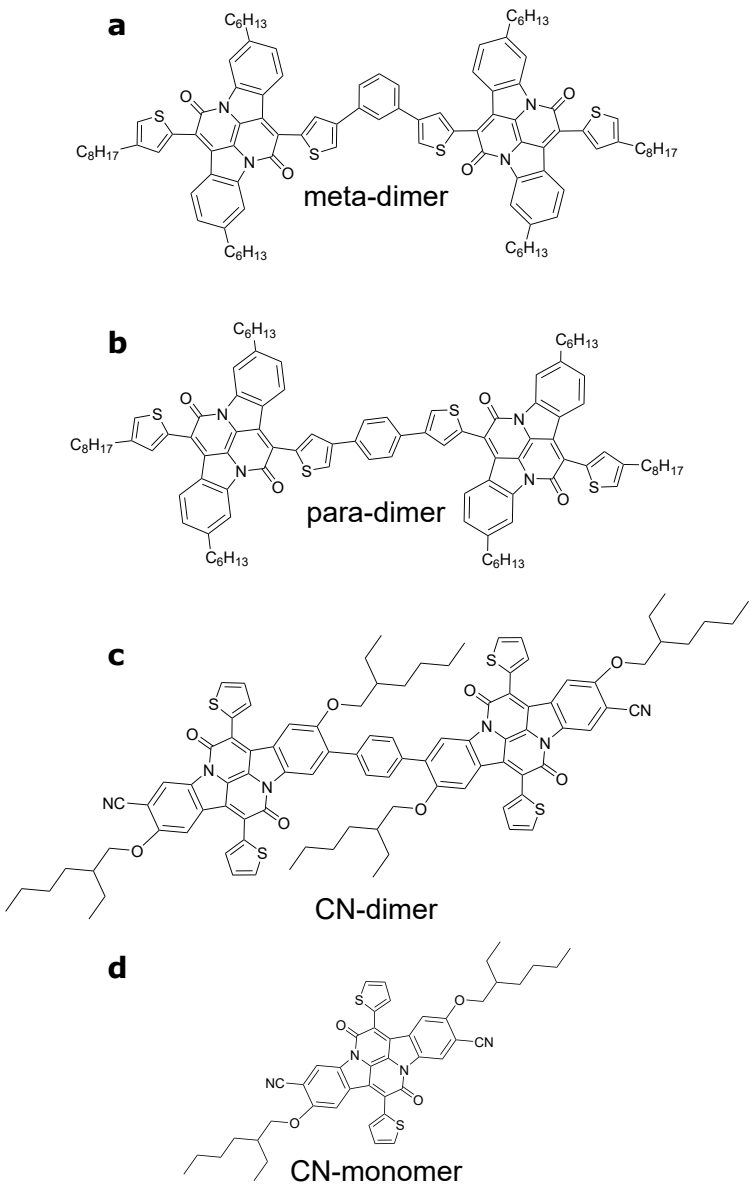

Fig. 5.23 Chemical structures of INDT dimers. a) meta-dimer, b) para-dimer, c) CN-dimer and d) CN-monomer.

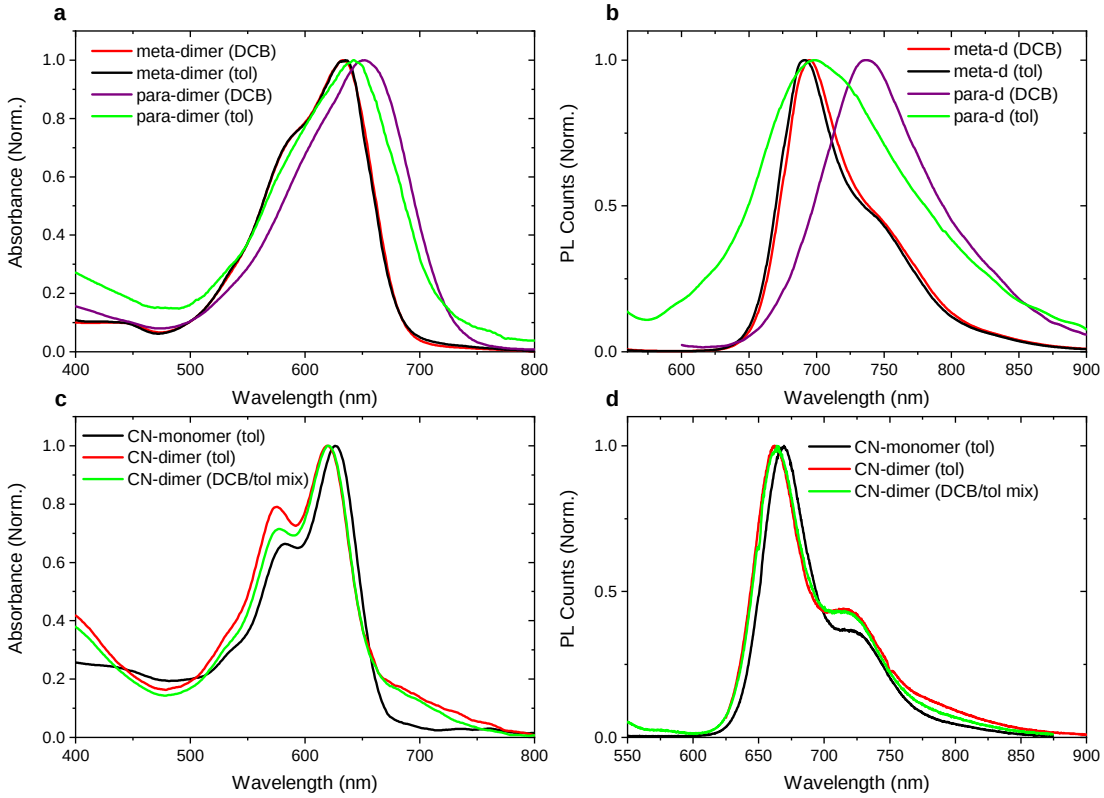

Fig. 5.24 Absorption and steady-state PL. a) Normalised absorption and b) normalised stead-state PL of meta- and para-dimers in toluene vs DCB. c) Normalised absorption and d) normalised stead-state PL of CN-monomer in toluene CN-monomer in toluene vs 50:50 mixture of DCB:toluene.

pairs cannot dissociate in the para isomer whereas they can in the meta isomer[146]. By contrast, in tetracene dimers, fission was favoured in the para isomer[147,148].

For the CN-dimer, the intention was to create a dimer with no conjugation across the bridge by making the monomer moieties orthogonal to each other using the sterics of bulky oxy-alkyl chains next to the bridge which will clash with the the other chromophore. We used the CN-INDT core in this case, to ensure that fission would definitely occur with the correct inter-chromophore coupling (such as that which occurs in the hot spots in our CN-INDT films).

5.11.1 Steady-state Characterisation

Solvent polarity dependence in intramolecular fission has been reported for various systems[142,145,155–157], where the stabilisation of a CT-intermediary in a more polar solvent is often invoked. We will compare behaviour in toluene and dichlorobenzene

Dimer	Solvent	PLQE (%)	PL lifetime(s) (ns)
Meta-dimer	DCB	24	2.3
Meta-dimer	toluene	39	3.5
Para-dimer	DCB	1	0.4; 2.9
Para-dimer	toluene	5	1.4; 3.0
CN-monomer	toluene	33	4.6
CN-dimer	DCB	-	2.8
CN-dimer	toluene	5	2.9

Table 5.2 INDT dimer PLQEs, measured with 520 nm CW excitation and PL decay lifetimes, measured by TCSPC (Figure 5.25). For para-dimer, a biexponential PL decay was measured, so we report two lifetimes.

(DCB) , with DCB being the more polar solvent. Figure 5.24 shows the UV-vis absorption of the para-, meta- and CN-dimers in toluene and DCB. For the CN-dimer, which was synthesized in very low yield, there was not sufficient material to create two stock solutions so instead we diluted the stock toluene solution with 50% DCB, to still test a more polar environment.

Generally, the meta-dimer is unaffected by the polarity of the solvent, but in the para-dimer there is a distinct red shift of absorption and PL in the more polar solvent. We note that the solubility of the para-dimer in toluene was poor, meaning that signal collection was difficult for the green PL spectrum in panel b, artificially broadening the spectrum. The peak could still be resolved, and demonstrates the red shift from toluene to DCB.

In the CN-dimer, there is a blue-shift from monomer to dimer, because in the dimer there is only one electron-withdrawing carbonitrile group per monomer due to the substitution with the bridge. There is no detectable solvent dependence on the PL spectrum from the CN-dimer, however there is a slight change in 0-0:0-1 peak ratio in the absorption spectrum.

We found significant differences in PLQE between the dimers that point towards trends in the success of fission in these dimers, listed in Table 5.2 Meta-dimer has a relatively high PLQE in both toluene and DCB, while para-dimer has a relatively low PLQE in toluene, 5%, but an extremely low PLQE in DCB, only 1%. This indicates that there is a singlet-quenching pathway available in para-dimer that is faster in a more polar solvent. CN-monomer has a PLQE of 33%, but in the CN-dimer this falls to 5%.

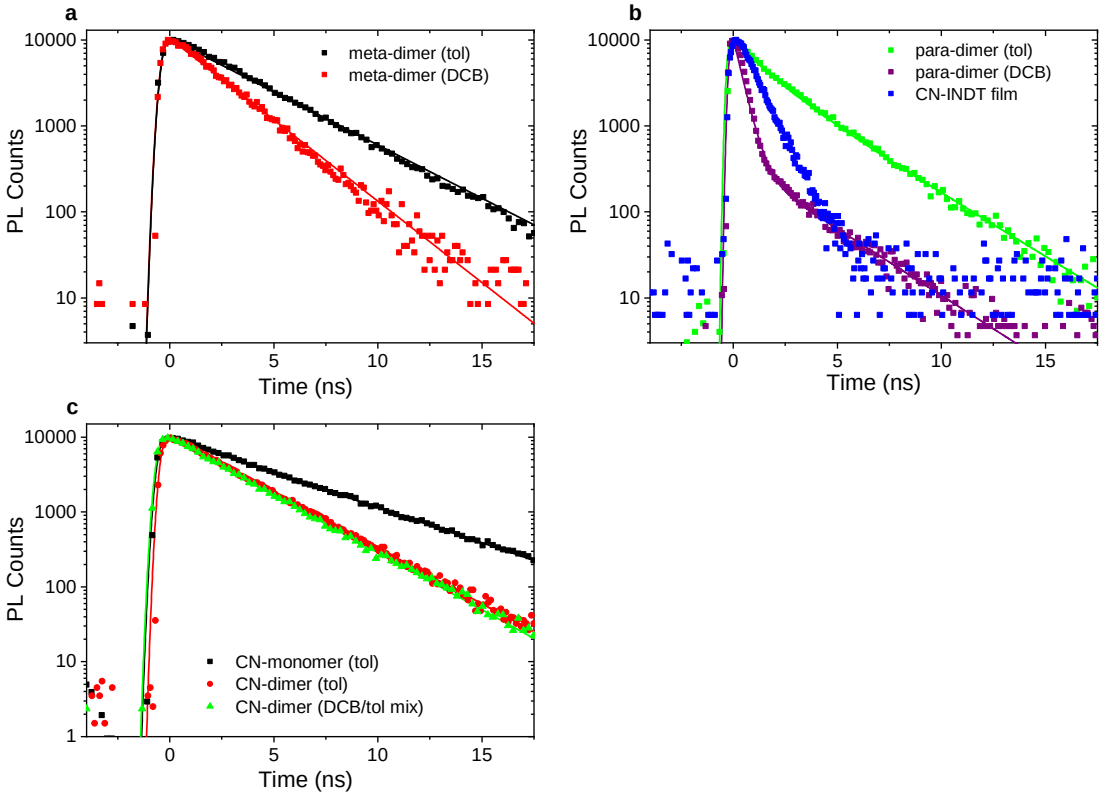

Fig. 5.25 Time-correlated single photon counting of PL from INDT dimers in toluene or DCB. a) meta-dimer, with mono-exponential fits. b) para-dimer, with bi-exponential fits. c) CN-dimer and CN-monomer, with mono-exponential fits. Lifetimes for the fits are given in Table 5.2.

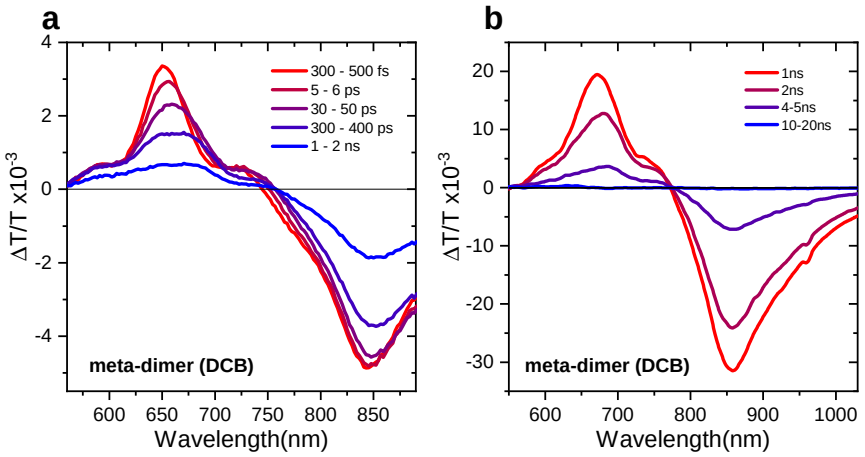

Fig. 5.26 a) Short-time and b) Long-time transient absorption of 0.1 mgml^{-1} meta-dimer in DCB.

5.11.2 Time-resolved PL

Quenching of the PL that we observed in the PLQE trends is also clear temporally when we measure PL kinetics using TCSPC, shown in Figure 5.25. Most interesting is the para-dimer, in Figure 5.25b, where in DCB the PL is quenched even faster than the best performing film of the X-INDTs, CN-INDT. This is clearly a polarity-induced effect, as the quenching is drastically reduced in toluene, although both kinetics required a bi-exponential model to fit, indicating that there is still a degree of quenching in toluene. By contrast, the meta- and CN-dimers both had approximately mono-exponential PL decays regardless of polarity. There was a faster decay seen in the meta-dimer in DCB than toluene, while the CN-dimer PL decay was identical in both solvent environments. We attribute the slower PL decay in the CN-monomer than the CN-dimer to the effect of having approximately half the oscillator strength per molecule compared to the CN-dimer.

5.11.3 Transient Absorption

Transient absorption of the meta-dimer was similar in both toluene and DCB. The data for DCB is shown in Figure 5.26 and reveals no sign of triplets in either ps or ns timescales. The excited state population decays in just a few nanoseconds, in accordance with our findings from TCSPC that the PL decays over 2.3 ns in DCB. There is little spectral evolution over the decay, indicating that the majority of the excitations simply decay as singlets. There is a small red-shift at the edge of the stimulated emission signal, indicating some conformational relaxation on the ps timescale.

By contrast, in the para-dimer, the behaviour observed in transient absorption depends strongly on the solvent polarity. In toluene, in Figure 5.27c, the evolution looks not particularly different to the meta-dimer, albeit with a faster decay. However, in DCB, as is clear when the spectra are normalised in Figure 5.27b, a triplet PIA grows in on a ∼100 ps timescale. The PIA at 700 nm, which is on top of a stimulated emission from residual singlets, is a good match to the triplet sensitisation spectrum taken in Figure 5.29. This suggests fission is only possible in a more polar solvent, which lowers the energy of charge transfer (CT) states. Consequently, we conclude that CT intermediates play an important role in intramolecular fission in these materials, as has been argued for acene and other covalent fission dimers[142,145,155–157].

It is clear that the increased polarity of DCB has allowed a new, highly efficient decay pathway for excitations in the para-dimer. Given the appearance of this triplet absorption concurrently with the singlet decay, we propose that singlet fission is proceeding to a triplet pair. However, given the absence of other chromophores for the triplets to dissociate outside of the dimer, the triplet pair annihilates rapidly. The full excited state population is almost entirely returned to the ground state by 500 ps. Similarly short lifetimes of closely contained triplet pairs in covalent dimers have previously been reported[143], while oligomers have been successfully designed to allow the triplets apart and these report much longer triplet lifetimes[111,153,154].

In short-time transient absorption, it seems the entire excited state population of para-dimer in DCB has decayed within 1 ns. However, we detected a small long-lived population of triplets in long-time transient absorption (Figure 5.27d). Looking at trESR, as measured by Leah Weiss and shown in Section A.3 of the appendix, we see triplets with the same ESR polarisation pattern as the dilute monomer (EEEAAA), indicating they are generated by ISC. This is consistent with all fission products decaying within 1 ns, but some small population being capable of ISC prior to fission. ISC results in a single triplet on a dimer, with no other excitation to annihilate with, and therefore live long enough to be detected by trESR, which has an instrument response function of ∼300 ns.

The ZFS D parameter extracted from trESR is smaller in the dimers than in the H-INDT monomer, indicating that the triplet is extended over a larger area. This means that a single triplet is able to delocalise over the two chromophores of the dimer, in both meta- and para-dimer. Given the very different early-time behaviour, it is interesting that the stronger conjugation across the para-linker does not lead to a more delocalised triplet than the meta-linker ($D = 840$ MHz for both).

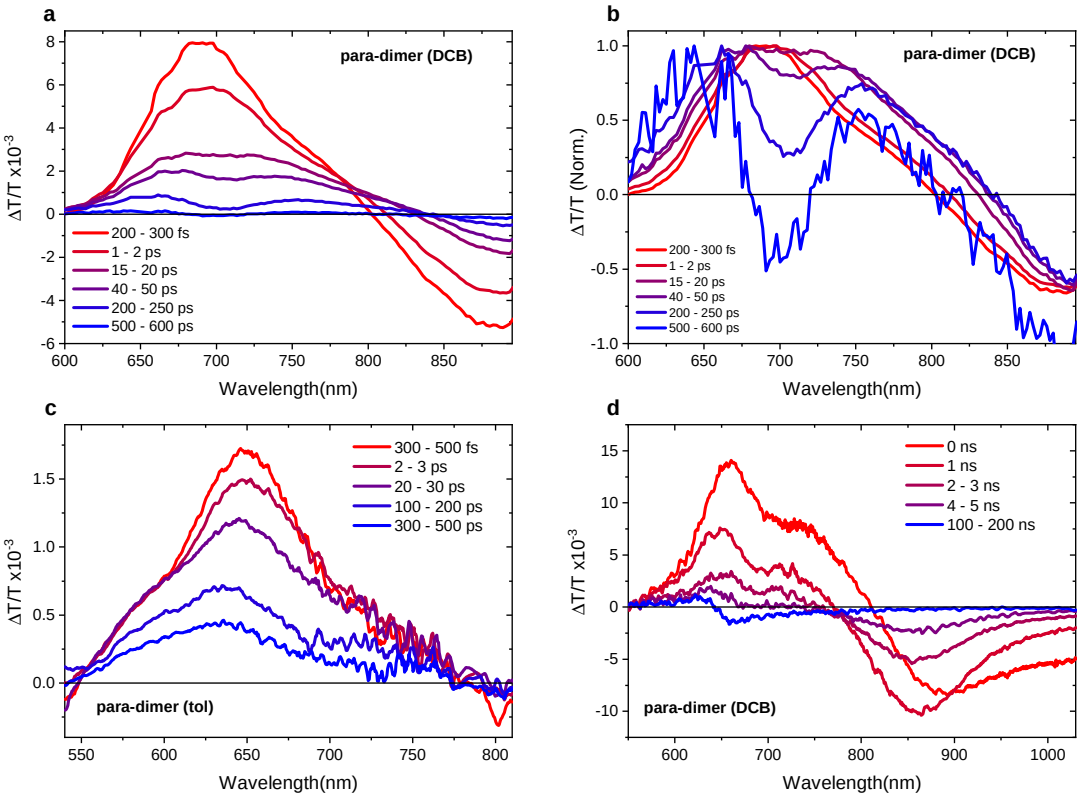

Fig. 5.27 a) Short-time and d) Long-time transient absorption of 0.1 mgml^{-1} para-dimer in DCB. b) shows the same spectra as a), normalised to the positive peak of the signal in order to see the triplet absorption at ∼700 nm. c) shows short-time transient absorption of para-dimer in toluene, at the saturation concentration at room temperature, estimated by UV-vis to be 0.015 mgml^{-1}.

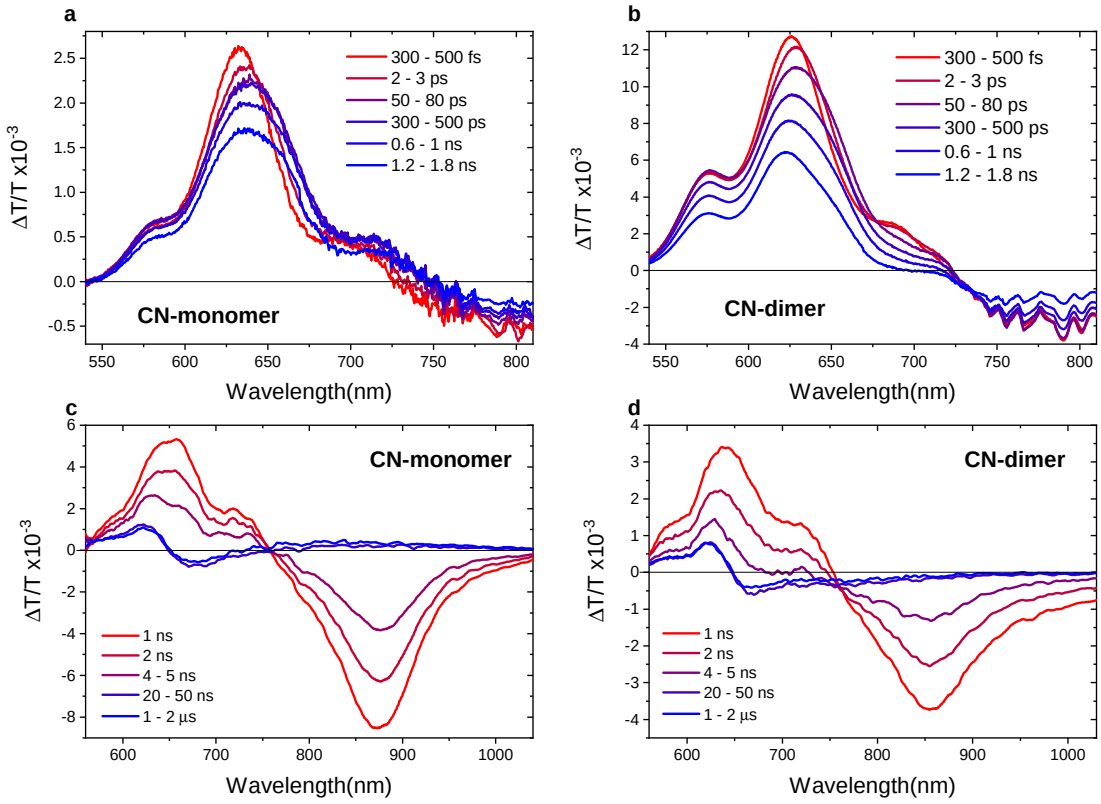

Fig. 5.28 Top row: short-time transient absorption of a) CN-monomer and b) CN-dimer. Bottom row: long-time transient absorption of c) CN-monomer and d) CN-dimer. All solutions were 0.1 mgml^{-1} in toluene.

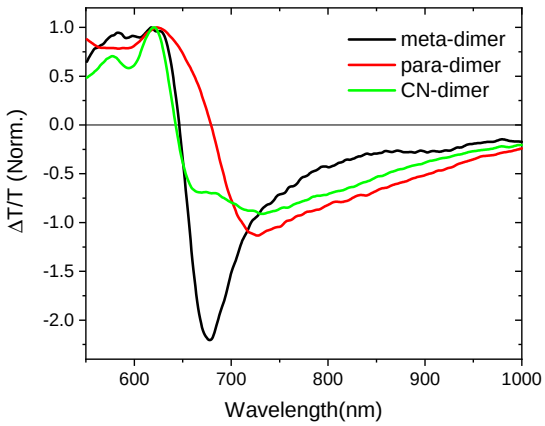

Fig. 5.29 Triplet sensitisation of INDT dimers using NMFP. Spectra shown are taken with a delay of 8–10 µs after 400 nm excitation.

Transient absorption confirms our findings from TCSPC that the excited state decays faster in the CN-dimer than the CN-monomer (Figure 5.29a-b). While there is no indication of fission-generated triplets, the CN-dimer does appear to form a dark state that is not present in the CN-monomer. The stimulated emission shoulder at ∼700 nm decays to zero by 1.2 ns, while there is still significant GSB and PIA signals, indicating an excited state with low oscillator strength.

Similarly to the para-dimer, there is a small population of ISC-generated triplets in both the CN-monomer and CN-dimer in long-time transient absorption. The similarity of the size of this population in CN-monomer and CN-dimer is further confirmation that these long-lived triplets are not generated by fission (which is not possible in a monomer).

5.12 Summary and Outlook

We have introduced a new family of singlet fission materials, indolonaphthyridine thiophene derivatives, that exploit excited-state aromaticity to lower the triplet energy level and allow singlet fission. In the best performing derivative, CN-INDT, we cautiously estimate the triplet yield to be in the region of 60–90%. Using transient absorption, and by noticing that the yield of triplets was unaffected by singlet-singlet annihilation, we have deduced that fission occurs at hot spot geometries in these materials, where the magnitude and orientation of intermolecular coupling allows pairs of triplets to form on ultrafast timescales.

We have shown that by altering the sample preparation protocol, or by changing the solubilising side groups, we can affect the density of hot spots and therefore the overall rate and yield of fission in these materials. Given that singlet fission at the hot spots themselves appears to be so fast, we see no reason that with the correct morphology, an INDT derivative could not be tuned to produce a quantitative singlet fission yield.

In addition to this, we used these materials as a platform to investigate intramolecular fission in INDT dimers, where we showed that CT intermediates play a role in triplet pair formation, and conjugation across the covalent linker is required to allow fission to proceed. This result, which was achieved using H-INDT monomers, points to morphology and intermolecular coupling as the deciding factor in the success of fission in these materials, rather than energetics. That is, all of the INDT materials investigated have sufficient energetics for fission, but only some form morphologies with the required intermolecular coupling.

Though our exploration has been limited to a single family of materials, the wide tuneability we have demonstrated and previous investigations of Baird-type aromaticity indicate that the same principles can be readily applied to other materials systems. In practical terms, the requirement of a [4n] cyclic contribution to a molecules' resonance structures translates into a simple design rule that target singlet fission systems. Examples of these (beyond INDT) are structures such as DPP (which has been proposed to undergo singlet fission, but no rationale for its large singlet-triplet energy gap has been suggested), indigo, isoindigo, pechmann dyes and fulvalenes. An interesting direction to take *cibalackrot* next would be to add aza- substitutions to reduce the planarity of the molecule, and try to induce a different morphology. The advantage of using *cibalackrot* which has phenyl groups where INDT has thiophenes, is that it has a higher band gap and could be more useful for photovoltaics.

Ground state aromaticity is a fundamental cornerstone of synthetic organic chemistry, providing stability and tuneability to unsaturated systems, underpinning the entire development of the field of organic electronics. The work we present here demonstrates that excited state aromaticity plays an equally important role to both the energetic position and stability of photoexcited triplet states. More broadly, we envisage the same approach may be used to tune the exchange energy in organic systems where triplets play a critical role, to mitigate losses in photovoltaics, harvest additional carriers in light-emitting diodes, enhance the stability of novel open-shell systems or broaden the materials library for photon up-conversion and singlet fission.

Chapter 6

Effects of Crystal Structure on Singlet Fission in Tetracene Derivatives

In this chapter we present a series of tetracene derivatives that are almost indistinguishable as monomers, but through differences to their crystal packing, exhibit vastly different photophysics in the solid state. We turn a particular focus to TMS-tetracene, which due its ability to pack in a close face-to-face motif, undergoes fission to a strongly-bound triplet pair state on a $\sim$50 fs timescale, unprecedented for an endothermic system. We also find that the close packing with large orbital overlap leads to triplet pairs with stronger binding and exchange coupling than more dispersed structures. Consequently, triplet pairs tend to decay geminately, while a minority population are able to dissociate and form free triplets through a temperature activated process.

The project described in this chapter was led by the author, and all steady-state optical characterisation, transient absorption, and time-resolved photoluminescence were measured by the author. Prof. John Anthony's research group at the University of Kentucky synthesized the molecules and characterised the crystal structures. Leah Weiss performed the transient electron spin resonance, Andrew Pearson performed the GIWAXS, and Elliot Taffet performed the modelling of the exchange coupling.

6.1 Background and Motivation

As we have discussed throughout this thesis, singlet fission offers the potential to extend the limits of efficiency in solar energy harvesting, but we have not yet found the right combination of materials and engineering to harness this potential[7,180,191]. One area of significant interest is the role that morphology or intermolecular arrangement has to play in singlet fission[115,123,164,165]. What is the optimal arrangement of molecules such that triplet pairs both form rapidly and dissociate to free triplets that can be extracted to form charges at quantitative yield? How can we design molecules and materials that take on this arrangement? Is it possible to achieve all of this while using an endothermic fission material to maximise the energy harvested?

To make progress with these crucial questions, an excellent tool is the use of systematic studies that aim to investigate the consequences of changing only one variable at a time. In this chapter, we aim to do this with the variable of morphology, as we examine the properties of a family of tetracene derivatives with subtle differences that change the intermolecular geometry, synthesized by Professor John Anthony at the University of Kentucky. Tetracene, and its derivative Triisopropylsilylethynyl- (TIPS-) tetracene, are prototypical endothermic fission systems, that have been extensively characterised[65,74,75,77,83]. Here, we investigate the effects of reducing the size of the solubilising side groups to make Triethylsilylethynyl- (TES-) and Trimethylsilylethynyl- (TMS-) tetracene, with chemical structures shown in Figure 6.1, together with their crystal structures as determined by X-ray diffraction of single crystals by Professor John Anthony.

As expected, reducing the size of the side groups changes the crystal structure and leads to a closer packing of the active tetracene cores. As these methyl/ethyl/isopropyl groups are non-conjugated, interchanging them has little effect on the electronic properties of the dispersed molecule, as evidenced by the similarity of the dilute solution absorption spectra in Figure 6.2. TIPS-tetracene's crystal structure has a $P2_12_12_1$ space group, with four inequivalent molecules in the unit cell that are all

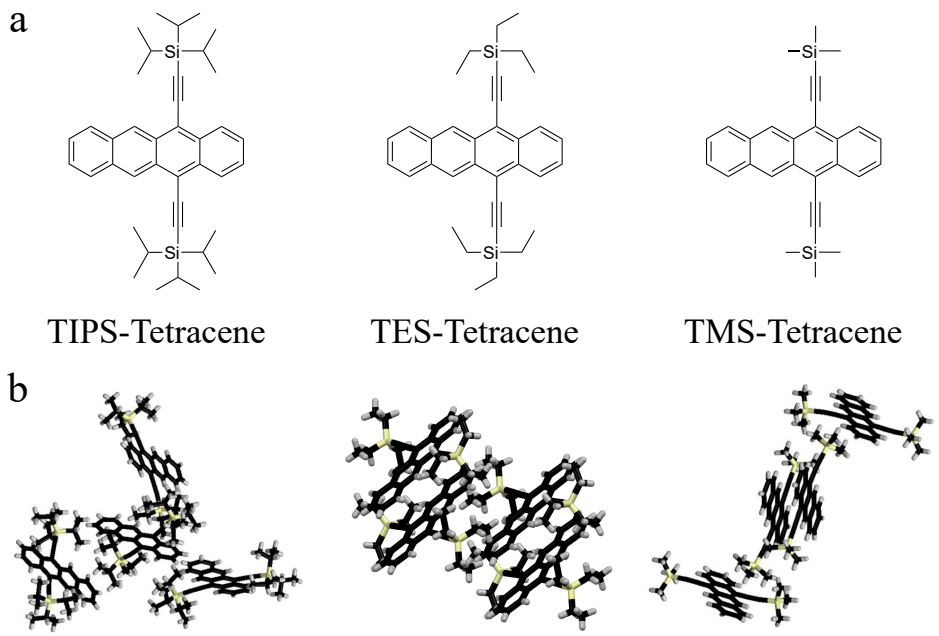

Fig. 6.1 a) Chemical structures of TIPS-tetracene, TES-tetracene and TMS-tetracene. b) Corresponding crystal structures for the molecules shown in a). TIPS-, TES- and TMS-tetracene crystals were measured by John Anthony's group at University of Kentucky, using X-ray diffraction to discern crystal structures with space groups of $P2_12_12_1$, $P\bar{1}$ and $P2_1/n$ respectively.

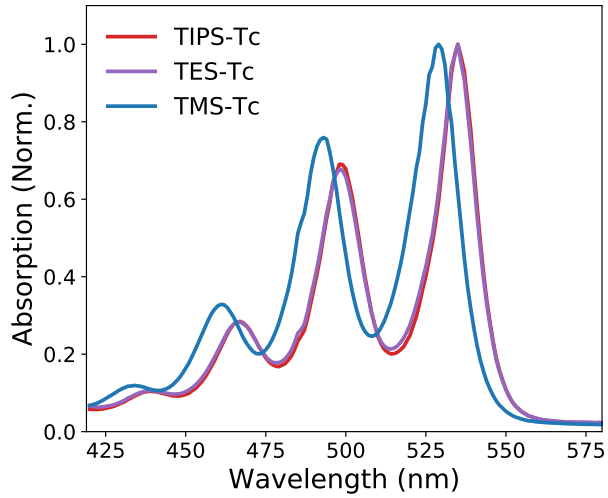

Fig. 6.2 Normalised UV-visible absorption spectra for dilute solutions of TIPS-tetracene (red), TES-tetracene (purple) and TMS-tetracene (blue) in chloroform.

offset and rotated with respect to one another, offering very limited overlap of the conjugated tetracene cores. TES-tetracene's crystal structure has a $P\bar{1}$ space group, with only two molecules per unit cell. Figure 6.1b shows four TES-tetracene molecules to demonstrate how they are arranged in slip-stacked pairs, offset along both the short and long molecular axes, which limits orbital overlap. TMS-tetracene's crystal structure has a $P2_1/n$ space group, with four molecules per unit cell. They are arranged in *pi*-stacked pairs, with only a small slip on each of the short and long molecular axes, and a significant π-orbital overlap.

A study by Pensack *et al.* demonstrated the potential for the approach of systematically editing the solubilising side groups of a fission material to investigate the effects of morphology[164]. They compared TIPS-pentacene to more and less bulky siblings, trisecbutylsilylethynyl- (TSBS-) and TES-pentacene, in amorphous nanoparticles synthesized by flash precipitation. Pensack *et al.* were able to demonstrate a slowing down of fission as the bulkiness of the side groups increased, increasing the intermolecular spacing. There are two important differences between the pentacene molecules in Pensack *et al.* and the tetracene samples presented in this chapter. Firstly, the tetracene samples are crystalline not amorphous, meaning that we know with a greater degree of precision the nature of the packing motifs. Secondly, singlet fission is exothermic in pentacene, but endothermic in tetracene. Endothermic fission is generally less robust to changes such as different molecular packing, whereas it is relatively difficult to turn off fission in pentacene as it is inherently so energetically favourable[163,182]. Nonetheless, if certain challenges can be overcome, the potential of harnessing endothermic fission offers greater efficiency gains when applied to a solar cell. Also, as discussed in Chapter 4, endothermic systems allow a radiative triplet-triplet annihilation (TTA) decay pathway, which if dominant, can limit non-radiative voltage losses in a singlet fission solar cell.

Given the comparatively large distances between neighbouring molecules in both TIPS-tetracene and TES-tetracene, we expect to learn the most from the example of TMS-tetracene, where the smaller side groups allow close π-stacking at 3.884 Å, compared to a distance of 8.046 Å between the slip-stacked neighbours in TES-tetracene. Therefore, the majority of the characterisation effort has been concentrated on TMS-tetracene, which we can directly compare to the extensive published work on TIPS-tetracene, as well as our characterisation of TES-tetracene, to understand the influence of crystal structure on the photophysics of these materials.

6.2 Steady-state Characterisation

6.2.1 UV-visible Absorption and Steady-state Photoluminescence

In contrast to TIPS-tetracene, TMS-tetracene does not readily form homogeneous films from solution processing, likely due to its poorer solubility and increased inclination to aggregate. Therefore, we have generally chosen to thermally evaporate thin films of TMS-tetracene to make reproducible, homogeneous films suitable for transient absorption experiments. This is a material-intensive method, with the majority of the material wasted on the surrounding surfaces of the evaporator rather than on the substrate, so spin-coating or drop-casting was used for TES-tetracene which solution processes well to make homogeneous, non-scattering films. Unless otherwise stated, from here on TES-tetracene films have been spin-coated and TMS-tetracene films have been evaporated.

Steady-state spectroscopy confirms that modifying the tetracene side-groups has an effect on intermolecular interactions and consequently the photophysics of these materials. In dilute solution, the absorption spectra are almost identical (Figure 6.2), because the unmodified conjugated core of the molecule dictates it's electronic and optical properties in isolation. However, there are big differences when comparing solution with crystalline films in Figure 6.3. The shift from dilute solution to crystalline film gets progressively more significant as the size of the side-groups decreases and packing gets closer from TIPS to TES to TMS.

Data from Stern *et al.* plotted in Figure 6.3a–b shows little to no shift in absorption from solution to film for TIPS-Tc, although the the absorption is inferred from an excitation scan with only 5 nm precision[77]. The photoluminescence (PL) is also similar, apart from a strongly suppressed 0-0 peak, which could be a result of self-absorption and/or H-aggregate intermolecular interactions[35]. The same is true of TES-Tc in Figure 6.3c–d, where there is a ∼2 nm slight red shift of the 0-0 absorption peak, and no discernable shift in the PL, although there is once again a suppression of the 0-0 luminescence peak from self absorption. The biggest shifts occur in TMS-tetracene, Figure 6.3e and f. There is a ∼12 nm red shift in the 0-0 absorption peak, and a ∼40 nm shift in PL peak, from solution to crystalline film. The apparent sub-band gap absorption in TMS-tetracene in Figure 6.3e is a result of scattering.

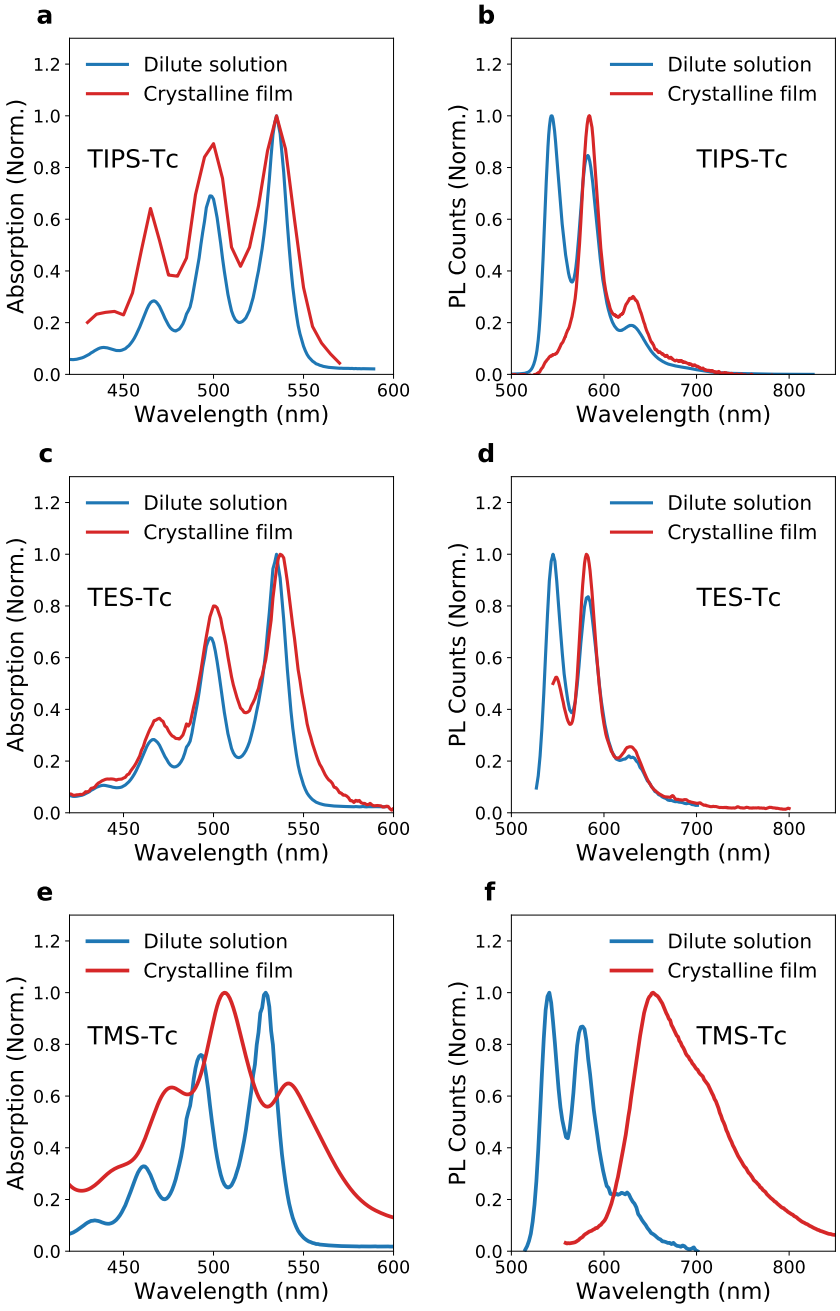

Fig. 6.3 UV-visible absorption and steady-state photoluminescence of dilute solutions (blue) compared with a crystalline films (red) for TIPS-tetracene (a and b), TES-tetracene (c and d) and TMS-tetracene (e and f). The TIPS-tetracene data is from Stern *et al.*[77], where the absorption spectrum for the film is obtained by an excitation scan of the photoluminescence. The TIPS-tetracene and TES tetracene films are spin-coated from chloroform, while the TMS-tetracene films are thermally evaporated due to problems with solution processing, however GIWAXS suggests all are crystalline (Figure 6.4).

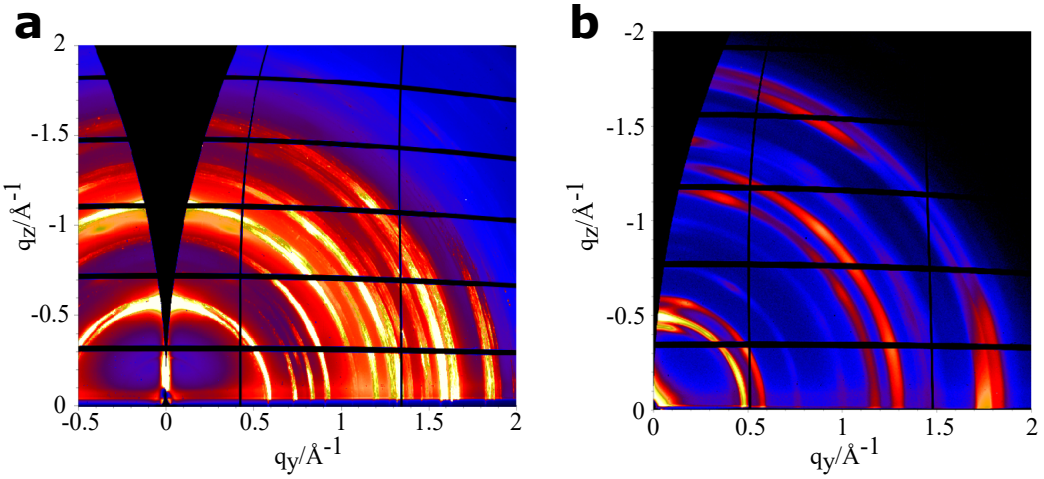

Fig. 6.4 GIWAXS of thin films of a) drop-cast TES-tetracene and b) evaporated TMS-tetracene, showing crystallinity in both samples, and some preferential alignment of crystal domains relative to the substrate. Measurements by Dr Andrew Pearson.

6.2.2 Crystallographic Characterisation

To confirm that the samples we have measured are crystalline, we used grazing incidence wide angle x-ray scattering (GIWAXS). These measurements were taken by Dr Andrew Pearson at the Diamond Light Source facility. Diffraction rings, known as Debye-Scherrer rings, are present in both samples, but are not complete rings, especially in the evaporated TMS-tetracene sample (Figure 6.4). This indicates that the crystal domains are not randomly orientated, and have some preferential alignment to the substrate. The crystalline order demonstrated by the strong Debye-Scherrer rings indicates that it is most likely valid to interpret results in terms of the crystal structures in Figure 6.1. Crystalline films of drop-cast TIPS-tetracene also show similar GIWAXS images, as reported by both Bayliss *et al.*[237] and Stern *et al.*[77]

6.3 Magnetic Field Effect in TMS-tetracene

It is well documented that morphology and intermolecular packing is critical for singlet fission to occur and in determining the rate of fission. First, to check if fission occurs in the series of derivatives, we measured the modulation of the PL from TES- and TMS-tetracene in a low magnetic field. This magnetic field effect (MFE), is the smoking gun of singlet fission that led to its original discovery in tetracene[65]. The results are

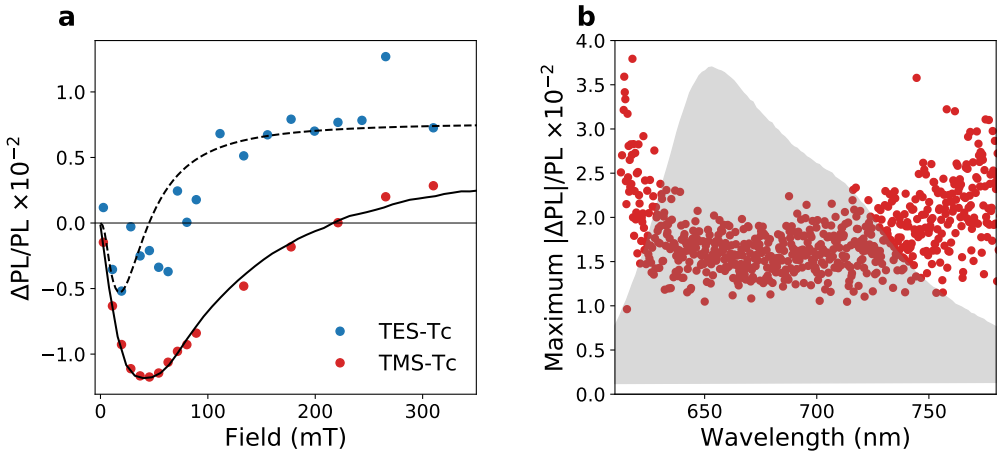

Fig. 6.5 Modulation of steady-state PL with low magnetic field. The samples were excited with a CW 520 nm pump. a) Change in integrated PL counts relative to 0 field is shown by blue circles for TES-tetracene and red circles for TMS-tetracene. The solid line is a fit for the TMS-tetracene data using the Merrifield model detailed in Chapter 4, with $J = 0.25D$ and $\epsilon = 13$. The dotted line is an indicative MFE for $J = 0.01D$ and $\epsilon = 1$. There is a large uncertainty ($\sim \pm 50\%$) associated with the x-axis due to the calibration from voltage across the electromagnet to B field at the sample position, however this error applies systematically to both TES- and TMS-tetracene. b) Magnitude of maximum change in TMS-tetracene PL under low magnetic field (representing the size of the negative peak at ∼50 mT in a) as a function of wavelength, showing very little dependence, indicating that the whole PL spectrum is modulated uniformly. Grey filled area shows steady-state PL spectrum.

shown in Figure 6.5, and are unambiguous in demonstrating the occurrence of singlet fission in both materials.

In TES-tetracene, due to low counts (possibly due to the low optical density of the spin-coated film), the noise on the MFE signal is too great to perform a fit. Nevertheless, there is evidence of a dip at low fields followed by an increase in PL at higher fields, and we have plotted a simulated MFE in the weak exchange coupling regime ($J \ll D$) in the dashed line. For the TMS-tetracene, we have performed a fit to the Merrifield model as described in Section 4.4, with parameters $J = 0.25D$ and $\epsilon = 13$, to fit the "stretched" line shape with a high crossing point from negative to positive field effect. This suggests that TMS-tetracene has a higher exchange coupling J between triplets than TES-tetracene, as we expect from the closer packing of the crystal structure[177,179]. We note that there is a large uncertainty, estimated to be $\sim \pm 50\%$, in the calibration of the x-axis of Figure 6.5a, which is very sensitive to both sample position within the electromagnet and the distance between the magnetic poles. While a calibration error could lead to a systematic error in the magnitude of J or ε extracted from this measurement, the difference in line shape between TES- and TMS-tetracene would not be affected by this error and thus we can still state that J and/or ε are higher in TMS-tetracene than TES-tetracene.

In Figure 6.5b we show how the magnitude of the TMS-tetracene MFE, which has the same profile across the spectrum, varies by wavelength. It is largely flat, suggesting that there is no non-fission emissive trap (as has been suggested to be the case in concentrated solutions of TIPS-tetracene[139]). Towards the edge of the spectrum, at lower and in particular higher energies, there appears to be an increase in MFE magnitude, however this is not significant and could be simply a result of the smaller PL signal, making the measurement of small changes in PL much noisier.

6.4 Transient Electron Spin Resonance

Leah Weiss measured transient electron spin resonance (trESR) for drop-cast samples of TES-tetracene and TMS-tetracene, shown in Figure 6.6. Alongside the MFE, this data is also clear evidence of singlet fission in these materials, as the polarisation pattern of AEEAAE (A = microwave absorption, or positive signal; E = microwave emission or negative signal as defined in more detail in Section 3.4) is consistent with the overpopulation of the $|0\rangle$ triplet sublevel relative to $|\pm\rangle$[68,86]. This overpopulation occurs for singlet fission because due to the relative singlet content of the different pair states in the high field basis, as calculated by Swenberg *et al.*[169] The AEEAAE

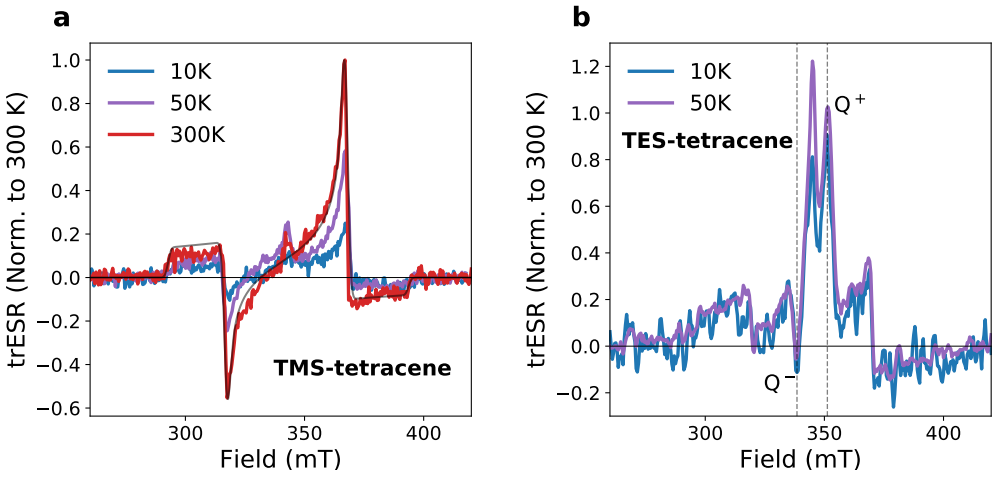

Fig. 6.6 trESR measured by Leah Weiss. a) trESR of drop-cast TMS-tetracene taken 300 ns after excitation with a 532 nm pump at 10, 50 and 300 K. Spectra are all normalised by the same factor (the peak of the 300 K spectra). A stronger signal was measured at higher temperatures. The polarisation pattern of AEEAAE is consistent with singlet fission. Black line shows a fit produced using Easyspin[233], with g = 2.002; D = 1415 MHz; E = 14 MHz and a line width of 2 mT. b) trESR of drop-cast TES-tetracene at 10 and 50 K taken 300 ns after excitation. Quintet peaks are indicated by the dashed lines.

polarisation pattern is not compatible with triplets formed from spin-orbit mediated intersystem crossing, which by biasing between the low-field $|x\rangle$, $|y\rangle$, $|z\rangle$ eigenstates can only form AAAEEE, AAEAEE, AEAEAE or the three inverse patterns of these[170].

The trESR of TMS-tetracene shows an intriguing temperature dependence - the signal increases substantially at higher temperatures, and is strongest at 300 K. This suggests that the trESR is sensitive to triplets formed by a temperature-activated process, namely the dissociation of strongly bound triplet pairs, particularly as at higher temperatures the spin-lattice relaxation time (T_1) is shorter. The zero-field splitting parameters for TMS, D and E, are the same (within error) as TIPS-tetracene[172], confirmed that the trESR signal is from dissociated triplets rather than strongly coupled pairs which would show shifts due to dipolar coupling. TES-tetracene did not show any clear trend with temperature, although the signal to noise ratio was too poor to measure at room temperatures. There were also more issues reported with light-induced degradation in TES-tetracene, with the central doublet signal dominating after prolonged exposure, indicating an accumulation of $S = \frac{1}{2}$ charges.

In trESR of TIPS-tetracene, as well as other singlet fission materials, $S = 2$ quintets have been observed, which form through the mixing of singlet and quintet manifolds

in strongly exchange-coupled triplet pairs[117,163,172–174]. These $S = 2$ triplet pairs are distinguished by an inner set of trESR peaks separated by approximately D/3 - one third of the separation of the outer peaks from weakly- or non-interacting triplets. There is a clear signal for quintets in the TES-tetracene trESR, with the transitions labelled as Q^+ and Q^- in Figure 6.6b, however we see no such quintet signature in the trESR of TMS-tetracene. This is consistent with the lifetime of the triplet pair, which from transient absorption and time-resolved photoluminescence we know has a lifetime of under 20 ns (Figures 6.10 and 6.12). The instrument response time for trESR is on the order of 300 ns, meaning that if quintets are formed, they are likely too short lived to be observed by this technique. The energies of the singlet and quintet pair states are split by $3J$, so another reason we may not see quintets is that the exchange coupling J could be greater than the thermal energy (25 meV at room temperature) which is available to activate the singlet-quintet mixing. Given that J in TIPS-tetracene has been measured as $\sim$5 meV[177], and expect J in TMS-tetracene to be stronger, $J \geq 25$ meV is plausible.

6.5 Transient Absorption of TMS-tetracene

6.5.1 Short-time Transient Absorption

Transient absorption, as described in Section 3.3, is one of our most powerful tools in studying singlet fission materials, allowing us to track populations of excited states from the fs to µs timescale. Figure 6.7 summarises the results of transient absorption measurements of evaporated films of TMS-tetracene with $\sim$100 fs time resolution, where the time delay is set by a mechanical delay stage with a range of $\sim$2 ns. A non-collinear parametric amplifier (NOPA) was tuned to 530 nm for the pump, close to the maximum ground state absorption and in close agreement to the non-tunable 532 nm excitation that was used for ns-resolution transient absorption (Figure 6.10). Three different broadband NOPAs were used to measure the visible, near infra red (NIR) and infra red (IR) transient absorption spectra in panels a, b and c of Figure 6.7 respectively.

Across all of these spectral regions, we see an evolution over the first picosecond followed by a slow decay of an approximately static spectrum. In the visible region, we see the edge of the ground state bleach (GSB) at the blue side of the spectrum, around 550 nm, in agreement with the absorption onset seen in the steady state (Figure 6.2e). There is a relatively sharp photoinduced absorption (PIA) at 630 nm, which increases

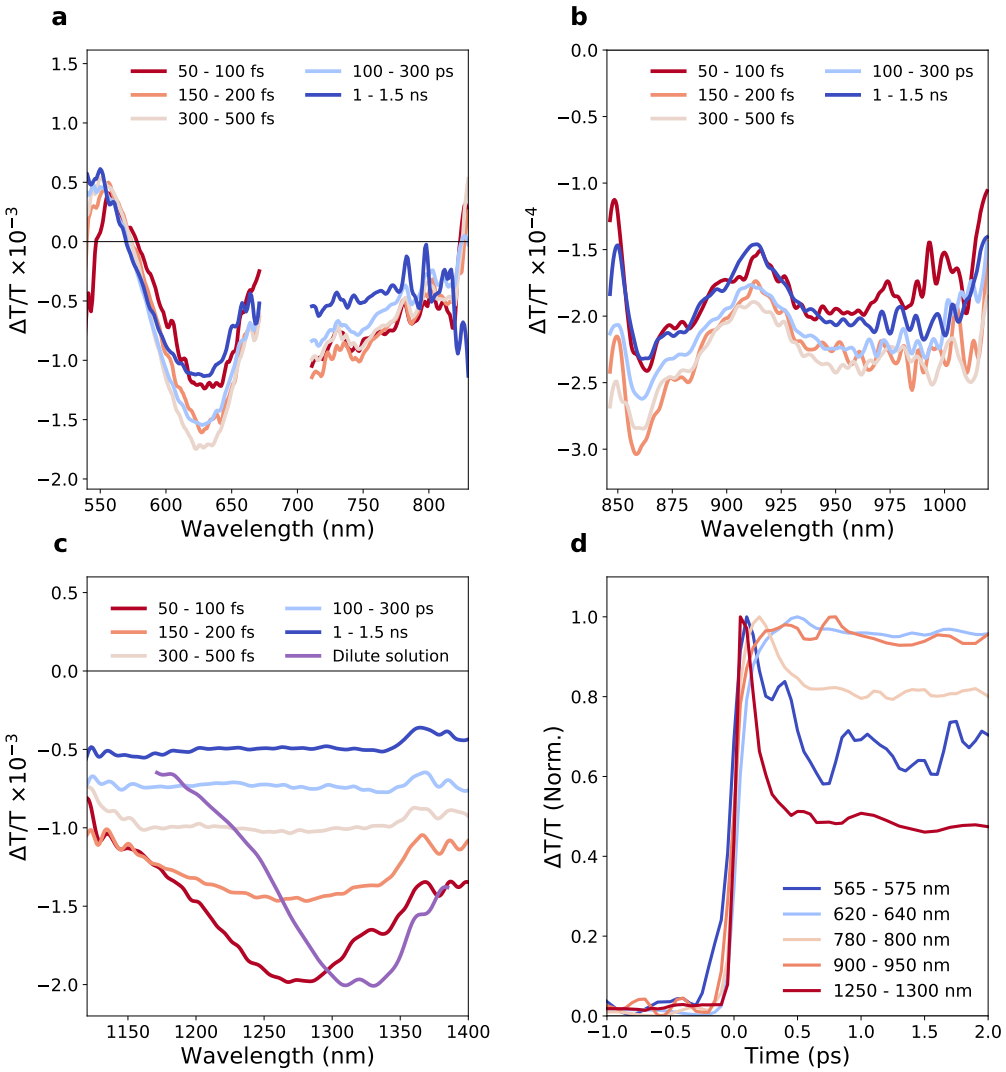

Fig. 6.7 fs-resolution transient absorption of films of TMS-tetracene. a) Visible NOPA probe, 530 nm pump with an excitation fluence of 44 μJcm^{-2}. A small part of the spectrum is omitted because the signal-to-noise ratio was too poor around 700 nm. b) NIR NOPA probe, 530 nm pump with an excitation fluence of 13 μJcm^{-2}. c) IR NOPA probe, 530 nm pump with an excitation fluence of 73 μJcm^{-2}. d) Early-time kinetics in the visible, NIR and IR regions showing concurrent evolution of the spectrum of the first 0.5 ps as the singlet exciton evolves to a correlated triplet pair.

over the first ps from excitation before decaying slowly. After a small spectral gap from 670–710 nm where the $\Delta T/T$ was too noisy at this fluence due to low counts in the probe NOPA, a broader PIA extends towards the NIR, out past 800 nm. Here, the spectrum notably evolves in the opposite direction, decreasing slightly, over the first ps. Transient absorption kinetics, plotting the magnitude of $\Delta T/T$ over the first 2 ps for some selected probe regions, are shown in Figure 6.7d, and show the concurrent evolution of the 630 nm and 790 nm PIAs, in opposite directions. In addition, we also observe a decrease in the magnitude of the positive $\Delta T/T$ at 570 nm. This is likely a short-lived stimulated emission (SE) signal, superimposed over the edge of the GSB, which decays concurrently with the evolutions of the PIAs observed in other parts of the spectrum.

In the NIR, there is a broad PIA with two overlapping peaks, all of which increases simultaneously at early times after excitation. The sharper spectral features in this region are likely a result of correlated noise from fluctuations in the NOPA. Regardless, the increase in magnitude of the spectrum over the first 500 fs is present across the whole NIR probe region.

The clearest result from this short-time TA is in the IR, where a distinct PIA peaked at 1275 nm decays over ∼100 fs to leave a broad featureless signal. Comparison to the IR transient absorption signal for a dilute solution, where singlet excitons are the only excited population present, verifies that the 1275 nm signal is from singlet excitons, which depopulate rapidly in the solid state but decay over nanoseconds, mostly radiatively, in dilute solution. There is a blue shift of this $S_1 \rightarrow S_N$ transition from solution to solid state, but this is not uncommon due to the different dielectric environment and shifted energy levels[120,267]. Fitting the decay of the 1275 nm kinetic gives a lifetime of 115 fs, shown in Figure 6.8a. However this is almost as fast as the instrument response function (IRF), which in the fit is modelled as a Gaussian with a full width half maximum (FWHM) of 102 fs. Therefore from this data we can only confidently place a lower limit on the speed of this depopulation of the singlet.

For better accuracy on the timescale of this early decay in the IR, we measured using an ultrafast compressed pump NOPA, in collaboration with Jesse Allardice. The pump, a NOPA that is itself pumped by the 38 kHz 1030 nm output of a light conversion PHAROS laser system, was broad in wavelength space to all it to be compressed in time using anti-chirp mirrors[220]. We used frequency-resolved optical gating (FROG), where the pulse is split in two and interfered with itself in a non-linear medium[268], to estimate the FWHM of the pulse to be 20 fs. With this pump and a broadband white-light probe from a yttrium aluminium garnet (YAG) crystal we were able to

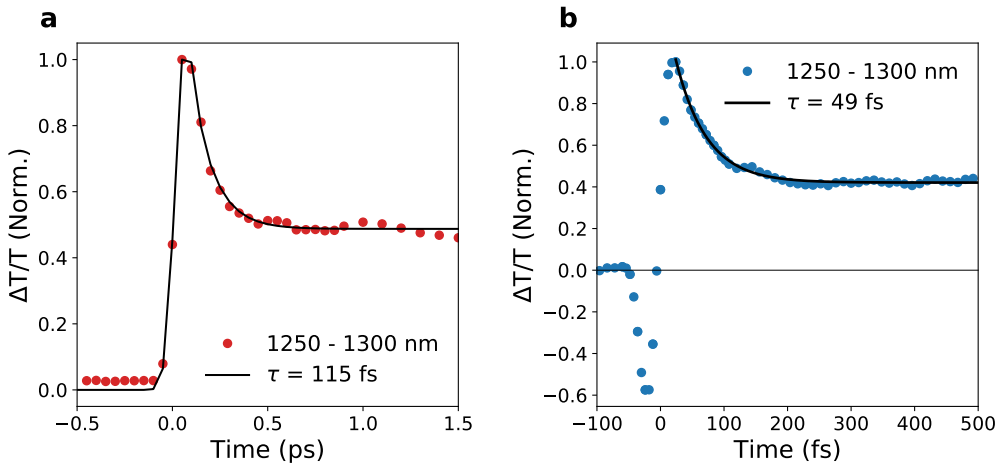

Fig. 6.8 a) Kinetic fit to the 1250–1300 nm kinetic in Figure 6.7d. The fit is a convolution of a Gaussian instrument response function with FWHM of 102 fs and an exponential decay of 115 fs with an offset to account for the residual signal from 500 fs onwards. b) Ultrafast transient absorption using a compressed 500 nm NOPA pump with FWHM ∼20 fs and a fluence of 44 µJcm^{-2}. Kinetic averaged over 1250–1300 nm white light probe generated using YAG. Black line shows an exponential fit after the coherent artefact with lifetime 49 fs. Ultrafast data measured in collaboration with Jesse Allardice.

measure the kinetic shown in Figure 6.8b. Due to the temporal compression of the pump, the coherent artefact, which is generally the result of non-linear processes in the sample[223], is much more significant. However, following the coherent artefact there is a relatively clean kinetic which fits extremely well to an 49 fs exponential decay.

Considering all of the spectra and their kinetics in Figure 6.7 we can see that there is an evolution of the singlet state occurring rapidly after photoexcitation. The initial excited state loses both its SE and IR PIA on sub-ps timescales, while concurrently there are more moderate shifts in the PIAs at 630 nm, 790 nm and 900–950 nm. Knowing from the trESR and MFE that this material definitely undergoes singlet fission, it follows that this ultrafast spectral evolution in the transient absorption is the transition from $S_1 \rightarrow (TT)_1$. The interpretation of the visible and NIR spectra is complicated by the fact that S_1 and $(TT)_1$ appear to have overlapping spectral transitions. Indeed, it seems that the 630 nm and 925 nm PIAs are slightly stronger transitions for $(TT)_1$ than for S_1, while the inverse is true at 790 nm. We also note that it is possible that at least some part of the increase in PIA at 630 nm is due to the decay of the SE, which from the steady-state PL (Figure 6.3f) we expect to extend out across much of the visible spectrum. It is not possible from transient absorption alone to distinguish

between a decaying SE or increasing PIA, however we will examine this further using time-resolved PL below in Section 6.6.

6.5.2 Triplet Sensitisation

In addition to using a dilute solution to obtain a reference spectrum for the singlet exciton (Figure 6.7c), we used a triplet sensitizer to measure a reference spectrum for the triplet exciton of TMS-tetracene in solution. A mixed solution in toluene of TMS-tetracene at 0.1 $\mathrm{mgml^{-1}}$ and N-methyl fulleropyrrolidine (NMFP) at its saturation concentration was excited with the third harmonic of a 1064 nm laser, 355 nm, and probed with a visible NOPA, with the delay controlled electronically with nanosecond resolution. Figure 6.9 shows the resulting spectra, normalised to the negative peak. TMS-tetracene is weakly absorbing at 355 nm, so the majority of photons are absorbed by NMFP. Over the first 5 ns, the photoexcited NMFP singlet intersystem crosses with >90% efficiency to a triplet exciton[232], which can be seen in the decay of the singlet PIA at 800 nm, leaving only the dominant NMFP triplet PIA at 685 nm. Then, over 5 µs, the triplets transfer from NMFP to TMS-tetracene. After 2–3 µs (pale orange) there is a mixture of NMFP and TMS-tetracene PIAs, and by 5–6 µs (pale blue) the 685 nm PIA from NMFP has completely decayed, leaving only the TMS-tetracene triplet spectrum, which has strong, narrow absorptions at 618 nm and 768 nm, and weaker absorptions at 560 nm and 690 nm.

The important caveat to both the reference triplet spectrum in Figure 6.9 and the reference singlet spectrum in Figure 6.7c, is that they are a reference for monomers in dilute solution. In the crystalline solid-state, excitons experience a vastly different dielectric environment, and can delocalise over neighbouring molecules. This affects their energy levels and the energies, broadening and intensities of the transitions between them, which dictate the transient absorption spectra we observe. While for the IR singlet PIA, the difference between solution and solid-state appears to be a blue shift with no major change in shape, there is no evidence of any spectral features similar to those of the reference triplet in solution, despite the convincing evidence that singlet fission is happening. It is not clear if this is purely a result of the move from solution to solid-state. In TIPS-tetracene, sharp triplet features present in solution are replicated in the solid-state[77], however as shown in Figure 6.3, the ground state absorption spectrum is not significantly broadened or shifted in TIPS-tetracene films, which is not true for TMS-tetracene. Given the significant broadening and shifting of the ground state absorption, it is likely the same would be true for the triplet absorptions. For example, in tetracene, which forms a closely packed herringbone

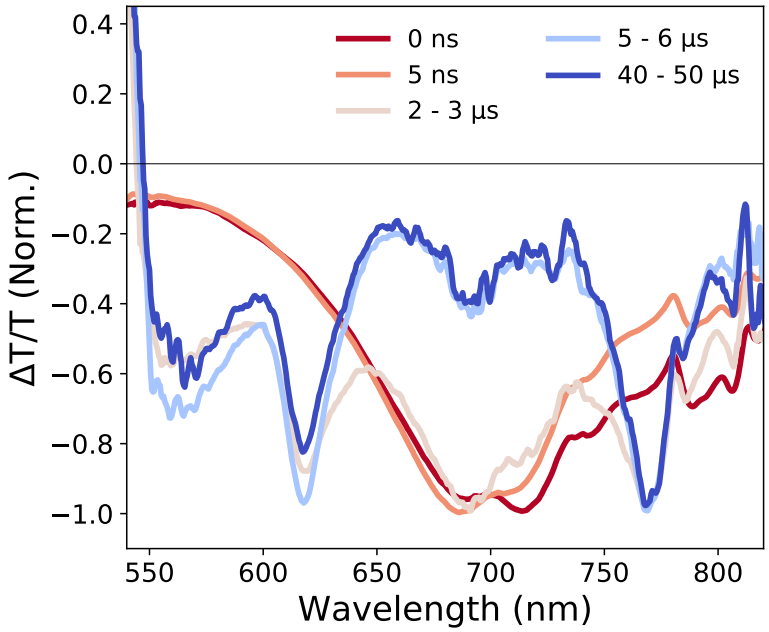

Fig. 6.9 Triplet sensitisation. Transient absorption spectra normalised to negative maximum for a solution of 0.2 mgml^{-1} TMS-tetracene and saturated N-methyl fulleropyrrolidine (NMFP) in toluene, excited at 355 nm. NMFP concentration is estimated to be 0.1 mgml^{-1}. Red-orange spectra show NMFP intersystem crossing from S_1 (red, 0 ns) to T_1 (orange, 5 ns). T_1 excitons transfer to TMS-tetracene over 5 µs to produce the blue triplet exciton absorption spectrum for TMS-tetracene, which persists for >50 µs.

structure thanks to the total absence of side groups and where almost quantitative fission has been observed, the PIAs present at long transient absorption delays are broad and relatively flat[74,75,228]. In general, triplet PIAs in acenes are difficult to measure in the solid state[76,269]. This is partially due to the preferential alignment of the crystalline domains with the long molecular axis, which is parallel to the $T_1 \rightarrow T_N$ transition dipole, close to normal to the surface of the substrate[76,270–273]. With a probe beam propagating in the direction of the normal to the substrate, there is relatively small $\vec{E}$-field intensity in the direction of the transition dipole for triplets. This is the opposite of case for singlets, because the $S_1 \rightarrow S_N$ is along the short molecular axis of acenes[76].

We also speculate that the correlated pair state here is sufficiently coupled that it rearranges the excited state absorptions, although the magnitude of this effect is unknown. In this system we cannot distinguish by the spectral shape whether the transient absorption signals seen at 1 ns are from correlated pairs or free triplets (or a combination of both). We speculate that clear, narrow triplet PIA signals, as well as the distinction between (TT) and $T + T$ PIAs, are present in TIPS-tetracene[77], but not tetracene or TMS-tetracene, thanks to the weak intermolecular coupling inherent to the TIPS-tetracene crystal structure.

6.5.3 Long-Time Transient Absorption

To observe the subsequent decay of the state present at the end of the 1.5 ns of mechanical delay in Figure 6.7, we use a ns-resolution electronic delay generator to trigger a ∼1 ns pulse length laser, with a second harmonic module to convert the 1064 nm fundamental to 532 nm. Visible and NIR NOPA probes were used, and are plotted together in Figure 6.10a. The visible and NIR PIAs decay concomitantly, with the kinetics taken around 640 nm shown in Figure 6.10b–d. Present in both the 1–3 µs spectrum in panel a and the kinetics in panel b, is an anomalous positive signal at long times after the main signal has decayed that covers the visible and NIR. Genuine positive ΔT/T signals present from changes to the populations of electronic states arise from either GSB or SE. There cannot be a GSB at these wavelengths as there is no ground state absorption, and there is no significant PL at these long time delays (see Figure 6.11), ruling out a SE signal. Therefore we can deduce that this is an artefact caused by pump-induced heating. When we experiment with much higher fluences in panel c, we see that the relative magnitude of the artefact grows with respect to the real signal. This non-linear behaviour of the artefact occurs due to the limited capacity of the substrate to absorb and dissipate the increasingly extreme amounts of energy

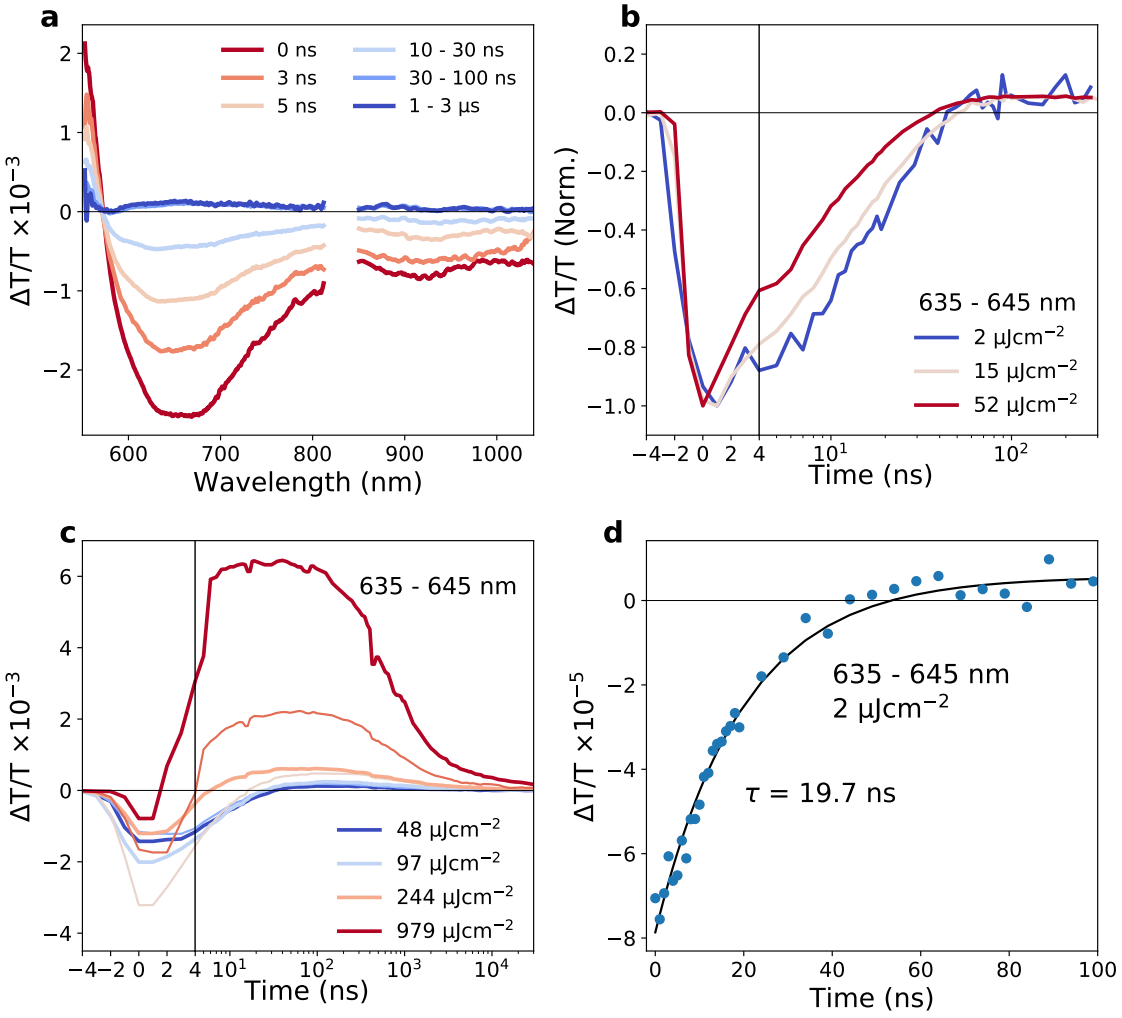

Fig. 6.10 Nanosecond-resolution transient absorption of evaporated films of TMS-tetracene. a) Visible and NIR NOPA probes, 532 nm pump with excitation fluences of 52 and 127 µJcm^{-2} for visible and NIR respectively. b) Kinetics at 635–645 nm, scaled to -1 for the peak response, for a range of low fluences, all showing an anomalous positive signal at long times. c) Kinetics at 635–645 nm at higher fluences showing the non-linear nature of the anomalous positive feature, demonstrating it to be an artefact, likely a result of thermal modulation due to the dissipation of heat from the pump pulse. d) An exponential fit to the lowest fluence shown in b), with the decay constant of 19.7 ns.

absorbed by the sample from the excitation pulse. Residual heat in the sample can modulate its refractive index, changing the proportion of the probe that is transmitted and therefore giving an anomalous $\Delta T/T$.

In Figure 6.10b, the excitation fluences are low enough that the artefact appears to be in a linear regime, as the normalised kinetics show the same relative size of the artefact at 1 µs compared to the peak at t=0. However, there is still some fluence dependence on the decay of the triplet-pair signal. This is presumed to be a result of annihilation between triplet pairs, although the mechanism and products of such annihilation events are not known. At the lowest measured fluence for TMS-tetracene, $2\,\mu J cm^{-2}$ per pulse, where the peak $\Delta T/T$ signal is only 8×10^{-5}, the decay fits well to a single exponential lifetime of 19.7 ns (see Figure 6.10d). A lifetime of ∼20 ns is very short for triplets in an acene material, where there is little spin-orbit coupling that could allow transitions from T_1 to S_0. Therefore, we propose that this lifetime is for strongly-bound correlated triplet pairs which remain in the singlet manifold and therefore efficiently couple to the ground-state. The long-lived signals in trESR of free triplets are from a minority population, that is not visible in transient absorption at low fluences due to the small population and at high fluences due to the strong thermal artefact. Further evidence to support this interpretation comes from the time-resolved PL below.

6.6 Time-resolved Photoluminescence of TMS- and TES-tetracene

6.6.1 TMS-tetracene

We have already noted that the PL of solid-state TMS-tetracene is strongly red-shifted from the dilute spectrum, and in this chapter we add temporal resolution and temperature dependence to describe further how the novel crystal structure is affecting the PL of TMS-tetracene. Using an intensified charge-coupled device (ICCD) we can detect PL over a large dynamic range, especially compared to transient absorption, where we can only probe 1 or 2 orders of magnitude depending on peak the size of the signal. Having said that, we add the caveat that the photoluminescence quantum efficiency (PLQE) in evaporated films of TMS-tetracene at room temperature is around 1%. This is comparable to the 1–3% reported for different films of TIPS-tetracene[77]. However, this means that when studying the PL of these materials we are effectively

blind to 99% of the excitations, and must be wary of attributing too much significance to minority species that only appear to have a large significance in the PL.

Using a helium cryostat together with an ICCD, which has a time resolution of ∼3 ns, we studied the PL of TMS-tetracene from 10–296 K, with the results summarised in Figure 6.11. Panel a shows the results at room temperature. Regrettably, pump scatter and PL from contamination which could not be removed from the cryostat dominates the first two time-slices. This is particularly problematic for TMS-tetracene because it is so weakly emitting, with a PLQE of around 1%. However, by comparing the "No sample" spectrum (dashed purple), which was measured with a blank substrate in the cryostat, with the 0 ns spectrum, we can infer that the sample is emitting significantly in these first two spectra. When scaling up the "No sample" spectrum to match the 0 ns spectrum at 800 nm, we see that the largest difference between the two spectra is around 620 nm, significantly higher energy than 650 nm peak of the spectra from 6 ns onwards, with the 3 ns spectrum in between. Therefore we conclude that there is a red shift of the sample PL over the first 6 ns, and it is likely that this is a result of some PL from the singlet exciton, before it forms the triplet pair state. However, according to our ultrafast transient absorption measurements (Figure 6.8b) the triplet pair forms ∼60,000 times faster than the IRF of the ICCD even without the issue of contamination, so we cannot resolve this process using these measurements.

In panel b, the spectra at 6 ns, after stray pump light and any PL from the stubborn contamination within the cryostat has decayed, is compared over the full range of temperatures studied. The spectrum at 296 K matches the steady-state PL spectrum reported in Figure 6.3f. In general as the temperature lowers, the spectrum narrows and the PL yield increases very slightly (the integrated area beneath the 50 K spectrum is only 16% greater than that of the 296 K spectrum). This trend follows from 296 K down to 50 K, however at 10 K, the lowest temperature measured, the spectrum is somewhere in the middle of the pack, between 150 K and 200 K. Interestingly, we do not see a significant increase in PLQE as the temperature lowers, as was the case for polycrystalline samples of TIPS-tetracene[77]. A similar break from the trend at 10 K is seen in the kinetics of the PL decay, shown in Figure 6.11c. The initial exponential PL decay gets slower as the temperature lowers down to 150 K, below which it is approximately constant. However, beyond ∼200 ns, the PL kinetic deviates from an exponential decay, and there is an additional delayed component. The magnitude of this delayed component relative to the initial component decreases as the temperature decreases down to 100 K, with 50 and 10 K anomalously slightly above 100 K.

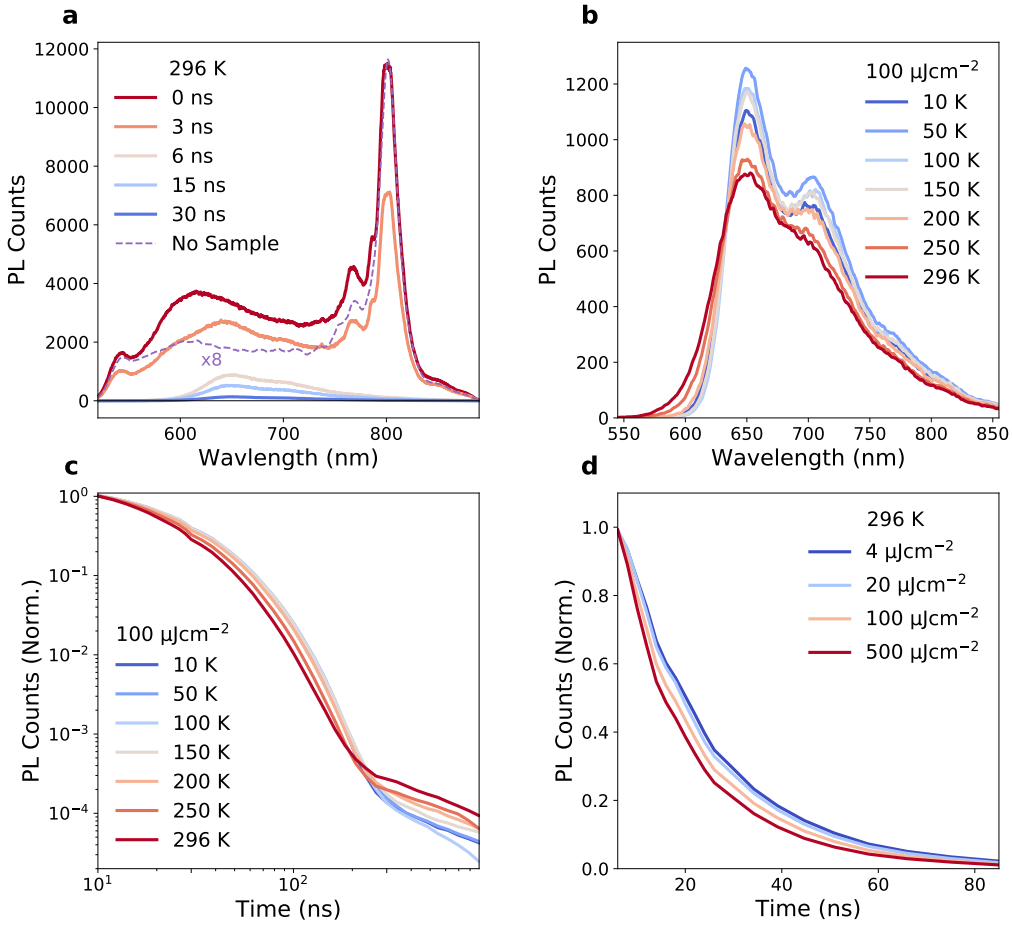

Fig. 6.11 Time-resolved and temperature-dependent PL of evaporated films of TMS-tetracene, measured using an intensified CCD (ICCD) and liquid Helium cryostat. a) Spectra at room temperature and an excitation fluence of 100 µJcm^{-2}, showing the large artefact at early times from a combination of pump scatter (800 nm is the fundamental which drives the pump NOPA and is not fully filtered out) and stubborn contaminants in the cryostat. Dashed purple spectrum is a reference of the pump scatter and cryostat contaminant PL which could not be removed, measured with a blank substrate in the cryostat. b) Spectra 6 ns after excitation with 500 nm pump at a range of temperatures, with an excitation fluence of 100 µJcm^{-2}. c) Kinetics of the 650 nm PL peak shown on a log-log plot for a range of temperatures, normalised to the counts 10 ns after excitation for each temperature. d) Normalised kinetics at room temperature for a range of excitation fluences, showing a weak dependence of the early decay on excitation density, that might arise from singlet-singlet or pair-pair annihilation.

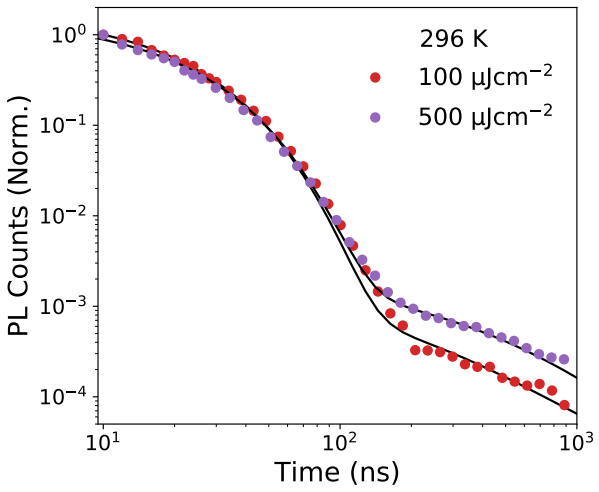

Fig. 6.12 A kinetic fit for the 650 nm PL peak of an evaporated TMS-tetracene film, to a model with a combination of an exponential decay with $\tau = 16.6$ and 17.5 ns and non-geminate triplet-triplet annihilation with annihilation constant $\gamma = 0.0038$ and 0.0021 $\mathrm{cm^3 ns^{-1}}$ for 100 and 500 $\mu\mathrm{Jcm^{-2}}$ respectively. Full details of the TTA model are in Chapter 4.

In a parallel to TTBP films studied in Chapter 4, we assign this delayed PL to TTA. Using the same model as Chapter 4, we can capture the delayed PL behaviour (Figure 6.12). This model has an initial exponential decay with a lifetime of 17 ns. The delayed PL is fit with a bimolecular TTA component (PL $\propto$ [T]^2 and $\frac{d[T]}{dt} = -\gamma[T]^2$). The exponential decay of 17 ns is close to that of the PIA in Figure 6.10d which has a lifetime of 19.7 ns, and we can interpret this as either geminate TTA or direct emission from the correlated pair state. If, as the decay lifetime in transient absorption and PL results suggest, the strongly-coupled pair state in TMS-tetracene remains in a singlet state, it can couple radiatively to the ground state, and we can consider this to be direct emission from a triplet pair, and the difference becomes semantic. The low radiative efficiency of the 17 ns decay, even at cryogenic temperatures, is surprising and remains an open question for further investigation.

We were able to observe a weak fluence dependence of the monomolecular decay, shown in Figure 6.11d and it was in agreement with the fluence dependence observed in transient absorption Figure 6.10b. The weak delayed PL was unresolvable from the noise at pulse energies lower than 100 $\mu\mathrm{Jcm^{-2}}$ (for example those shown in light and dark blue in Figure 6.11d). However, comparing just 100 and 500 $\mu\mathrm{Jcm^{-2}}$ per pulse in Figure 6.12, we can see an increase in the relative intensity of the delayed component. In effect we also have a third data point to confirm this trend, as the 4 and 20 $\mu\mathrm{Jcm^{-2}}$

measurements have no detectable delayed PL after the initial decay. This is a result of the quadratic nature of bimolecular processes - below a given initial concentration, triplets will be further apart than their diffusion length and will decay non-radiatively before they have the chance to meet and annihilate.

Time resolved PL has deepened our insight to the photophysics of TMS-tetracene relative to looking at the transient absorption in isolation, by highlighting the presence of delayed PL from bimolecular TTA, which indicates two things. Firstly, triplet pairs, which we understand are strongly bound in the closely packed crystal structure of TMS-tetracene, are to some extent able to separate and form free triplets (even at cryogenic temperatures), which can go on to annihilate with each other and emit a photon. The delayed PL lasts for at least 1 µs, much longer than the lifetime of the transient absorption signal, implying that the long-lived population of triplets is small, and does not have a detectable absorption cross-section. This is confirmed by our interpretation of the µs-lifetime trESR signal as free triplets. Secondly, the temperature dependence of the delayed PL suggests that there is a higher rate of pair dissociation at higher temperatures, leading to higher triplet concentrations at a given excitation density, again in agreement with our interpretation of the trESR. This is in line with other endothermic fission systems such as TIPS-tetracene[77], tetracene[171], and the study of TTBP in Chapter 4.

6.6.2 TES-tetracene

We also measured the kinetic dependence of photoluminescence of TES-tetracene, which is shown in Figure 6.13. Although this PL is dominated by monomer-like singlet emission, if we look closely we can see that there is some tell-tale signs that fission is happening. Over the first 30 ns, an increasing contribution at at 640 nm peak can be attributed to triplet pair emission, while at very long times, after triplet pairs have dissociated/decayed, there is a "pure" singlet spectrum (300–500 ns) which can be attributed to TTA to the singlet. This is reminiscent of the PL of TIPS-tetracene in concentrated solution, as reported by Stern *et al.*[82] and Dover *et al.*[139], where a red-shifted feature dominates at medium delays, but the monomer singlet spectrum dominates at early and very late times. The similarity of the PL behaviour and the quintet formation in trESR implies a similar coupling regime for the two materials, in contrast to TMS-tetracene.

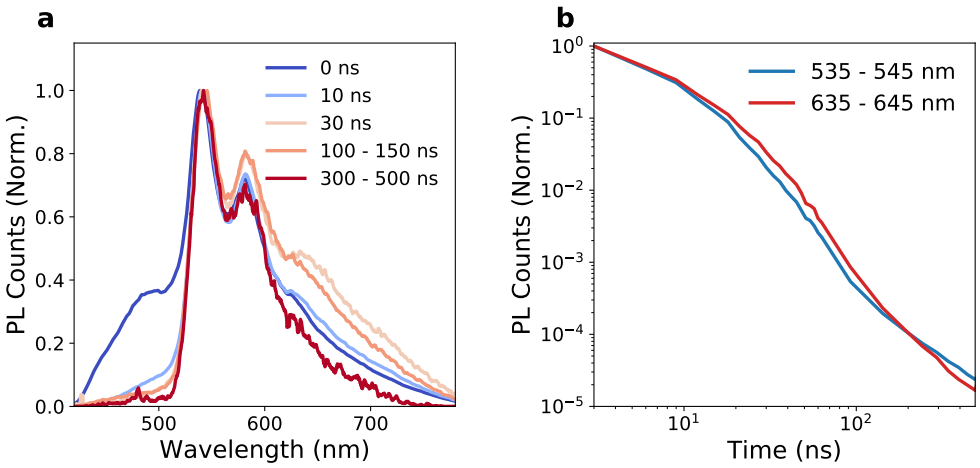

Fig. 6.13 Time-resolved PL of a TES-tetracene film, measured using ICCD. a) Spectra at room temperature, excited at 400 nm with a fluence of 100 µJcm^{-2} per pulse, with an artefact at early times around 420-500 nm from epoxy PL. b) Normalised kinetics at room temperature for the two main features in the spectrum, showing a difference in their decay over time.

6.7 Discussion

Above, we have described the evidence that in TMS-tetracene, singlet excitons undergo ultrafast (∼50 fs) fission to form strongly coupled triplet pairs, which are weakly emissive and decay monomolecularly with a lifetime of <20 ns. A subset of these triplet pairs dissociate, as we observed both free triplets in trESR and delayed PL from bimolecular TTA, which is suppressed at lower temperatures and excitation densities.

In TIPS-tetracene, there has been some debate over the role of the red-shifted, delayed PL within the singlet fission mechanism. Since its original observation, it has typically been assigned to emission from an intermediate triplet pair state[77,82,177], but interpreted by others as an excimeric trap state which is detrimental to singlet fission yields[139]. This argument centres on a microscopic reversibility question - if a process must proceed one direction through an intermediate state, must the reverse process also proceed via the same intermediate? Given the energetics of endothermic fission compared to exothermic TTA, this appears to be an unnecessary constraint, validating the interpretation of the red-shifted PL as emission from an intermediate pair state.

The majority of the PL from TMS-tetracene is from a significantly red-shifted state, suggesting that if this state were a trap, then the majority of excitations are falling into it. Given the rapid formation of the pair state (Figure 6.8) and the fact that the whole spectrum has a similar magnitude MFE (Figure 6.5), we assert that the red-shifted

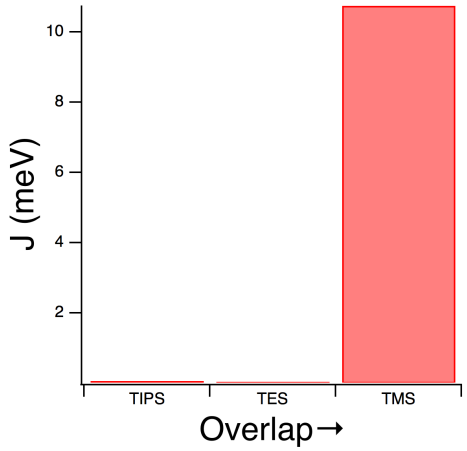

Fig. 6.14 Calculations of the inter-triplet exchange coupling for the closest pairs of molecules in the crystal structures of TIPS-, TES- and TMS-tetracene. Calculations by Dr Elliot Taffet

PL is a triplet pair state rather than a trap. We were not able to directly measure the TMS-tetracene triplet energy by phosphorescence, but based on its similarity to tetracene and TIPS-tetracene we expect the total energy of two independent triplets to be higher than that of a singlet. Despite this, the energy of the emissive pair state is evidently lower than that of the singlet, and we attribute this to a binding energy related to the strong coupling between the triplets and excimeric reorganisation of the molecules in the excited state (i.e. moving away from the ground state minimum on the potential energy surface - see Figure 2.4). It has been demonstrated that greater exchange couplings (J) in TIPS-tetracene lead to larger red-shifts in the spectrum of triplet pair emission[177]. Given the closely π-stacked morphology of TMS-tetracene, we anticipate J would be significantly larger than even the largest couplings in TIPS-tetracene. Indeed, calculations by Dr Elliot Taffet, using a methodology that has been experimentally verified in TIPS-tetracene[179], indicate that J for nearest-neighbour dimers in TMS-tetracene should be $\sim$2 orders of magnitude larger than TES- and TIPS-tetracene (see Figure 6.14). This stronger coupling seemingly presents a larger energetic barrier to the separation of the triplet pair, in line with the small free triplet population that we have observed via trESR and bimolecular TTA at higher excitation densities. In addition, the stronger coupling could explain the lack of quintet pairs seen in trESR, by putting singlet-quintet mixing energetically out of reach. We propose that the lack of singlet/quintet mixing acts on the triplet pair lifetime by two possible

functions. Firstly, while there is not evidence that it is necessary for the pair to dissociate via the quintet state in all cases[61], dissociation is easier when the binding energy is less than the thermal energy kT, which is more likely to be the case when J is small enough to allow singlet-quintet mixing (because binding energy scales with J). Secondly, singlet-quintet mixing allows some degree of spin protection from TTA to the singlet, as while the pair is in the quintet state it will be less strongly coupled to the ground state, and the lifetime of the pair will be extended, allowing more time for triplet hopping and pair dissociation to happen.

Interestingly, when comparing to tetracene[75] or TIPS-tetracene[77], we do not see the same increase in PLQE or extension of PL lifetime when temperature is lowered for TMS-tetracene. The 20-fold increase in PLQE at 10 K (60%) vs room temperature (3%) in TIPS-tetracene has been interpreted as temperature activated pair separation[77]. At higher temperatures, a majority of triplet pairs separate before they have time to decay geminately, while at lower temperatures separation is much slower, allowing more time for the pairs to decay radiatively before separation can happen, as evidenced by the extended lifetime of the PL at lower temperatures. By contrast, in TMS-tetracene, the pair lifetime at room temperature is only 17 ns and this does not increase substantially at lower temperatures ($\tau = 16.6$ ns at room temperature and $\tau = 21.8$ ns at 10 K). We interpret this to be a result of the strongly coupled pair state in TMS-tetracene, which does not mix between singlet and quintet spin states, allowing relatively fast radiative and non-radiative recombination pathways to the ground state (the low PLQE of ∼1% requires that the majority of the pairs must be decaying non-radiatively). Having said this, while the pair lifetime is only extended by 30% (compared to 2000% in TIPS-tetracene) at lower temperatures, there is still a detectable reduction in pair dissociation across our trESR and delayed PL measurements.

Another likely factor in the low population of free triplets in TMS-tetracene, distinct from the strong coupling within the pair, is the relatively distant position of the next-nearest neighbour outside of the π-stacked dimers. Triplet pair separation is driven by hopping of one of the triplets to the next-nearest molecule[61]. Given the crystal structure of TMS-tetracene is made up of closely-packed dimers that are relatively distant from each other, it is possible that the limited opportunities for triplet hopping outside of the close dimers plays a role in the low yield of free triplets. Compared to tetracene, where the herringbone crystal structure[274] made possible by the lack of side groups has equal distances between nearest and next-nearest neighbours, we expect triplet hopping in TMS-tetracene to be significantly impeded, despite the greater intermolecular contact within the nearest-neighbour dimers. In TIPS-tetracene's crystal structure (Figure 6.1),

all of the molecules are further apart (analogous to the next-nearest neighbours in TMS-tetracene), and indeed in polycrystalline TIPS-tetracene films triplet pair separation is also suppressed, presumably a result of slow triplet hopping due to the spaced-out crystal structure[77].

6.8 Conclusions and Outlook

In this chapter we have introduced two new materials that are closely related to the canonical endothermic singlet fission material, tetracene, and the previously characterised TIPS-tetracene: TES-tetracene and TMS-tetracene. As monomers, their photophysics are effectively identical to tetracene or TIPS-tetracene, however the reduction in bulkiness of the solubilising side groups leads to different crystal structures, especially in the case of TMS-tetracene, which packs in π-stacked pairs separated by only $\sim$3.8 Å. Through trESR and the magnetic field effect on luminescence we have confirmed that despite this radically different packing motif, singlet fission is still active in both TMS-tetracene and TES-tetracene.

We used ultrafast transient absorption to show that photoexcitations lose singlet character in $\sim$50 fs, a timescale that outcompetes tetracene[75,228], TIPS-tetracene[77] and any other endothermic fission system to our knowledge. A weakly emissive triplet pair state is formed, which decays on a 17–19 ns timescale, verified by time-resolved PL. From trESR and delayed bimolecular PL after the pair states have decayed, we know that some sub-population of the triplet pairs are able to dissociate to free triplets, and that this is a larger population at higher temperatures, indicating some degree of temperature activation is involved, as in TIPS-tetracene[77]. However, the free triplet population is too small to observe in transient absorption. Comparing to crystalline tetracene, which forms a herringbone structure with edge-on packing that has less orbital overlap between neighbours, we notice that triplet pair formation rate correlates with intermolecular contact.

We conclude that the close packing of TMS-tetracene is to some degree a double-edged sword - while the significant orbital overlap drives unprecedentedly fast pair formation for an endothermic system, it also seems to limit the degree to which pairs can dissociate, and the pair state's relatively short lifetime does not increase appreciably as the temperature is lowered, unlike TIPS-tetracene[77].

From these results we propose that when designing singlet fission systems, closer packing with increased orbital overlap is desirable to speed up fission, but only up to a certain point, beyond which there can be drawbacks in terms of triplet dissociation.

Triplet hopping away from the strongly coupled pair must also be optimised to allow for efficient dissociation as well as formation of the pair state. Future work focused on triplet dissociation and the nature of the binding of the correlated triplet pair would be very interesting.

Chapter 7

Conclusions and Outlook

In this thesis, we have studied singlet fission in three different contexts. Through our case studies, we have expanded the library of confirmed fission materials, particularly in the direction of better photostability, and sought to extract generalised design lessons from our examples.

First, in Chapter 4, we looked at TTBP, an acene that has been modified to enhance its stability by benzannulation to give it triphenylene "wings". We found that although this modification does not prevent singlet fission, it does change the photophysics, giving TTBP a remarkably high photoluminescence quantum efficiency (PLQE) despite the fact that photoexcitations rapidly convert to triplet pairs with a quantitative yield. Through transient absorption, time-resolved photoluminescence and optically detected magnetic resonance, we showed that this high PLQE is a result of triplet-triplet annihilation - both geminate and non-geminate - and proposed that it is a sign of suppressed non-radiative triplet decay. The high PLQE from radiative TTA should be a benchmark against which fission materials are compared, in order to make sure that when implemented in a device, they do not suffer from significant non-radiative voltage losses.

The time-resolved photoluminescence of TTBP is particularly complex, with a red-shifting then blue-shifting peak illustrating the processes of pair formation, dissociation, and annihilation. We used cryogenic photoluminescence and transient electron spin resonance to show that triplet pairs dissociate by a temperature-activated process. While the incomplete dissociation of triplet pairs means that TTBP itself is not the perfect singlet fission material, the benzannulation of acenes shows much promise as a route towards stable materials that can use singlet fission to surpass the single-junction solar cell limit.

In Chapter 5, we investigated a different strategy for stable singlet fission materials: using excited-state aromaticity to stabilise the triplet state and design resilient chromophores with the requisite $E(T_1)/E(S_1) \sim 0.5$. Quantum chemical calculations indicate that triplet aromaticity is correlated to the singlet-triplet energy gap, and by deliberately devising molecules which include a [4n] cyclic contribution in their resonance structure, for example by the inclusion of five-membered heterocycles, the excited triplet state can be made more aromatic. This application of Baird aromaticity has the twin benefits of both lowered triplet energy to make fission more favourable, and stabilising the triplet state - equivalent to the way that benzene is more stable than cyclobutadiene in the ground state.

We applied this principle of excited-state aromaticity to the designing of a family of singlet fission candidates based on the industrial dye *cibalackrot* to produce six indolonaphthyridine thiophene (INDT) derivatives. Five out of six of the materials tested showed evidence of singlet fission, and in the best performing derivative, CN-INDT, we estimate the triplet yield to be in the region of 60–90%. Importantly this is in a molecule which demonstrated far superior stability to TIPS-pentacene, a material without excited-state aromaticity. The reason for the sub-optimal yield is that fission only occurs at morphological hot spots in these materials. However, we demonstrated that we can tune the density of hot spots by editing the sample preparation method, or by changing the solubilising side groups. Given that singlet fission at the hot spots themselves appears to be fast, we see no reason that with the correct morphology, an INDT derivative could not be tuned to produce a quantitative singlet fission yield. We imagine that this would be a very productive direction to take this work next.

We also used these materials as a platform to investigate intramolecular fission in covalent dimers. Of three INDT dimers tested, only one, with a para-phenyl linker, exhibited signs of fission. Even in this case, the generation of triplets depended on solvent polarity, implying that CT intermediates play a role in triplet pair formation in these dimers. This result was achieved using dimers synthesised from H-INDT monomers, despite the fact that in the films studied, H-INDT was the only candidate not to show fission. The evidence from the dimers indicates that it was the outlier morphology of H-INDT that was the limiting factor, rather than the energetics.

Though our exploration of aromaticity has been limited to a single family of materials, we demonstrated wide tuneability and the same design rules can be applied to other materials systems. Examples of molecules beyond INDT with a [4n] cyclic contribution to their resonance structures, indicating they should have an aromatic triplet state, include DPP (where fission has already been documented[122–124]), indigo,

isoindigo, pechmann dyes and fulvalenes. All of these might be productive avenues for singlet fission studies, and in particular it would be interesting to look for molecules with higher band gaps that might pair better with silicon than INDT or *cibalackrot*. More broadly, the same approach may be used to tune the exchange energy in other organic systems where triplets play a critical role: to mitigate losses in organic photovoltaics, harvest additional carriers in light-emitting diodes, or broaden the materials library for photon up-conversion.

In Chapter 6 we introduced two new materials, TES-tetracene and TMS-tetracene, which as monomers in dilute solution behave identically to the well-characterised fission material TIPS-tetracene. However, TES-tetracene has smaller side groups than TIPS-tetracene, and TMS-tetracene smaller still, which leads them to crystallise in starkly different structures. Particularly of interest is TMS-tetracene, which forms close π-stacked dimers separated by only $\sim$3.8 Å but which are relatively isolated from each other. This results in photoexcitations that lose singlet character in $\sim$50 fs, unprecedented for an endothermic system. However, the frustrated hopping to next-nearest neighbour molecules outside of the closely-packed pairs seems to prevent pair dissociation and leads to the majority of triplet pairs in TMS-tetracene decaying on a 17–19 ns timescale. These triplet pairs are strongly exchange coupled, as evidenced by their significantly red-shifted photoluminescence, the seemingly forbidden mixing into the quintet manifold, and calculations based on the TMS-tetracene crystal structure. Still, a subset of the population are able to dissociate, and this process is temperature-activated, with a higher free triplet population observed at higher temperatures.

We conclude that the close dimer packing of TMS-tetracene is responsible for both the fast pair formation and the limited ability to dissociate these pairs. From this we propose that when designing optimal fission systems, closer packing with increased orbital overlap is desirable to speed up fission, but there must also be opportunities for triplet hopping away from the strongly coupled pair in order to allow long triplet lifetimes and to harvest triplets for photovoltaic applications. This has already been shown to be the case in dimers and oligomers in solution, where triplet pairs trapped on dimers are outlived by those where the triplets hop apart[154].

There are also cross-cutting findings between these studies. Most strikingly, there are similarities between the behaviour of TTBP and TMS-tetracene, such as the lack of quintet features seen in trESR. In both cases, it seems that the exchange coupling regime may be too strong to allow singlet-quintet mixing. Likewise, in both cases, not all triplet pairs are able to separate, and we speculate that this could indicate a role for the quintet state in the efficient separation of the pair state. Further investigation

of different coupling regimes is needed to reveal more about the binding of the triplet pair state and how to optimise its dissociation. We are also interested by the question of why the PLQE of TTBP is so much higher than that of TMS-tetracene. While the greater relative contribution from non-geminate TTA in TTBP is likely a factor, it also seems that the strongly-coupled pair is a much more efficient emitter in TTBP (and TIPS-tetracene) than TMS-tetracene, for which we do not yet have an explanation.

More generally, we have shown in multiple systems the importance of morphology in designing an optimal singlet fission system, and how a balance must be struck between a morphology that optimises pair formation and one that optimises pair separation. In addition, we have demonstrated two unique strategies that can improve the stability of singlet fission materials, which is a necessary direction for further development to move towards commercial singlet fission photovoltaics. These lessons could help enable the development of the next generation of solar technology, making better use of the sun's spectrum, and eventually helping to wean humanity off its destructive fossil fuel addiction and mitigate the effects of climate change.

List of Publications

The following peer-reviewed publications relate to work presented in this dissertation.

1. **Budden, P.***, Fallon, K.*, Salvadori, E., Ganose, A., Savory, C., Eyre, L., Dowland, S., Ai, Q., Goodlett, S., Risko, C., Scanlon, D., Kay, C., Rao, A., Friend, R., Musser, A., Bronstein, H., "Exploiting excited-state aromaticity to design highly stable singlet fission materials", J. Am. Chem. Soc. 2019 (*equally contributing authors)

2. **Budden, P.**, Weiss, L. R., Müller, M., Panjwani, N., Dowland, S., Allardice, J., Ganschow, M., Freudenberg, J., Behrends, J., Bunz, U. H. F., Friend, R. H., "Singlet Exciton Fission in a Modified Acene with High Photoluminescence Yield", *in review, Nature Communications*

The following list of peer-reviewed publications represent work contributed to during this PhD but that were lead by others.

3. Allardice, J., Thampi, A., Dowland, S., Xiao, J., Gray, V., Zhang, Z., **Budden, P.**, Petty, A., Davis, N., Greenham, N., Anthony, J., Rao, A., "Engineering Molecular Ligand Shells on Quantum Dots for Quantitative Harvesting of Triplet Excitons Generated by Singlet Fission." J. Am. Chem. Soc. 2019

4. Booker, E., Price, M., **Budden, P.**, Abolins, H., del Valle-Inclan Redondo, Y., Eyre, L., Nasrallah, I., Phillips, R., Friend, R., Deschler, F., Greenham, N., "Vertical Cavity Biexciton Lasing in 2-Dimensional Dodecylammonium Lead Iodide Perovskites", Advanced Optical Materials, 2018

Appendix A

Supporting Information for Chapter 5

A.1 Thermal Artefacts in X-INDT Transient Absorption

In both the ground state bleach region and the NIR, transient absorption signals from the X-INDT films arose due to thermal effects rather than the changes in electronic states that we intend to probe. This can be directly demonstrated by comparing films of Cl-INDT (the derivative which exhibited the most significant thermal artefacts) on fused silica substrate with those on sapphire substrate, which has a higher thermal conductivity and so can dissipate heat faster[224]. The effects of this only become pronounced in the ns-resolution measurement, but we note that the relevant thermal effects are already present in the ultrafast data. There is a clear change in the kinetics of both the ground state bleach signal (Figure A.1) and the NIR photoinduced absorption (Figure A.2) between the two substrates, demonstrating that there is a significant thermal contribution to both.

In the case of the ground state bleach, the thermal effect is of the same sign as the underlying electronic signal ($\Delta T/T>0$), resulting in a misleading apparent increase in lifetime on fused silica. In the NIR, the initial negative signal is an S_1 photoinduced absorption which decays within a few nanoseconds, whilst the pump-induced thermal effect again produces positive $\Delta T/T$ and lasts for microseconds. There is no ground-state absorption in this region, and the bleach-like signal is unexpected; we suggest this most probably arises due to changes in the refractive index, causing a decrease in reflectivity and scattering which results in an increase in transmission. This effect

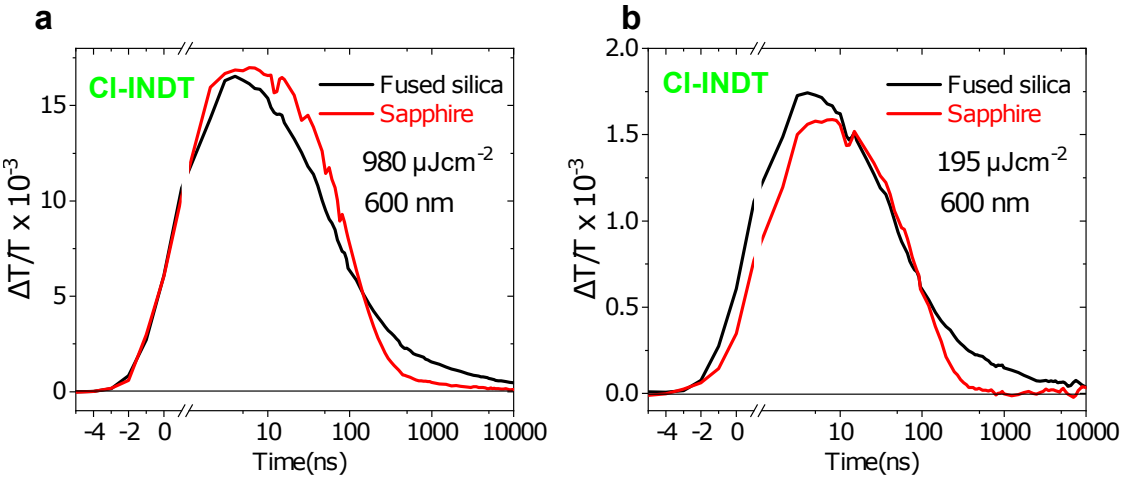

Fig. A.1 a) and b) show kinetics at 600 nm, showing the ground state bleach for Cl-INDT on sapphire (red) and fused silica (black) at two excitation densities. c) shows spectra 20 - 30 ns after exciation for three different excitation densities, normalised to the 550 nm GSB peak, showing how the thermal artefact affects the spectrum from the red into the NIR.

scales non-linearly with excitation fluence, as the relative size of the long-lived positive artefact to the short-lived negative S_1 signal is larger at high power in Figure A.2a than at lower power in Figure A.2b. This thermal feature became less pronounced when we optimise processing conditions to generate smoother films. The magnitude of the NIR thermal artefact relative to S_1 PIA is strongly fluence dependent (Figure A.1c), as is the decay of the PIA. At higher fluences, there is proportionally more singlet-singlet annihilation which generates heat in the sample, causing the thermal artefact. This has been previously observed in perylene diimides[112].

In the region of the triplet photoinduced absorption, we saw that even at much higher laser power than typically applied in our study, there is no dependence of the long-time kinetics on substrate thermal conductivity (Figure A.3). This assures us that at excitation densities lower than this, the triplet lifetimes extracted from these photoinduced absorption signatures, on the order of microseconds, are not effected by thermal artefacts. Figure A.1c shows how the triplet PIA is superimposed over the approximately flat thermal artefact.

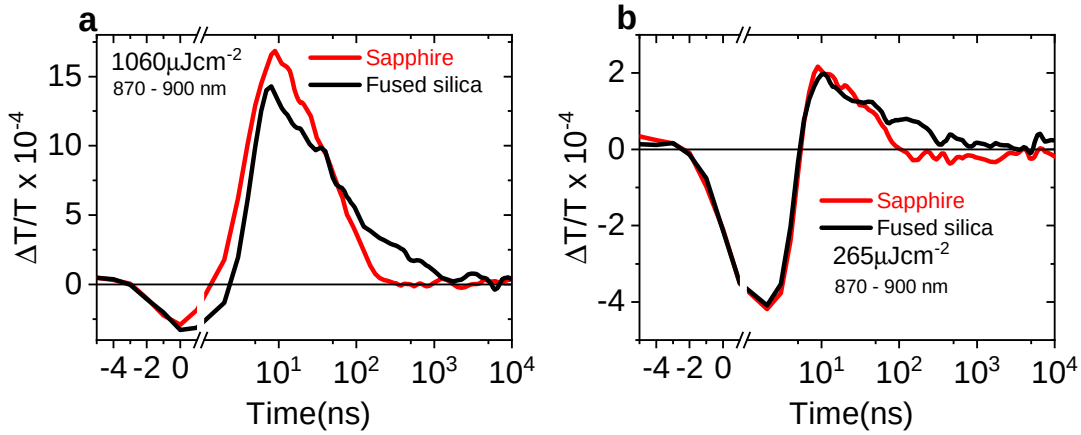

Fig. A.2 ns-transient absorption kinetics at 870-900 nm showing the interplay between photoinduced absorption ($\Delta T/T<0$) and thermal artefact ($\Delta T/T>0$) at two excitation densities for Cl-INDT films on different substrates: sapphire (red) and fused silica (black).

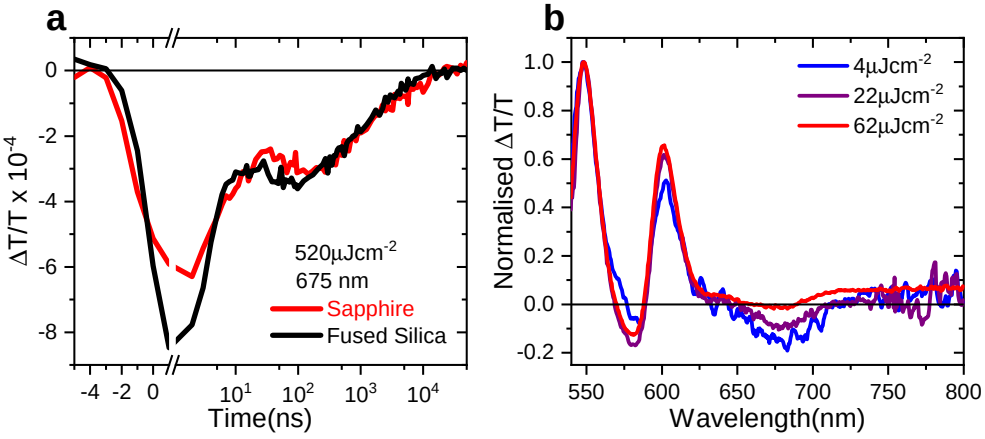

Fig. A.3 ns-transient absorption kinetics for 665-685 nm showing the characteristic triplet photoinduced absorption in Cl-INDT on sapphire (black) and fused silica (red).

A.2 trESR Simulations for X-INDT films

The mesaurements and simulations in this section were performed by Enrico Salvadori, and are included as an appendix as they are helpful context for the optical measurements we detail in Chapter 5.

Time resolved ESR (trESR) is a continuous wave ESR method for the detection and characterisation of transient photo-excited paramagnetic species. 2D surfaces, correlating signal intensity to both time and magnetic field, are recorded by detecting the transient magnetization after the laser pulse and stepping the magnetic-field strength over the resonance region. In the case of photoexcited triplet states ($S = 1$), the zero-field splitting (ZFS) interaction and the triplet sublevel populations can be extracted from the ESR spectra. The ZFS tensor describes the magnetic dipole-dipole interaction between the two unpaired electron spins in the triplet state. In organic molecules, where the spin-orbit and crystal field contributions can be safely neglected, the ZFS tensor is only dependent on the spin-spin contribution and reduces to the point-dipole approximation. The components of the ZFS tensor can then be expressed as a function of just two parameters, D and E. The magnitude of D is directly proportional to the average inter-electronic distance between the two unpaired electrons and its sign relates to the symmetry of the electronic distribution. A positive D corresponds to an oblate distribution (i.e. disk-like, axis of maximum dipolar coupling, Z, perpendicular to the molecular plane), whereas a negative D corresponds to a prolate distribution (i.e. rod-like, axis of maximum dipolar coupling, Z, parallel to the long molecular axis). The magnitude of E is indicative of the rhombicity of the electronic distribution: $E = 0$ indicates axial symmetry, $E \neq 0$ (with $0 \leq E \leq 1/3D$) indicates rhombic symmetry. The sign of E is not univocal and depends on the assignment of the X and Y ZFS axes. However, while the absolute magnitude of the ZFS parameters can be estimated from a trESR experiment, the corresponding signs cannot usually be determined directly. Triplets formed via radical-pair recombination, back electron transfer, triplet-triplet annihilation or singlet fission, where the T_0 triplet sublevel is preferentially populated in high field, constitute an exception to this rule. In these cases the unique polarisations AEEAAE or EAAEEA, which cannot be accounted for by invoking intersystem crossing, stem from a positive and negative sign of D, respectively.

The trESR spectrum of CN-INDT in the solid state, Figure 5.8 is complex and presents more than the 6 turning points expected for a single triplet species. Component A was simulated by using ZFS parameters derived for the ISC triplet in dilute solution and assuming that the T_0 triplet sublevel is preferentially populated in high field

Compound	Form	|D| (MHz)	|E| (MHz)	$P_Z : P_Y : P_X$
H-INDT	Solution	880	150	0.00:0.50:0.50
	Film	850	150	0.00:0.40:0.60
F-INDT	Solution	910	185	0.00:0.40:0.60
	Film	880	170	0.10:0.50:0.40
Cl-INDT	Solution	860	185	0.00:0.40:0.60
	Film	910	185	0.05:0.60:0.35
Br-INDT	Solution	880	185	0.00:0.50:0.50
	Film	910	185	0.20:0.60:0.20
CN-INDT	Solution	800	180	0.00:0.40:0.60
	Film Component A	830	180	-
	Film Component B	-600	60	-

Table A.1 trESR simulation parameters for frozen solutions and films at 10 K, as plotted in Figure 5.7.

yielding a polarisation pattern of the type AEEAAE, as it can be inferred from the low and high field transitions. This is consistent with a positive D value usually found in planar molecules, such as pentacene, TIPS-pentacene and TIPS-tetracene. Component B was obtained as a difference between the experimental spectrum and the simulation for component A and it displays an opposite polarisation. The EAAEEA pattern observed for component B can be explained with a change in sign of the D parameter, and therefore a change in the electronic distribution from oblate to prolate as compared to component A. The formation of ordered aggregates could account for the reduction in the magnitude of D (as seen for instance for porphyrin J-aggregates[260]), and for the change in sign, if the overall symmetry of the electronic distribution moved from disk-like to rod-like (as seen by comparing a monomeric porphyrin and a covalently linked dimer[275]). It could then be speculated that in CN-INDT film there exists a different morphology, possibly chain-like aggregates, that contribute to the measured spectrum at 10 K. Alternatively, if one assumes that the sign of D remains positive, the observed polarisation pattern observed for component B would imply the preferential population of the $T_{\pm1}$ triplet sublevels. This can happen if there exists an additional triplet state lying lower in energy[276] or if the magnetic interactions at play (e.g. exchange coupling, J) favour the mixing of the excited singlet state with the $T_{\pm1}$ triplet sublevels. However, we note that the signal-to-noise ratio of the experimental data and the fact that the spectrum of component B could only be obtained as a difference make it difficult to drawn definitive conclusions.

Table A.1 summarises the ZFS parameters and triplet sublevel populations from the simulations in Figure 5.7. The minimal changes in the ZFS parameter D derived

from spectral simulations between dilute solution (no intermolecular interactions) and casted film for each compound suggests the triplet wavefunction is always localised over one molecular unit. The average D value for X-INDT derived from spectral simulations is 876 MHz. Assuming the point dipole approximation as valid for the ZFS parameters D, the average inter-spin distance can be then estimated to be 3.5 Å. In comparison, the low lowing triplet state of pentacene is characterised by a D of 1400 MHz and a corresponding inter-spin distance of 3 Å. ESR data are then consistent with a more extended triplet for X-INDT than pentacene.

In the assumption of a positive D for the X-INDT compounds, as we have justified for CN-INDT film, and assuming $E > 0$, the relative energy order for the triplet sublevels is $P_X > P_Y > P_Z$. From the population analysis of the trESR spectra, it follows that the P_Y and P_X sublevels are preferentially populated in dilute solution for all of the molecules measures. This is consistent with vibronically assisted ISC as observed for other planar molecules such as metal-free porphyrins. However, in the case of Br-INDT, the close packing imposed by the deposition as a film alters the triplet sublevel populations resulting in the preferential occupation of the P_Y sublevel. Although it is clear that aggregation promotes a different mechanism of populating Br-INDT triplet state, the observed polarisation pattern is not in line with what has previously been observed for pentacene, TIPS-pentacene/tetracene[172], pentacene dimers[173] and CN-INDT upon singlet fission. The observed polarisation could then result from triplet transfer processes following the initial singlet fission event. Considering that the measured trESR spectrum of Br-INDT film is both well defined and has similar ZFS parameters to those measured in dilute solution, it can be concluded that: i) if aggregates are present they must be well ordered, as confirmed by steady-state UV-Vis spectra and ii) the final triplet exciton is localised over one Br-INDT unit. An alternative hypothesis is that the observed trESR spectrum belongs to a different triplet exciton resulting from aggregation and populated through ISC. However we can rule this out given that the ZFS parameters should change as result of aggregation and the typical timescales for ISC are not consistent with the triplet features observed in sub-nanosecond transient absorption data.

The TA data indicated Cl-INDT undergoes singlet fission, an observation which was not confirmed in the ESR data. As the ESR was performed at 10 K we suggest that at these temperatures singlet fission is no longer energetically accessible. This is not unreasonable; TD-DFT suggests that the exothermicity of singlet fission is greatest for Br-INDT and CN-INDT, consistent with their ability to undergo fission at low temperatures. If we consider that TD-DFT is typically prone to underestimate the

electronic energy of triplet states, it is possible that the least-exothermic materials may indeed require some slight thermal activation, at least to produce sufficiently long-lived triplets for ESR.

A.3 trESR for INDT Dimers

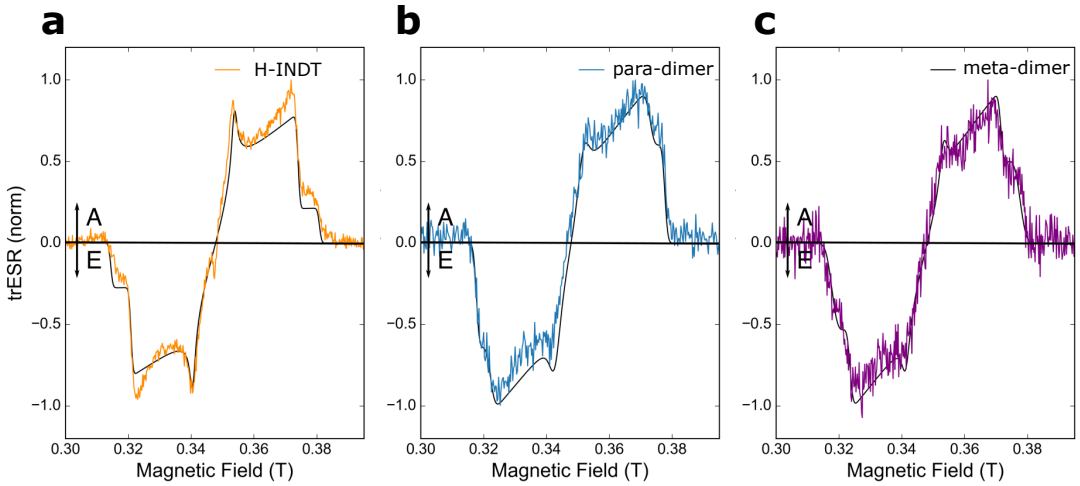

Fig. A.4 trESR spectra integrated between 0.5 - 2 µs after laser flash with 532 nm excitation, 30 dB microwave attenuation, 9.6 GHz (X-band) in frozen solution of DCB at 100 K for (a) H-INDT monomer, (b) para-dimer, and (c) meta-dimer. Spectral simulations are shown in black solid lines with parameters given in Table A.2.

Material	D (MHz)	E (MHz)	P_z:P_y:P_x
H-INDT	930	182	0.20:0.39:0.41
meta-dimer	840	195	0.10:0.42:0.48
para-dimer	840	195	0:0.49:0.51

Table A.2 trESR simulation parameters for frozen solutions of INDT dimers at 100 K, as plotted in Figure A.4.

References

1. IPCC. *Summary for Policymakers. Global warming of 1.5°C* tech. rep. (2018) (cit. on p. 1).
2. Yamamoto, K., Yoshikawa, K., Uzu, H. & Adachi, D. High-efficiency heterojunction crystalline Si solar cells. *Japanese Journal of Applied Physics* **57.** ISSN: 13474065 (2018) (cit. on p. 1).
3. Rühle, S. Tabulated values of the Shockley–Queisser limit for single junction solar cells. *Solar Energy* **130,** 139–147. ISSN: 0038092X (2016) (cit. on pp. 1, 2, 49).
4. NREL. *Best Research-Cell Efficiency Chart* 2020 (cit. on p. 1).
5. Schaller, R. D. & Klimov, V. I. High Efficiency Carrier Multiplication in PbSe Nanocrystals: Implications for Solar Energy Conversion. *Physical Review Letters* **92,** 186601 (2004) (cit. on pp. 2, 51).
6. Davis, N. J. L. K. *et al.* Multiple-exciton generation in lead selenide nanorod solar cells with external quantum efficiencies exceeding 120% ¨. *Nature Communications* (2015) (cit. on pp. 2, 51).
7. Tayebjee, M. J. Y., Gray-Weale, A. A. & Schmidt, T. W. Thermodynamic limit of exciton fission solar cell efficiency. *Journal of Physical Chemistry Letters* **3,** 2749–2754. ISSN: 19487185 (2012) (cit. on pp. 2, 70, 158).
8. Kohler, A. & Bassler, H. *Electronic Processes in Organic Semiconductors* ISBN: 9788578110796. arXiv: arXiv:1011.1669v3 (Wiley-VCH, 2015) (cit. on pp. 5–10, 16–19, 21, 22, 117).
9. Salehi, A., Fu, X., Shin, D. & So, F. Recent Advances in OLED Optical Design. *Advanced Functional Materials* **29,** 1808803. ISSN: 1616-301X (2019) (cit. on p. 5).
10. Yan, C. *et al.* Non-fullerene acceptors for organic solar cells. *Nature Reviews Materials* (2018) (cit. on p. 5).
11. Di Carlo Rasi, D. & Janssen, R. A. Advances in Solution-Processed Multijunction Organic Solar Cells. *Advanced Materials* **31.** ISSN: 15214095 (2019) (cit. on p. 5).
12. Huang, L. *et al.* Expanding Anti-Stokes Shifting in Triplet-Triplet Annihilation Upconversion for In Vivo Anticancer Prodrug Activation. *Angewandte Chemie International Edition* **56,** 14400–14404. ISSN: 14337851 (2017) (cit. on p. 5).
13. Smyser, K. & Eaves, J. Singlet fission for quantum information and quantum computing: The parallel JDE model. *arXiv Preprint.* arXiv: 2004.00103v1 (2020) (cit. on p. 5).

14. Pope, M. & Swenberg, C. *Electronic processes in organic crystals and polymers.* (Oxford University Press, 1999) (cit. on pp. 5, 8–10, 12, 27, 31).
15. Barford, W. *Electronic and Optical Properties of Conjugated Polymers* ISBN: 978–0–19–852680–3 (Oxford University Press, 2005) (cit. on pp. 5–8, 10, 12, 19, 26–28).
16. Schwoerer, M. & Wolf, H. C. *Organic Molecular Solids* 1–427. ISBN: 9783527405404 (John Wiley and Sons, 2008) (cit. on pp. 8, 9, 26).
17. Hückel, E. Quantum-theoretical contributions to the benzene problem. i. The electron configuration of benzene and related compounds. *Z. Physik* **70,** 204–286 (1931) (cit. on p. 9).
18. Hückel, E. in *Quantum Chemistry: Classic Scientific Papers* 452–478 (World Scientific, 2000) (cit. on p. 9).
19. Atkins, P. & Friedman, R. *Molecular Quantum Mechanics* 3rd edn Ox (Oxford University Press, Oxford, 1996) (cit. on p. 9).
20. Frenkel, J. On the transformation of light into heat in solids. I. *Physical Review* **37,** 17–44 (1931) (cit. on p. 12).
21. Köhler, A. & Bässler, H. Triplet states in organic semiconductors. *Materials Science and Engineering R: Reports* **66,** 71–109. ISSN: 0927796X (2009) (cit. on pp. 13–15, 27, 28).
22. Griffiths, D. & Schroeter, D. F. *Introduction to Quantum Mechanics, Third Edition* (Cambridge University Press, 2004) (cit. on p. 14).
23. Monkman, A. P. *et al.* Triplet energies of π-conjugated polymers. *Physical Review Letters* **86,** 1358–1361. ISSN: 00319007 (2001) (cit. on p. 15).
24. Dirac, P. A. M. The quantum theory of the emission and absorption of radiation. *Proceedings of the Royal Society of London. Series A, Containing Papers of a Mathematical and Physical Character* **114,** 243–265. ISSN: 0950-1207 (1927) (cit. on p. 15).
25. Hamm, P. & Zanni, M. *Concepts and Methods of 2D Infrared Spectroscopy* ISBN: 9780511675935 (Cambridge University Press, Cambridge, 2011) (cit. on p. 17).
26. Tokmakoff, A. *Time-Dependent Quantum Mechanics and Spectroscopy* 2007 (cit. on p. 18).
27. Birks, J. B. *Photophysics of aromatic molecules* (Wiley-Interscience, 1970) (cit. on p. 19).
28. Siebrand, W. Radiationless Transitions in Polyatomic Molecules I. Calculation of Franck-Condon Factors. *Journal of Chemical Physics* **46,** 440–447. ISSN: 18695868 (1967) (cit. on p. 22).
29. Englman, R. & Jortner, J. The energy gap law for radiationless transitions in large molecules. *Molecular Physics* **18,** 145–164. ISSN: 0026-8976 (1970) (cit. on p. 22).
30. Yarkony, D. R. Conical Intersections: Diabolical and Often Misunderstood. *Accounts of Chemical Research* **31,** 511–518. ISSN: 00014842 (1998) (cit. on p. 23).

31. Yarkony, D. R. Nonadiabatic Quantum Chemistry-Past, Present, and Future. *Chem. Rev* **112,** 481–498 (2012) (cit. on p. 23).
32. Polli, D. *et al.* Conical intersection dynamics of the primary photoisomerization event in vision. *Nature* **467,** 440–443. ISSN: 14764687 (2010) (cit. on p. 23).
33. Davydov, A. The theory of molecular excitons. *Uspekhi Fizicheskih Nauk* **82,** 393–448. ISSN: 0042-1294 (1964) (cit. on p. 26).
34. Kasha, M. Energy Transfer Mechanisms and the Molecular Exciton Model for Molecular Aggregates. *Radiation Research* **20,** 55. ISSN: 00337587 (1963) (cit. on p. 26).
35. Spano, F. C. The spectral signatures of frenkel polarons in H- And J-aggregates. *Accounts of Chemical Research* **43,** 429–439. ISSN: 00014842 (2010) (cit. on pp. 26, 117, 161).
36. Spano, F. C. & Silva, C. H- and J-Aggregate Behavior in Polymeric Semiconductors. *Annual Review of Physical Chemistry* **65,** 477–500. ISSN: 0066-426X (2014) (cit. on p. 26).
37. Hestand, N. J. & Spano, F. C. *Expanded Theory of H- and J-Molecular Aggregates: The Effects of Vibronic Coupling and Intermolecular Charge Transfer* 2018 (cit. on p. 26).
38. Birks, J. B. & Christophorou, L. G. Excimer fluorescence spectra of pyrene derivatives. *Spectrochimica Acta* **19,** 401–410. ISSN: 03711951 (1963) (cit. on p. 27).
39. Laquai, F., Park, Y. S., Kim, J. J. & Basché, T. Excitation energy transfer in organic materials: From fundamentals to optoelectronic devices. *Macromolecular Rapid Communications* **30,** 1203–1231. ISSN: 10221336 (2009) (cit. on pp. 27, 28, 31).
40. Dexter, D. L. A theory of sensitized luminescence in solids. *The Journal of Chemical Physics* **21,** 836–850. ISSN: 00219606 (1953) (cit. on p. 28).
41. Closs, G. L., Piotrowiak, P., Johnson, M. D. & Miller, J. R. A Connection between Intramolecular Long-Range Electron, Hole, and Triplet Energy Transfers. *Journal of the American Chemical Society* **111,** 3751–3753. ISSN: 15205126 (1989) (cit. on p. 28).
42. Liu, J. *et al.* Fast charge separation in a non-fullerene organic solar cell with a small driving force. *Nature Energy* **1,** 1–7. ISSN: 20587546 (2016) (cit. on p. 30).
43. Li, Y. *et al.* Non-fullerene acceptor with low energy loss and high external quantum efficiency: Towards high performance polymer solar cells. *Journal of Materials Chemistry A* **4,** 5890–5897. ISSN: 20507496 (2016) (cit. on p. 30).
44. Baran, D. *et al.* Reduced voltage losses yield 10% efficient fullerene free organic solar cells with >1 V open circuit voltages. *Energy and Environmental Science* **9,** 3783–3793. ISSN: 17545706 (2016) (cit. on p. 30).
45. Cheng, P. *et al.* Realizing Small Energy Loss of 0.55 eV, High Open-Circuit Voltage >1 V and High Efficiency >10% in Fullerene-Free Polymer Solar Cells via Energy Driver. *Advanced Materials* **29,** 1–6. ISSN: 15214095 (2017) (cit. on p. 30).

46. Clarke, T. M. & Durrant, J. R. Charge photogeneration in organic solar cells. *Chemical Reviews* **110,** 6736–6767. ISSN: 00092665 (2010) (cit. on p. 31).

47. Deibe, C., Strobe, T. & Dyakonov, V. Role of the charge transfer state in organic donor-acceptor solar cells. *Advanced Materials* **22,** 4097–4111. ISSN: 09359648 (2010) (cit. on p. 31).

48. Bakulin, A. A. *et al.* The Role of Driving Energy and Delocalized States for Charge Separation in Organic Semiconductors. *Science* **335,** 1340–1344 (2012) (cit. on p. 31).

49. Few, S., Frost, J. M. & Nelson, J. Models of charge pair generation in organic solar cells. *Physical Chemistry Chemical Physics* **17,** 2311–2325. ISSN: 14639076 (2015) (cit. on p. 31).

50. Menke, S. M. *et al.* Order enables efficient electron-hole separation at an organic heterojunction with a small energy loss. *Nature Communications* **9,** 277. ISSN: 2041-1723 (2018) (cit. on p. 31).

51. Gélinas, S. *et al.* Ultrafast Long-Range Charge Separation in Organic Semiconductor Photovoltaic Diodes. *Science* **343,** 512 LP –516. ISSN: 0036-8075 (2014) (cit. on p. 31).

52. Bässler, H. & Kohler, A. "hot or cold": How do charge transfer states at the donor-acceptor interface of an organic solar cell dissociate? *Physical Chemistry Chemical Physics* **17,** 28451–28462. ISSN: 14639076 (2015) (cit. on p. 31).

53. Singh, S., Jones, W. J., Siebrand, W., Stoicheff, B. P. & Schneider, W. G. Laser generation of excitons and fluorescence in anthracene crystals. *The Journal of Chemical Physics* **42,** 330–342. ISSN: 00219606 (1965) (cit. on pp. 32, 33, 39).

54. Parker, C. A. & Hatchard, C. G. Delayed fluorescence from solutions of anthracene and phenanthrene. *Proceedings of the Chemical Society,* 147. ISSN: 03698718 (1962) (cit. on p. 32).

55. Kepler, R. G., Caris, J. C., Avakian, P. & Abramson, E. Triplet excitons and delayed fluorescence in anthracene crystals. *Physical Review Letters* **10,** 400–402. ISSN: 00319007 (1963) (cit. on p. 32).

56. Siebrand, W. Trapping of triplet excitons and the temperature dependence of delayed fluorescence in anthracene crystals. *The Journal of Chemical Physics* **42,** 3951–3954. ISSN: 00219606 (1965) (cit. on p. 32).

57. Johnson, R. C., Merrifield, R. E., Avakian, P. & Flippen, R. B. Effects of magnetic fields on the mutual annihilation of triplet excitons in molecular crystals. *Physical Review Letters* **19,** 285–287. ISSN: 00319007 (1967) (cit. on p. 32).

58. Merrifield, R. E. Diffusion and Mutual Annihilation of Triplet Excitons in Organic Crystals. *Accounts of Chemical Research* **1,** 129–135. ISSN: 15204898 (1968) (cit. on p. 32).

59. Merrifield, R. E. Theory of Magnetic Field Effects on the Mutual Annihilation of Triplet Excitons. *The Journal of Chemical Physics* **48,** 4318–4319. ISSN: 0021-9606 (1968) (cit. on p. 32).

60. Suna, A. Kinematics of Exciton-Exciton Annihilation in Molecular Crystals. *Physical Review B* **1,** 1716–1739. ISSN: 0556-2805 (1970) (cit. on p. 32).

61. Musser, A. J. & Clark, J. Triplet-Pair States in Organic Semiconductors. *Annual Review of Physical Chemistry Annu. Rev. Phys. Chem* **70,** 323–351 (2019) (cit. on pp. 33, 35, 45, 182).

62. Swenberg, C. E. & Stacy, W. T. Bimolecular radiationless transitions in crystalline tetracene. *Chemical Physics Letters* **2,** 327–328. ISSN: 00092614 (1968) (cit. on p. 33).

63. Pope, M., Geacintov, N. E. & Vogel, F. Singlet Exciton Fission and Triplet-Triplet Exciton Fusion in Crystalline Tetracene. *Molecular Crystals* **6,** 83–104. ISSN: 0369-1152 (1969) (cit. on p. 33).

64. Geacintov, N., Pope, M. & Vogel, F. Effect of magnetic field on the fluorescence of tetracene crystals: Exciton fission. *Physical Review Letters* **22,** 593–596. ISSN: 00319007 (1969) (cit. on p. 34).

65. Merrifield, R. E., Avakian, P. & Groff, R. Fission of singlet excitons into pairs of triplet excitons in tetracene crystals. *Chemical Physics Letters* **3,** 386–388. ISSN: 00092614 (1969) (cit. on pp. 34–36, 70, 83, 85, 158, 163).

66. Groff, R. P., Avakian, P. & Merrifield, R. E. Magnetic field dependence of delayed fluorescence from tetracene crystals. *Journal of Luminescence* **2,** 218–223 (1970) (cit. on p. 34).

67. Merrifield, R. E. Magnetic effects on triplet exciton interactions. *Pure and Applied Chemistry* **27,** 481–498. ISSN: 1365-3075 (1971) (cit. on pp. 34, 85).

68. Yarmus, L., Rosenthal, J. & Chopp, M. EPR of triplet excitions in tetracene crystals: spin polarization and the role of singlet exciton fission. *Chemical Physics Letters* **16,** 477–481. ISSN: 00092614 (1972) (cit. on pp. 34, 45, 66, 123, 125, 165).

69. Dexter, D. L. Two ideas on energy transfer phenomena: Ion-pair effects involving the OH stretching mode, and sensitization of photovoltaic cells. *Journal of Luminescence* **18-19,** 779–784. ISSN: 00222313 (1979) (cit. on p. 34).

70. Hanna, M. C. & Nozik, A. J. Solar conversion efficiency of photovoltaic and photoelectrolysis cells with carrier multiplication absorbers. *Journal of Applied Physics* **100,** 074510. ISSN: 00218979 (2006) (cit. on pp. 34, 51).

71. Smith, M. B. & Michl, J. Singlet Fission. *Chemical Reviews* **110,** 6891–6936. ISSN: 0009-2665 (2010) (cit. on pp. 34, 36).

72. Wilson, M. W. B. *et al.* Ultrafast Dynamics of Exciton Fission in Polycrystalline Pentacene. *Journal of the American Chemical Society* **133,** 11830–11833. ISSN: 0002-7863 (2011) (cit. on pp. 34, 38, 70, 114).

73. Rao, A., Wilson, M. W. B., Albert-Seifried, S., Di Pietro, R. & Friend, R. H. Photophysics of pentacene thin films: The role of exciton fission and heating effects. *Physical Review B* **84,** 195411. ISSN: 1098-0121 (2011) (cit. on pp. 34, 38, 64, 119).

74. Burdett, J. J., Gosztola, D. & Bardeen, C. J. The dependence of singlet exciton relaxation on excitation density and temperature in polycrystalline tetracene thin films: Kinetic evidence for a dark intermediate state and implications for singlet fission. *Journal of Chemical Physics* **135.** ISSN: 00219606 (2011) (cit. on pp. 34, 36, 37, 158, 173).

75. Wilson, M. W. B. *et al.* Temperature-Independent Singlet Exciton Fission in Tetracene. *Journal of the American Chemical Society* **135,** 16680–16688. ISSN: 0002-7863 (2013) (cit. on pp. 34–37, 70, 73, 101, 114, 158, 173, 182, 183).

76. Burdett, J. J., Müller, A. M., Gosztola, D. & Bardeen, C. J. Excited state dynamics in solid and monomeric tetracene: The roles of superradiance and exciton fission. *Journal of Chemical Physics* **133.** ISSN: 00219606 (2010) (cit. on pp. 34, 36, 70, 173).

77. Stern, H. L. *et al.* Vibronically coherent ultrafast triplet-pair formation and subsequent thermally activated dissociation control efficient endothermic singlet fission. *Nature Chemistry* **9,** 1205–1212. ISSN: 17554349. arXiv: 1704.01695 (2017) (cit. on pp. 35, 37–39, 42, 44, 70, 76, 81, 114, 131, 158, 161–163, 171, 173, 175, 176, 179, 180, 182, 183).

78. Yong, C. K. *et al.* The entangled triplet pair state in acene and heteroacene materials. *Nature Communications* **8,** in press. ISSN: 2041-1723 (2017) (cit. on p. 35).

79. Smith, M. & Michl, J. Recent advances in singlet fission. *Annual review of physical chemistry* **64,** 361–86. ISSN: 1545-1593 (2013) (cit. on pp. 35, 115, 117).

80. Yost, S. R. *et al.* A transferable model for singlet-fission kinetics. *Nat Chem* **6,** 492–497. ISSN: 1755-4330 (2014) (cit. on pp. 35, 37, 114, 139).

81. Zimmerman, P. M., Bell, F., Casanova, D. & Head-Gordon, M. Mechanism for singlet fission in pentacene and tetracene: From single exciton to two triplets. *Journal of the American Chemical Society* **133,** 19944–19952. ISSN: 00027863 (2011) (cit. on p. 35).

82. Stern, H. L. *et al.* Identification of a triplet pair intermediate in singlet exciton fission in solution. *Proceedings of the National Academy of Sciences* **112,** 7656–7661. ISSN: 0027-8424 (2015) (cit. on pp. 36, 39, 40, 42, 70, 76, 131, 133, 179, 180).

83. Tayebjee, M. J. Y., Clady, R. G. C. R. & Schmidt, T. W. The exciton dynamics in tetracene thin films. *Physical Chemistry Chemical Physics* **15,** 14797. ISSN: 1463-9076 (2013) (cit. on pp. 36, 114, 158).

84. Grumstrup, E. M., Johnson, J. C. & Damrauer, N. H. Enhanced triplet formation in polycrystalline tetracene films by femtosecond optical-pulse shaping. *Physical Review Letters* **105,** 1–4. ISSN: 00319007 (2010) (cit. on p. 36).

85. Burdett, J. J. & Bardeen, C. J. Quantum Beats in Crystalline Tetracene Delayed Fluorescence Due to Triplet Pair Coherences Produced by Direct Singlet Fission. *Journal of the American Chemical Society* **134,** 8597–8607. ISSN: 0002-7863 (2012) (cit. on pp. 36–38).

86. Bayliss, S. L. *et al.* Spin signatures of exchange-coupled triplet pairs formed by singlet fission. *PHYSICAL REVIEW B* **94,** 45204 (2016) (cit. on pp. 36, 66, 86, 165).

87. Chan, W.-L., Ligges, M. & Zhu, X.-Y. The energy barrier in singlet fission can be overcome through coherent coupling and entropic gain. *Nature Chemistry* **4,** 840–845. ISSN: 1755-4330 (2012) (cit. on pp. 37, 38).

88. Thorsmolle, V. K. *et al.* Morphology Effectively Controls Singlet-Triplet Exciton Relaxation and Charge Transport in Organic Semiconductors. *Physical Review Letters* **102,** 17401 (2009) (cit. on p. 37).

89. Piland, G. B. & Bardeen, C. J. How Morphology Affects Singlet Fission in Crystalline Tetracene. *The Journal of Physical Chemistry Letters* **6,** 1841–1846. ISSN: 1948-7185 (2015) (cit. on pp. 37, 44).

90. Morrison, A. F. & Herbert, J. M. Evidence for Singlet Fission Driven by Vibronic Coherence in Crystalline Tetracene. *The Journal of Physical Chemistry Letters,* acs.jpclett.7b00230. ISSN: 1948-7185 (2017) (cit. on p. 38).

91. Wan, Y. *et al.* Cooperative singlet and triplet exciton transport in tetracene crystals visualized by ultrafast microscopy. *Nat Chem* **7,** 785–792. ISSN: 1755-4330 (2015) (cit. on p. 38).

92. Zhu, T. & Huang, L. Exciton Transport in Singlet Fission Materials: A New Hare and Tortoise Story. *The Journal of Physical Chemistry Letters* **9,** 6502–6510. ISSN: 1948-7185 (2018) (cit. on p. 38).

93. Wilson, M. W. B., Rao, A., Ehrler, B. & Friend, R. H. Singlet exciton fission in polycrystalline pentacene: From photophysics toward devices. *Accounts of Chemical Research* **46,** 1330–1338. ISSN: 00014842 (2013) (cit. on p. 38).

94. Zimmerman, P. M., Zhang, Z. & Musgrave, C. B. Singlet fission in pentacene through multi-exciton quantum states. *Nat Chem* **2,** 648–652. ISSN: 1755-4330 (2010) (cit. on p. 38).

95. Musser, A. J. *et al.* Evidence for conical intersection dynamics mediating ultrafast singlet exciton fission. *Nature Physics* **11,** 352–357. ISSN: 1745-2473 (2015) (cit. on pp. 39, 40, 70, 114).

96. Bakulin, A. A. *et al.* Real-time observation of multiexcitonic states in ultrafast singlet fission using coherent 2D electronic spectroscopy. *Nat Chem* **8,** 16–23. ISSN: 1755-4330 (2016) (cit. on pp. 39, 40, 114).

97. Northrop, B. H., Houk, K. N. & Maliakal, A. Photostability of pentacene and 6,13-disubstituted pentacene derivatives: a theoretical and experimental mechanistic study. *Photochemical & Photobiological Sciences* **7,** 1463–1468. ISSN: 1474-905X (2008) (cit. on pp. 39, 114).

98. Zade, S. S. *et al.* Products and Mechanism of Acene Dimerization. A Computational Study. *Journal of the American Chemical Society* **133,** 10803–10816. ISSN: 0002-7863 (2011) (cit. on pp. 39, 114).

99. Gray, V. *et al.* Direct vs Delayed Triplet Energy Transfer from Organic Semiconductors to Quantum Dots and Implications for Luminescent Harvesting of Triplet Excitons. *ACS nano* **14,** 4224–4234. ISSN: 1936086X (2020) (cit. on pp. 39, 48).

100. Busby, E. *et al.* Multiphonon relaxation slows singlet fission in crystalline hexacene. *Journal of the American Chemical Society* **136,** 10654–10660. ISSN: 15205126 (2014) (cit. on p. 39).

101. Thampi, A. *et al.* Elucidation of Excitation Energy Dependent Correlated Triplet Pair Formation Pathways in an Endothermic Singlet Fission System. *Journal of the American Chemical Society* **140,** 4613–4622. ISSN: 15205126 (2018) (cit. on p. 39).

102. Walker, B. J., Musser, A. J., Beljonne, D. & Friend, R. H. Singlet exciton fission in solution. *Nature Chemistry* **5,** 1019–1024. ISSN: 1755-4330 (2013) (cit. on pp. 40, 70, 114, 131).

103. Herz, J. *et al.* Unveiling Singlet Fission Mediating States in TIPS-pentacene and its Aza Derivatives. *The Journal of Physical Chemistry A* **119,** 6602–6610. ISSN: 1089-5639 (2015) (cit. on pp. 40, 114).

104. Pensack, R. D. *et al.* Solution-processable, crystalline material for quantitative singlet fission. *Mater. Horiz.* **4,** 915–923. ISSN: 2051-6347 (2017) (cit. on pp. 40, 45).

105. Lee, T. S. *et al.* Triplet Energy Transfer Governs the Dissociation of the Correlated Triplet Pair in Exothermic Singlet Fission. *The Journal of Physical Chemistry Letters,* 4087–4095. ISSN: 1948-7185 (2018) (cit. on p. 40).

106. Hudson, R. J. *et al.* Organizing Crystalline Functionalized Pentacene Using Periodicity of Poly(Vinyl Alcohol). *Journal of Physical Chemistry Letters* (2019) (cit. on p. 40).

107. Jones, A. C., Kearns, N. M., Ho, J.-J. J., Flach, J. T. & Zanni, M. T. Impact of non-equilibrium molecular packings on singlet fission in microcrystals observed using 2D white-light microscopy. *Nature Chemistry* **12,** 40–47. ISSN: 1755-4330 (2019) (cit. on pp. 40, 45).

108. Bae, Y. J. *et al.* Singlet Fission in 9,10-Bis(phenylethynyl)anthracene Thin Films. *Journal of the American Chemical Society* **140,** 15140–15144 (2018) (cit. on p. 40).

109. Thompson, N. J., Hontz, E., Chang, W., Van Voorhis, T. & Baldo, M. Magnetic field dependence of singlet fission in solutions of diphenyl tetracene. *Philosophical Transactions of the Royal Society A: Mathematical, Physical and Engineering Sciences* **373,** 20140323. ISSN: 1364-503X (2015) (cit. on pp. 40, 42).

110. Breen, I. *et al.* Triplet Separation Drives Singlet Fission after Femtosecond Correlated Triplet Pair Production in Rubrene. *Journal of the American Chemical Society* **139,** 11745–11751. ISSN: 15205126 (2017) (cit. on p. 40).

111. Korovina, N. V., Chang, C. H. & Johnson, J. C. Spatial separation of triplet excitons drives endothermic singlet fission. *Nature Chemistry,* 1–8. ISSN: 1755-4330 (2020) (cit. on pp. 40, 44, 70, 151).

112. Le, A. K., Bender, J. A. & Roberts, S. T. Slow Singlet Fission Observed in a Polycrystalline Perylenediimide Thin Film. *The Journal of Physical Chemistry Letters* **7,** 4922–4928. ISSN: 1948-7185 (2016) (cit. on pp. 40, 70, 114, 119, 126, 131, 192).

113. Le, A. K. *et al.* Singlet Fission Involves an Interplay between Energetic Driving Force and Electronic Coupling in Perylenediimide Films. *Journal of the American Chemical Society* **140,** 814–826. ISSN: 15205126 (2018) (cit. on pp. 40, 70, 114).

114. Schierl, C. *et al.* Singlet fission in self-assembled PDI nanocrystals †. *Nanoscale* (2018) (cit. on pp. 40, 70).

115. Masoomi-Godarzi, S. *et al.* Competitive Triplet Formation and Recombination in Crystalline Films of Perylenediimide Derivatives: Implications for Singlet Fission. *The Journal of Physical Chemistry C.* ISSN: 1932-7447 (2020) (cit. on pp. 40, 45, 70, 158).

116. Eaton, S. W. *et al.* Singlet Exciton Fission in Thin Films of tert -Butyl-Substituted Terrylenes. *The Journal of Physical Chemistry A* **119,** 4151–4161. ISSN: 1089-5639 (2015) (cit. on pp. 40, 70, 114).

117. Bae, Y. J. *et al.* Spin Dynamics of Quintet and Triplet States Resulting from Singlet Fission in Oriented Terrylenediimide and Quaterrylenediimide Films. *The Journal of Physical Chemistry C,* acs.jpcc.0c03189. ISSN: 1932-7447 (2020) (cit. on pp. 40, 45, 70, 167).

118. Chen, M., Powers-Riggs, N. E., Coleman, A. F., Young, R. M. & Wasielewski, M. R. Singlet Fission in Quaterrylenediimide Thin Films. *Journal of Physical Chemistry C* **124,** 2791–2798. ISSN: 19327455 (2020) (cit. on pp. 40, 70).

119. Wang, C. & Tauber, M. J. High-Yield Singlet Fission in a Zeaxanthin Aggregate Observed by Picosecond Resonance Raman Spectroscopy. *Journal of the American Chemical Society* **132,** 13988–13991. ISSN: 0002-7863 (2010) (cit. on pp. 40, 71, 114).

120. Musser, A. J. *et al.* The Nature of Singlet Exciton Fission in Carotenoid Aggregates. *Journal of the American Chemical Society* **137,** 5130–5139. ISSN: 0002-7863 (2015) (cit. on pp. 40, 71, 114, 119, 122, 169).

121. Taffet, E. J., Fassioli, F., Toa, Z. S. D., Beljonne, D. & Scholes, G. D. Uncovering dark multichromophoric states in Peridinin–Chlorophyll–Protein. *Journal of The Royal Society Interface* **17,** 20190736. ISSN: 1742-5689 (2020) (cit. on p. 40).

122. Mauck, C. M. *et al.* Singlet Fission via an Excimer-Like Intermediate in 3,6-Bis(thiophen-2-yl)diketopyrrolopyrrole Derivatives. *Journal of the American Chemical Society* **138,** 11749–11761. ISSN: 0002-7863 (2016) (cit. on pp. 40, 71, 186).

123. Hartnett, P. E. *et al.* Effects of Crystal Morphology on Singlet Exciton Fission in Diketopyrrolopyrrole Thin Films. *The Journal of Physical Chemistry B* **120,** 1357–1366. ISSN: 1520-6106 (2016) (cit. on pp. 40, 45, 71, 158, 186).

124. Mauck, C. M. *et al.* Singlet Fission within Diketopyrrolopyrrole Nanoparticles in Water. *Chemistry of Materials* **29,** 6810–6817. ISSN: 0897-4756 (2017) (cit. on pp. 40, 186).

125. Dillon, R. J., Piland, G. B. & Bardeen, C. J. Different rates of singlet fission in monoclinic versus orthorhombic crystal forms of diphenylhexatriene. *Journal of the American Chemical Society* **135,** 17278–17281. ISSN: 00027863 (2013) (cit. on pp. 40, 44, 71).

126. Katoh, R. *et al.* Singlet Fission in Fluorinated Diphenylhexatrienes. *The Journal of Physical Chemistry C* **121,** 25666–25671. ISSN: 1932-7447 (2017) (cit. on pp. 40, 71).

127. Wakasa, M. *et al.* What Can Be Learned from Magnetic Field Effects on Singlet Fission: Role of Exchange Interaction in Excited Triplet Pairs. *The Journal of Physical Chemistry C* **119,** 25840–25844. ISSN: 1932-7447 (2015) (cit. on pp. 40, 46, 86).

128. Johnson, J. C., Nozik, A. J. & Michl, J. High Triplet Yield from Singlet Fission in a Thin Film of 1,3-Diphenylisobenzofuran. *Journal of the American Chemical Society* **132,** 16302–16303. ISSN: 00027863 (2010) (cit. on pp. 40, 71, 131).

129. Ryerson, J. L. *et al.* Two Thin Film Polymorphs of the Singlet Fission Compound 1,3-Diphenylisobenzofuran. *The Journal of Physical Chemistry C* **118,** 12121–12132. ISSN: 1932-7447 (2014) (cit. on p. 40).

130. Wang, L. *et al.* Singlet Fission in a Pyrrole-Fused Cross-Conjugated Skeleton with Adaptive Aromaticity. *Journal of the American Chemical Society,* jacs.0c00089. ISSN: 0002-7863 (2020) (cit. on p. 40).

131. Lukman, S. *et al.* Efficient Singlet Fission and Triplet-Pair Emission in a Family of Zethrene Diradicaloids. *Journal of the American Chemical Society* **139.** ISSN: 15205126 (2017) (cit. on pp. 40, 114, 119).

132. Ullrich, T. *et al.* Singlet Fission in Carbene Derived Diradicaloids. *Angewandte Chemie International Edition.* ISSN: 14337851 (2020) (cit. on p. 40).

133. Austin, R. H., Baker, G. L., Etemad, S. & Thompson, R. Magnetic field effects on triplet exciton fission and fision in a polydiacetylene. *The Journal of Chemical Physics* **90,** 6642–6646. ISSN: 00219606 (1989) (cit. on p. 40).

134. Pandya, R. *et al.* Optical projection and spatial separation of spin entangled triplet-pairs from the S1 (21Ag-) state of pi-conjugated systems. *arXiv Preprint* (2020) (cit. on p. 40).

135. Musser, A. J. *et al.* Activated Singlet Exciton Fission in a Semiconducting Polymer. *Journal of the American Chemical Society* **135,** 12747–12754. ISSN: 0002-7863 (2013) (cit. on pp. 40, 71, 114, 119).

136. Musser, A. J., Al-Hashimi, M., Heeney, M. & Clark, J. Heavy-atom effects on intramolecular singlet fission in a conjugated polymer. *Journal of Chemical Physics* **151,** 044902. ISSN: 00219606 (2019) (cit. on p. 40).

137. Hu, J. *et al.* New insights into the design of conjugated polymers for intramolecular singlet fission. *Nature Communications* **9,** 2999. ISSN: 2041-1723 (2018) (cit. on p. 40).

138. Busby, E. *et al.* A design strategy for intramolecular singlet fission mediated by charge-transfer states in donor–acceptor organic materials. *Nature Materials* **14,** 426–433. ISSN: 1476-1122 (2015) (cit. on pp. 40, 114, 131).

139. Dover, C. B. *et al.* Endothermic singlet fission is hindered by excimer formation. *Nature Chemistry* **10,** 305–310. ISSN: 1755-4330 (2018) (cit. on pp. 40, 42, 165, 179, 180).

140. Müller, A. M., Avlasevich, Y. S., Müllen, K. & Bardeen, C. J. Evidence for exciton fission and fusion in a covalently linked tetracene dimer. *Chemical Physics Letters* **421,** 518–522. ISSN: 00092614 (2006) (cit. on p. 42).

141. Müller, A. M., Avlasevich, Y. S., Schoeller, W. W., Müllen, K. & Bardeen, C. J. Exciton fission and fusion in bis(tetracene) molecules with different covalent linker structures. *Journal of the American Chemical Society* **129,** 14240–14250. ISSN: 00027863 (2007) (cit. on p. 42).

142. Johnson, J. C. *et al.* Toward designed singlet fission: Solution photophysics of two indirectly coupled covalent dimers of 1,3-diphenylisobenzofuran. *Journal of Physical Chemistry B* **117,** 4680–4695. ISSN: 15205207 (2013) (cit. on pp. 42, 44, 147, 151).

143. Sanders, S. N. *et al.* Quantitative Intramolecular Singlet Fission in Bipentacenes. *Journal of the American Chemical Society* **137,** 8965–8972. ISSN: 0002-7863 (2015) (cit. on pp. 42, 43, 133, 151).

144. Basel, B. S. *et al.* Unified model for singlet fission within a non-conjugated covalent pentacene dimer. *Nature Communications* **8,** 1–8 (2017) (cit. on pp. 43, 46, 122).

145. Zirzlmeier, J. *et al.* Singlet fission in pentacene dimers. *Proceedings of the National Academy of Sciences* (2015) (cit. on pp. 43, 44, 133, 145, 147, 151).

146. Khan, S. & Mazumdar, S. Free Triplets Versus Bound Triplet-Triplet Biexciton in Intramolecular Singlet Fission Materials: Structure-Property Correlations. *Journal of Physical Chemistry C.* ISSN: 19327455 (2020) (cit. on pp. 43, 147).

147. Korovina, N. V. *et al.* Singlet Fission in a Covalently Linked Cofacial Alkynyltetracene Dimer. *Journal of the American Chemical Society* **138,** 617–627. ISSN: 15205126 (2016) (cit. on pp. 43, 147).

148. Korovina, N. V. *et al.* Linker-Dependent Singlet Fission in Tetracene Dimers. *Journal of the American Chemical Society* **140,** 10179–10190. ISSN: 15205126 (2018) (cit. on pp. 43, 147).

149. Shizu, K., Adachi, C. & Kaji, H. Effect of Vibronic Coupling on Correlated Triplet Pair Formation in the Singlet Fission Process of Linked Tetracene Dimers. *The journal of physical chemistry. A* **124,** 3641–3651. ISSN: 15205215 (2020) (cit. on p. 43).

150. Mora-Fuentes, J. P. *et al.* Singlet Fission in Pyrene-Fused Azaacene Dimers. *Angewandte Chemie International Edition.* ISSN: 14337851 (2019) (cit. on pp. 43, 71).

151. Mukhopadhyay, T. *et al.* Is the Chemical Strategy for Imbuing "Polyene" Character in Diketopyrrolopyrrole-Based Chromophores Sufficient for Singlet Fission? *The Journal of Physical Chemistry Letters* **8,** 984–991. ISSN: 1948-7185 (2017) (cit. on p. 43).

152. Kumarasamy, E. *et al.* Tuning Singlet Fission in π-Bridge-π Chromophores. *Journal of the American Chemical Society* **139,** 12488–12494. ISSN: 0002-7863 (2017) (cit. on pp. 43, 122).

153. Liu, H. *et al.* A Covalently Linked Tetracene Trimer: Synthesis and Singlet Exciton Fission Property. *Organic Letters,* acs.orglett.6b03739. ISSN: 1523-7060 (2017) (cit. on pp. 44, 151).

154. Pun, A. B. *et al.* Ultra-fast intramolecular singlet fission to persistent multiexcitons by molecular design. *Nature Chemistry* **11,** 821–828. ISSN: 1755-4330 (2019) (cit. on pp. 44, 151, 187).

155. Lukman, S. *et al.* Tuneable Singlet Exciton Fission and Triplet–Triplet Annihilation in an Orthogonal Pentacene Dimer. *Advanced Functional Materials* **25,** 5452–5461. ISSN: 1616-301X (2015) (cit. on pp. 44, 147, 151).

156. Hong, Y. *et al.* Efficient Multiexciton State Generation in Charge-Transfer-Coupled Perylene Bisimide Dimers via Structural Control. *Journal of the American Chemical Society* (2020) (cit. on pp. 44, 147, 151).

157. Lukman, S. *et al.* Tuning the role of charge-transfer states in intramolecular singlet exciton fission through side-group engineering. *Nature Communications* **7,** 13622 (2016) (cit. on pp. 44, 147, 151).

158. Basel, B. S. *et al.* Influence of the heavy-atom effect on singlet fission: A study of platinum-bridged pentacene dimers. *Chemical Science* **10,** 11130–11140. ISSN: 20416539 (2019) (cit. on p. 44).

159. Papadopoulos, I., Gao, Y., Hetzer, C., Tykwinski, R. R. & Guldi, D. M. Singlet Fission in Enantiomerically Pure Pentacene Dimers. *ChemPhotoChem,* cptc.202000016. ISSN: 2367-0932 (2020) (cit. on p. 44).

160. Arias, D. H., Ryerson, J. L., Cook, J. D., Damrauer, N. H. & Johnson, J. C. Polymorphism influences singlet fission rates in tetracene thin films. *Chem. Sci.* **7.** ISSN: 2041-6520 (2016) (cit. on p. 44).

161. Bhattacharyya, K. & Datta, A. Polymorphism Controlled Singlet Fission in TIPS-Anthracene: Role of Stacking Orientation. *The Journal of Physical Chemistry C* **121,** 1412–1420. ISSN: 1932-7447 (2017) (cit. on p. 44).

162. Tian, X. *et al.* Nanoscale exponential distance dependence and electron-transfer model for intermolecular singlet exciton fission observed in rubrene-doped organic films. *Organic Electronics* **50,** 429–434. ISSN: 15661199 (2017) (cit. on p. 44).

163. Lubert-Perquel, D. *et al.* Identifying triplet pathways in dilute pentacene films. *Nature Communications* **9.** ISSN: 20411723 (2018) (cit. on pp. 44, 46, 65, 89, 92, 122, 160, 167).

164. Pensack, R. D. *et al.* Striking the right balance of intermolecular coupling for high-efficiency singlet fission. *Chemical Science* **9,** 6240–6259. ISSN: 2041-6520 (2018) (cit. on pp. 44, 45, 158, 160).

165. Pensack, R. D. *et al.* Exciton Delocalization Drives Rapid Singlet Fission in Nanoparticles of Acene Derivatives. *Journal of the American Chemical Society* **137,** 6790–6803. ISSN: 0002-7863 (2015) (cit. on pp. 45, 114, 158).

166. Roberts, S. T. *et al.* Efficient Singlet Fission Discovered in a Disordered Acene Film. *Journal of the American Chemical Society* **134,** 6388–6400. ISSN: 0002-7863 (2012) (cit. on pp. 45, 70, 114, 126, 131).

167. Mou, W., Hattori, S., Rajak, P., Shimojo, F. & Nakano, A. Nanoscopic mechanisms of singlet fission in amorphous molecular solid. *Applied Physics Letters* **102,** 173301. ISSN: 00036951 (2013) (cit. on p. 45).

168. Margulies, E. A. *et al.* Sub-Picosecond Singlet Exciton Fission in Cyano-Substituted Diaryltetracenes. *Angewandte Chemie International Edition* **54,** 8679–8683. ISSN: 14337851 (2015) (cit. on pp. 45, 131).

169. Swenberg, C. E., van Metter, R. & Ratner, M. Comments on exciton fission and electron spin resonance in tetracene single crystals. *Chemical Physics Letters* **16,** 482–485. ISSN: 00092614 (1972) (cit. on pp. 45, 66, 123, 125, 165).

170. Kraffert, F. *et al.* Charge separation in PCPDTBT:PCBM blends from an EPR perspective. *Journal of Physical Chemistry C* **118,** 28482–28493. ISSN: 19327455 (2014) (cit. on pp. 45, 166).

171. Bayliss, S. L. *et al.* Tuning Spin Dynamics in Crystalline Tetracene. *J. Phys. Chem. Lett* **10,** 46 (2019) (cit. on pp. 45, 46, 179).

172. Weiss, L. R. *et al.* Strongly exchange-coupled triplet pairs in an organic semiconductor. *Nature Physics* **13,** 176–181. ISSN: 17452481 (2017) (cit. on pp. 45, 89, 122, 125, 166, 167, 196).

173. Tayebjee, M. J. Y. *et al.* Quintet multiexciton dynamics in singlet fission. *Nature Physics* **13,** 182–188. ISSN: 1745-2473 (2017) (cit. on pp. 45, 89, 122, 125, 167, 196).

174. Chen, M. *et al.* Quintet-triplet mixing determines the fate of the multiexciton state produced by singlet fission in a terrylenediimide dimer at room temperature. *Proceedings of the National Academy of Sciences* **116,** 201820932. ISSN: 0027-8424 (2019) (cit. on pp. 45, 167).

175. Matsui, Y. *et al.* Exergonic Intramolecular Singlet Fission of an Adamantane-Linked Tetracene Dyad via Twin Quintet Multiexcitons. *The Journal of Physical Chemistry C,* acs.jpcc.9b04503. ISSN: 1932-7447 (2019) (cit. on p. 46).

176. Collins, M. I., McCamey, D. R. & Tayebjee, M. J. Fluctuating exchange interactions enable quintet multiexciton formation in singlet fission. *Journal of Chemical Physics* **151.** ISSN: 00219606 (2019) (cit. on p. 46).

177. Bayliss, S. L. *et al.* Site-selective measurement of coupled spin pairs in an organic semiconductor. *Proceedings of the National Academy of Sciences* **115,** 5077–5082. ISSN: 10916490. arXiv: 1803.05225 (2018) (cit. on pp. 46, 86, 108, 111, 165, 167, 180, 181).

178. Yunusova, K. M. *et al.* Spin fine-structure reveals bi-exciton geometry in an organic semiconductor. *arXiv Preprint.* arXiv: 1912.04191v1 (2019) (cit. on p. 46).

179. Taffet, E. J., Beljonne, D. & Scholes, G. D. Overlap-Driven Splitting of Triplet Pairs in Singlet Fission. *Journal of the American Chemical Society.* ISSN: 0002-7863 (2020) (cit. on pp. 46, 86, 165, 181).

180. Gish, M. K., Pace, N. A., Rumbles, G. & Johnson, J. C. Emerging Design Principles for Enhanced Solar Energy Utilization with Singlet Fission. *The Journal of Physical Chemistry C* **123,** 3923–3934. ISSN: 1932-7447 (2019) (cit. on pp. 46, 158).

181. Lee, J. *et al.* Singlet Exciton Fission. *Accounts of Chemical Research* **46,** 11–12 (2013) (cit. on p. 46).

182. Rao, A. *et al.* Exciton Fission and Charge Generation via Triplet Excitons in Pentacene/C60 Bilayers. *Journal of the American Chemical Society* **132,** 12698–12703. ISSN: 0002-7863 (2010) (cit. on pp. 46, 160).

183. Congreve, D. N. *et al.* External quantum efficiency above 100% in a singlet-exciton-fission-based organic photovoltaic cell. *Science* **340,** 334–7. ISSN: 1095-9203 (2013) (cit. on pp. 46, 70).

184. Zukun, W. *et al.* Ultrafast Electron Transfer Before Singlet Fission and Slow Triplet State Electron Transfer in Pentacene Single Crystal/C 60 Heterostructure. *The Journal of Physical Chemistry A.* ISSN: 1089-5639 (2020) (cit. on p. 46).

185. Reusswig, P. D., Congreve, D. N., Thompson, N. J. & Baldo, M. A. Enhanced external quantum efficiency in an organic photovoltaic cell via singlet fission exciton sensitizer. *Applied Physics Letters* **101,** 113304. ISSN: 00036951 (2012) (cit. on pp. 47, 85).

186. Jadhav, P. J. *et al.* Triplet Exciton Dissociation in Singlet Exciton Fission Photovoltaics. *Advanced Materials* **24,** 6169–6174. ISSN: 09359648 (2012) (cit. on pp. 47, 85).

187. Kim, H. *et al.* Enacting Two-Electron Transfer from a Double-Triplet State of Intramolecular Singlet Fission. *Journal of the American Chemical Society* **140,** 7760–7763. ISSN: 0002-7863 (2018) (cit. on p. 47).

188. Einzinger, M. *et al.* Sensitization of silicon by singlet exciton fission in tetracene. *Nature* **571,** 90–94. ISSN: 0028-0836 (2019) (cit. on pp. 47, 70, 111).

189. Daiber, B. *et al.* A method to detect triplet exciton transfer from singlet fission materials into silicon solar cells: Comparing different surface treatments. *The Journal of Chemical Physics* **152,** 114201. ISSN: 0021-9606 (2020) (cit. on p. 47).

190. Niederhausen, J. *et al.* Tetracene ultrathin film growth on silicon. *arXiv Preprint.* arXiv: 2004.08562 (2020) (cit. on p. 47).

191. Rao, A. & Friend, R. H. Harnessing singlet exciton fission to break the Shockley–Queisser limit. *Nature Reviews Materials* **2,** 17063 (2017) (cit. on pp. 47, 70, 111, 158).

192. Futscher, M. H., Rao, A. & Ehrler, B. The Potential of Singlet Fission Photon Multipliers as an Alternative to Silicon-Based Tandem Solar Cells. *ACS Energy Letters* **3,** 2587–2592. ISSN: 23808195 (2018) (cit. on p. 47).

193. Bardeen, C. J. Bringing dark states to light. *Nature Materials* **13,** 1001–1003. ISSN: 1476-1122 (2014) (cit. on p. 47).

194. Thompson, N. J. *et al.* Energy harvesting of non-emissive triplet excitons in tetracene by emissive PbS nanocrystals. *Nat Mater* **13,** 1039–1043. ISSN: 1476-1122 (2014) (cit. on p. 47).

195. Tabachnyk, M. *et al.* Resonant energy transfer of triplet excitons from pentacene to PbSe nanocrystals. *Nature Materials* **13,** 1033–1038. ISSN: 1476-1122 (2014) (cit. on pp. 47, 70).

196. Davis, N. J. *et al.* Singlet Fission and Triplet Transfer to PbS Quantum Dots in TIPS-Tetracene Carboxylic Acid Ligands. *Journal of Physical Chemistry Letters* **9,** 1454–1460. ISSN: 19487185 (2018) (cit. on pp. 47, 70).

197. Allardice, J. *et al.* Engineering Molecular Ligand Shells on Quantum Dots for Quantitative Harvesting of Triplet Excitons Generated by Singlet Fission. *Journal of the American Chemical Society,* jacs.9b06584. ISSN: 0002-7863 (2019) (cit. on pp. 47, 70).

198. Steiner, A. M., Lissel, F., Fery, A., Lauth, J. & Scheele, M. Prospects of Coupled Organic-Inorganic Nanostructures for Charge and Energy Transfer Applications. *Angewandte Chemie International Edition.* ISSN: 1433-7851 (2020) (cit. on p. 48).

199. Cotton, D. E., Moon, A. P. & Roberts, S. T. Using Electronic Sum-Frequency Generation to Analyze the Interfacial Structure of Singlet Fission-Capable Perylenediimide Thin Films. *The Journal of Physical Chemistry C.* ISSN: 1932-7447 (2020) (cit. on p. 48).

200. Luo, X. *et al.* Mechanisms of triplet energy transfer across the inorganic nanocrystal/organic molecule interface. *Nature Communications* **11,** 1–10. ISSN: 20411723 (2020) (cit. on p. 48).

201. Shockley, W. & Queisser, H. J. Detailed Balance Limit of Efficiency of p-n Junction Solar Cells. *Journal of Applied Physics* **32,** 510–519. ISSN: 0021-8979 (1961) (cit. on pp. 48, 49, 70, 71).

202. Planck, M. *The Theory of Heat Radiation* (Courier Corporation, 2013) (cit. on p. 49).

203. Hirst, L. C. & Ekins-Daukes, N. J. Fundamental losses in solar cells. *Progress in Photovoltaics: Research and Applications* **19,** 286–293. ISSN: 10627995 (2011) (cit. on p. 49).

204. De Vos, A. Detailed balance limit of the efficiency of tandem solar cells. *Journal of Physics D: Applied Physics* **13,** 839–846. ISSN: 00223727 (1980) (cit. on p. 49).

205. Gray, V., Dzebo, D., Abrahamsson, M., Albinsson, B. & Moth-Poulsen, K. Triplet-triplet annihilation photon-upconversion: Towards solar energy applications. *Physical Chemistry Chemical Physics* **16,** 10345–10352. ISSN: 14639076 (2014) (cit. on p. 50).

206. Schmidt, T. W. Kinetic Analysis of Photochemical Upconversion by Triplet - Triplet Annihilation: Beyond Any Spin Statistical Limit €. *Journal of Physical Chemistry Letters,* 1795–1799 (2010) (cit. on p. 50).

207. Nishimura, N. *et al.* Photon Upconversion from Near-Infrared to Blue Light with TIPS-Anthracene as an Efficient Triplet–Triplet Annihilator. *ACS Materials Letters* **1,** 660–664. ISSN: 2639-4979 (2019) (cit. on p. 50).

208. Ye, C. *et al.* Optimizing photon upconversion by decoupling excimer formation and triplet triplet annihilation. *Phys. Chem. Chem. Phys* **22,** 1715 (2020) (cit. on p. 50).

209. Gray, V., Moth-Poulsen, K., Albinsson, B. & Abrahamsson, M. Towards efficient solid-state triplet–triplet annihilation based photon upconversion: Supramolecular, macromolecular and self-assembled systems. *Coordination Chemistry Reviews* **362,** 54–71. ISSN: 00108545 (2018) (cit. on p. 50).

210. Felter, K. M. *et al.* Solid-State Infrared Upconversion in Perylene Diimides Followed by Direct Electron Injection. *ACS Energy Letters* **5,** 124–129. ISSN: 2380-8195 (2020) (cit. on p. 50).

211. Lin, T., Perkinson, C. F. & Baldo, M. A. Strategies for High-Performance Solid-State Triplet–Triplet-Annihilation-Based Photon Upconversion. *Advanced Materials* **1908175,** 1908175. ISSN: 0935-9648 (2020) (cit. on p. 50).

212. Imperiale, C. J., Green, P. B., Miller, E. G., Damrauer, N. H. & Wilson, M. W. B. Triplet-Fusion Upconversion Using a Rigid Tetracene Homodimer. *The Journal of Physical Chemistry Letters* **10,** 7463–7469. ISSN: 1948-7185 (2019) (cit. on p. 50).

213. Fischer, S., Fröhlich, B., Steinkemper, H., Krämer, K. & Goldschmidt, J. Absolute upconversion quantum yield of β-NaYF4 doped with Er3+ and external quantum efficiency of upconverter solar cell devices under broad-band excitation considering spectral mismatch corrections. *Solar Energy Materials and Solar Cells* **122,** 197–207. ISSN: 09270248 (2014) (cit. on p. 50).

214. Hudry, D., Howard, I. A., Popescu, R., Gerthsen, D. & Richards, B. S. Structure–Property Relationships in Lanthanide-Doped Upconverting Nanocrystals: Recent Advances in Understanding Core–Shell Structures. *Advanced Materials* **31.** ISSN: 15214095 (2019) (cit. on p. 50).

215. Ekins-Daukes, N. J. *et al.* Photovoltaic efficiency enhancement through thermal up-conversion. *Applied Physics Letters* **82,** 1974–1976. ISSN: 0003-6951 (2003) (cit. on p. 50).

216. Tayebjee, M. J., McCamey, D. R. & Schmidt, T. W. Beyond shockley-queisser: Molecular approaches to high-efficiency photovoltaics. *Journal of Physical Chemistry Letters* **6,** 2367–2378. ISSN: 19487185 (2015) (cit. on p. 50).

217. Jiang, Y *et al.* Singlet fission and tandem solar cells reduce thermal degradation and enhance lifespan. *arXiv Preprint.* arXiv: 2003.05565 (2020) (cit. on p. 51).

218. De Mello, J. C., Wittmann, H. F. & Friend, R. H. An improved experimental determination of external photoluminescence quantum efficiency. *Advanced Materials* **9,** 230–232. ISSN: 0935-9648 (2004) (cit. on pp. 55, 74).

219. Chen, K., Gallaher, J. K., Barker, A. J. & Hodgkiss, J. M. Transient Grating Photoluminescence Spectroscopy: An Ultrafast Method of Gating Broadband Spectra. *The Journal of Physical Chemistry Letters* **5,** 1732–1737. ISSN: 1948-7185 (2014) (cit. on pp. 58, 126, 128).

220. Manzoni, C., Polli, D. & Cerullo, G. Two-color pump-probe system broadly tunable over the visible and the near infrared with sub-30 fs temporal resolution. *Review of Scientific Instruments* **77.** ISSN: 00346748 (2006) (cit. on pp. 60, 63, 64, 169).

221. Brida, D. *et al.* Generation of 8.5-fs pulses at 1.3 µm for ultrabroadband pump-probe spectroscopy. *Opt. Express* **17,** 12510–12515 (2009) (cit. on p. 60).

222. Tan, D., Sharafudeen, K. N., Yue, Y. & Qiu, J. Femtosecond laser induced phenomena in transparent solid materials: Fundamentals and applications. *Progress in Materials Science* **76,** 154–228. ISSN: 00796425 (2016) (cit. on p. 63).

223. Kovalenko, S. A., Dobryakov, A. L., Ruthmann, J. & Ernsting, N. P. Femtosecond spectroscopy of condensed phases with chirped supercontinuum probing. *Physical Review A - Atomic, Molecular, and Optical Physics* **59,** 2369–2384. ISSN: 10502947 (1999) (cit. on pp. 64, 170).

224. Albert-Seifried, S. & Friend, R. H. Measurement of thermal modulation of optical absorption in pump-probe spectroscopy of semiconducting polymers. *Applied Physics Letters* **98,** 223304. ISSN: 0003-6951 (2011) (cit. on pp. 64, 119, 191).

225. Sloop, D. J., Yu, H. L., Lin, T. S. & Weissman, S. I. Electron spin echoes of a photoexcited triplet: Pentacene inp-terphenyl crystals. *The Journal of Chemical Physics* **75,** 3746–3757. ISSN: 00219606 (1981) (cit. on pp. 65, 92).

226. Yang, T. C., Sloop, D. J., Weissman, S. I. & Lin, T. S. Zero-field magnetic resonance of the photo-excited triplet state of pentacene at room temperature. *Journal of Chemical Physics* **113,** 11194–11201. ISSN: 00219606 (2000) (cit. on pp. 65, 92).

227. ITRPV. *International Technology Roadmap for Photovoltaic 2020* 2020 (cit. on p. 70).

228. Burdett, J. J. & Bardeen, C. J. The Dynamics of Singlet Fission in Crystalline Tetracene and Covalent Analogs. *Accounts of Chemical Research* **46,** 1312–1320. ISSN: 0001-4842 (2013) (cit. on pp. 70, 114, 173, 183).

229. Liu, X. *et al.* Pyrene-stabilized acenes as intermolecular singlet fission candidates: Importance of exciton wave-function convergence. *J. Phys.: Condens. Matter* **32,** 184001. ISSN: 0953-8984 (2020) (cit. on p. 71).

230. Müller, M. *et al.* "Butterfly Wings" Stabilize Heptacene. *Chemistry - A European Journal* **24,** 8087–8091. ISSN: 09476539 (2018) (cit. on pp. 71, 111).

231. Di, D. *et al.* Efficient Triplet Exciton Fusion in Molecularly Doped Polymer Light-Emitting Diodes. *Advanced Materials* **29,** 1605987. ISSN: 09359648 (2017) (cit. on p. 71).

232. Chow, P. C. Y., Albert-Seifried, S., Gélinas, S. & Friend, R. H. Nanosecond Intersystem Crossing Times in Fullerene Acceptors: Implications for Organic Photovoltaic Diodes. *Advanced Materials* **26,** 4851–4854. ISSN: 09359648 (2014) (cit. on pp. 81, 133, 171).

233. Stoll, S. & Schweiger, A. EasySpin, a comprehensive software package for spectral simulation and analysis in EPR (2005) (cit. on pp. 88, 91, 92, 94, 95, 105, 109, 110, 166).

234. Müller, M. *et al.* Stabilization by Benzannulation: Butterfly-Azaacenes. *Chemistry - A European Journal,* 1–6. ISSN: 09476539 (2018) (cit. on pp. 90, 92).

235. Poletayev, A. D. *et al.* Triplet Dynamics in Pentacene Crystals: Applications to Fission-Sensitized Photovoltaics. *Advanced Materials* **26,** 919–924. ISSN: 09359648 (2014) (cit. on p. 99).

236. Shinar, J. & Swanson, L. S. Optically detected magnetic resonance (ODMR) studies of conducting polymers: an overview. *Synthetic Metals* **50,** 621–630. ISSN: 03796779 (1992) (cit. on p. 105).

237. Bayliss, S. L. *et al.* Geminate and Nongeminate Recombination of Triplet Excitons Formed by Singlet Fission. *Physical Review Letters* **112,** 238701. ISSN: 0031-9007 (2014) (cit. on pp. 106, 163).

238. Miller, O. D., Yablonovitch, E & Kurtz, S. R. Strong Internal and External Luminescence as Solar Cells Approach the Shockley–Queisser Limit. *IEEE Journal of Photovoltaics* **2,** 303–311. ISSN: 2156-3403 VO - 2 (2012) (cit. on p. 111).

239. Ross, R. T. Some thermodynamics of photochemical systems. *The Journal of Chemical Physics* **46,** 4590–4593. ISSN: 00219606 (1967) (cit. on p. 111).

240. Yao, J. *et al.* Quantifying Losses in Open-Circuit Voltage in Solution-Processable Solar Cells (2015) (cit. on p. 111).

241. Rau, U. Reciprocity relation between photovoltaic quantum efficiency and electroluminescent emission of solar cells. *Physical Review B* **76,** 085303. ISSN: 10980121 (2007) (cit. on p. 111).

242. Margulies, E. A. *et al.* Enabling singlet fission by controlling intramolecular charge transfer in π-stacked covalent terrylenediimide dimers. *Nature Chemistry* **8.** ISSN: 1755-4330 (2016) (cit. on pp. 114, 131).

243. Kasai, Y., Tamai, Y., Ohkita, H., Benten, H. & Ito, S. Ultrafast Singlet Fission in a Push–Pull Low-Bandgap Polymer Film. *Journal of the American Chemical Society* **137,** 15980–15983. ISSN: 0002-7863 (2015) (cit. on p. 114).

244. Huynh, U. N. V. *et al.* Transient Magnetophotoinduced Absorption Studies of Photoexcitations in pi-Conjugated Donor-Acceptor Copolymers. *Physical Review Letters* **119,** 017401. ISSN: 0031-9007 (2017) (cit. on p. 114).

245. Miyata, K. *et al.* Coherent singlet fission activated by symmetry breaking. *Nature Chemistry* **9,** 983–989. ISSN: 1755-4330 (2017) (cit. on p. 114).

246. Grieco, C. *et al.* Direct Observation of Correlated Triplet Pair Dynamics During Singlet Fission Using Ultrafast Mid-IR Spectroscopy. *The Journal of Physical Chemistry C* **122,** 2012–2022. ISSN: 19327455 (2018) (cit. on p. 114).

247. Folie, B. D., Haber, J. B., Refaely-Abramson, S., Neaton, J. B. & Ginsberg, N. S. Long-Lived Correlated Triplet Pairs in a π-Stacked Crystalline Pentacene Derivative. *Journal of the American Chemical Society* **140,** 2326–2335. ISSN: 0002-7863 (2018) (cit. on p. 114).

248. Hu, P. & Wu, J. Modern zethrene chemistry. *Canadian Journal of Chemistry* **95,** 223–233. ISSN: 0008-4042 (2017) (cit. on p. 114).

249. Hückel, E. Grundzüge der Theorie ungesättigter und aromatischer Verbindungen. Von . Verlag Chemie, G. m. b. H., Berlin 1938. Preis br. RM. 8,–. *Angewandte Chemie* **51,** 310–310. ISSN: 00448249 (1938) (cit. on p. 114).

250. Baird, N. C. Quantum Organic Photochemistry. II. Resonance and Aromaticity in the Lowest3$\pi\pi$ State of Cyclic Hydrocarbons. *Journal of the American Chemical Society* **94,** 4941–4948. ISSN: 15205126 (1972) (cit. on p. 114).

251. Ottosson, H. Exciting excited-state aromaticity. *Nature Chemistry* **4,** 969 (2012) (cit. on p. 114).

252. Möllerstedt, H., Piqueras, M. C., Crespo, R. & Ottosson, H. Fulvenes, fulvalenes, and azulene: Are they aromatic chameleons? *Journal of the American Chemical Society* **126,** 13938–13939. ISSN: 00027863 (2004) (cit. on p. 114).

253. Ayub, R., Bakouri, O. E., Jorner, K., Solà, M. & Ottosson, H. Can Baird's and Clar's Rules Combined Explain Triplet State Energies of Polycyclic Conjugated Hydrocarbons with Fused 4nπ- and (4n + 2)π-Rings? *The Journal of Organic Chemistry* **82,** 6327–6340. ISSN: 0022-3263 (2017) (cit. on p. 114).

254. Villaume, S., Fogarty, H. A. & Ottosson, H. Triplet-State Aromaticity of 4nπ-Electron Monocycles: Analysis of Bifurcation in the π Contribution to the Electron Localization Function. *ChemPhysChem* **9,** 257–264. ISSN: 1439-7641 (2008) (cit. on p. 114).

255. Engi, G. Über neue Derivate des Indigos und anderer indigoider Farbstoffe. *Angewandte Chemie* **27,** 144–148. ISSN: 1521-3757 (1914) (cit. on p. 115).

256. Buchanan, E. A., Havlas, Z. & Michl, J. in *Advances in Quantum Chemistry* 175–227 (Academic Press, 2017). ISBN: 9780128128886 (cit. on pp. 115, 117).

257. Schleyer, P. V. R., Maerker, C., Dransfeld, A., Jiao, H. & Van Eikema Hommes, N. J. Nucleus-independent chemical shifts: A simple and efficient aromaticity probe. *Journal of the American Chemical Society* **118,** 6317–6318. ISSN: 00027863 (1996) (cit. on p. 115).

258. Peach, M. J. G., Williamson, M. J. & Tozer, D. J. Influence of Triplet Instabilities in TDDFT. *Journal of Chemical Theory and Computation* **7,** 3578–3585. ISSN: 1549-9618 (2011) (cit. on p. 117).

259. Eaton, S. W. *et al.* Singlet Exciton Fission in Polycrystalline Thin Films of a Slip-Stacked Perylenediimide. *Journal of the American Chemical Society* **135,** 14701–14712. ISSN: 0002-7863 (2013) (cit. on pp. 119, 131).

260. Bolzonello, L., Albertini, M., Collini, E. & Di Valentin, M. Delocalized triplet state in porphyrin J-aggregates revealed by EPR spectroscopy. *Physical Chemistry Chemical Physics* **19,** 27173–27177. ISSN: 1463-9076 (2017) (cit. on pp. 125, 195).

261. Walker, B., Musser, A., Beljonne, D. & Friend, R. Singlet exciton fission in solution. *Nature Chemistry* **5.** ISSN: 17554330 (2013) (cit. on p. 131).

262. Arroyo, C. R. *et al.* Quantum interference effects at room temperature in OPV-based single-molecule junctions. *Nanoscale Research Letters* **8,** 2–7. ISSN: 1556276X (2013) (cit. on p. 145).

263. Sangtarash, S., Sadeghi, H. & Lambert, C. J. Exploring quantum interference in heteroatom-substituted graphene-like molecules. *Nanoscale* **8,** 13199–13205. ISSN: 20403372 (2016) (cit. on p. 145).

264. Liu, X. *et al.* Gating of Quantum Interference in Molecular Junctions by Heteroatom Substitution. *Angewandte Chemie - International Edition* **56,** 173–176. ISSN: 15213773 (2017) (cit. on p. 145).

265. Alanazy, A. *et al.* Cross-conjugation increases the conductance of: Meta-connected fluorenones. *Nanoscale* **11,** 13720–13724. ISSN: 20403372 (2019) (cit. on p. 145).

266. Schäfer, J. *et al.* Hole Transfer Processes in meta- and para-Conjugated Mixed Valence Compounds: Unforeseen Effects of Bridge Substituents and Solvent Dynamics. *Journal of the American Chemical Society* **139,** 6200–6209. ISSN: 15205126 (2017) (cit. on p. 145).

267. Fallon, K. J. *et al.* Exploiting Excited-State Aromaticity To Design Highly Stable Singlet Fission Materials. *Journal of the American Chemical Society* **141,** 13867–13876. ISSN: 0002-7863 (2019) (cit. on p. 169).

268. Trebino, R. *et al.* Measuring ultrashort laser pulses in the time-frequency domain using frequency-resolved optical gating. *Review of Scientific Instruments* **68,** 3277–3295. ISSN: 00346748 (1997) (cit. on p. 169).

269. Priestley, E. B. & Robinson, G. W. On the apparent absence of triplet-triplet absorption in pure organic molecular crystals. *Molecular Physics* **26,** 159–167. ISSN: 13623028 (1973) (cit. on p. 173).

270. Schiefer, S., Huth, M., Dobrinevski, A. & Nickel, B. Determination of the crystal structure of substrate-induced pentacene polymorphs in fiber structured thin films. *Journal of the American Chemical Society* **129,** 10316–10317. ISSN: 00027863 (2007) (cit. on p. 173).

271. Schwieger, T., Liu, X., Olligs, D., Knupfer, M. & Schmidt, T. Orientation and electronic properties of pentacene molecules on SiO 2 and GeS(0001) studied using x-ray absorption spectroscopy. *Journal of Applied Physics* **96,** 5596–5600. ISSN: 00218979 (2004) (cit. on p. 173).

272. Milita, S., Santato, C. & Cicoira, F. Structural investigation of thin tetracene films on flexible substrate by synchrotron X-ray diffraction. *Applied Surface Science* **252,** 8022–8027. ISSN: 01694332 (2006) (cit. on p. 173).

273. Abthagir, P. S. *et al.* Studies of tetracene- and pentacene-based organic thin-film transistors fabricated by the neutral cluster beam deposition method. *Journal of Physical Chemistry B* **109,** 23918–23924. ISSN: 15206106 (2005) (cit. on p. 173).

274. Della Valle, R. G., Venuti, E., Brillante, A. & Girlande, A. Inherent structures of crystalline tetracene. *Journal of Physical Chemistry A* **110,** 10858–10862. ISSN: 10895639 (2006) (cit. on p. 182).

275. Tait, C. E., Neuhaus, P., Anderson, H. L. & Timmel, C. R. Triplet State Delocalization in a Conjugated Porphyrin Dimer Probed by Transient Electron Paramagnetic Resonance Techniques. *Journal of the American Chemical Society* **137,** 6670–6679. ISSN: 0002-7863 (2015) (cit. on p. 195).

276. Franco, L. *et al.* Time-Resolved EPR of Photoinduced Excited States in a Semiconducting Polymer/PCBM Blend. *The Journal of Physical Chemistry C* **117,** 1554–1560. ISSN: 1932-7447 (2013) (cit. on p. 195).